Aix-Marseille Université
The University of Sydney
Ecole doctorale 352
Institut Fresnel/Equipe Clarté

Thèse présentée pour obtenir le grade universitaire de docteur

Discipline: Physique et sciences de la matière
Spécialité: Optique, Photonique et Traitement d'Image

Rémi COLOM

Etude théorique et expérimentale des résonances optiques des résonateurs de Mie diélectriques pour exalter les intéractions lumière-matière

Theoretical and experimental study of optical resonances in dielectric Mie resonators to enhance light-matter interactions

Soutenue le 25/01/2018 devant le jury composé de:

Gérard COLAS DES FRANCS	Université de Bourgogne	Rapporteur
Juan José SAENZ	Donostia International Physics Center	Rapporteur
Isabelle STAUDE	Abbe center of photonics	Examinateur
Giuseppe LEO	Laboratoire Matériaux et Phénomènes Quantiques	Examinateur
Martijn DE STERKE	The university of Sydney	Examinateur
Stefano PALOMBA	The university of Sydney	Examinateur
Brian STOUT	Institut Fresnel	Examinateur
Nicolas BONOD	Institut Fresnel	Directeur de thèse

Acknowledgements

Avant de remercier, comme c'est de tradition, toutes les personnes qui m'ont permis par leur aide et leur soutien d'aller au bout de ce doctorat, j'aimerais profiter de l'opportunité qui m'est ici donnée pour prendre un peu de recul et tirer un bilan de ces trois dernières années.
Je ne pense pas exagérer en commençant par dire que j'en ressors changé. Cette thèse fut d'abord l'occasion de radicalement chambouler l'image que je pouvais me faire du milieu de la recherche. J'ai pu y découvrir une foule de personnes profondément passionnées par leur travail qui ont contribué à rendre cette expérience si enrichissante. Ce fut aussi l'occasion de découvrir à quoi ressembler la science "en pleine action". J'étais un peu frustré par la manière dont la science m'avait été enseignée durant mes études supérieures. J'en suis ressorti avec le sentiment de n'avoir fait qu'effleurer un grand nombre de domaines de la physique sans jamais avoir l'opportunité d'approfondir aucun d'entre eux. Mes travaux de thèse furent au contraire l'occasion d'aller plus en profondeur et de sans-cesse chercher à améliorer ma compréhension des problèmes que je considérais. Il m'est bien entendu arrivé de m'égarer durant ce laborieux processus mais j'ai toujours pu compter sur l'aide de mes (nombreux) encadrants pour me conseiller et me guider. J'aimerais donc commencer remercier aussi bien mes encadrants en France, Nicolas et Brian, qu'en Australie Boris et Stefano. J'ai conscience de leur devoir en grande partie les travaux présentés dans ce manuscrit.
Tout d'abord Nicolas qui m'a été d'un grand soutien tout au long de ces trois années et dont l'aide a été précieuse jusque dans les derniers instants de la rédaction de ce manuscrit. Merci en particulier d'avoir si souvent consenti à te lever aux aurores pour nos nombreuses réunions par skype lorsque j'étais en Australie.
Brian ensuite qui a su m'enseigner au cours de nos innombrables discussions les subtilités de la théorie multipolaire et bien plus encore.
I also would like to thank Stefano who has patiently trained me to the difficult task of making experiments in non-linear optics.
Je tiens finalement à remercier Boris qui a aussi été d'une grande aide lors de mon séjour à Sydney. J'ai aussi conscience de la chance qui m'a été offerte de réaliser ce doctorat en cotutelle entre l'institut Fresnel à Marseille et l'université de Sydney. Je voudrais par conséquent

exprimer toute ma gratitude à Stefan qui a rendu cette collaboration franco-australienne possible.

Je tiens également à remercier toutes les personnes qui ont collaboré de près ou de loin au travail exposé dans ce manuscrit. Merci tout particulièrement à Alexis, Julien et Xavi qui ont été d'une grande aide dans les premiers mois de ce doctorat. Merci aussi à Fred et Igor du CINAM qui m'ont initié à la nanofabrication et qui ont fabriqué les échantillons pour l'étude expérimentale présentée ci-après. Je tiens finalement à remercier Thomas Begou et l'équipe RCMO à l'institut Fresnel qui ont déposé les couches minces de silicium.
I finally would like to thank Dragomir Neshev, Andrey Miroshnichenko and Yuri Kivshar who have played an instrumental role in the experimental project presented in the final chapter.

Je voudrais remercier et souhaiter bon courage à tous mes collègues doctorants aussi bien à Marseille qu'à Sydney. I would especially like to thank Kaizad, my officemate both in Marseille and Sydney for our motivating discussions.

Je voudrais finalement remercier ma famille pour le soutien qu'ils m'ont apporté durant toutes ces années. Tout d'abord mes parents qui m'ont permis d'aller au bout de mes études supérieures. Mes deux soeurs Sophie et Anne-Cécile qui ont été tout au long de ces années des exemples pour moi.

Abstract

Nanophotonics is the study of the interaction of light with nanometer scale structures. At such a scale, structures may exhibit a resonant behavior as their size is close to the wavelength of visible light. This resonant behavior enhances light-matter interactions and could therefore be beneficial for countless applications ranging from biosensing, light harvesting to even cancer therapy. Plasmonic resonators have consequently been of interest to the scientific community because of their resonant interaction with light. High refractive index subwavelength resonators made of dielectrics or semi-conductors (silicon for instance) have also recently emerged as a promising way of enhancing light-matter interactions through the excitation of Mie resonances while suffering from less dissipative losses than plasmonic resonators. The work presented in the scope of this thesis is mostly concerned with the theoretical and experimental study of the resonant interaction between light and high refractive-index scatterers. We first studied the optimal interactions of light with subwavelength resonant scatterers. The objective was in fact to determine the conditions that optimize the scattering or absorption of light by subwavelength sized scatterers. Asymptotic resonance conditions for Mie resonators were subsequently determined and were used to derive approximate models capable of predicting the resonant behavior of high-index dielectric resonators. High-refractive index resonators can be seen as open photonic cavities. The modes of this type of cavities, that only have a finite lifetime as they suffer from radiative losses, are usually referred to as Quasi Normal Modes (QNM). Using pole expansions of the S matrix associated with high refractive index scatterers, we derived QNM expansions of the scattered field of Mie resonators that also evidenced the presence of a non-resonant response. We then showed how QNM expansions could be used to describe the scattering problem in the time domain. Finally, we experimentally studied nonlinear effects in silicon nanodisks. In particular, we measured the degenerate four-wave mixing signal obtained while pumping at two different wavelengths. We observed a large enhancement of the four-wave mixing signal from the nanodisks as compared to an unpatterned silicon thin film when the two pump wavelengths were close to the wavelengths of two resonances of the nanodisk.

Résumé en français

La nanophotonique a pour objet l'étude de l'intéraction résonante entre la lumière et des structures à l'échelle nanométrique. A de telles échelles, les structures dont la taille est de l'ordre de la longueur d'onde de la lumière visible peuvent en effet présenter un comportement résonant lorsqu'elles intéragissent avec la lumière. Ce comportement résonant, comme il permet d'exalter les intéractions lumière matière, pourraient être bénéfique pour bon nombre d'applications touchant aussi bien à la biologie ou la médecine qu'au photovoltaique.

C'est pour cette raison que les résonateurs plasmoniques qui sont des diffuseurs sub-longeur d'onde constitués de métaux nobles et qui supportent des resonances dues à l'oscillation collective de leurs électrons de conduction font depuis longtemps l'objet d'un vif intérêt. Les résonateurs sub-longueur d'onde à haut indice de réfraction, supportant des résonances de Mie, ont récemment émergé comme une bonne plateforme pour exalter les interactions lumière-matière. Ce type de structures présente aussi l'avantage de supporter à la fois des résonances de type électriques et magnétiques ce qui permet, entre autre, de contrôler la direction dans laquelle la lumière est rayonnée de manière privilégiée. Les travaux présentés dans ce manuscrit ont pour objet l'étude de l'interaction résonante entre la lumière et les résonateurs diélectriques haut indice. Cette interaction sera étudié à la fois d'un point de vue théorique et expérimental.

Dans le chapitre 3, nous commencerons par présenter les outils théoriques sur lesquels reposeront les études théoriques réalisées par la suite. L'intéraction d'une excitation électromagnétique avec une structure photonique donne naissance à un champ diffusé. L' étude de la diffusion élastique de la lumière a pour but de déterminer le champ diffusé par une structure ayant une géométrie et des propriétés optiques définies. La réponse électromagnétique des structures de forme et de composition arbitraires peut être prédite au moyen d'outils informatiques reposant sur des méthodes numériques pour la résolution des équations de Maxwell. L'emploi de ces méthodes numériques pour étudier la diffusion de la lumière ne permettent cependant pas toujours d'accéder à une meilleure compréhension des phénomènes physiques à l'origine des comportements résonants observés. La théorie de Mie, basée sur la décomposotion des champs sur la base multipolaire, présente l'avantage

d'être l'une des rares solutions exactes à un problème de diffusion électromagnétique non trivial. Cette théorie qui permet de prédire la réponse électromagnétique de diffuseur sphérique est par conséquent un outil puissant pour décrire et comprendre l'intéraction de la lumière avec des strctures sub-longueur d'onde.
Le chapitre 3 aura pour but de présenter la formulation multipolaire du problème de la diffusion électromagnétique. Après une introduction générale de la théorie multipolaire et une présentation de nos notations, nous introduirons trois formulations différentes du problème de la diffusion électromagnétique dans la base multipolaire. Nous verrons en particulier qu'une de ces fomulations, basée sur la matrice S permet une expression très simple de la loi de conservation de l'énergie. Une autre de ces formulations apparaitra comme étant particulièrement utile pour traiter des pertes par radiation que subissent aussi bien les résonateurs plasmoniques que les résonateurs de Mie.

Le chapitre 4 est quant à lui dévolu à l'étude des conditions optimales d'interaction entre la lumière et des résonateurs sub-longueur d'onde. En bref, l'objectif y est de déteminer quelles sont les conditions pour lesquelles l'absorption ou la diffusion de la lumière par un diffuseur sub-longueur d'onde peuvent être maximisées. Nous débuterons ce chapitre en introduisant les sections efficaces d'absorption, d'extinction et de diffusion qui servent à quantifier l'interaction de la lumière avec un objet en champ lointain. En utilisant la base multipolaire, il est possible de montrer que toutes ces quantités peuvent être decomposées en une somme de section efficaces partielles, chacun des termes de cette somme étant associé à un multipole donné. Dans ce chapitre, nous commencerons par déterminer les limites supérieures des sections efficaces partielles d'absorption et de diffusion associées à chaque multipole. Alors que la limite supérieure des sections efficaces d'absorption sera désignée sous le terme d'absorption idéale, la limite supérieure des sections efficaces de diffusion sera appelée limite d'unitarité. Nous déterminerons ensuite quelles sont les conditions qui permettent d'atteindre ces limites. Il s'agira en particulier de déterminer quelle est la permittivité requise pour atteindre ces limites pour un diffuseurs sphériques de taille donnée. L'interaction résonante de la lumière avec des structures photoniques n'est pas seulement avantageuses dans le domaine du champ lointain. Elles présente aussi un intérêt par les exaltations du champ proche qu'elle peut produire. Nous conclurons donc ce chapitre par une étude du champ proche et nous montrerons en particulier que les résonances du champ proche sont déplacées vers le rouge par rapport aux résonances obervées en champ lointain.

Le chapitre 5 aura deux objectifs. Le premier objectif sera de déterminer des conditions de résonances asymptotiques pour les résonateurs diélectriques à haut indice. Il est connu de longue date que les résonances plasmoniques de particules très petites devant la longueur d'onde peuvent être prédites par la condition de résonance quasi-statique $\varepsilon_s = -2$. Il s'agira ici, de manière analogue, de déterminer des condi-

tions de résonance asymptotiques pour les résonateurs de Mie. Il sera en particulier démontré que la résonance de type dipôle magnétique de sphéres possédant un haut indice de réfraction n_s peut se produire au voisinage de la longueur d'onde suivante: $\lambda = 2n_sR$ où R est le rayon de la sphère considérée. Il sera parallèlement démontré que la résonance de type dipôle électrique se produisent au voisinage d'une longueur d'onde plus courte $\lambda_{res} = n_s\frac{2\pi}{r_1}R$ où $r_1 = 4.49$ représente le premier zéro de la fonction fonction de Bessel d'ordre 1.
Le second obectif sera d'utiliser ces conditions de résonance pour calculer des modèles approximés capable de prédire le comportement de diffuseurs haut indice sub-longueur d'onde au voisinage de leurs résonances.

Dans le chapitre 6, nous procèderons à l'étude modale de l'interaction entre la lumière et des résonateurs diélectriques haut indice. Ces résonateurs peuvent être vu comme des cavités optiques ouvertes. Les modes de ces structures ont par conséquent une durée de vie limitée en raison des pertes par radiation qu'ils subissent et sont communément appelés modes quasi normaux (quasi normal modes). Ils peuvent par conséquent être décrit en introduisant des fréquence complexes $\omega_n = \omega_{n,r} + i\omega_{n,i}$ dont la partie imaginaire traduit la décroissance exponentielle subie par ces modes. Comme ces modes doivent aussi obéir aux conditions d'onde sortante, leur dépendance radiale doit asymptotiquement tendre vers $\frac{e^{i\frac{\omega_n}{c}r}}{r}$ en champ lointain ce qui entraine un comportement divergent en champ lointain. Nous tenterons dans ce chapitre d'étudier l'interaction résonante de la lumière avec des résonateurs à haut indice de réfraction en utilisant leurs modes. Deux problèmes devront en particulier être résolus: la base des modes quasi-normaux est-elle complète pour exprimer le champ diffusé ou doit-on aussi prendre en compte des contributions non-résonantes? Le deuxième problème concernera la divergence de ces modes quasi-normaux : comment est-il possible d'exprimer le champ diffusé dans cette base alors que le champ des modes quasi-normaux diverge en champ lointain?
Cette étude qui est basée sur des développement en terme de pôles des coefficients de la matrice S nous permettra de mettre en évidence la présence d'un terme non-résonant en plus des contributions résonantes dues à l'excitation de modes quasi-normaux. Nous montrerons ensuite que l'interférence entre les termes résonants et non-résonants est à l'origine de la forme asymmétrique des résonances de résonateurs de Mie. Nous montrerons enfin que les expansions du champ diffusé en terme de QNM permettent l'étude de la diffusion de la lumière par un résonateur dans le domaine temporel.

Le dernier chapitre aura pour objet l'étude expérimentale d'effets d'optique non-linéaire dans des résonateurs de Mie. Nous nous intéresserons plus particulièrement au processus de mélange à quatre ondes dégénéré dans des nanodisques de silicium sub-longueur d'onde. Les résonances du champ diffusé s'accompagnent souvent d'une exaltation du champ électrique à l'intérieur de ces résonateurs. Ces

exaltations du champ peuvent être bénéfique pour bon nombre d'applications et en particulier l'optique non-linéaire. Ici nous mesurerons le signal de mélange à quatre onde dégénéré produit lorsque l'on illumine un nanodisque de silicium avec deux pompes aux fréquences distinctes ω_1 et ω_2. Nous nous intéresserons plus particulièrement au cas où les fréquences des pompes sont proches de deux résonances du nanodisque de silicium donnant lieu à une exaltation du champ interne.

Contents

Chapter 1

Introduction:

The study of the resonant interaction of light with nano- or micro-structures has long been the subject of a keen interest in optics and photonics. Numerous potential applications would indeed be enabled by the use of such resonators allowing to increase light-matter interactions. In particular, their ability to confine and control light at the nanoscale could be beneficial for a large set of applications ranging from optical biosensing [1] or light harvesting [2], to cancer therapy in medicine [3].
Many photonic structures exhibiting a resonant interaction with light have been proposed. These photonic structures can be seen as open optical cavities and their resonant behavior relies on the excitation of modes having a finite lifetime, otherwise called Quasi-Normal Modes. The nature and the physical origin of these modes widely varies however depending on the kind of photonic structures that is being considered. It is consequently convenient to start by carrying out a comparison between various types of resonant structures and their associated modes. To do so, following [4], it proves to be convenient to introduce two characteristic quantities associated with each type of resonances: their mode volume V and their quality factor Q. While Q is associated with the spectral density of the quasi normal mode and characterizes how long light can be trapped by the structure when this resonance is excited, $1/V$ can be related to the spatial density of the mode. For enhancing light-matter interactions, light has to be trapped for a long time in a volume as tiny as possible.
This is illustrated by the expression of the Purcell factor F_p that describes how the decay rate Γ of a quantum emitter interacting with a mode of a cavity will be enhanced compared to its decay rate in vacuum Γ_0:

$$F_p = \frac{\Gamma}{\Gamma_0} = \frac{6\pi c^3}{\omega^3}\frac{Q}{V} \tag{1.1}$$

The Purcell factor is proportional to Q and inversely proportionnal to V. Even though the Purcell factor was first employed in the case of closed cavities, it was also recently generalized to open optical cavities by means of QNM expansions [5]. It is consequently desirable to find photonic structures possessing resonances with a

quality factor Q as large as possible and a mode volume V as small as possible. This criterion also applies for phenomena different from the Purcell effect and structures supporting high Q and small V resonances would also be beneficial for other types of applications like the enhancement of non-linear effects or biosensing.
Optical microcavities such as microposts, whispering gallery mode cavities or photonic crystal cavities are known to possess very large quality factor ranging from 10^3 to 10^6. Their mode volume however cannot usually be smaller than λ^3 [6].
On the other hand, the resonant interaction of plasmonic resonators with light originates from the excitation of collective oscillations of the conduction electrons in subwavelength metallic particles. The quality factors of these resonances are consequently limited to relatively small values $Q \sim 10$ because of both intrinsic losses, i.e. absorption, and radiative losses. Nonetheless, these resonances also have very small mode volumes $V \sim 10^{-4}\lambda$ as the field is mainly confined near the surface of plasmonic resonators [4].
Each type of resonances has advantages and drawbacks. For instance, even though resonances with very large Q factors are advantageous as they allow to confine light for a long time, their very sharp linedwidth can be detrimental. That is the reason why even if they support resonances with much smaller quality factor, the use of plasmonic resonators have been expected to be beneficial for a number of potential applications [7]. However, large optical losses in plasmonic nanoresonators have greatly jeopardized the practical implementation of devices based on this type of resonators.
In the meantime, high-refractive-index dielectric and semiconductor nanostructures have recently emerged as an alternative to plasmonic nanostructures since they support resonances with both quality factors and mode volumes comparable to those of plasmonic resonators while suffering from smaller optical losses. On top of that, they support both electric and magnetic type resonances that allow for the unique possibility of manipulating their far-field radiation pattern when being carefully designed. These interesting properties of high refractive index resonators, otherwise called Mie resonators, make them a good alternative to plasmonic nanoresonators. As a consequence, theoretical and experimental studies leading to a better understanding of Mie resonators will help to determine applications for which the use of Mie resonators may be beneficial.

That is why the work carried out in the framework of this joint-PhD between the Institut Fresnel in Marseille and the university of Sydney was mostly concerned with the study of Mie resonators from both a theoretical and an experimental point-of-view. While the theoretical work was mainly realized in collaboration with my supervisors in Marseille, most of the experimental work was performed in Sydney with samples fabricated at the Institut Fresnel and at the CINAM laboratory also in Marseille.

Outline of the thesis:

The present thesis is organized as follows:

In Chapter 2, an overview of the field of Mie resonators will be presented. After a quick introduction on the origin of the resonant behavior of Mie resonators, we will proceed with a short review of the fabrication techniques used for structuring matter at the nanoscale and fabricating Mie resonators. Some of the numerical methods that can be applied to predict the electromagnetic response of arbitrarily shaped high index scatterers will also be presented. Finally, applications of Mie resonators that can be found in the literature will be reviewed.

Chapter 3 is a technical introduction presenting the theoretical tools that will be used to study light-scattering by subwavelength-sized resonators. We will in particular introduce three different but equivalent formulations of the scattering problem. One of these formulations will in particular be shown to simplify the expression of energy conservation. Another of these formulations will appear to be particularly suited for describing radiative losses.

In Chapter 4, a discussion about the definition of resonances will be carried out. The notion of resonances clearly appears to be central in nanophotonics. However, there is an ambiguity on the definition of resonances. What is called a resonance from a theoretical point of view will indeed slightly differ from the experimental definition of resonances. In this chapter, we will present a definition of resonances in relation to optimal interaction conditions. Resonances of the scattering cross section will be related to the so-called unitary limit. On the other hand, resonances of the absorption cross section will be linked to the so-called ideal absorption limit.

The objective of Chapter 5 will be twofold. First, asymptotic resonance conditions for both electric and magnetic resonances of high refractive index scatterers will be derived by asssuming their size to be very small compared to the wavelength while their permittivity will be assumed to be very large. Second, we will try to use these resonance conditions to derive approximate models capable of predicting the resonant behavior of Mie as well as plasmonic resonators.

In Chapter 6, the resonant behavior of high-refractive index scatterers will be discussed in the light of their modes, i.e. their quasi-normal modes. We will in particular try to explain the asymmetric shape of the resonances appearing in the scattering cross-section spectrum by use of the quasi-normal modes. Finally, it will be shown that Quasi-Normal Mode expansions enable the study of light-scattering in the time domain.

Finally, the last chapter will be devoted to an experimental study of Mie resonators. In particular, the possibility of enhancing nonlinear effects in a silicon nanodisk will be investigated. More precisely, we will try to see if the degenerate four-wave mixing process can be enhanced if the two pumping laser wavelengths are set close to two resonances of a silicon nanodisk.

Chapter 2

Mie resonators

Summary In this Chapter, an overview of the work carried out in connection with Mie resonators in nanophotonics will be presented. As often in fields related to nanophotonics, theoretical and experimental aspects will appear to be closely intertwined in this field. Early theoretical studies have for example motivated the development of new nanofabrication methods. On the other hand, the possibility offered by new nanofabrication methods to structure matter at the nanoscale requires the development of novel theoretical tools facilitating the prediction and the understanding of the electromagnetic response of increasingly complex photonic structures. That is why here, after a short introduction to Mie theory, we will quickly review nanofabrication methods as well as electromagnetic simulation methods used in relation to Mie resonators. We shall then provide an overview of the new potential applications that are now being considered for these high-refractive index resonators.

2.1 Mie resonances in high refractive index scatterers:

In their early works, Lorenz and Mie [8, 9] have shown that the optical response of spherically symmetric scatterers, regardless of their size and constituting medium, could be analytically predicted by expanding the electromagnetic fields in the multipolar basis. This result is now commonly referred to as the Lorenz-Mie theory that will be presented in detail in Chapter 3. Here, we can however point out that, assuming no dispersion, the scattering properties at the vacuum wavelength λ of a high refractive-index spherical scatterer of radius R can be fully determined when two parameters are specified: its permittivity ε_s and its size parameter $z = \frac{2\pi}{\lambda}R$ [10]. The total optical response can then be determined by summing up the contributions from all the multipolar orders.

A study of the scattering properties of high refractive index spherical scatterers clearly reveals the existence of a whole set of resonances as can be seen in Fig.

2.1. In fact, this resonant behavior is not limited to spherically-symmetric scatterers as it can also be observed in 2D light-scattering in the scattering cross-section of cylinders, and from nonspherical scatterers in 3D light-scattering [11]. In fact, while in sub-wavelength spherical plasmonic scatterers only electric type resonances can usually be excited, high refractive index scatterers exhibit both magnetic and electric type resonances, otherwise called Mie resonances. This resonant behavior of subwavelength high-refractive index scatterers in the visible and near-infrared region was first evidenced while studying the optical response of silicon nanowires [12, 13] as predicted when studying light-scattering from cylinders in 2D.

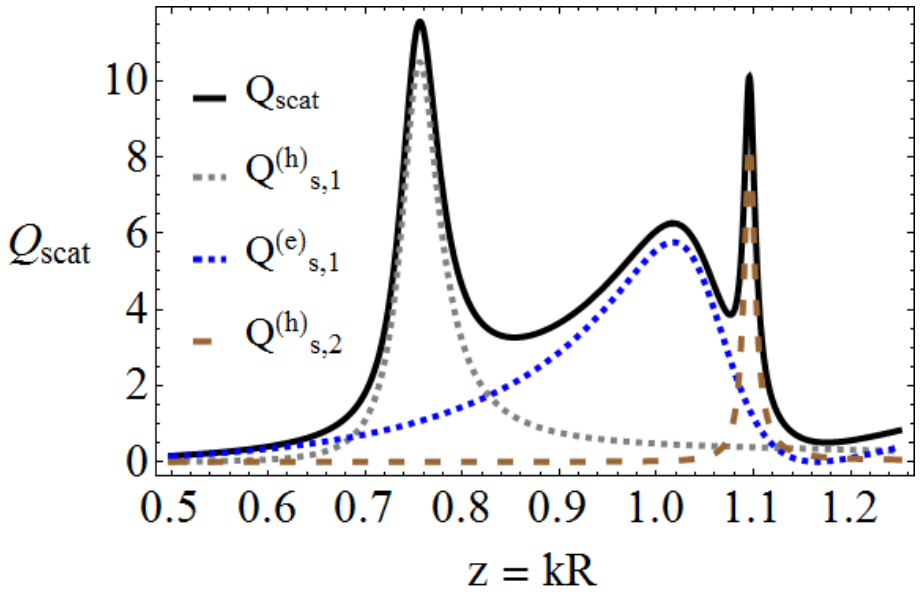

Figure 2.1: Scattering efficiency of a $\varepsilon = 16$ sphere in function of the size parameter $z = \frac{2\pi}{\lambda}R$. The total scattering efficiency Q_{scat} is plotted in full black line. The magnetic dipole partial scattering efficiency $Q^h_{s,1}$ is in dotted gray line. The electric dipole partial scattering efficiency $Q^e_{s,1}$ is in dotted blue line. Finally the magnetic quadrupole partial scattering efficiency $Q^h_{s,2}$ is plotted in dashed brown line.

In Fig. 2.1, the scattering cross-section of a $\varepsilon_s = 16$ sphere is shown. One can first notice that magnetic type resonances of a given multipolar order occur at a smaller size parameter or equivalently at a larger wavelength than their electric counterparts. A better understanding on the physical origin of these resonances could be gained by determining resonance conditions. Such numerically-derived predictions were already provided in [14]. In Chapter 5, approximate approaches will be used to derive Mie resonance conditions.

2.2 Experimental observation of Mie resonances

In the field of nanophotonics, the observation of Mie resonances was recently allowed by the advances of fabrication and experimental methods. The resonant optical response of high refractive-index was in fact observed from silicon spherical particles by dark-field spectroscopy [14, 15]. These silicon nanospheres whose size range from 100 nm to 200 nm were fabricated by laser ablation. We can however point out that laser ablation methods employed in [14] and [15] were slightly different. In [14], the nanospheres were made by direct laser ablation: an ultrashort-laser-pulse focused on the silicon substrate induces the material fragmentation into spherical nanoparticles that are then deposited back on the substrate near the focus area [16]. On the other hand, in [15], the silicon nanospheres were produced by laser induced transfer where the spherical silicon particles produced by the ablation of a silicon substrate are transferred onto a transparent substrate placed on top of the silicon substrate. In Fig. 2.2, dark field spectra from [10] are reproduced. These laser-induced ab-

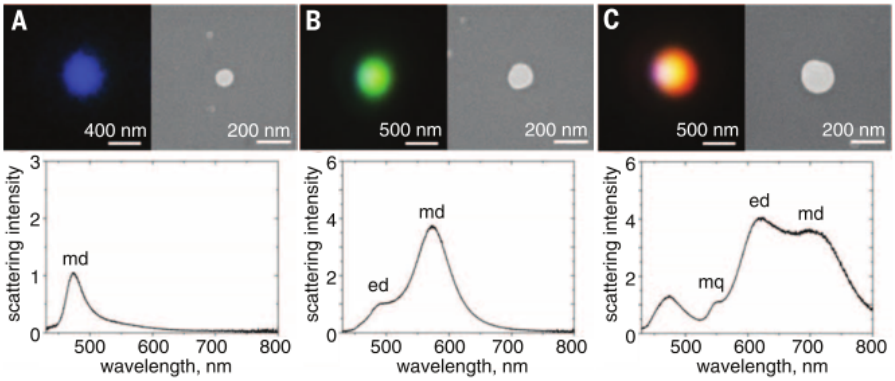

Figure 2.2: Figure adapted from [10]: scanning electron microscope (SEM) images and dark-field images of the silicon nanospheres on top of the silicon substrate. The corresponding dark-field spectroscopy measurements are plotted under the SEM images.

lation methods were first employed on account of being one of the rare techniques allowing for the fabrication of isolated and almost perfectly spherically symmetric silicon scatterers. They consequently opened the way for a verification of Mie theory predictions on the resonant behavior of high refractive index scatterers detailed in section 2.1. These techniques suffer nonetheless from important handicaps that would limit their use for practical applications. In particular, it is not possible to have a control over the spherical particle size or position while performing a simple laser ablation [16]. It should however be pointed out that laser induced transfer permits a better control of the position and size of the nanospheres [17, 18].
As already pointed out in section 2.1, this resonant behavior is not just specific to spherically-symmetric scatterers as non-spherical scatterers such as nanocubes or nanocylinders were also shown to support electric and magnetic Mie resonances [11].

Unlike spheres, these latter shapes can be fabricated by means of electron beam and photo-lithography methods that offer a good precision over both the shape and the position along with a good repetability and versatility [19, 20]. It is also possible with these types of shapes to have a better control over the spectral position of the resonances by tuning their height and diameter[19]. More complicated structures such as hollow nanocylinders have also been fabricated by electron-beam lithography and were shown to allow for a further control of the position of the resonances [21].

Besides laser-assisted and lithography methods, other fabrication techniques have

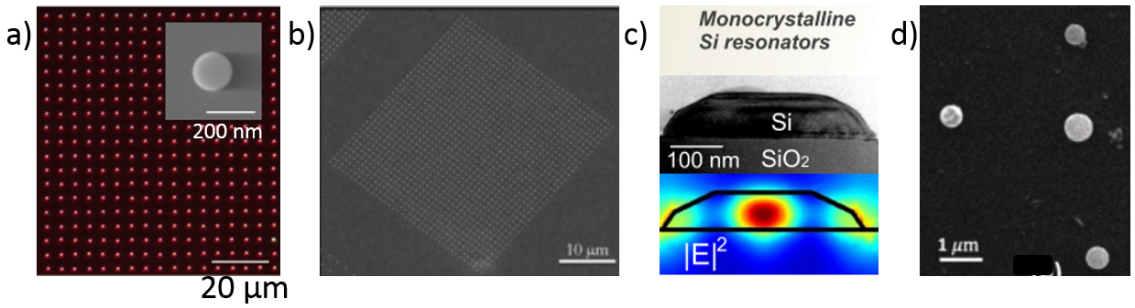

Figure 2.3: Several example of high refractive index scatterer made by means of different fabrication techniques. a) Figure adapted from [17], silicon nanospheres on top of a transparent substrate fabricated by laser ablation and laser induced transfer. b) Figure adapted from [20], scanning electron microscope image of silicon nanodisks fabricated by electron-beam lithography. c) Figure adapted from [22], silicon resonator fabricated by a dewetting-based process from a silicon-on-isulator substrate. d) Figure adapted from [23], silicon colloids fabricated by chemical vapor deposition techniques.

successfully been applied to the fabrication of subwavelength silicon resonators. Chemical methods are considered to be particularly promising on account of potentially allowing for large scale fabrication at a relatively low cost.

We can in particular mention the fabrication of silicon nanoparticles by means of chemical vapor deposition techniques [23, 24]. Crystalline silicon Mie resonators were also made by electron beam lithography on a crystalline silicon substrate followed by alkaline chemical etching [25]. Finally, fabrication techniques based on dewetting of thin films may also permit large scale fabrications of ensembles of high refractive-index resonators [22, 26]. A review about the fabrication and experimental methods in the context of silicon-based nanophotonics may be found in [27]. Another review regarding more generally the experimental aspects of all-dielectric nanophotonics has also recently been published [16].

As was shown in this Section, the advances of fabrication techniques now permit to make silicon resonators with increasingly complex geometries. With this ability to structure matter at will at the nanoscale comes the need to predict the optical response of arbitrarily-shaped nanostructures. As a consequence, before addressing

the issue of potential applications of these high-refractive index resonators, we should first start by reviewing some of the numerical methods permitting to calculate their electromagnetic response.

2.3 Numerical methods for calculating the optical responses of Mie resonators

Even if the Mie theory has played an instrumental role by facilitating the understanding of the resonant behavior of high refractive index scatterers, it is unable to predict the optical response of nonspherical scatterers. As a consequence, alternative methods had to be employed in order to model the electromagnetic interaction between light and arbitrarily-shaped nano-objects.
Aside from Mie theory in which only spherical scatterers are considered, the multipolar theory can also be used to predict the optical response of nonspherical scatterers. The T-matrix will be introduced in Chapter 3 and allows to calculate the scattered field for a given incident field. Methods generalizing the T-matrix method to nonspherical scatterers have been developed. The Waterman method has in particular long been used to calculate the optical response of nonspherical scatterers. The use of the discrete dipole approximations (D.D.A.) has for example been shown to accurately predict the optical response of nonspherical scatterers. This method relies on the assumption that the electromagnetic response of an arbitrary object can be accurately computed by subdividing this object into a set of unit cells very small compared to the wavelength. Each of these unit cell is then modeled as an electric dipole induced by both the incident electromagnetic field and the field scattered by all the other unit cells. This technique was successfully employed to predict the electromagnetic response of nonspherical scatterers [11, 19]. It has the additional benefit of allowing a multipolar expansion of the computed optical response [11].
In the majority of the studies however, the scattering properties of resonant high index dielectric nanostructures are computed by means of numerical solvers of Maxwell equations relying on either the finite difference time domain method (FDTD) or on the finite element method (FEM). Open source or commercial solvers of the Maxwell equations based on these methods have indeed greatly democratized their use to model the interaction of light with arbitrarily shaped scatterers. The fully numerical resolution of Maxwell equations comes however at the price of a loss of insight into the physical origin of the resonant behavior exhibited by the nanostructures considered.
In order to compensate for this lack of physical understanding, a subsequent multipolar expansion of the numerically calculated scattered or internal fields can be performed to further identify the origin of the resonant response of a scatterer [28, 29]. In the scope of the present work, the multipolar formulations of the scattering problem will be discussed in Chapter 3. We will in particular present 3 different but

equivalent formulations of the scattering problem and show how each of these formulations provides a different picture of the scattering problem.
Finally, a great physical insight on the resonant properties of high refractive-index scatterers may also be gained by considering the modes supported by these structures. In fact, as was already pointed out, these optical resonators can be seen as open photonic cavities in which light is trapped for a certain time before leaking and being radiated away from the resonator. In order to account for this decay in time, their modes that are otherwise called Quasi-Normal Modes are associated with complex frequencies $\omega_n = \omega_{n,r} + i\omega_{n,i}$ where $\omega_{n,i} < 0$ for a $\exp(-i\omega t)$ time dependence. These modes should also satisfy outgoing boundary condition, i.e. their radial dependence should tend towards $\frac{e^{i\frac{\omega_n}{c}r}}{r}$ as $r \to \infty$ which leads to a divergence in the far-field region for complex frequencies ω_n. A great effort has been carried out to better understand the scattering properties of these open photonic resonators in terms of their Quasi-Normal Modes [4, 5, 30–33]. Resonant scattering by Mie resonators was also studied in the light of their resonant states [34, 35]. However, several fundamental questions are still to be addressed in order to study the scattering properties of optical resonators and this will be the subject of Chapter 6.

Now that the issue of fabrication of high refractive-index subwavelength resonators as well as the issue of the modeling of the electromagnetic properties of such kind of resonators have been addressed, we can proceed to a quick review of the interesting properties and potential applications for which the use of Mie resonators might be beneficial.

2.4 Properties and applications of Mie resonators

2.4.1 Directional scattering of light

It is of common knowledge that any object much smaller than the wavelength should behave as a dipole and consequently should scatter light in a quite symmetric way with regards to its dipole axis. In the early 1980's, Kerker et al. pointed out that a completely different behavior would be observed if the assumption that the scatterer medium is non magnetic was relaxed [36]. In fact, they showed that if the relative permittivity is different from $\mu = 1$, the total suppression of the back-scattered field was possible under given conditions. On the other hand, the field scattered in the forward direction could also almost be suppressed at another condition. These conditions are otherwise called Kerker's conditions.
Mie resonators featuring both electric and magnetic responses were however seen as a promising platform capable of leading to a practical realization of these Kerker conditions with non magnetic materials [37]. An experimental verification of the Kerker effect in high-refractive index scatterers was carried out in the microwave range [38]; it was subsequently observed in the visible range with silicon nanoparticles [39] and

in GaAs (Gallium Arsenide) nanoparticles [40]. In the examples listed above, the Kerker effect was due to the interference between the fields radiated by the induced electric and magnetic dipoles. It was however shown that a generalization of this effect to higher order multipoles was also possible [41–43].

2.4.2 Applications of isolated high refractive index nanoresonators:

The capacity of Mie resonators to confine light at the nanoscale as well as their ability to scatter light in a directive way make them good candidates to act as antennas for light.

2.4.2.1 Optical nanoantennas:

Not only do nanoresonators allow for a confinement of light in very small volumes but they can also help to achieve an enhancement and an improvement of the directivity of the emission when being coupled to quantum emitters [44]. The resonant behavior of these resonators leads to a modification of the local density of states that in turn allows to modify the decay rate and the quantum yield of a quantum emitter that would be located in the vicinity of these resonators. The Purcell factor, describing how the decay rate of a quantum emitter is modified when it is coupled to an optical cavity, was recently generalized to open photonic resonators [5, 45]. On top of the Purcell effect, the coupling of a quantum emitter to a high-index dielectric resonators may lead to an enhancement of the directivity of the emitted radiation. It was shown that these two effects could be obtained in a hybrid antenna constiting of a dimer of plasmonic antenna that would modify the decay rate of an emitter and a dielectric nanosphere that would improve the directivity [46, 47]. In addition to enhancing the electric dipolar emission, the possibility of enhancing light emission *via* the magnetic dipole transition [48, 49] was also investigated with Mie resonators [45, 50, 51] on account of their strong magnetic response.
The ability of Mie resonators to act as antennas for light comes also from their capacity to confine light at the nanoscale. Near-field enhancement can already be observed at the vicinity of isolated Mie resonators, it is however worth pointing out that the wavelength at which the near field response is maximized may be slightly red-shifted compared to the wavelength at which the far-field response is maximized. This should be further discussed in chapter 4. Structures based on several coupled Mie resonators were also shown to further enhance both the electric and magnetic near fields [52–55]. However, unlike plasmonic resonators, the field enhancement is not only restricted to the surface of Mie resonators since the field can also be greatly enhanced inside.

2.4.2.2 Nonlinear optics in dielectric resonators:

Field enhancements were in particular shown to be especially large inside Mie resonators at the magnetic resonances [56]. This property can enhance effects largely dependent on field intensities as, for instance, non linear phenomena. A thorough review on the subject will be carried out in chapter 7. Here we merely present a quick introduction.
Following a pioneering work [56] where an enhancement of the third harmonic generation was reported to occur at the dipole magnetic resonances, potential enhancements of the third harmonic generation were investigated in different resonant dielectric nanostructures [57–59]. It was also shown that the Kerker effect could help shape the radiation pattern of the nonlinear field [60, 61]. Second-harmonic enhancements were also considered in AlGaAs nanoresonators [62–64]. Raman scattering in silicon nanoresonators was studied too and shown to be enhanced [65, 66]. A review on the subject has recently been published [61].

2.4.2.3 Optoelectronic devices based on Mie resonators:

These Mie resonators are also promising building blocks in diverse optoelectronic devices. Their resonant interaction with light can lead to an enhanced absorption of light inside these resonators. This property could be beneficial to improve the performances of photodetectors [12, 67]. Implemented at a larger scale, they could also allow to enhance the efficiency of solar cells [2, 68]. They may be used to create more efficient light sources. The control of the photoluminescence from InP (indium phosphide) nanowires has in particular been demonstrated [69].

2.4.2.4 Biosensors based on Mie resonators:

Plasmonic resonators have long been considered to be good building blocks of biosensing devices able to quantify the concentration of chemical and biological substances. Such biosensors rely on the high sensitivity of plasmonics resonances to the surrounding environment of the resonator. A modification of their surrounding refractive index would indeed lead to a shift of the resonance supported by metallic nanoparticle. Simple models predicting this shift were recently derived by use of the quasi-normal modes of these structures [70]. Similarly, the use of Mie resonators for biosensing applications has also recently been considered [71]. In particular, it was pointed out that a change of the refractive-index outside a Mie resonator would lead to a modification of their scattering response in two different ways: not only would their extinction efficiency sprectrum be modified, but the scattering pattern of these scatterers would also change [72]. An experimental demonstration of this kind of biosensors was recently carried out [73].
The very sharp Fano resonance featured by the structure in [74] could help make

devices highly sensitive to a very small change of the refractive index of its environment.

While we have mostly listed so far potential applications relying on isolated Mie resonators, we conclude this part by reviewing some of the appealing functionalities that could be performed by large arrays of Mie resonators that may also be called dielectric metasurfaces.

2.4.3 Dielectric resonators as a building block for metasurfaces:

The possibility of structuring large area surfaces at the nanometer scale has opened the way to the field of metasurfaces. These patterned subwavelength-thick surfaces were first used to shape and manipulate the wavefront of the electromagnetic field impinging on them. Different approaches were explored to perform such a wavefront contro: several papers recently released relied on a method developed nearly two decades ago and based on blazed binary diffractive elements [75–77]. Another approach was based on a dielectric gradient metasurfaces [78]. Finally another method relying on the electric and magnetic resonances of silicon nanodisks was also shown to allow for a control of the phase of the incident field [79] and was applied to the generation of vortex beams [80]. These methods for controlling the wavefront of an incident field shows also a great potential to create metalenses [78, 81, 82].
On the other hand, the resonant behavior of dielectric nanostructures gives those structures very vivid colors. The possibility of tuning their resonance wavelengths by changing their geometry can consequently allow for a control over the apparent color of these resonators. The first studies that took advantage of this property of Mie resonators to implement structural color were based on silicon nanowires [13, 83]. It was then shown that dielectric colored metasurfaces could be made by tuning the resonances of silicon nanodisks [20, 84]. Optimization algorithms can even be employed to improve the design of these color metasurfaces [85]. Some examples of these all-dielectric colored metasurfaces may be found in Fig. 2.4.

The possibility of implementing actively tunable metasurfaces was explored in several recent papers. One of the possible ways to achieve this active tuning is to embed an array of silicon nanoresonators into a liquid crystal. The refractive index of the liquid could be tuned by changing its temperature, the optical response of the embedded array of silicon nanodisks could consequently be controlled by adjusting the liquid crystal temperature [86]. Further in the infrared region, an active tuning of PbTe (lead telluride) Mie resonator was also shown to be possible by taking advantage of the large thermo-optic coefficients of PbTe [87]. The refractive index and consequently the optical response of these PbTe resonators could be controlled by a change of temperature. Electrical tuning of metasurfaces based on heterojunction resonators was also shown to be possible [88].

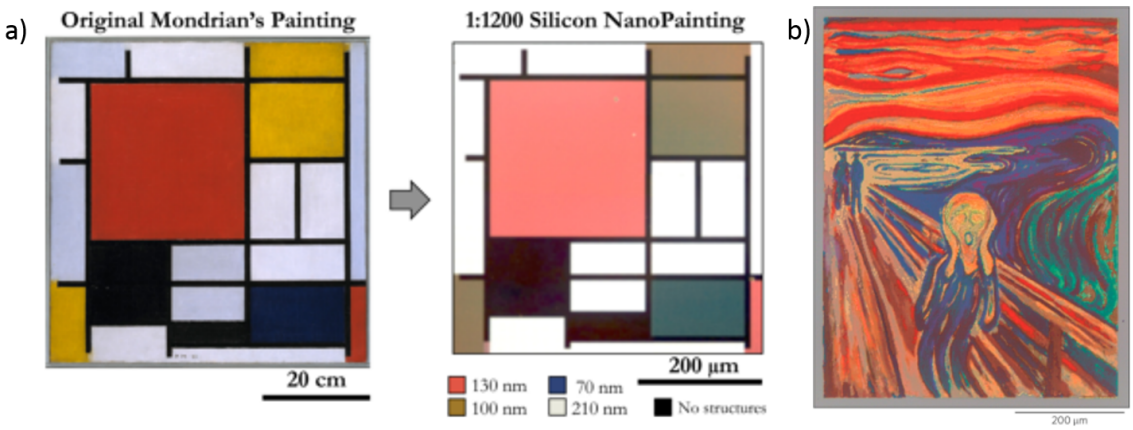

Figure 2.4: Several examples of all-dielectric colored metasurfaces. a) adapted from [20], reproduction of a mondrian painting made by e-beam patterning silicon nanopillars with various diameters on a glass substrate b) adapted from [84], reproduction the painting *The scream* made with arrays of silicon nanodisks with varying pitches and varying sizes.

2.5 Conclusion:

In this chapter, the field of high-refractive index Mie resonators have been introduced. It is worth noticing that a number of review articles have already been published on this relatively new but very active field. An overview on the whole field can in particular be found in two recently published review articles [10, 89]. Reviews focusing on the fabrication and experimental aspects have also been written. One is mostly concerned with silicon Mie resonators [27]. Another one explores a set of potential materials that may be employed for fabricating Mie resonators [16]. A review with a focus on non-linear Mie resonators has also been written [61]. Finally, a review especially focusing on the promising field of metalenses can be found in [81].

Chapter 3

Multipolar formulation of the scattering problem

Summary In this Chapter, we aim to introduce the theoretical tools that are used throughout this thesis to study the resonant interaction between light and a scatterer. After introducing the Vector Partial Waves basis (hereafter referred as VPWs), we will present several formalisms based on the T, S and K matrices. Each of these formalisms will help us see the scattering problem from a different perspective: while the T-matrix approach is probably the most intuitive, the S matrix allows us to formulate the conservation of energy in a simple way. Finally, the K matrix is very convenient to deal with radiative losses.

3.1 Introduction

Here, the theoretical tools for studying elastic light-scattering in 3D are introduced. An obstacle located in a homogeneous and lossless medium is illuminated by an excitation field which can generally be described as a plane wave or as a superposition of plane wave. The interaction of the excitation field with the obstacle gives rise to the generation of a scattered field that is radiated away from the obstacle. All these electromagnetic fields fulfill the Maxwell equations, defined hereafter.
Computational tools capable of numerically solving the Maxwell equations and based on numerical methods such as the Finite Element Methods or the Finite Difference Time Domain [90, 91] have been developed. The development of these numerical methods opened up in turn the possibility of studying light-scattering by arbitrary-shaped scatterers. The use of numerical methods may however come at the prize of a loss of physical insight into the scattering problem and can also be very demanding in computational resources.
On the other hand, the Lorenz-Mie theory has the benefit of being one the few exact solutions to a non-trivial scattering problem. It originates from the seminal works of Lorenz and Mie [8, 92] in which the scattering of a plane wave by a trans-

parent sphere was considered. This theory which is based on the expansion of the electromagnetic field on the multipolar basis was then generalized by the T matrix method for the description of the scattering of an arbitrary excitation field by an arbitrarily shaped scatterer [93–96]. It is now playing a central role for describing the interaction of light with small sized particles in nanophotonics.

Here, we will start by quickly recalling the basics of electromagnetism [97, 98] before introducing the multipolar (or Vector Partial Waves) basis. Several alternative formulations of the scattering problem will then be introduced, each of them bringing a different point of view on this problem.

3.2 Multipolar formalism

3.2.1 Maxwell equations

Let $\mathbf{E}(\mathbf{r},t)$, $\mathbf{B}(\mathbf{r},t)$ be the time-dependent electric field and magnetic induction while $\mathbf{D}(\mathbf{r},t)$ and $\mathbf{H}(\mathbf{r},t)$ are the time-dependent electric displacement and the magnetic field. These fields verify the source-free Maxwell equations that may be written in SI units as follows:

$$\begin{aligned} \nabla.\mathbf{D}(\mathbf{r},t) &= 0 \\ \nabla\times\mathbf{E}(\mathbf{r},t) &= -\frac{\partial\mathbf{B}}{\partial t}(\mathbf{r},t) \\ \nabla.\mathbf{B}(\mathbf{r},t) &= 0 \\ \nabla\times\mathbf{H}(\mathbf{r},t) &= \frac{\partial\mathbf{D}}{\partial t}(\mathbf{r},t) \end{aligned} \tag{3.1}$$

The relation between $\mathbf{D}(\mathbf{r},t)$ and $\mathbf{E}(\mathbf{r},t)$ as well as between $\mathbf{H}(\mathbf{r},t)$ and $\mathbf{B}(\mathbf{r},t)$ are provided by the following constitutive relations:

$$\begin{aligned} \mathbf{D}(\mathbf{r},t) &= \epsilon_0\mathbf{E}(\mathbf{r},t)+\mathbf{P}(\mathbf{r},t) \\ \mathbf{H}(\mathbf{r},t) &= \frac{\mathbf{B}}{\mu_0}(\mathbf{r},t)-\mathbf{M}(\mathbf{r},t) \end{aligned} \tag{3.2}$$

$\mathbf{P}(\mathbf{r},t)$ and $\mathbf{M}(\mathbf{r},t)$ being the electric polarization and the magnetization while ϵ_0 and μ_0 are respectively the permittivity and the magnetic permeability of vacuum. We restrict ourselves to the study of non-magnetic media leading $\mathbf{M}(\mathbf{r},t)$ to vanish. Moreover, we consider homogeneous media presenting no spatial dispersion and non-linear responses from the medium will also be neglected in this first part. The

constitutive relations then become:

$$\begin{aligned}\mathbf{D}(\mathbf{r},t) &= \int_{-\infty}^{t} \epsilon_0(1+\chi(t-t^{'}))\mathbf{E}(\mathbf{r},t^{'})dt^{'} \\ \mathbf{H}(\mathbf{r},t) &= \frac{\mathbf{B}}{\mu_0}(\mathbf{r},t)\end{aligned} \tag{3.3}$$

where $\chi(t-t^{'})$ is the electric susceptibility. The previous equations are greatly simplified in the harmonic domain where fields are assumed to have a $e^{-i\omega t}$ time dependence:

$$\mathbf{D}(\mathbf{r},\omega) = \epsilon_0\varepsilon_r(\omega)\mathbf{E}(\mathbf{r},\omega) \text{ and } \mathbf{B}(\mathbf{r},\omega) = \mu_0\mathbf{H}(\mathbf{r},\omega) \tag{3.4}$$

where the permittivity is defined by $\varepsilon_r(\omega) - \epsilon_0 = \int_0^\infty \chi(t)e^{i\omega t}dt$, causality imposing that $\chi(t)$ should vanish for $t < 0$. In the harmonic domain, Eqs (3.1) can also be rewritten as follows:

$$\begin{aligned}\nabla.\mathbf{E}(\mathbf{r},\omega) &= 0 \\ \nabla \times \mathbf{E}(\mathbf{r},\omega) &= i\omega\mu_0\mathbf{H}(\mathbf{r},\omega) \\ \nabla.\mathbf{B}(\mathbf{r},\omega) &= 0 \\ \nabla \times \mathbf{H}(\mathbf{r},\omega) &= -i\omega\epsilon_0\varepsilon_r(\omega)\mathbf{E}(\mathbf{r},\omega)\end{aligned} \tag{3.5}$$

By combining the two previous equations, one can finally obtain the vector wave equation fulfilled by the electric and magnetic fields:

$$\begin{aligned}\nabla \times (\nabla \times \mathbf{E}) - \left(\frac{\omega}{c}\right)^2 \epsilon_r(\omega)\mathbf{E} = 0 \\ \nabla \times (\nabla \times \mathbf{H}) - \left(\frac{\omega}{c}\right)^2 \epsilon_r(\omega)\mathbf{H} = 0\end{aligned} \tag{3.6}$$

where $c = \frac{1}{\sqrt{\epsilon_0\mu_0}}$ is the speed of light in vacuum.

Finally, the conditions of continuity of the field at an interface will be required to solve the problem of scattering and they can be expressed in the following way:

$$\begin{aligned}\hat{\mathbf{n}}_{12} \times (\mathbf{E}_2 - \mathbf{E}_1) &= \mathbf{0} \\ (\mathbf{D}_2 - \mathbf{D}_1) \cdot \hat{\mathbf{n}}_{12} &= \rho_s \\ (\mathbf{B}_2 - \mathbf{B}_1) \cdot \hat{\mathbf{n}}_{12} &= 0 \\ \mathbf{n}_{12} \times (\mathbf{H}_2 - \mathbf{H}_1) &= \mathbf{j}_s\end{aligned} \tag{3.7}$$

where the $(\mathbf{E}_1, \mathbf{H}_1)$ and $(\mathbf{E}_2, \mathbf{H}_2)$ account for the fields in the two different media. ρ_s and $\mathbf{j}_s$ are respectively the surface charge density and the surface current at the interface. Finally, $\hat{\mathbf{n}}_{12}$ is the vector normal to the interface.

3.2.2 Vector partial waves basis:

The Vector Partial Wave basis, well suited for the study of 3D scattering, is a set of solutions of Eqs. (3.6) in a spherical coordinate system. Such solutions can be generated from the solutions of the scalar Helmholtz equation.

By first making use of the following vector identity to (3.6):

$$\nabla \times (\nabla \times \mathbf{A}) = \nabla (\nabla.\mathbf{A}) - \nabla.(\nabla \mathbf{A}) \tag{3.8}$$

one readily shows that the electric and magnetic fields $\mathbf{E}$ and $\mathbf{H}$ are both solutions of the vector Helmholtz equations:

$$\begin{aligned} \nabla.(\nabla \mathbf{E}) + k^2 \mathbf{E} = 0 \\ \nabla.(\nabla \mathbf{H}) + k^2 \mathbf{H} = 0 \end{aligned} \tag{3.9}$$

where $k^2 = \left(\frac{\omega}{c}\right)^2 \epsilon_r(\omega)$.

Following the method employed in [93, 99], a basis of the solutions of the vector Helmholtz equations can be constructed in the following way: First, if we look for a solution under the following form:

$$\mathbf{M} = \frac{\nabla \times (\mathbf{c}\psi)}{\sqrt{n(n+1)}}, \tag{3.10}$$

where $\mathbf{c}$ is a pilot vector and ψ is a generating function, it can be shown that:

$$\nabla.(\nabla \mathbf{M}) + k^2 \mathbf{M} = \nabla \times \left[\mathbf{c}\left(\nabla^2 \psi + k^2 \psi\right)\right]. \tag{3.11}$$

It turns out that if ψ is a solution of the scalar Helmholtz, $\mathbf{M}$ will be a solution of its vectorial counterpart. Another solution of Eq. (3.9) may also be constructed from $\mathbf{M}$:

$$\mathbf{N} = \frac{\nabla \times \mathbf{M}}{k} \tag{3.12}$$

The vector functions $\mathbf{M}$ and $\mathbf{N}$ satisfy all the properties of the electric and magnetic fields . They are by definition solutions of the vector wave equation, they are divergence free and they are both proportional to the curl of one another:

$$\mathbf{N} = \frac{\nabla \times \mathbf{M}}{k} \tag{3.13}$$

$$\mathbf{M} = \frac{\nabla \times \mathbf{N}}{k} \tag{3.14}$$

A complete basis for the electromagnetic field can consequently be constructed by finding solutions of the scalar Helmholtz equation.

For the sake of completeness, it is worth pointing out that according to the Helmholtz theorem, an arbitrary vector field should be decomposed onto a divergence-free part and a curl-free part. In order to form a complete basis, an additional vector function accounting for the non-transverse part of the field should consequently be introduced. Such a vector could also be defined from the generating function $\psi(\mathbf{r})$ ([99], pp 387-397):

$$\mathbf{L}(\mathbf{r}) = \nabla\psi(\mathbf{r}) \tag{3.15}$$

However, such longitudinal fields cannot be excited in the scattering problem considered here. That is why we will not need to introduce this additional vector.

3.2.2.1 Solutions of the scalar Helmholtz equation

$$\nabla^2\psi + k^2\psi = 0 \tag{3.16}$$

A solution $\psi(r,\theta,\phi)$ of the scalar Helmholtz equation (3.16) in the spherical coordinate system is yet to be derived in order to construct the VPWs basis. The spherical coordinate system is displayed in Fig. 3.1.

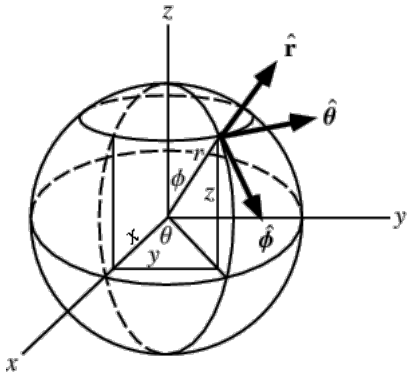

Figure 3.1: system of spherical coordinates

Using the separation of variables, solutions will be assumed to take the following form: $\psi(r,\theta,\phi) = \psi_r(r)\psi_\theta(\theta)\psi_\phi(\phi)$.
The θ and ϕ dependence of $\psi(r,\theta,\phi)$ can be shown to be given by the normalized scalar spherical harmonics [93, 99, 100]:

$$\begin{aligned} \psi(r,\theta,\phi) &= \psi_r(r)Y_{n,m}(\theta,\phi) \\ \text{with } Y_{n,m}(\theta,\phi) &= \left[\frac{2n+1}{4\pi}\frac{(n-m)!}{(n+m)!}\right] e^{im\phi}P_n^m(cos(\theta)) \end{aligned} \tag{3.17}$$

where the functions P_n^m are the Legendre polynomials for $n = 0, 1, 2.....\infty$ and $m = -n, ..., n$. n is the total angular momentum and is related to the θ dependence

of the wave. Waves with $n = 0$ are isotropic and are generally referred as s waves but are not excited in the light-scattering problem considered here. For larger n, the θ dependence can be described as a standing wave with nodes and anti-nodes in fixed directions. As the wave should be well behaved in all directions of $\mathbf{r}$, n has to be restricted to integer values [100]. On the other hand, m is the angular momentum number and $m = -n, ..., n$.
Regarding the radial dependence of the waves, one can show by means of Eqs. (3.17) and (3.16) that the functions $\psi_r(r)$ verify the following equation:

$$\frac{d^2u(r)}{dr^2} + \left(\varepsilon_{\mathrm{r}}k^2 - \frac{n(n+1)}{r^2}\right)u(r) = 0 \tag{3.18}$$

where $u(r) \equiv r\psi_r(r)$.

Spherical Bessel functions $j_n(z)$ and spherical Neumann functions $y_n(z)$ are solutions of the preceding equation. Moreover the wronskian of these two functions is equal to:

$$W\left(j_n(z), y_n(z)\right) = j_n(z)\frac{dy_n(z)}{dz} - \frac{dj_n(z)}{dz}y_n(z) = z^{-2} \tag{3.19}$$

Since $W\left(j_n(z), y_n(z)\right) \neq 0$, $j_n(z)$ and $y_n(z)$ are two linearly independent solutions of Eq. (3.18) and they thus form a complete set of solutions of equation 3.18.

It will also prove very useful to construct another complete set of linearly independent solutions from $(j_n(z), y_n(z))$. This can be done by defining the Hankel functions of first and second kind: $h_n^{(+)}(z) = j_n(z) + iy_n(z)$ and $h_n^{(-)}(z) = j_n(z) - iy_n(z)$ which are obviously solutions of Eq. (3.18) and also linearly independent since their wronskian is equal to:

$$W\left(h_n^{(+)}(z), h_n^{(-)}(z)\right) = -2iz^{-2} \tag{3.20}$$

And they are also linearly independent with $j_n(z)$ and $y_n(z)$. It can then be concluded that a complete basis for the solutions of the scalar equation (3.18) can be constructed by forming any combination of 2 partial waves among the following functions:

$$\begin{aligned}
\psi_{n,m}^{(1)}(k\mathbf{r}) &= \quad j_n(kr)Y_{n,m}(\theta,\phi) \\
\psi_{n,m}^{(2)}(k\mathbf{r}) &= \quad y_n(kr)Y_{n,m}(\theta,\phi) \\
\psi_{n,m}^{(+)}(k\mathbf{r}) &= h_n^{(+)}(kr)Y_{n,m}(\theta,\phi) \\
\psi_{n,m}^{(-)}(k\mathbf{r}) &= h_n^{(-)}(kr)Y_{n,m}(\theta,\phi)
\end{aligned} \tag{3.21}$$

Now that a basis for the scalar Helmholtz equation has been constructed, we will define a basis for the solutions of the vector wave equation (3.6).

3.2.2.2 Vector partial waves

The vector partial wave expressions can then be readily obtained by injecting the solutions (3.21) into the vector partial wave definitions (3.10), (3.14) while choosing $\mathbf{c} = \hat{\mathbf{r}}$ as a pilot vector. It is however worth expressing them in terms of the Vector Spherical Harmonics (VSH). Since the definition of these VSH varies in the literature, let us start by introducing our notations:

$$\begin{aligned} \mathbf{Y}_{n,m}(\theta,\phi) &= Y_{n,m}(\theta,\phi)\hat{\mathbf{r}} \\ \mathbf{Z}_{n,m}(\theta,\phi) &= \frac{r\nabla Y_{n,m}(\theta,\phi)}{\sqrt{n(n+1)}} \\ \mathbf{X}_{n,m}(\theta,\phi) &= \mathbf{Z}_{n,m}(\theta,\phi)\times\hat{\mathbf{r}} \end{aligned} \tag{3.22}$$

The vector spherical harmonics form a complete basis permitting to describe the angular variations of any vector fields. They are also orthogonal according to the following scalar product:

$$\langle \mathbf{W}^{(l)}_{n,m} | \mathbf{W}^{(k)}_{n,m} \rangle = \int_0^{4\pi} \mathbf{W}^{(l)*}_{n,m}.\mathbf{W}^{(k)}_{n,m} d\Omega = \delta_{ij}\delta_{n\nu}\delta_{m\mu} \tag{3.23}$$

where $k = 1, 2$ or 3 and $\mathbf{W}^{(1)}_{n,m} = \mathbf{X}_{n,m}$, $\mathbf{W}^{(2)}_{n,m} = \mathbf{Y}_{n,m}$ and $\mathbf{W}^{(3)}_{n,m} = \mathbf{Z}_{n,m}$.
The Vector partial waves expression in terms of the vector spherical harmonics is thus:

$$\begin{aligned} \mathbf{M}^{(i)}_{n,m}(k\mathbf{r}) &= R^{(i)}_n(kr)\mathbf{X}_{n,m}(\theta,\phi) \\ \mathbf{N}^{(i)}_{n,m}(k\mathbf{r}) &= \frac{1}{kr}\left[\sqrt{n(n+1)}R^{(i)}_n(kr)\mathbf{Y}_{n,m}(\theta,\phi) + [krR^{(i)}_n(kr)]'\mathbf{Z}_{n,m}(\theta,\phi)\right] \end{aligned} \tag{3.24}$$

where $R^{(1)}_n(kr) = j_n(kr)$, $R^{(2)}_n(kr) = y_n(kr)$, $R^{(+)}_n(kr) = h^{(+)}_n(kr)$ and $R^{(-)}_n(kr) = h^{(-)}_n(kr)$. In what follows, we will make use of the Ricatti-Bessel, Ricatti-Neumann and Ricatti Hankel functions in order to simplify the notations:

$$\begin{aligned} \psi_n(z) &= zj_n(z) \\ \chi_n(z) &= zy_n(z) \\ \xi^{(\pm)}_n(z) &= zh^{(\pm)}_n(z) \end{aligned} \tag{3.25}$$

The vector partial waves have here been defined but their expressions appear to be quite complicated. This might obscure their physical meaning. A better physical insight may however be gained by studying the far-field behavior of each of the VPWs as will be done in the following section.

3.2.2.3 Far field behavior of the vector partial waves:

Let us start by studying the VPWs ($\mathbf{M}^{(\pm)}_{n,m}(k\mathbf{r})$,$\mathbf{N}^{(\pm)}_{n,m}(k\mathbf{r})$) that are defined as follows:

$$\begin{aligned}\mathbf{M}^{(\pm)}_{n,m}(k\mathbf{r}) &= h^{(\pm)}_n(kr)\mathbf{X}_{n,m}(\theta,\phi)\\ \mathbf{N}^{(\pm)}_{n,m}(k\mathbf{r}) &= \frac{1}{kr}\left[\sqrt{n(n+1)}h^{(\pm)}_n(kr)\mathbf{Y}_{n,m}(\theta,\phi)+\xi^{(\pm)'}_n\mathbf{Z}_{n,m}(\theta,\phi)\right]\end{aligned} \tag{3.26}$$

In order to study their far-field behavior, one has to use the asymptotic limit of the Hankel functions:

$$\lim_{|z|\to\infty} h^{(+)}_n(z) = (-i)^{n+1}\frac{e^{iz}}{z},\ \lim_{|z|\to\infty} h^{(-)}_n(z) = i^{n+1}\frac{e^{-iz}}{z}. \tag{3.27}$$

That leads to the following far-field behavior for the VPWs:

$$\begin{aligned}\lim_{r\to\infty}\mathbf{M}^{(\pm)}_{n,m}(k\mathbf{r}) &= (\mp i)^{n+1}\frac{e^{\pm ikr}}{kr}\mathbf{X}_{n,m}(\theta,\phi)\\ \lim_{r\to\infty}\mathbf{N}^{(\pm)}_{n,m}(k\mathbf{r}) &= (\mp i)^{n}\frac{e^{\pm ikr}}{kr}\mathbf{Z}_{n,m}(\theta,\phi)+O\left(\frac{e^{\pm ikr}}{(kr)^2}\right).\end{aligned} \tag{3.28}$$

Recalling that throughout this work a $e^{-i\omega t}$ time dependence is assumed, one clearly sees that the VPWs $\mathbf{M}^{(+)}_{n,m}(k\mathbf{r})$ and $\mathbf{N}^{(+)}_{n,m}(k\mathbf{r})$ asymptotically behave as outgoing waves with a $e^{-i\omega(t-\frac{r}{c})}$ radial dependence. That is why ($\mathbf{M}^{(+)}_{n,m}(k\mathbf{r})$,$\mathbf{N}^{(+)}_{n,m}(k\mathbf{r})$) will be referred as outgoing Vector Partial Waves. On the other hand, near the scatterer when r is small, the outgoing character of these waves is somehow hidden due to the excitation of evanescent waves. $h^{(+)}_n(z)$ are in fact irregular in $r=0$ as $\lim_{z\to 0} h^{(+)}_n(z) = i\frac{(2l+1)!!}{z^n}$. This divergence can be interpreted as being related to the presence of sources.
Similarly, $\mathbf{M}^{(-)}_{n,m}(k\mathbf{r})$ and $\mathbf{N}^{(-)}_{n,m}(k\mathbf{r})$ are readily shown to asymptotically behave as ingoing waves with a $e^{-i\omega(t+\frac{r}{c})}$ radial dependence and will be called incoming Vector Partial Waves. $h^{(-)}_n(z)$ are also irregular in $r=0$ with $\lim_{z\to 0} h^{(+)}_n(z) = -i\frac{(2l+1)!!}{z^n}$ and this is due to the collapse of the incoming waves at $r=0$.

Concerning the far-field behavior of ($\mathbf{M}^{(1,2)}_{n,m}(k\mathbf{r})$,$\mathbf{N}^{(1,2)}_{n,m}(k\mathbf{r})$) that are defined as follows:

$$\begin{aligned}\mathbf{M}^{(1)}_{n,m}(k\mathbf{r}) &= j_n(kr)\mathbf{X}_{n,m}(\theta,\phi)\\ \mathbf{M}^{(2)}_{n,m}(k\mathbf{r}) &= y_n(kr)\mathbf{X}_{n,m}(\theta,\phi)\\ \mathbf{N}^{(1)}_{n,m}(k\mathbf{r}) &= \frac{1}{kr}\left[\sqrt{n(n+1)}j_n(kr)\mathbf{Y}_{n,m}(\theta,\phi)+\psi^{'}_n\mathbf{Z}_{n,m}(\theta,\phi)\right]\\ \mathbf{N}^{(2)}_{n,m}(k\mathbf{r}) &= \frac{1}{kr}\left[\sqrt{n(n+1)}y_n(kr)\mathbf{Y}_{n,m}(\theta,\phi)+\chi^{'}_n\mathbf{Z}_{n,m}(\theta,\phi)\right]\end{aligned} \tag{3.29}$$

Since the Bessel and Neumann functions asymptotically tend towards:

$$\lim_{|z|\to\infty} j_n(z) = \frac{\sin\left(z - \frac{n\pi}{2}\right)}{z}, \quad \lim_{|z|\to\infty} y_n(z) = \frac{\cos\left(z - \frac{n\pi}{2}\right)}{z}, \tag{3.30}$$

The following asymptotic expressions for $(\mathbf{M}^{(1)}_{n,m}(k\mathbf{r}),\mathbf{N}^{(1)}_{n,m}(k\mathbf{r}))$ is obtained:

$$\begin{aligned} \lim_{r\to\infty} \mathbf{M}^{(1)}_{n,m}(k\mathbf{r}) &= \frac{\sin\left(kr - \frac{n\pi}{2}\right)}{kr}\mathbf{X}_{n,m}(\theta,\phi) \\ \lim_{r\to\infty} \mathbf{N}^{(1)}_{n,m}(k\mathbf{r}) &= \frac{\sin\left(kr - \frac{(n-1)\pi}{2}\right)}{kr}\mathbf{Z}_{n,m}(\theta,\phi) + O\left(\frac{\sin\left(kr - \frac{n\pi}{2}\right)}{(kr)^2}\right) \end{aligned} \tag{3.31}$$

Asymptotic expressions of $(\mathbf{M}^{(2)}_{n,m}(k\mathbf{r}),\mathbf{N}^{(2)}_{n,m}(k\mathbf{r}))$ are readily obtained by replacing sin by cos in the previous expressions. It then appears that unlike the incoming and outgoing vector partial waves which represent propagating waves, $(\mathbf{M}^{(1,2)}_{n,m}(k\mathbf{r}),\mathbf{N}^{(1,2)}_{n,m}(k\mathbf{r}))$ represent static waves. One can also study their behavior when $r \to 0$: since $j_n(0) = 0$ $(\mathbf{M}^{(1)}_{n,m}(k\mathbf{r}),\mathbf{N}^{(1)}_{n,m}(k\mathbf{r}))$ are regular and they represent sourceless fields such as plane waves. On the other hand $\lim_{z\to\infty} y_n(z) = \frac{(2l+1)!!}{z^n}$, $(\mathbf{M}^{(2)}_{n,m}(k\mathbf{r}),\mathbf{N}^{(2)}_{n,m}(k\mathbf{r}))$ are then irregular.

Now that the multipolar formalism has been introduced, the rest of the Chapter is devoted to the study of the light-scattering problem by means of the Vector Partial Wave basis.

3.3 Different formulations of the scattering problem:

The aim of this section is to present the formulation of the scattering problem making use of the VPWs previously defined. We will show that one can benefit from the variety of VPWs presented in the preceding section and introduce 3 alternative formulations of the scattering problem. Each of these formulations will be shown to illustrate different physical aspects of the interaction of light with a scatterer.

3.3.1 S-matrix formulation

3.3.1.1 Definition of the S matrix

We shall start by introducing the S-matrix representation of the scattering problem. According to this representation, the scattering process may be divided into three distinct stages [101, 102]:

1. First, an incoming field freely propagates towards the scatterer.

2. As the field gets closer, it can then interact with the scatterer.

3. Finally, an outgoing field resulting from the interaction that occurred during the second stage freely propagates in the far-field zone away from the scatterer.

The S matrix is defined as the operator transforming the initial stage into the final stage. Being able to fully characterize the interaction of a scatterer with light by simply measuring the transformation of the field between the initial and final stages was in fact the central motivation behind the Heisenberg's program that led to the development of the S matrix. The S matrix is in a sense analogous to the transfer function that relates the output to the input of an electronic system.
All the information about the interaction are therefore contained in the analytical properties of the S-matrix coefficients. We will see in one of the following sections what is the constraint imposed by energy conservation on the S-matrix coefficients. The implications of Causality on the analytic properties of the S matrix will also be discussed in Chapter 6 but let us start by defining the S matrix in the vector partial wave basis.

3.3.1.2 Multipolar formulation of the S matrix

Coming back to the formulation of the scattering problem in the VPWs basis, it has been shown above that a complete basis for the fields outside the scatterer could be obtained by combining the VPWs ($\mathbf{M}^{(-)}_{n,m}(k\mathbf{r})$,$\mathbf{N}^{(-)}_{n,m}(k\mathbf{r})$) and ($\mathbf{M}^{(+)}_{n,m}(k\mathbf{r})$,$\mathbf{N}^{(+)}_{n,m}(k\mathbf{r})$). Consequently, the following expansion of the total electric field outside the scatterer holds:

$$\begin{aligned}\mathbf{E}_{\text{tot}}(k\mathbf{r}) &= \mathbf{E}_{\text{in}}(k\mathbf{r})+\mathbf{E}_{\text{out}}(k\mathbf{r}) \\ &= E_0 \sum_{n=1}^{\infty} \sum_{m=-n}^{n} s^{(h,-)}_{n,m}\mathbf{M}^{(-)}_{n,m}(k\mathbf{r}) + s^{(e,-)}_{n,m}\mathbf{N}^{(-)}_{n,m}(k\mathbf{r}) \\ &\qquad +s^{(h,+)}_{n,m}\mathbf{M}^{(+)}_{n,m}(k\mathbf{r}) + s^{(e,+)}_{n,m}\mathbf{N}^{(+)}_{n,m}(k\mathbf{r})\end{aligned} \tag{3.32}$$

The superscripts (e) and (h) respectively refer to the electric and magnetic multipoles as $\mathbf{M}_{n,m}$ are the magnetic-type VPWs whereas $\mathbf{N}_{n,m}$ are the electric-type VPWs. The S matrix being the linear relationship between the incoming and the outgoing parts of the field, its coefficients in the multipolar formalism are readily found to be:

$$S^{(e)}_{n,m} = \frac{s^{(e,+)}_{n,m}}{s^{(e,-)}_{n,m}},\ S^{(h)}_{n,m} = \frac{s^{(h,+)}_{n,m}}{s^{(h,-)}_{n,m}} \tag{3.33}$$

The total electric field expansion can consequently be rewritten in the following way by using the S-matrix coefficients:

$$\begin{aligned}\mathbf{E}_{tot}(k\mathbf{r}) = E_0 \sum_{n=1}^{\infty}\sum_{m=-n}^{n} & s_{n,m}^{(h,-)}\left(\mathbf{M}_{n,m}^{(-)}(k\mathbf{r}) + S_{n,m}^{(h)}\mathbf{M}_{n,m}^{(+)}(k\mathbf{r})\right) \\ & + s_{n,m}^{(e,-)}\left(\mathbf{N}_{n,m}^{(-)}(k\mathbf{r}) + S_{n,m}^{(e)}\mathbf{N}_{n,m}^{(+)}(k\mathbf{r})\right)\end{aligned} \tag{3.34}$$

By means of the Maxwell-Faraday equation for non-magnetic media: $\mathbf{H_{tot}} = \frac{1}{i\omega\mu_0}\nabla\times \mathbf{E_{tot}}$ along with the relations (3.14) between $\mathbf{M}$ and $\mathbf{N}$, one also finds the following expansion of the magnetic field:

$$\begin{aligned}\mathbf{H}_{tot}(k\mathbf{r}) = \frac{kE_0}{i\mu_0\omega} \sum_{n=1}^{\infty}\sum_{m=-n}^{n} & s_{n,m}^{(e,-)}\left(\mathbf{M}_{n,m}^{(-)}(k\mathbf{r}) + S_{n,m}^{(e)}\mathbf{M}_{n,m}^{(+)}(k\mathbf{r})\right) \\ & + s_{n,m}^{(h,-)}\left(\mathbf{N}_{n,m}^{(-)}(k\mathbf{r}) + S_{n,m}^{(h)}\mathbf{N}_{n,m}^{(+)}(k\mathbf{r})\right)\end{aligned} \tag{3.35}$$

The internal field existing inside the scatterer has to satisfy regular boundary conditions at $\mathbf{r} = \mathbf{0}$, it should then be expanded on the regular VPWs basis ($\mathbf{M}_{n,m}^{(1)}, (k_s\mathbf{r})$, $\mathbf{N}_{n,m}^{(1)}(k_s\mathbf{r})$) where $k_s = n_s k$ and n_s is the refractive index of the scatterer:

$$\begin{aligned}\mathbf{E}_{int}(k\mathbf{r}) &= E_0 \sum_{n=1}^{\infty}\sum_{m=-n}^{n} u_{n,m}^{(h)}\mathbf{M}_{n,m}^{(1)}(k_s\mathbf{r}) + u_{n,m}^{(e)}\mathbf{N}_{n,m}^{(1)}(k_s\mathbf{r}) \\ \mathbf{H}_{int}(k\mathbf{r}) &= \frac{k_s E_0}{i\mu_0\omega} \sum_{n=1}^{\infty}\sum_{m=-n}^{n} u_{n,m}^{(e)}\mathbf{M}_{n,m}^{(1)}(k_s\mathbf{r}) + u_{n,m}^{(h)}\mathbf{N}_{n,m}^{(1)}(k_s\mathbf{r})\end{aligned} \tag{3.36}$$

A matrix relating the internal field $E_{int}(k_s\mathbf{r})$ to the incoming field $E_{in}(k\mathbf{r})$ can thus be introduced. It will be called the Ξ matrix in what follows and the definition of its coefficients are:

$$\Xi_{n,m}^{(e)} = \frac{u_{n,m}^{(e)}}{s_{n,m}^{(e,-)}},\ \Xi_{n,m}^{(h)} = \frac{u_{n,m}^{(h)}}{s_{n,m}^{(h,-)}} \tag{3.37}$$

3.3.1.3 S and Ξ matrices of a spherically symmetric scatterer

As the angular momentum is conserved when light is scattered by a spherically symmetric scatterer, the S and Ξ matrices are diagonal. Moreover, their coefficients are independent of the variable m.

Analytic expressions of the S-matrix and Ξ matrix coefficients can therefore be derived by using the Vector Partial Wave expansion of the internal and external fields (3.34), (3.35) and (3.52) along with the continuity conditions of the electromagnetic field at an interface (A.1) and the orthogonality conditions of the vector spherical harmonics. The following expressions are obtained (detailed calculations can be

found in Appendix A):

$$S_n^{(e,h)} = -\frac{N_{S,n}^{(e,h)}(kR)}{D_n^{(e,h)}(kR)},\ \Xi_n^{(e,h)} = \frac{1}{D_n^{(e,h)}(kR)} \tag{3.38}$$

where we have introduced the numerator $N_{S,n}^{(e,h)}$ and denominator $D_n^{(e,h)}(kR)$ functions defined as follows:

$$\begin{aligned}
N_{S,n}^{(e)}(kR) &= kR\frac{\varepsilon_s\xi_n^{(-)'}(kR)j_n(k_sR) - \psi_n'(k_sR)h_n^{(-)}(kR)}{2in_s} \\
N_{S,n}^{(h)}(kR) &= kR\frac{\xi_n^{(-)'}(kR)j_n(k_sR) - \psi_n'(k_sR)h_n^{(-)}(kR)}{2i} \\
D_n^{(e)}(kR) &= kR\frac{\varepsilon_s\xi_n^{(+)'}(kR)j_n(k_sR) - \psi_n'(k_sR)h_n^{(+)}(kR)}{2in_s} \\
D_n^{(h)}(kR) &= kR\frac{\xi_n^{(+)'}(kR)j_n(k_sR) - \psi_n'(k_sR)h_n^{(+)}(kR)}{2i}
\end{aligned} \tag{3.39}$$

3.3.1.4 Energy conservation constraints on the S-matrix coefficients:

The conservation of energy during the scattering process can be expressed under the integral form of the Poynting theorem:

$$-\frac{\partial}{\partial t}\iiint_V u(\mathbf{r})d\mathbf{r} = \oiint_{\partial V}\mathbf{S}\cdot d\mathbf{A} \tag{3.40}$$

where $u(\mathbf{r}) = \frac{1}{2}(\mathbf{E}\cdot\mathbf{D} + \mathbf{B}\cdot\mathbf{H})$ is the energy density whereas $\mathbf{S}$ is the Poynting vector. The integral on the left hand side of the previous equation is performed over the volume V. On the other hand, the surface integral on the right hand side is performed over the surface δV that limits the volume V. In the harmonic domain, the time average Poynting vector $\langle\mathbf{S}\rangle_\omega = \frac{1}{2}\mathrm{Re}(\mathbf{E}\times\mathbf{H}^*)$ is the Poynting vector. In the far field, incoming and outgoing fields are transverse and the $\mathbf{H}$ field is readily obtained from the electric field using: $\lim_{r\to\infty}\mathbf{H}_{in} = -\frac{k}{\mu_0\omega}\hat{\mathbf{r}}\times\mathbf{E}_{in}$ and $\lim_{r\to\infty}\mathbf{H}_{out} = \frac{k}{\mu_0\omega}\hat{\mathbf{r}}\times\mathbf{E}_{out}$. If the volume V is chosen to be a sphere and if we let the radius of this sphere tend towards infinity while using the field expansion (6.41), the following multipolar expansion of the power is found:

$$\begin{aligned}
\lim_{r\to\infty}\oiint_\Omega \hat{\mathbf{r}}\cdot\langle\mathbf{S}\rangle_\omega r^2 d\Omega &= \lim_{r\to\infty}\frac{1}{2}\frac{kr^2}{\omega\mu_0}\oiint_\Omega \mathbf{E}_{out}\cdot\mathbf{E}_{out}^* d\Omega - \lim_{r\to\infty}\frac{1}{2}\frac{kr^2}{\omega\mu_0}\oiint_\Omega \mathbf{E}_{in}\cdot\mathbf{E}_{in}^* d\Omega \\
&= \frac{c|E_0|^2}{2\omega^2\mu_0}\sum_{n=1}^{\infty}\sum_{m=-n}^{n}|s_{n,m}^{(e,-)}|^2\left(\left|S_n^{(e)}\right|^2 - 1\right) + |s_{n,m}^{(h,-)}|^2\left(\left|S_n^{(h)}\right|^2 - 1\right)
\end{aligned} \tag{3.41}$$

For passive media, i.e. without optical gain, Eq. (3.40) implies that $\iint_{\partial V} \mathbf{S} \cdot d\mathbf{A} \leq 0$. By using the orthogonality of the VPWs, one can finally show:

$$|S_{n,m}^{(e,h)}|^2 \leq 1 \tag{3.42}$$

The previous relation is the constraint imposed by energy conservation on the S-matrix coefficients. When there is no loss in the scatterer that is considered, the S-matrix coefficients are unitary: $|S_{n,m}^{(e,h)}| = 1$. In the following section, we will study the implication of the previous relation to the case of a lossless scatterer.

3.3.1.5 Definition of the phase shift for a lossless scatterer:

For lossless spherical scatterers, the modulus of the S-matrix coefficients reach their upper limit: $|S_n^{(e,h)}|^2 = 1$. It follows that $S_n^{(e,h)}$ can be seen as mere phase factors (see for example [100] p 301, [101] pp 57-58 or [103]):

$$S_n^{(e,h)} = e^{2i\delta_n^{(e,h)}} \tag{3.43}$$

The physical meaning of $\delta_n^{(e,h)}$ is found by deriving the far-field expression of Eq. (6.41) :

$$\begin{aligned}\lim_{r\to\infty} \mathbf{E}_{tot}(k\mathbf{r}) = E_0 \sum_{n=1}^{\infty} \sum_{m=-n}^{n} & i^{n+1} \frac{s_{n,m}^{(h,-)}}{kr} \left(e^{-ikr} - (-1)^n S_n^{(h)} e^{ikr}\right) \mathbf{X}_{n,m}(\theta,\phi) \\ & + i^n \frac{s_{n,m}^{(e,-)}}{kr} \left(e^{-ikr} - (-1)^{n-1} S_n^{(e)} e^{ikr}\right) \mathbf{Z}_{n,m}(\theta,\phi)\end{aligned} \tag{3.44}$$

If now the phase expression of $S_n^{(e,h)}$ of Eq. (3.43) is used and using the following equalities $e^{-in\pi} = (-1)^n$ and $e^{in\frac{\pi}{2}} = i^n$, it can be shown that Eq. (3.44) becomes:

$$\begin{aligned}\lim_{r\to\infty} \mathbf{E}_{tot}(k\mathbf{r}) = E_0 \sum_{n=1}^{\infty} \sum_{m=-n}^{n} & 2e^{i\delta_n^{(h)}} \frac{s_{n,m}^{(h,-)}}{kr} \sin\left(kr - \frac{n\pi}{2} + \delta_n^{(h)}\right) \mathbf{X}_{n,m}(\theta,\phi) \\ & + 2e^{i\delta_n^{(e)}} \frac{s_{n,m}^{(e,-)}}{kr} \sin\left(kr - \frac{(n-1)\pi}{2} + \delta_n^{(e)}\right) \mathbf{Z}_{n,m}(\theta,\phi)\end{aligned} \tag{3.45}$$

Let us recall that, according to Eqs. (3.31), in the absence of scatterer, the total field would asymptotically tend towards:

$$\begin{aligned}\lim_{r\to\infty} \mathbf{E}_{tot}(k\mathbf{r}) = E_0 \sum_{n=1}^{\infty} \sum_{m=-n}^{n} & 2\frac{s_{n,m}^{(h,-)}}{kr} \sin\left(kr - \frac{n\pi}{2}\right) \mathbf{X}_{n,m}(\theta,\phi) \\ & + 2\frac{s_{n,m}^{(e,-)}}{kr} \sin\left(kr - \frac{(n-1)\pi}{2}\right) \mathbf{Z}_{n,m}(\theta,\phi)\end{aligned} \tag{3.46}$$

It then becomes clear that $\delta_n^{(e,h)}$ is the phase shift resulting from the interaction of the excitation field with the scatterer. This is an illustration of the usefulness of the S-matrix, by simply measuring in the far field the phase shift caused by the interaction of the wave with the scatterer, one gets a full description of the interaction between the light and the scatterer. In Chapter 4, we will give the expressions of observable quantities such as the cross sections in terms of the phase shifts $\delta_n^{(e,h)}$.

3.3.2 T-matrix formulation and polarizability

3.3.2.1 Definition of the T matrix

In the previous section, we have seen the advantages of employing a S matrix description of the scattering problem, in particular in regard to the energy conservation laws. It was also shown that physical insight could also be gained by introducing the phase shift.
One could however argue that using the S matrix representation is not the most intuitive way of dealing with the scattering problem in particular when one wants to compare theoretical predictions to experimental results. The interaction of a scatterer with purely incoming spherically-symmetric fields is rarely studied experimentally.
From an experimental point of view, it would be much more natural to introduce a matrix permitting to calculate the scattered field while knowing the incident or excitation field (containing both incoming and outgoing parts) illuminating the scatterer. Knowing the scattered field in turn allows to derive experimentally measurable quantities such as extinction or scattering cross sections.
Such a matrix is called the T matrix in the literature [93, 100, 103]. From a mathematical standpoint, its existence is a consequence of the linearity of the Maxwell equations and of the continuity conditions at an interface leading the coefficients of the scattered field to be linearly related to those of the incident field.
On top of being convenient for describing experiments, the T-matrix method has also proved to be very well suited for studying multiple-scattering from an ensemble of scatterers [104]. All these advantages have motivated the development of the T matrix method and an abundant literature can be found on this topic [95].

In this section, we shall start by introducing the multipolar formulation of the T-matrix. Analytical expressions of spherically symmetric scatterers will then be provided along with their relation to the Mie coefficients. Finally, the link between the dipolar Mie coefficients of a scatterer and its electric and magnetic polarizabilities will then be discussed.

3.3.2.2 Multipolar formulation of the T matrix:

Coming back to the discussion of section 3.2.2.2, a complete basis of the total field outside the scatterer can be formed by use of $(\mathbf{M}^{(1)}_{n,m}(k\mathbf{r}),\mathbf{N}^{(1)}_{n,m}(k\mathbf{r}))$ and $(\mathbf{M}^{(+)}_{n,m}(k\mathbf{r}),\mathbf{N}^{(+)}_{n,m}(k\mathbf{r}))$. The incident field being a plane wave or a superposition of plane waves, it should be expanded on the set of regular VPWs:

$$\begin{aligned}\mathbf{E}_{inc}(k\mathbf{r}) &= E_0 \sum_{n=1}^{\infty}\sum_{m=-n}^{n} e^{(h)}_{n,m}\mathbf{M}^{(1)}_{n,m}(k\mathbf{r}) + e^{(e)}_{n,m}\mathbf{N}^{(1)}_{n,m}(k\mathbf{r}) \\ \mathbf{H}_{inc}(k\mathbf{r}) &= \frac{kE_0}{i\mu_0\omega}\sum_{n=1}^{\infty}\sum_{m=-n}^{n} e^{(e)}_{n,m}\mathbf{M}^{(1)}_{n,m}(k\mathbf{r}) + e^{(h)}_{n,m}\mathbf{N}^{(1)}_{n,m}(k\mathbf{r})\end{aligned} \tag{3.47}$$

Recalling the relation between Bessel and Hankel function: $j_n(x) = \frac{h_n^{(+)}(x)+h_n^{(-)}(x)}{2}$, it clearly appears that the incident field is a superposition of incoming and outgoing waves. On the other hand, the scattering wave that satisfies outgoing boundary condition is to be expanded on the set of VPWs $(\mathbf{M}^{(+)}_{n,m}(k\mathbf{r}),\mathbf{N}^{(+)}_{n,m}(k\mathbf{r}))$:

$$\begin{aligned}\mathbf{E}_{scat}(k\mathbf{r}) &= E_0 \sum_{n=1}^{\infty}\sum_{m=-n}^{n} f^{(h)}_{n,m}\mathbf{M}^{(+)}_{n,m}(k\mathbf{r}) + f^{(e)}_{n,m}\mathbf{N}^{(+)}_{n,m}(k\mathbf{r}) \\ \mathbf{H}_{scat}(k\mathbf{r}) &= \frac{kE_0}{i\mu_0\omega}\sum_{n=1}^{\infty}\sum_{m=-n}^{n} f^{(e)}_{n,m}\mathbf{M}^{(+)}_{n,m}(k\mathbf{r}) + f^{(h)}_{n,m}\mathbf{N}^{(+)}_{n,m}(k\mathbf{r})\end{aligned} \tag{3.48}$$

The T matrix coefficients can then be defined as the coefficient of proportionality between the coefficients $(f^{(e)}_{n,m},\ f^{(h)}_{n,m})$ and $(e^{(e)}_{n,m},\ e^{(h)}_{n,m})$:

$$T^{(e)}_{n,m} = \frac{f^{(e)}_{n,m}}{e^{(e)}_{n,m}},\ T^{(h)}_{n,m} = \frac{f^{(h)}_{n,m}}{e^{(h)}_{n,m}} \tag{3.49}$$

And the total field can be rewritten in terms of the T-matrix as follows:

$$\begin{aligned}\mathbf{E}_{tot}(k\mathbf{r}) = E_0 \sum_{n=1}^{\infty}\sum_{m=-n}^{n} & e^{(h)}_{n,m}\left(\mathbf{M}^{(1)}_{n,m}(k\mathbf{r}) + T^{(h)}_{n,m}\mathbf{M}^{(+)}_{n,m}(k\mathbf{r})\right) \\ & + e^{(e)}_{n,m}\left(\mathbf{N}^{(1)}_{n,m}(k\mathbf{r}) + T^{(e)}_{n,m}\mathbf{N}^{(+)}_{n,m}(k\mathbf{r})\right)\end{aligned} \tag{3.50}$$

By comparing eqs. (3.34) and (3.50), one can then derive the relation between the T and S matrices by means of the relation between the Bessel and Hankel functions:

$$S = I + 2T \tag{3.51}$$

Finally, recalling the expansion of the internal field:

$$\begin{aligned}\mathbf{E}_{int}(k\mathbf{r}) &= E_0 \sum_{n=1}^{\infty} \sum_{m=-n}^{n} u_{n,m}^{(h)} \mathbf{M}_{n,m}^{(1)}(k_s\mathbf{r}) + u_{n,m}^{(e)} \mathbf{N}_{n,m}^{(1)}(k_s\mathbf{r}) \\ \mathbf{H}_{int}(k\mathbf{r}) &= \frac{k_s E_0}{i\mu_0\omega} \sum_{n=1}^{\infty} \sum_{m=-n}^{n} u_{n,m}^{(e)} \mathbf{M}_{n,m}^{(1)}(k_s\mathbf{r}) + u_{n,m}^{(h)} \mathbf{N}_{n,m}^{(1)}(k_s\mathbf{r})\end{aligned} \tag{3.52}$$

One can finally introduce the Ω matrix relating the incident field to the internal field:

$$\Omega_{n,m}^{(e)} = \frac{u_{n,m}^{(e)}}{e_{n,m}^{(e)}},\ \Omega_{n,m}^{(h)} = \frac{u_{n,m}^{(h)}}{e_{n,m}^{(h)}} \tag{3.53}$$

3.3.2.3 T and Ω matrices of a spherically symmetric scatterer

For spherically symmetric scatterers, the T matrix is also diagonal and the expression of the T-matrix coefficients in terms of the phase shift is given by: $T_n^{(e,h)} = i \sin\left(\delta_n^{(e,h)}\right) e^{i\delta_n^{(e,h)}}$. Similarly to what was done with the S matrix, it is also possible to derive analytical expressions for the T and Ω-matrix coefficients. Here, we will provide only the results but detailed calculations can be found in Appendix A:

$$T_n^{(e,h)} = -\frac{N_{T,n}^{(e,h)}(kR)}{D_n^{(e,h)}(kR)},\ \Omega_n^{(e,h)} = \frac{1}{2}\frac{1}{D_n^{(e,h)}(kR)} \tag{3.54}$$

where the new numerator functions $N_{T,n}^{(e,h)}(kR)$ are being used:

$$\begin{aligned}N_{T,n}^{(e)}(kR) &= kR\frac{\varepsilon_s \psi_n'(kR) j_n(k_sR) - j_n(kR)\psi_n'(k_sR)}{2in_s} \\ N_{T,n}^{(h)}(kR) &= kR\frac{\psi_n'(kR) j_n(k_sR) - \psi_n'(k_sR) j_n(kR)}{2i}\end{aligned} \tag{3.55}$$

The interaction between the incident field and a spherical scatterer is also often described by using the electric and magnetic Mie coefficients a_n and b_n. They can be linked to the T-matrix coefficients by means of the following relations:

$$\begin{aligned}T_n^{(e)} &= -a_n \\ T_n^{(h)} &= -b_n\end{aligned} \tag{3.56}$$

3.3.2.4 Dipolar T-matrix coefficients and polarizability for small sized scatterers:

When scatterers are very small compared to the wavelength, their optical response is dominated by the dipolar (electric and magnetic) contributions. In this case, the interaction between the excitation field and the scatterer can be well-described in

terms of electric and magnetic moments:

$$\begin{aligned} \mathbf{p} &= \epsilon_0 \varepsilon_b \alpha_e \mathbf{E}_{exc} \\ \mathbf{m} &= \alpha_h \mathbf{H}_{exc} \end{aligned} \tag{3.57}$$

ε_b being the permittivity of the background medium in which the scatterer is located. These induced dipoles oscillate at the same frequency as the excitation field: ω. These dipoles in turn radiate a field, otherwise called the scattered field, that asymptotically tends towards:

$$\begin{aligned} \lim_{r\to\infty} \mathbf{E}_{scat}(\mathbf{r}) &= k^2 \frac{e^{ikr}}{4\pi\epsilon_0\varepsilon_b r} (\hat{\mathbf{r}} \times \mathbf{p}) \times \hat{\mathbf{r}} \\ \lim_{r\to\infty} \mathbf{H}_{scat}(\mathbf{r}) &= \frac{k}{\mu_0 \omega} \hat{\mathbf{r}} \times \mathbf{E}_{scat} \end{aligned} \tag{3.58}$$

The electromagnetic field radiated by a magnetic dipole can be obtained in a similar way (see for example [98] pp 431-438). The polarizability expressions can be related to the dipolar T-matrix coefficients or Mie coefficients:

$$\begin{aligned} \alpha_e &= -i\frac{6\pi}{k^3} T_1^{(e)} = i\frac{6\pi}{k^3} a_1 \\ \alpha_h &= -i\frac{6\pi}{k^3} T_1^{(h)} = i\frac{6\pi}{k^3} b_1 \end{aligned} \tag{3.59}$$

3.3.3 K-matrix formulation

We will finally introduce the K matrix. Even if it has been used for years in the context of the quantum scattering theory [100], it has not been employed for the study of electromagnetic scattering until recently [105, 106]. As we will see, by definition, the K matrix links the regular part of the field to the irregular part of the field. It is then much more complicated to provide a physical interpretation of the K-matrix than it was for the S and T matrices.
However, this matrix proves to be very useful when dealing with radiative losses. The quality factors of plasmonics and Mie resonators are usually limited to low values because light can only be stored for a short time in these types of resonators before being radiated away. This effect can be described by introducing radiative losses besides the intrinsic losses reflecting the absorption occuring inside the resonators.
Due to the existence of radiative losses, the T and S-matrix coefficients are complex even for non-absorbing scatterers. On the other hand, the K-matrix coefficients become real as soon as non-absorbing scatterers are considered and that is the reason why it is well suited to study radiative losses.
Here, after introducing the K-matrix definition, we will discuss the link between the K-matrix formulation of the scattering problem with the radiative losses. We

will finally show that the reformulation of the polarizability in terms of the K matrix allows for the derivation of polarizability approximations including radiative corrections.

3.3.3.1 Definition of the K matrix:

In the K-matrix formalism, the total field outside the scatterer is splitted into its regular part expanded on the regular VPWs ($\mathbf{M}^{(1)}_{n,m}(k\mathbf{r})$,$\mathbf{N}^{(1)}_{n,m}(k\mathbf{r})$):

$$\mathbf{E}_{\text{reg}}(k\mathbf{r}) = E_0 \sum_{n=1}^{\infty} \sum_{m=-n}^{n} r^{(h)}_{n,m} \mathbf{M}^{(1)}_{n,m}(k\mathbf{r}) + r^{(e)}_{n,m} \mathbf{N}^{(1)}_{n,m}(k\mathbf{r}) \tag{3.60}$$

and its irregular part expanded on ($\mathbf{M}^{(2)}_{n,m}(k\mathbf{r})$,$\mathbf{N}^{(2)}_{n,m}(k\mathbf{r})$):

$$\mathbf{E}_{\text{irreg}}(k\mathbf{r}) = E_0 \sum_{n=1}^{\infty} \sum_{m=-n}^{n} i^{(h)}_{n,m} \mathbf{M}^{(2)}_{n,m}(k\mathbf{r}) + i^{(e)}_{n,m} \mathbf{N}^{(2)}_{n,m}(k\mathbf{r}) \tag{3.61}$$

The K matrix relates the irregular part of the total field to its regular part. Consequently, its coefficients are defined as follows:

$$K^{(e)}_{n,m} = \frac{i^{(e)}_{n,m}}{r^{(e)}_{n,m}},\ K^{(h)}_{n,m} = \frac{i^{(h)}_{n,m}}{r^{(h)}_{n,m}} \tag{3.62}$$

The regular part of the total field is constituted of both the excitation field and the regular part of the scattered field. The irregular part of the total field is constituted of only the irregular part of the scattered field. It is then somehow more complicated to find a physical interpretation for the K matrix.
The relationship between the K matrix and the T and S matrices is:

$$\begin{aligned} K = iT(I+T)^{-1} &\Leftrightarrow T^{-1} = iK^{-1} - I \\ K = i(S-I)(I+S)^{-1} &\Leftrightarrow S = (I-iK)(I+iK)^{-1} \end{aligned} \tag{3.63}$$

Finally for a spherically-symmetric scatterer, similarly to the T and S matrix coefficients an analytical expression of the K-matrix coefficients can be derived (see appendix A for detailed calculations)

$$K^{(e,h)}_n = -\frac{N^{(e,h)}_{T,n}(kR)}{D^{(e,h)}_{K,n}(kR)} \tag{3.64}$$

where the new denominator functions are used $D_{K,n}^{(e,h)}(kR)$:

$$\begin{aligned} D_{K,n}^{(e)}(kR) &= kR\frac{\varepsilon_s\chi_n^{(+)'}(kR)j_n(k_sR) - \psi_n'(k_sR)y_n(kR)}{2in_s} \\ D_{K,n}^{(h)}(kR) &= kR\frac{\chi_n^{(+)'}(kR)j_n(k_sR) - \psi_n'(k_sR)y_n(kR)}{2i} \end{aligned} \tag{3.65}$$

Finally one can also express the K-matrix in terms of the phase shift leading to $K_n^{(e,h)} = -\tan\delta_n^{(e,h)}$

3.3.3.2 K-matrix and radiative losses

For lossless scatterers, it has already been shown that the energy conservation is equivalent to the unitarity of S. By use of the relation (3.63), it can be shown that this condition is equivalent to the following conditions for the T and K matrices:

$$\begin{aligned} T + T^\dagger &= -2T^\dagger T \\ K &= K^\dagger \end{aligned} \tag{3.66}$$

$T^\dagger$ being the conjugate transpose of T. For lossless scatterers, the K-matrix coefficients are then real. On the other hand, when lossy scatterers are considered, the coefficients $K_n^{(e,h)}$ become complex with $\mathrm{Im}\left(K_n^{(e,h)}\right) \geq 0$. The imaginary part of $K_n^{(e,h)}$ is then related to intrinsic absorption and does not include radiative losses. The Mie coefficients can be reformulated in the following way:

$$\begin{aligned} a_n^{-1} &= -i\left(K_n^{(e)}\right)^{-1} + 1 \\ b_n^{-1} &= -i\left(K_n^{(h)}\right)^{-1} + 1 \end{aligned} \tag{3.67}$$

This expression can be seen as a multipole generalization of the well-known energy-conserving representation of the electric dipolar polarizability α_e [105, 107, 108]:

$$\alpha_e^{-1} = \alpha_{\text{n.r.}}^{-1} - i\frac{k^3}{6\pi} \tag{3.68}$$

The term $\alpha_{\text{n.r.}}$ accounts for the non-radiative polarizability and is often approximated by its electrostatic value α_0. One can however show from (3.67) that $\alpha_{\text{n.r.}} = -\frac{6\pi K_1^{(e)}}{k^3}$. On the other hand, all the information about radiation losses is contained in the $+1$ terms in (3.67) or equivalently in the $-\frac{k^3}{6\pi}$ term in (3.68) which are often referred to as radiative corrections.
Following [105], it is interesting to give an interpretation of these radiative corrections by use of the self field. The self field $\mathbf{E}_{\text{SF}}$ can be interpreted as a feedback of the scattered field on the scatterer. If the self-field is taken into account, the electric dipolar moment can be cast $\mathbf{p} = \epsilon_0\epsilon_b\alpha_{\text{n.r.}}(\mathbf{E}_{\text{exc}} - \mathbf{E}_{\text{SF}})$. By definition, if the scatterer is located at $\mathbf{r}_0$, the self field is $\mathbf{E}_{\text{SF}} = G(\mathbf{r}_0, \mathbf{r}_0)\,\mathbf{p}$ where $G(\mathbf{r}_0, \mathbf{r}_0)$ is the dyadic

Green function evaluated in vacuum at the scatterer position $\mathbf{r}_0$. Recalling that the electric dipolar moment usual definition is $\mathbf{p} = \epsilon_0 \epsilon_b \alpha_e \mathbf{E}_{\text{exc}}$, it can be shown that:

$$\alpha_e^{-1} = \alpha_{\text{n.r.}}^{-1} - G(\mathbf{r}_0, \mathbf{r}_0) \tag{3.69}$$

By comparison of eqs. (3.68) and (3.69), it clearly appears that radiative corrections are linked to the imaginary part of the Green function at the position of the scatterer [109]. This radiative loss term is then dependent on the environment of the scatterer. Consequently radiative losses can be modified, either inhibited or enhanced by changing the environment of the scatterer [110]. This effect is completely analogous to the control of the decay rate of a quantum emitter by a structured environment [111] and to the impedance matching for antenna emission.

3.3.3.3 Approximations of the polarizabily for small sized scatterers:

In nanophotonics, we are usually concerned with the study of the scattering properties of scatterers very small compared to the wavelength. As a consequence, it can safely be assumed that their optical response is dominated by their electric and magnetic dipole terms and neglect higher order contributions. It is possible to go further and derive approximations of the dipolar polarizabilities (or equivalently the Mie coefficients) in the long-wavelength limit.
According to Eqs (3.66) and (3.67), any real-valued approximation of K_n will preserve the energy conservation relations for the Mie coefficients for non-absorbing scatterers. The formulations (3.67) are therefore well-adapted for deriving approximations of the Mie coefficients. That is why in this section, we will be using expressions (3.67) to derive approximations of the Mie coefficients for small sized scatterers by using the Laurent-series expansions of the K-matrix coefficients.
The Laurent series development of the inverse K-matrix elements, K_n, in powers of $x = kR$ is given in Appendix A.3.1. Restricting our attention to the dipole term, $n = 1$, for small scatterers yields:

$$[K_1^{(e)}]^{-1} = -\frac{3(\bar{\varepsilon}_s + 2)}{2(kR)^3(\bar{\varepsilon}_s - 1)} \left(1 - \frac{3(kR)^2(\bar{\varepsilon}_s - 2)}{5(\bar{\varepsilon}_s + 2)} - \frac{3(kR)^4(\bar{\varepsilon}_s^2 - 24\bar{\varepsilon}_s + 16)}{350(\bar{\varepsilon}_s + 2)}\right) \tag{3.70a}$$

$$[K_1^{(h)}]^{-1} = -\frac{45}{(kR)^5(\bar{\varepsilon}_s - 1)} \left(1 - \frac{(kR)^2(2\bar{\varepsilon}_s - 5)}{21} - \frac{(kR)^4(\bar{\varepsilon}_s^2 + 100\bar{\varepsilon}_s - 125)}{2205}\right) \tag{3.70b}$$

The fourth order, x^4 size corrections, of Eqs.(3.70), will usually suffice, but the order x^6 size corrections in the parenthesis are given in Appendix A.3.1.

Long wavelength approximations of the electric mode Mie coefficients, like that

found by inserting Eq.(3.70a) into Eq.(3.67), have already been shown to accurately describe the electric response of small metallic spheres [105, 112] as illustrated in Fig.(3.2) where we compare exact and approximate a_1 coefficients of a $R = 60$nm radius gold sphere [113]. It is much less appreciated however, that the analogous procedure for magnetic modes of inserting Eq.(3.70b) into Eq.(3.67) produces good approximations to magnetic dipole resonances in high index dielectric spheres. The results displayed in Fig.(3.3) illustrate the accuracy of this method to describe the magnetic dipole coefficient of a $R = 80$ nm, $\varepsilon = 16$ dielectric sphere (despite the fact that the quasi-static magnetic polarizability is zero due to the absence of permeability contrasts).

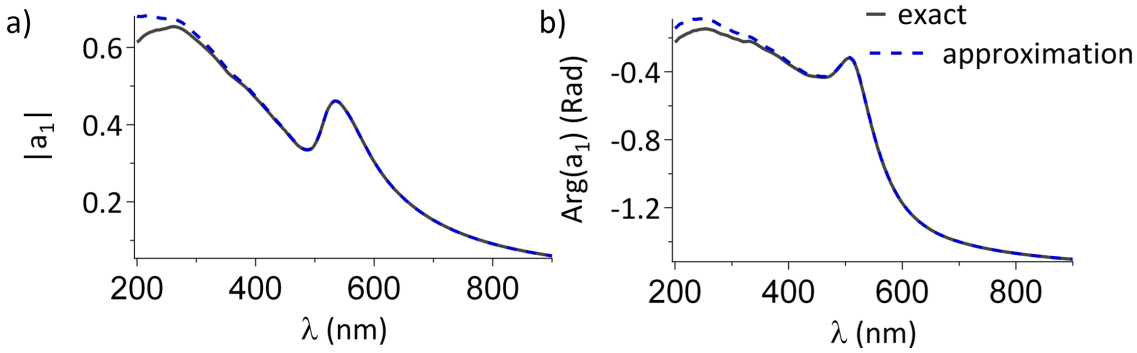

Figure 3.2: Approximate values for the electric dipole Mie coefficient, a_1, (amplitude and phase) compared with the exact values (solid black) ; $R = 60$nm gold sphere.

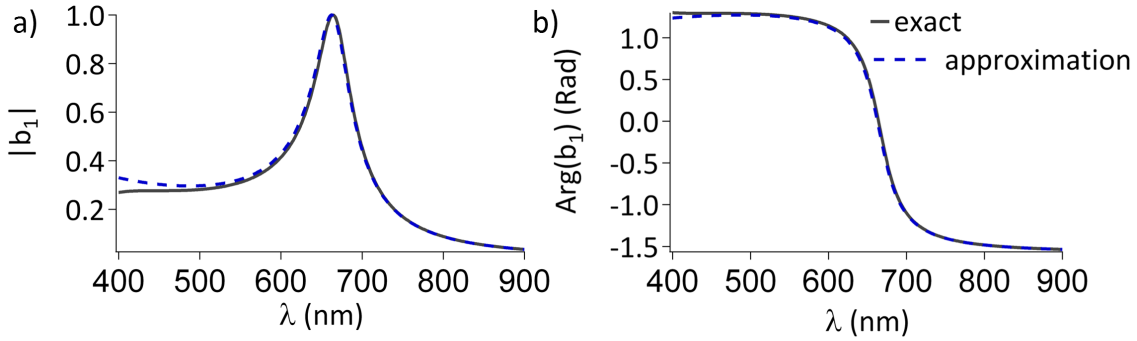

Figure 3.3: Approximate values for the magnetic dipole Mie coefficient, b_1, (amplitude and phase) compared with the exact values (solid black) ; $R = 80$nm, $\varepsilon = 16$.

These approximations will be used in Chapter 4 to predict the conditions of optimal interaction.

3.4 Conclusion:

In this Chapter, we have introduced the theoretical tools allowing us to study the interaction between light and spherical scatterers in the scope of this thesis. These

tools will in particular be used in the following Chapter in order to determine the optimal interaction between light and resonant scatterers. Approximation of the Mie coefficients and of the dipolar polarizability introduced in this Chapter will also be derived in Chapter 5. Finally, in Chapter 6 a pole expansion of the S matrix will be derived and will be used to describe the resonant behavior of Mie resonators by use of their quasi-normal modes.

Chapter 4

Optimal interaction between light and resonant scatterers:

Summary: In this Chapter, we will show how the tools introduced in the previous chapter can be used to determine the conditions of optimal interaction between light and a scatterer, i.e conditions at which an object best scatters or absorbs light, for a given multipolar order. In addition, we shall be concerned with the study of the maxima of the scattering and absorption cross sections. In particular, we will see that for a given multipolar order n, the maximum of scattering is reached near the poles of the corresponding K-matrix coefficients $K_n^{(e,h)}$. On the other hand, at the same multipolar order the maximum of absorption will be seen to be reached at the zeros of the corresponding S-matrix coefficients $S_n^{(e,h)}$.

4.1 Introduction:

The ability of plasmonic and high refractive index scatterers to enhance light-matter interactions originates from their resonant interaction with light. The resonances of these structures have consequently been the subject of strong interest. However, what is precisely referred to as a resonance appears to vary depending on the context. From a theoretical point of view, resonances or resonant states are synonyms with modes or quasi-normal modes [5] that will be the subject of chapter 6. These quasi-normal modes correspond to the solutions of Maxwell equations without sources satisfying outgoing boundary conditions to account for radiative loss. They can equivalently be defined as the poles of the S and T matrix coefficients introduced in chapter 3. These conditions can only be satisfied at complex frequencies $\omega_n = \omega_{n,\mathrm{r}} + i\omega_{n,\mathrm{i}}$, the imaginary part $\omega_{n,\mathrm{i}}$ accounting for the finite lifetime of these modes. These complex frequencies are not very suitable for interpreting experimental results. That is why from an experimental standpoint, the term resonance often designates peaks or local maxima appearing in the spectrum of observable quantities such as scattering, extinction or absorption cross sections.

In the particular case of the scattering cross section, the partial cross section $\sigma_{n,\mathrm{s}}^{(q)}$ associated with one multipole order to the scattering cross section will be shown to be equal to $\sigma_{n,\mathrm{s}}^{(q)} = \frac{(2n+1)\lambda^2}{2\pi}\left|T_n^{(q)}\right|^2$. Peaks of the scattering cross-section can consequently be expected to occur at the vicinity of the maxima of $\left|T_n^{(q)}\right|^2$. It would be tempting to assume that such maxima arise at the frequencies $\omega_{n,\mathrm{r}} = \mathrm{Re}\left(\omega_n\right)$. That would amount to inferring that peaks in the cross section spectra are of lorentzian-type. Nonetheless, as will be discussed in chapter 6 and shown in Figs. 6.3, these resonances clearly appear to have asymmetric shapes rather than lorentzian shapes. Consequently, the simple assumption of $\omega_{n,\mathrm{r}} = \mathrm{Re}\left(\omega_n\right)$ being in general the position of these peaks is not strictly valid.

After defining the expression of the cross sections, we will study the conditions at which peaks in the scattering and absorption cross-section can occur. We will in particular discuss how the peaks of the scattering cross section can be related to the Unitary Limit which is the upper bound of the partial scattering cross section $\sigma_{n,\mathrm{s}}^{(q)}$. Equivalently, the relation between the peaks of the partial absorption cross section and the Ideal Absorption corresponding to the upper bound of the partial absorption cross section $\sigma_{n,\mathrm{a}}^{(q)}$ will be discussed. In addition, permittivity required to reach either of these bounds for a given size parameter $z = \frac{\omega}{c}R$ will be provided. Finally, the relation between near and far-field spectra will also be considered.

4.2 Optimal light-particle interactions:

4.2.1 Cross-sections:

First, it is obviously necessary to define quantities that quantify the interaction between light and a scatterer. For that purpose, we will introduce the absorption, scattering and extinction cross sections.
Let us start by recalling that the time-averaged Poynting vector associated with the total field is equal to $\langle \mathbf{S}_{\mathrm{tot}} \rangle = \frac{1}{2}\mathrm{Re}\left(\mathbf{E}_{\mathrm{tot}} \times \mathbf{H}_{\mathrm{tot}}^*\right)$. Splitting the total field into its incident $\mathbf{E}_{\mathrm{inc}}$ and scattered $\mathbf{E}_{\mathrm{scat}}$ parts, the time-average Poynting vector of the total field can consequently be expressed:

$$\langle \mathbf{S}_{\mathrm{tot}} \rangle = \langle \mathbf{S}_{\mathrm{inc}} \rangle + \langle \mathbf{S}_{\mathrm{ext}} \rangle + \langle \mathbf{S}_{\mathrm{scat}} \rangle \tag{4.1}$$

where $\langle \mathbf{S}_{\text{inc}} \rangle$, $\langle \mathbf{S}_{\text{ext}} \rangle$ and $\langle \mathbf{S}_{\text{scat}} \rangle$ are defined as follows:

$$\begin{aligned} \langle \mathbf{S}_{\text{inc}} \rangle &= \frac{1}{2}\text{Re}\left(\mathbf{E}_{\text{inc}} \times \mathbf{H}^*_{\text{inc}}\right) \\ \langle \mathbf{S}_{\text{ext}} \rangle &= \frac{1}{2}\text{Re}\left(\mathbf{E}_{\text{inc}} \times \mathbf{H}^*_{\text{scat}} + \mathbf{E}_{\text{scat}} \times \mathbf{H}^*_{\text{inc}}\right) \\ \langle \mathbf{S}_{\text{scat}} \rangle &= \frac{1}{2}\text{Re}\left(\mathbf{E}_{\text{scat}} \times \mathbf{H}^*_{\text{scat}}\right). \end{aligned} \tag{4.2}$$

As was already done in chapter 3, one can integrate $\langle \mathbf{S}_{\text{tot}} \rangle$ over an arbitrary closed surface A that contains the scatterer in order to compute the rate W_{abs} at which energy is absorbed by the scatterer:

$$W_{\text{abs}} = -\oiint_A \langle \mathbf{S}_{\text{tot}} \rangle \cdot \hat{\mathbf{r}} dA \tag{4.3}$$

The absorption cross section $\sigma_{\text{a}} = \frac{W_{\text{abs}}}{I_{\text{inc}}}$ is then derived by normalizing W_{abs} by the irradiance of the incident field I_{inc} and has the dimension of an area. Equivalently, it is possible to define σ_{s} and σ_{e} as being equal to:

$$\begin{aligned} \sigma_{\text{s}} &= \frac{W_{\text{scat}}}{I_{\text{inc}}} = \frac{\oiint_A \langle \mathbf{S}_{\text{scat}} \rangle \cdot \hat{\mathbf{r}} dA}{I_{\text{inc}}} \\ \sigma_{\text{e}} &= \frac{W_{\text{ext}}}{I_{\text{inc}}} = -\frac{\oiint_A \langle \mathbf{S}_{\text{ext}} \rangle \cdot \hat{\mathbf{r}} dA}{I_{\text{inc}}}. \end{aligned} \tag{4.4}$$

Finally, if the scatterer is located in a non-absorbing medium, the integration of $\langle \mathbf{S}_{\text{inc}} \rangle$ over a closed surface is null. It can consequently be shown by means of Eq. (4.2) that the extinction cross section σ_{e} is the sum of the scattering cross section σ_{s} and the absorption cross section σ_{a}:

$$\sigma_{\text{e}} = \sigma_{\text{s}} + \sigma_{\text{a}}, \tag{4.5}$$

In the particular case of a plane wave impinging on a spherical scatterer located in a medium whose refractive index is N_b, it is convenient to make use of the orthogonality of the VPWs (see chapter 3) in order to derive an expression of the cross sections as a sum of the contributions from all multipolar orders:

$$\sigma = \sum_{n=1}^{\infty} \left\{ \sigma_n^{(e)} + \sigma_n^{(h)} \right\}, \tag{4.6}$$

where σ can be either the scattering (σ_{s}), extinction (σ_{e}), or absorption (σ_{a}) cross sections and the n^{th} multipolar mode contributions are respectively denoted $\sigma_{n,\text{s}}^{(q)}$, $\sigma_{n,\text{e}}^{(q)}$, $\sigma_{n,\text{a}}^{(q)}$, with $(q) = (e)$ or (h) for (electric or magnetic modes) and can be expressed

in terms of the T matrix coefficients [93, 103]:

$$\begin{aligned}\sigma_{n,\mathrm{e}}^{(q)} &= -\frac{(2n+1)\lambda^2}{2\pi}\mathrm{Re}\left\{T_n^{(q)}\right\} \\ \sigma_{n,\mathrm{s}}^{(q)} &= \frac{(2n+1)\lambda^2}{2\pi}\left|T_n^{(q)}\right|^2 \\ \sigma_{n,\mathrm{a}}^{(q)} &= \sigma_{n,\mathrm{e}}^{(q)} - \sigma_{n,\mathrm{s}}^{(q)}\end{aligned} , \tag{4.7}$$

Expressing the multipolar contributions to the cross sections, σ_s, σ_e and σ_a in terms of the S matrix will also prove to be convenient for determining the optical response limits [114]:

$$\begin{aligned}\sigma_{n,\mathrm{e}}^{(q)} &= \frac{(2n+1)\lambda^2}{4\pi}\mathrm{Re}\left\{1 - S_n^{(q)}\right\} \\ \sigma_{n,\mathrm{s}}^{(q)} &= \frac{(2n+1)\lambda^2}{8\pi}\left|1 - S_n^{(q)}\right|^2 \\ \sigma_{n,\mathrm{a}}^{(q)} &= \frac{(2n+1)\lambda^2}{8\pi}\left(1 - \left|S_n^{(q)}\right|^2\right)\end{aligned} , \tag{4.8}$$

where $\lambda = \lambda_0/N_b$ is the in-medium wavelength. The $(2n+1)$ factor in Eq.(4.8) results from the $2n+1$ degeneracy of the projection quantum numbers for each angular momentum number, n. For non-absorbing scatterers, it is also interesting to express the scattering and extinction cross sections in terms of the phase shift $\delta_n^{(e,h)}$ introduced in chapter 3:

$$\sigma_{n,\mathrm{e}}^{(q)} = \sigma_{n,\mathrm{s}}^{(q)} = \frac{(2n+1)\lambda^2}{2\pi}\sin^2\left(\delta_n^{(e,h)}\right) \tag{4.9}$$

Finally, it is particularly useful to introduce the absorption, scattering and extinction efficiencies that are equal to the cross sections normalized by the geometrical cross sections πR^2 of the spherical scatterer:

$$Q_n^{(e,h)} = \frac{\sigma_n^{(e,h)}}{\pi R^2} \tag{4.10}$$

4.2.2 Optimal scattering condition: unitary limit

According to Eqs. (4.7) and (4.8), the definition of the partial scattering cross sections is:

$$\sigma_{n,\mathrm{s}}^{(q)} = \frac{(2n+1)\lambda^2}{2\pi}\left|T_n^{(q)}\right|^2 = \frac{(2n+1)\lambda^2}{8\pi}\left|1 - S_n^{(q)}\right|^2 \tag{4.11}$$

A maximum of this partial scattering cross section can consequently be assumed to happen at the vicinity of the maximum of the factors $\left|T_n^{(q)}\right|^2$ or $\left|1 - S_n^{(q)}\right|^2$. Energy conservation entails the following condition $|S_1^{(q)}| \leq 1$ for passive media ($|S_1^{(q)}| = 1$ for lossless media). Consequently, one can show that the condition maximizing $\left|1 - S_n^{(q)}\right|^2$, that will henceforth be called the Unitary Limit (UL), is reached when:

$$\begin{aligned} S_{n,\mathrm{UL}}^{(q)} &= -1 \\ T_{n,\mathrm{UL}}^{(q)} &= -1 \\ \left(K_{n,\mathrm{UL}}^{(q)}\right)^{-1} &= 0 \end{aligned} \tag{4.12}$$

The unitary limit is consequently reached at the poles of the K-matrix coefficients, defined in Chapter 3, and will thus be calculated by solving the equation $D_{K,n}^{(e,h)} = 0$ where $D_{K,n}^{(e,h)}$ is the denominator function defined in chapter 3. At this condition, the partial scattering cross section reaches the following upper bound [106, 115]:

$$\sigma_{n,\mathrm{s}}^{(q)} = \sigma_{n,\mathrm{e}}^{(q)} = \frac{(2n+1)\lambda^2}{2\pi} \tag{4.13}$$

Permittivities allowing to reach the unitary limit for a given size parameter $z = kR$ can be derived by finding the solution of $D_{K,n}^{(e,h)} = 0$. In Fig.(4.1), we compare the smallest permittivies that are solutions of the unitary limit as a function of the particle size parameter, $z = kR$, with the algebraically obtained predictions employing the approximations of Eq.(3.70). One remarks that the UL permittivities are real as required by unitarity and inspection of Eq.(4.8). The approximate predictions are in good agreement for small size parameters ($kR < 1$) and remain close even for larger kR. In practice, permittivities required to reach the unitary limit in the dipole electric multipole are shown to be close of those of materials possessing plasmonic responses, like gold or silver, while for the dipole magnetic multipole, high-index low-loss materials like silicon, $\varepsilon_{\mathrm{Si}} \sim 14$ are required.

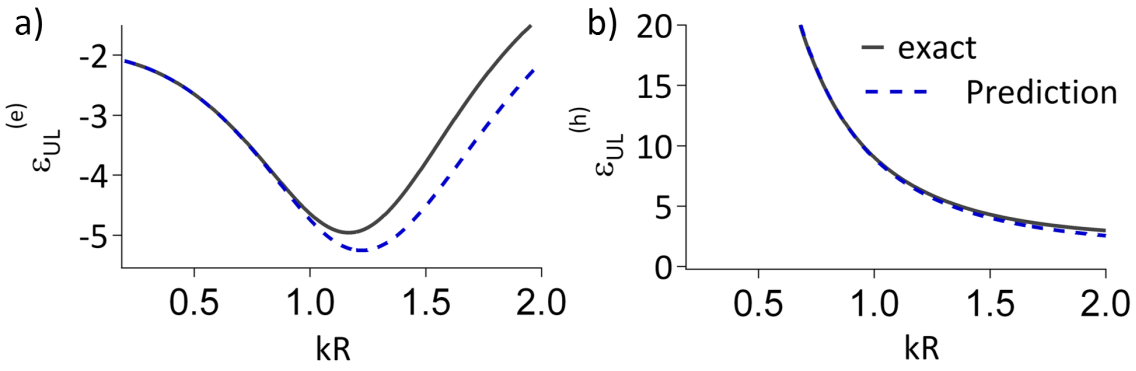

Figure 4.1: Values of permittivity required to reach the UL for the electric (a) and magnetic (b) dipole modes as a function of kR. Exact predictions (full black lines) and approximate predictions (dashed blue).

4.2.3 Optimal absorption condition: ideal absorption

Equivalently to what was done for scattering, one can also study the maxima and the upper bounds of the partial absorption cross section. The partial absorption

cross sections for a given multipole takes the following expression in terms of the S-matrix coefficients:

$$\sigma_{n,\mathrm{a}}^{(q)} = \frac{(2n+1)\lambda^2}{8\pi}\left(1 - \left|S_n^{(q)}\right|^2\right) \tag{4.14}$$

$\left(1 - \left|S_n^{(q)}\right|^2\right)$ reaches its maxima at the condition:

$$S_{n,\mathrm{IA}}^{(q)} = 0 \tag{4.15}$$

The partial absorption cross section $\sigma_{n,\mathrm{a}}^{(q)}$ can consequently be assumed to reach its maxima at the vicinity of the zeros of the S-matrix coefficients. These conditions will be called Ideal Absorption (IA) in what follows and are associated with the following upper bound of the partial absorption cross section [114–116]:

$$\sigma_{n,\mathrm{a}}^{(q)} = \sigma_{n,\mathrm{s}}^{(q)} = \frac{(2n+1)\lambda^2}{8\pi} \tag{4.16}$$

Consequently, for the absorption to be maximized, the scatterer should scatter as much light as it absorbs it in a given multipolar order. Permittivities required to reach ideal absorption for a given size parameter $z = kR$ can consequently be computed by looking for the solution of $N_{S,n}^{(e,h)} = 0$, where $N_{S,n}^{(e,h)}$ is the numerator function of the S-matrix coefficients introduced in chapter 3. In Fig.(4.1), we again proceed to a comparison between the exact solutions with predictions obtained by using the approximations of Eq.(3.70) for the permittivities allowing to reach ideal absorption. Approximate expressions turn out to be even more useful here while dealing with Ideal Absorption since exact IA solutions require solving a complex transcendental equation. Exact calculations and predictions of IA again appear to agree quite well for small size parameters ($kR < 1$). The electric mode Ideal absorption turns out to be most readily attainable with materials possessing plasmonic responses, like gold or silver, while for magnetic modes, high-index low-loss materials (like silicon in the visible) are required.

4.2.4 Algebraic expressions for optimal magnetic light-particle interactions

The previous results have shown that the conditions to reach IA and UL in the magnetic dipole mode are in fact very close to one another. From Fig.(4.1b) and Fig.(4.2c), one finds that the permittivity required to reach UL at $kR = 0.5$ and the real part of the permittivity necessary to reach IA at that same size are both approximately $\varepsilon \approx 38$. We further illustrate this point by comparing the exact values of $\varepsilon_{\mathrm{UL}}$ and $\mathrm{Re}\{\varepsilon_{\mathrm{IA}}\}$ over a range of kR in Fig.(4.3a).

An explanation of this property is found by examining the limit equations giving

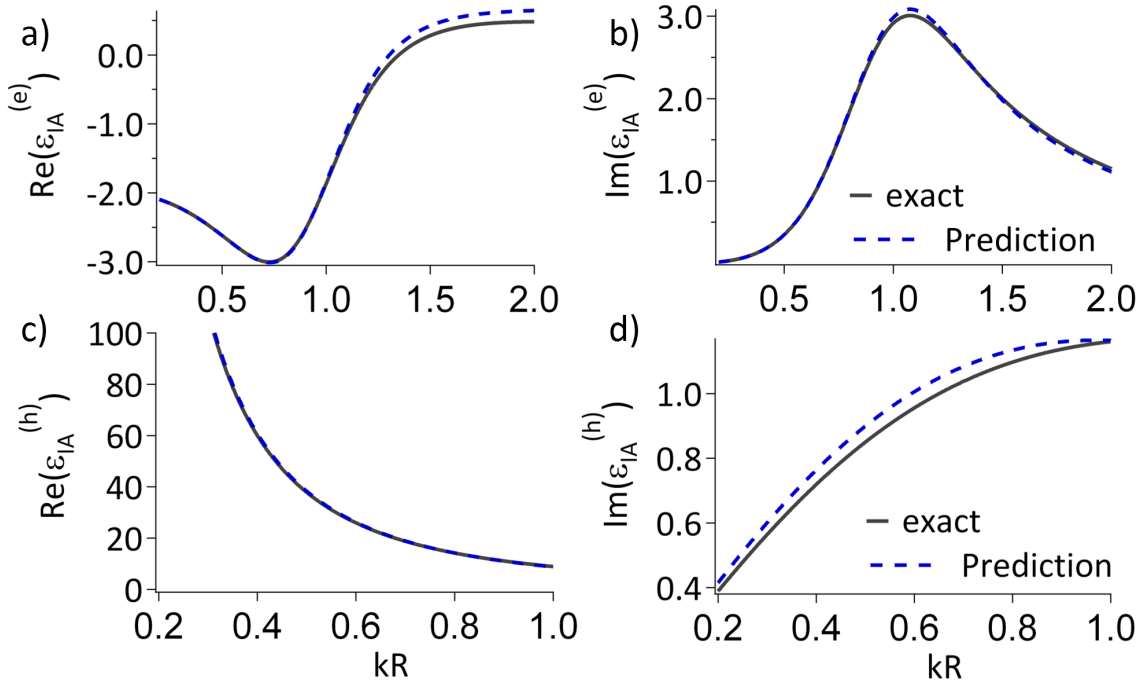

Figure 4.2: Real (a,c) and imaginary (b,d) parts of the dielectric permittivity satisfying IA in the electric (a,b) and magnetic (c,d) dipole modes. Exact predictions (full black lines) and approximate predictions (dashed blue lines).

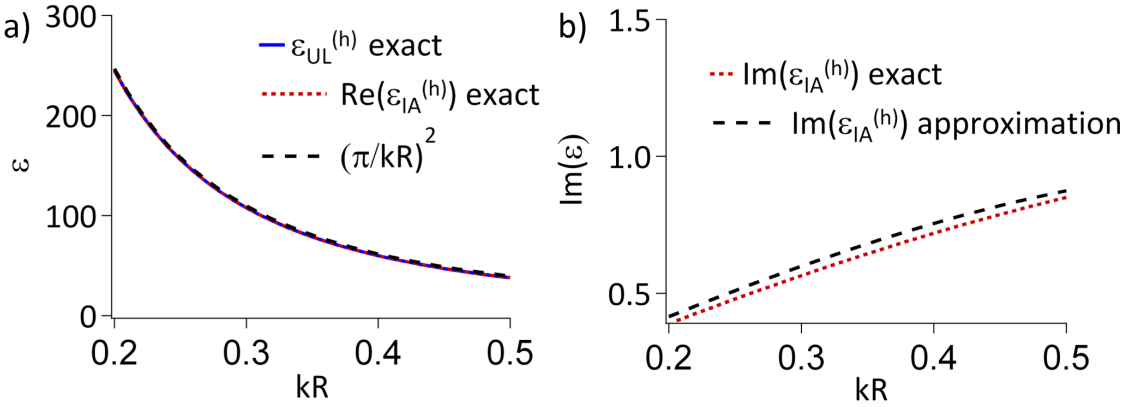

Figure 4.3: Permittivities satisfying magnetic dipole UL, $\varepsilon_{\mathrm{UL}}^{(h)}$, (solid blue) and satisfying magnetic IA, $\varepsilon_{\mathrm{IA}}^{(h)}$ (dotted red) as functions of kR: Real parts (a) and imaginary parts (b). Approximate algebraic expressions of Eqs.(4.20) and (4.21) are plotted in dashed black.

the UL and IA conditions (see appendix B for additional details). From inspection of Eq.(4.15), one sees that the condition for IA in the magnetic dipole mode is:

$$S_1^{(h)} = 0 \iff \varphi_1(k_s R) = \varphi_1^{(-)}(kR) \tag{4.17}$$

where the φ functions are defined in Eq.(A.12). In the small particle limit, $\lim_{x\to 0} h_n^{(-)}(x) =$

$-iy_n(x)$, and the equation for IA becomes:

$$\text{For } kR \ll 1 \quad S_1^{(h)} = 0 \iff \varphi_1(k_s R) \simeq \varphi_1^{(2)}(kR), \tag{4.18}$$

which is identical to the magnetic dipole UL (see Eq. (4.15) and (4.12):

$$(K_1^{(h)})^{-1} = 0 \iff \varphi_1(k_s R) = \varphi_1^{(2)}(kR). \tag{4.19}$$

If the previous equations are solved in the $kR \to 0$ limit, the following simple expressions are found for the IA and UL conditions:

$$\varepsilon_{\text{UL}} \simeq \text{Re}(\varepsilon_{\text{IA}}) \simeq \frac{10}{(kR)^2} \simeq \left(\frac{\pi}{kR}\right)^2 \tag{4.20}$$

$$\text{Im}\{\varepsilon_{\text{IA}}\} \simeq \frac{49}{2}\left(1 - \sqrt{\frac{5}{6}}\right) kR - \frac{203}{24\sqrt{30}}(kR)^3 \tag{4.21}$$

This approximate expression is compared with exact calculations in Fig.(4.3b).

4.3 Near and far field spectra

So far, we have been considering the optimal interactions for the far-field response of subwavelength scatterers. Absorption and scattering extrema were found to occur at the vicinity of IA and UL conditions where the upper bound of absorption and scattering cross sections are reached. We should however emphasize here that the position of the extrema cross section may slightly differ from the wavelengths at which ideal absorption or unitary limit are reached. This comes from the the presence of a λ^2 factor in the cross-section expression. This factor leads to a red-shift of the maximum position as compared to the ideal absorption or unitary limit condition. As seen in Fig. 4.4 and 4.5, the broader the resonance width the larger the red-shift of the maximum of the cross section compared to the IA or UL condition.

Resonant response of a scatterer is also of interest due to the near-field enhancements it induces. It has recently been pointed out however that there is a red shift of the optimal near field enhancements with respect to the cross section maxima [117–119]. We derived approximate and *exact* formulas in Eqs.(4.22) and (B.1) respectively in order to quantify these near-field spectral shifts for *both* electric and magnetic field enhancements. Our approximate expression for the electric field enhancement factor $\left\langle I_{\text{enh}}^{(e)} \right\rangle$, given in Eq.(4.22a) below, is quite similar to a formula derived by Yuffa *et al.*,[119] but those authors used somewhat different definitions of field enhancements (apparently due to the fact that they looked at scattered fields rather than the total fields considered here).

Angle-averaged local electric and magnetic field intensity enhancement factors,

$\left\langle I_{\text{enh}}^{(e)} \right\rangle$, and $\left\langle I_{\text{enh}}^{(h)} \right\rangle$ are functions of the normalized distance to the particle center, $\eta \equiv kr$, and can be defined as:

$$\begin{aligned} \left\langle I_{\text{enh}}^{(e)} \right\rangle &\equiv \frac{\int d\Omega \left\| \mathbf{E}_{\text{tot}}(\eta \widehat{\mathbf{r}}) \right\|^2}{4\pi \left\| \mathbf{E}_{\text{exc}}(\mathbf{0}) \right\|^2} \qquad (4.22a) \\ &\simeq 1 + \sum_{n=1}^{\infty} g_n^{(1)}(\eta) \left| b_n \right|^2 + g_n^{(2)}(\eta) \left| a_n \right|^2 \\ \left\langle I_{\text{enh}}^{(h)} \right\rangle &\equiv \frac{\int d\Omega \left\| \mathbf{H}_{\text{tot}}(\eta \widehat{\mathbf{r}}) \right\|^2}{4\pi \left\| \mathbf{H}_{\text{exc}}(\mathbf{0}) \right\|^2} \qquad (4.22b) \\ &\simeq 1 + \sum_{n=1}^{\infty} g_n^{(1)}(\eta) \left| a_n \right|^2 + g_n^{(2)}(\eta) \left| b_n \right|^2 \end{aligned}$$

where $\mathbf{E}_{\text{tot}}$ and $\mathbf{H}_{\text{tot}}$ are respectively the *total* electric and magnetic fields outside the particle. The functions $g_n^{(1)}(\eta)$ and $g_n^{(2)}(\eta)$ of Eq.(4.22) are given by:

$$\begin{aligned} g_n^{(1)}(\eta) &\equiv \frac{2n+1}{2} \left| h_n^{(+)}(\eta) \right|^2 \\ g_n^{(2)}(\eta) &\equiv \frac{1}{2} \left[(n+1) \left| h_{n-1}^{(+)}(\eta) \right|^2 + n \left| h_{n+1}^{(+)}(\eta) \right|^2 \right] \end{aligned} \qquad (4.23)$$

The approximation used in deriving Eqs.(4.22) is accurate only as long as the respective electric and magnetic excitation fields can be approximated by their values at the center of the particle, $\mathbf{E}_{\text{exc}}(\mathbf{0})$ and $\mathbf{H}_{\text{exc}}(\mathbf{0})$. Although this is generally quite accurate at small kr values, its validity can be tested with the exact expressions for near field enhancements given in appendix B.1.

The electric field enhancement formulas in Eq.(4.22) explain why the maximum of the near field enhancements are generally red-shifted with respect to their cross section maxima. The spherical Hankel functions are rapidly diverging functions in the $kr \to 0$ limit (due to existence of evanescent waves near the current sources [117, 120]), which shifts the near-field maximum to smaller values of k compared to values of k which maximize the amplitude of a Mie coefficient.

In Figs.(4.4a,c), we plot the scattering efficiencies, $Q_{\text{scat}} = \sigma_{\text{scat}}/\sigma_{\text{geom}}$ ($\sigma_{\text{geom}} = \pi R^2$ is the geometrical cross section) of $R = 40$nm radii spheres whose permittivities are chosen so that electric (magnetic) dipole UL are respectively reached when $kR = 0.5$ ($\bar{\varepsilon}_{UL}^{(e)} = -2.65$, $\bar{\varepsilon}_{UL}^{(h)} = 37.9$). Total efficiencies are plotted in dashed blue while dipole electric and magnetic contributions are plotted in dotted red. Unitary limit dipole efficiencies are plotted as solid black lines as a reference. Angle averaged field enhancements, $\left\langle I_{\text{enh}}^{(e,h)} \right\rangle$ for both electric and magnetic fields at the particle surface are plotted in Figs.(4.4b,d). The plots of maximal dipole contributions to Q and $\left\langle I_{\text{enh}}^{(e,h)} \right\rangle$ for electric and magnetic modes respectively are plotted as solid black lines in Figs.(4.4). Their strongly decreasing behaviors as a function of increasing size

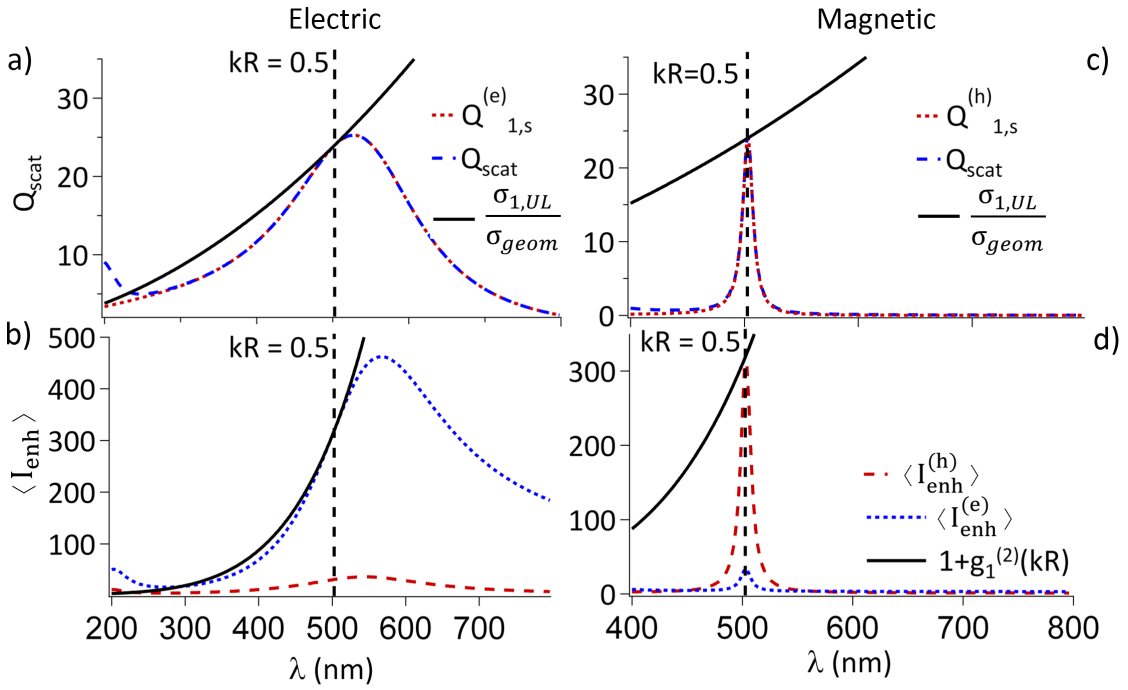

Figure 4.4: Cross section efficiencies (a,c) and field enhancements at the particle surface (b,d) for $R = 40$nm spheres satisfying dipole UL in electric (a,b) and magnetic (c,d) at $kR = 0.5$. Maximal dipole contributions to Q and $< I_{\rm enh}^{(e,h)} >$ are plotted as solid black lines.

parameter explains why we focused attention on small particle sizes (with respect to λ). The maximum field enhancement $\left\langle I_{\rm enh}^{(e,h)} \right\rangle$ are red shifted compared the cross sections according to the arguments presented after Eq.(4.23). This red-shift is far less pronounced for narrower resonances like those of the magnetic dipole UL and IA in Figs.(4.4c,d) and (4.5c,d).

Like in the UL case, the spectral behavior of IA spheres can be studied by plotting the evolution of the absorption efficiency, $Q_{\rm abs} = \sigma_{\rm abs}/\sigma_{\rm geom}$ as shown in Fig.(4.5a,c), for the dipole electric (a) and magnetic (b) modes of $R = 40$nm spheres designed to reach IA at a size parameter of $kR = 0.5$ ($\bar{\varepsilon}_{\rm IA}^{(e)} = -2.62 + 0.35i$, $\bar{\varepsilon}_{\rm IA}^{(h)} = 37.9 + i0.85$).

4.4 Transition from unitary limit to ideal absorption

One sees in Fig.(4.3) that a magnetic dipole UL response can transform into an IA response with the appropriate amount of added absorption. This is illustrated in Fig. (4.6) by plotting the values of the complex $S_1^{(h)}$ coefficient as the permittivity ranges from the UL permittivity, $\varepsilon_{\rm UL}^{(h)}$, to and beyond the IA permittivity, $\varepsilon_{\rm IA}^{(h)}$, according

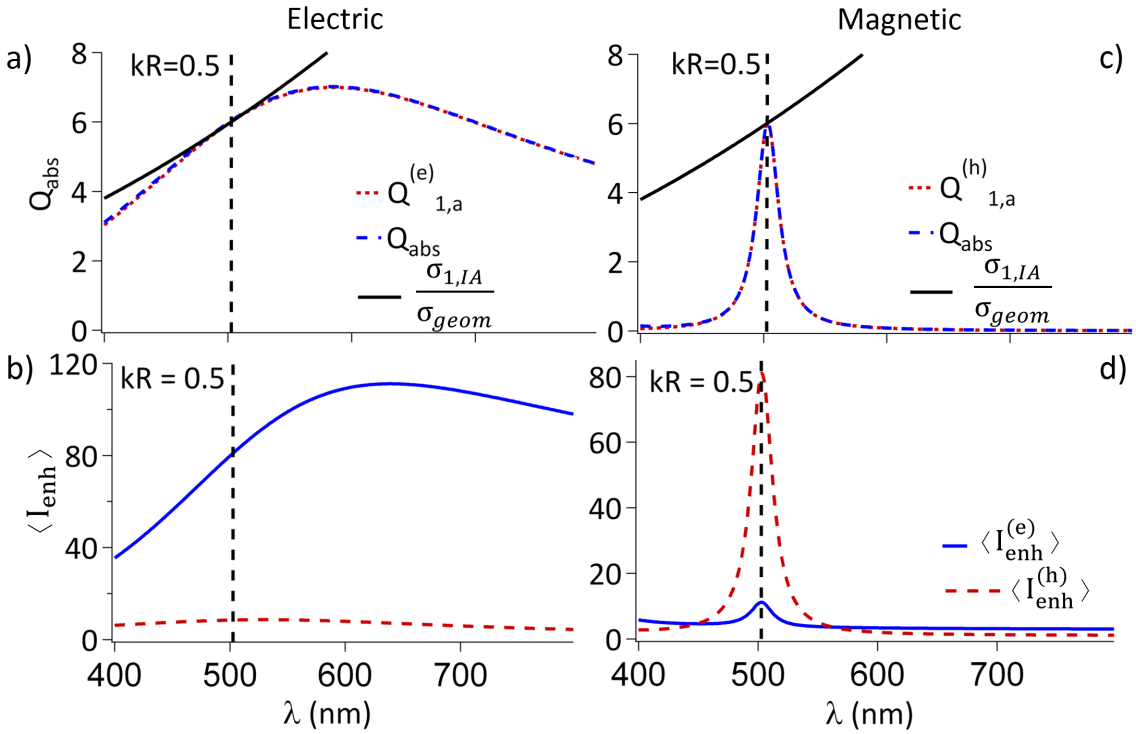

Figure 4.5: Same plots as in Fig.4.4 except for plotting absorption efficiencies in (a,c) in dipole IA particles at $kR = 0.5$. Dipole absorption limit efficiencies are plotted in solid black.

to the following function for spheres with $kR = 0.4$ and $kR = 0.8$:

$$\varepsilon = \varepsilon_{UL}^{(h)} + j\frac{(\varepsilon_{\rm UL}^{(h)} - \varepsilon_{\rm IA}^{(h)})}{3}$$

$kR = 0.4$	$kR = 0.8$
$\varepsilon_{\rm UL}^{(h)} = 59.94$	$\varepsilon_{\rm UL}^{(h)} = 14.3$
$\varepsilon_{\rm IA}^{(h)} = 59.93 + i0.72$	$\varepsilon_{\rm IA}^{(h)} = 14.2 + i1.1$

(4.24)

where j is an integer between 0 and 6 in each case. The UL value of $S_1^{(h)} = -1$ corresponds to $j = 0$, while the $S_1^{(h)} = 0$, IA limit occurs for $j = 3$. The permittivities, scattering efficiencies, and field enhancements at the surface of the particles for the values of Eq.(4.24) and Fig.(4.6) are given in Tables 4.1 and 4.2. A comparison of Tables 4.1 and 4.2 shows that although the larger $kR = 0.8$ spheres require considerably smaller permittivities, this comes at the expense of much weaker field enhancements.

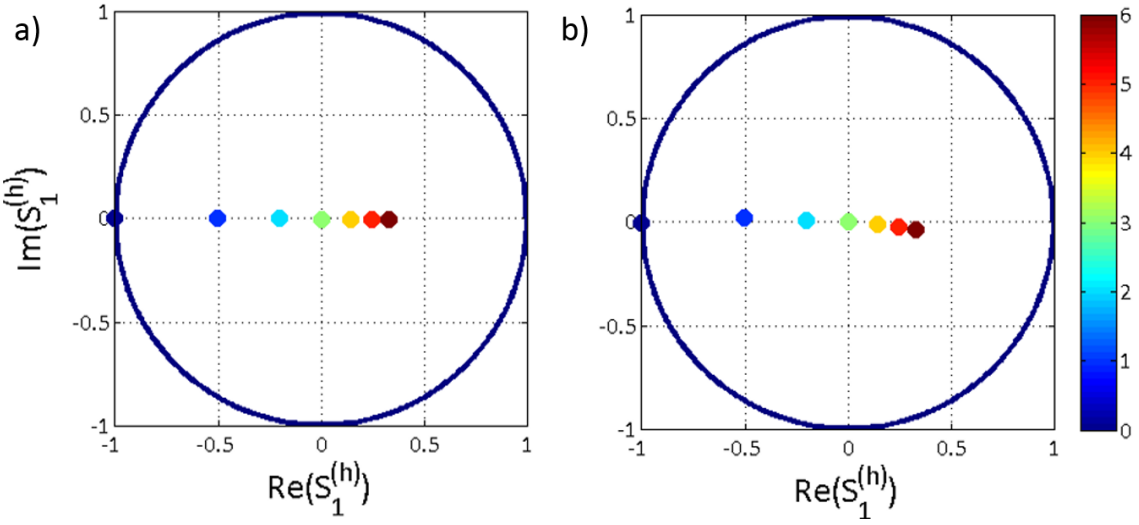

Figure 4.6: Values of $S_1^{(h)}$ for permittivities calculated from Eq.(4.24) for $kR = 0.4$ a) and for $kR = 0.4$ b), the color bar indicating the value of j at each point.

j	ε	$Q_{1,\mathrm{ext}}^{(h)}$	$Q_{1,\mathrm{scat}}^{(h)}$	$Q_{1,\mathrm{abs}}^{(h)}$	$\left\langle I_{\mathrm{enh}}^{(h)} \right\rangle$	$\left\langle I_{\mathrm{enh}}^{(e)} \right\rangle$
0	59.94	37.5	37.5	0	1168	71
1	$59.94 + 0.24i$	28.1	21.1	7	657	42
2	$59.94 + 0.48i$	22.5	13.5	9	421	28
3	$59.94 + 0.72i$	18.8	9.4	9.4	293	20
4	$59.94 + 0.96i$	16.1	6.9	9.2	215	16
5	$59.94 + 1.2i$	14.1	5.3	8.8	165	13
6	$59.94 + 1.44i$	12.5	4.2	8.3	131	11

Table 4.1: Cross section and magnetic and electric field enhancement factors for $kR = 0.4$ size particles.

j	ε	$Q_{1,\mathrm{ext}}^{(h)}$	$Q_{1,\mathrm{scat}}^{(h)}$	$Q_{1,\mathrm{abs}}^{(h)}$	$\left\langle I_{\mathrm{enh}}^{(h)} \right\rangle$	$\left\langle I_{\mathrm{enh}}^{(e)} \right\rangle$
0	14.3	9.4	9.4	0	25	10
1	$14.2 + 0.37i$	7	5.3	1.8	14.9	7.7
2	$14.2 + 0.73i$	5.6	3.4	2.3	10.2	6.4
3	$14.2 + 1.1i$	4.7	2.3	2.4	7.6	5.7
4	$14.2 + 1.5i$	4	1.7	2.3	6.1	5.3
5	$14.1 + 1.8i$	3.5	1.3	2.2	5.1	5
6	$14.1 + 2.2i$	3.2	1.1	2.1	4.4	4.8

Table 4.2: Cross section and magnetic and electric field enhancement factors for $kR = 0.8$ size particles.

4.5 Conclusion

In this chapter, we studied unitary limits and ideal absorption limits of the dipolar modes of small particles. We also derived formulas that allow a qualitative and quan-

titative analysis of the displacement of the near field-maxima with respect to far-field maxima. We applied this approach to both metallic and dielectric nanoparticles and emphasis was placed on magnetic dipolar resonances in high index dielectric particles. In this latter case, we derived closed expressions for UL and IA in the small particle limit. Although the study of particles that are small with respect to λ was privileged on account of their ability to produce large field enhancements, the full formulas given in the appendices are valid for spheres of arbitrary size and should prove useful in analyzing finite size corrections of larger resonant particles (as illustrated by a detailed analysis of the $kR = 0.8$ simulations of section 4.4). This study should help in the design of highly efficient photonic resonators that are of crucial importance to strengthen the light matter interaction at subwavelength scales.

Chapter 5

Polarizability Expressions for Predicting Resonances in Plasmonic and Mie Scatterers

Summary The purpose of this chapter is twofold. First, asymptotic resonance conditions of both high-refractive index spherical resonators and spherical plasmonic resonators are derived. The second purpose of this chapter is to use these asymptotic resonance conditions to derive accurate polarizability approximations. Such polarizability approximations are commonly used in optics and photonics to model light-scattering by small particles. However, approximate models based on Taylor series of the Mie coefficients fail to predict the morphological resonances hosted by dielectric particles. Here, we will show how the knowledge of the asymptotic resonance condition can help derive accurate approximations of the polarizabilities of both high-index dielectric and plasmonic scatterers. This work was presented in [121].

5.1 Introduction and motivations

In the framework of this work, we are mainly interested in the resonant behavior exhibited by subwavelength scatterers when they interact with light [93, 97, 103, 122–124]. The study of localized surface plasmon resonances in sub-wavelength metallic scatterers have long been the subject of a strong interest [125, 126]. These resonances come from the excitation of a collective oscillation of the conduction electrons inside subwavelength metallic scatterers by the impinging electromagnetic field. The presence of intrinsic losses, i.e. absorption, contributes however to damp this collective oscillation. Moreover, accelerating charges are known to give rise to a radiated field. This effect in turn affects the dynamic of the ensemble of electrons and gives rise to radiative losses as was explained in chapter 3.
However, at some particular frequencies depending on both the geometry and the

material of the resonator considered, the electromagnetic field can drive a resonance of the amplitude of oscillations of the free electrons yielding also a resonance of the electromagnetic field radiated by this scatterer. For very small plasmonic resonators, this resonance condition can be shown to be equal to the quasi-static resonance condition $\varepsilon \simeq -2$. This resonance condition has proved to be very useful to study the resonant behavior of very small plasmonic resonators.

Throughout this work, we are particularly interested in Mie resonances excited in high refractive-index scatterers. We can point out that some resonance conditions of Mie resonators were already derived in [127]. Here, we will however employ another method providing accurate predictions of the resonance conditions of resonators small compared to the wavelength with a large permittivity.

Furthermore, in order to study the localized surface plasmon resonances beyond the quasi-static limit, simple analytical approximations of the polarizability of plasmonic particles are also useful. Such approximate models have been widely used in the case of small metallic particles behaving like electric dipoles and hosting localized surface plasmon resonances (LSPR) [123, 128]. As was already discussed in chapter 3, the electric dipolar polarizability α_e relates the dipolar moment $\mathbf{p}$ to the excitation field $\mathbf{E}_{exc}$: $\mathbf{p} = \epsilon_0 \varepsilon_b \alpha_e \mathbf{E}_{exc}$. α_e may easily be linked to the dipolar Mie coefficient a_1 through the relation $\alpha_e = i\frac{6\pi}{k^3} a_1$ [106, 129]. Accurate approximations of α_e calculated in the long wavelength limit have greatly contributed to extend the understanding of the resonant behavior of small plasmonic scatterers [105, 107, 130–134].

The study of electric and magnetic Mie resonances in high refractive index dielectric subwavelength-sized particles could also greatly benefit from the use of such simplified models. However, the classical models widely used in plasmonics fail to predict the dipolar electric resonant response of these dielectric scatterers. We illustrate

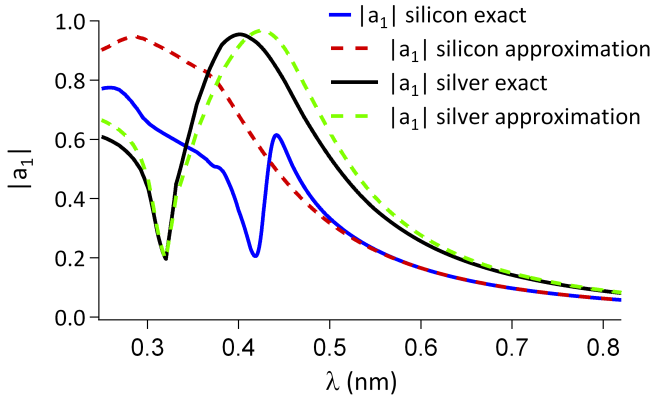

Figure 5.1: Mie coefficient $|a_1|$ plotted with respect to the wavelength in the case of a sphere of radius 60 nm made of silicon [135] and silver [136]. Full lines: calculated with the exact expression derived in Eq.1 with $n = 1$ with silicon (blue) and silver (black). Dashed lines: approximation $a_1^{(T1)}$ in Eq. (5.22) in red for silicon and green for silver.

this problem by plotting in Fig. 5.1 the real part of the first electric Mie coefficient calculated with the complete Mie theory (full line) and with a Taylor expansion (dashed line) derived up to the 3rd order, Eq. (11) in [133], in the case of a sphere, 120 nm in diameter, made of silver or made of silicon. It is clearly seen that while this expansion does predict the localized surface plasmon resonance around 410 nm, it fails to predict the morphological resonance at 450 nm. This issue motivates the development of a generalized point-like model working for both positive and negative dielectrics.

Here, asymptotic resonance conditions for both Mie and plasmonic resonators will be provided. We will then propose to derive approximations of the Mie coefficients and of the polarizabilities from the Weierstrass factorization of Bessel functions.

5.2 Resonance conditions in subwavelength spheres

Here, we propose to determine the resonance conditions (i) graphically and (ii) in the asymptotic limit $z_0 \to 0$ for any arbitrary made material homogeneous particles. For that purpose, we will be using the formulation of the Mie coefficients in terms of the K matrix coefficients already used in chapter 3:

$$(a_n)^{-1} = -i(K_n^{(e)})^{-1} + 1, \tag{5.1}$$
$$(b_n)^{-1} = -i(K_n^{(h)})^{-1} + 1. \tag{5.2}$$

The exact definition of the K-matrix coefficients is provided in Appendix A. Let us however recall it here using the reduced logarithmic derivative of Neumann and Bessel functions $\varepsilon_s\varphi_n^{(2)}(z_0)$ and $\varphi_n^{(1)}(z_s)$:

$$K_n^{(e)} = -\frac{j_n(z_0)}{y_n(z_0)}\frac{\varepsilon_s\varphi_n^{(1)}(z_0)-\varphi_n^{(1)}(z_s)}{\varepsilon_s\varphi_n^{(2)}(z_0)-\varphi_n^{(1)}(z_s)} \tag{5.3}$$
$$K_n^{(h)} = -\frac{j_n(z_0)}{y_n(z_0)}\frac{\varphi_n^{(1)}(z_0)-\varphi_n^{(1)}(z_s)}{\varphi_n^{(2)}(z_0)-\varphi_n^{(1)}(z_s)} \tag{5.4}$$

where j_n and y_n are respectively the spherical Bessel functions and the spherical Neumann functions. As the K-matrix is hermitian for non-absorptive particles [105, 106] and as a consequence the coefficients $K_n^{(e)}$ and $K_n^{(h)}$ of a lossless spherical scatterer are real.

5.2.1 Definitions of resonances:

Here, as was explained in chapter 4, light-scattering will be considered to be at resonance when one of the Mie coefficients reaches the unitary limit, *i.e.* when $a_n = 1$ or $b_n = 1$ [106, 126, 137]. This corresponds to the upper limit imposed to the Mie coefficients by the energy conservation for lossless scatterers. As was also pointed out in chapter 4, this definition of resonances is equivalent to the following condition on the K-matrix coefficients:

$$a_n = 1 \Rightarrow \left(K_n^{(e)}\right)^{-1} = 0, \tag{5.5}$$

$$b_n = 1 \Rightarrow \left(K_n^{(h)}\right)^{-1} = 0. \tag{5.6}$$

Resonances thus correspond to the poles of the K-matrix coefficients. The resonance conditions provided by Eqs. (5.5) are displayed graphically for a constant and positive permittivity equal to 16 in Fig. 5.2a. According to Eqs. (5.3) and (5.5), resonances of the magnetic dipole occur at the intersections between $\varphi_1^{(2)}(z_0)$ (solid blue line) and $\varphi_1^{(1)}(z_s)$ (dashed green line) denoted by (h) whereas resonances of the electric dipole correspond to the intersections between $\varepsilon_s\varphi_1^{(2)}(z_0)$ (dotted red line) and $\varphi_1^{(1)}(z_s)$ (dashed green line) denoted by (e) in Fig. 5.2.

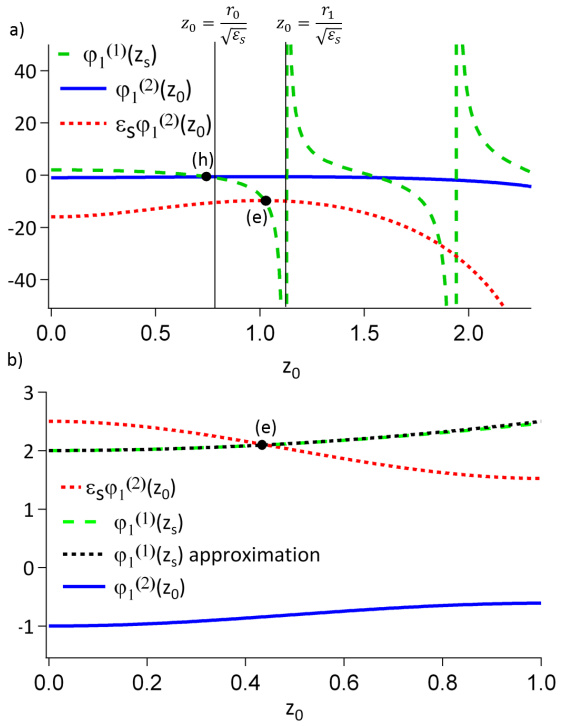

Figure 5.2: Graphic representation of the resonance condition as a function of the size parameter z_0 for (a) $\varepsilon = 16$ and (b) $\varepsilon = -2.5$: the electric and magnetic resonances are marked by the black dots, predictions of those resonances provided by Eqs. 5.9 (full black vertical lines), function $\varphi_1^{(1)}(z_s)$ (dashed green line), function $\varphi_1^{(2)}(z_0)$ (full blue line), $\varepsilon_s\varphi_1^{(2)}(z_0)$ (dotted red line). Dashed black line in (b): $\varphi_1^{(1)}(z_s) = 2 - \frac{z^2}{5}$ calculated with Eq. (5.12) at the 1st order with n=1.

One can also choose to set a permittivity negative and purely real. Even if materials with such a permittivity do not exist, this can be enlightening to study what happens in this case to provide a better understanding of the plasmonic resonances. As illustrated in Fig. 5.2b, a resonance of the electric dipole also occurs at the intersection between $\varepsilon_s\varphi_1^{(2)}(z_0)$ (dotted red line) and $\varphi_1^{(1)}(z_s)$ (dotted green line) denoted by (e). Since $\varphi_1^{(2)}(z_0)$ is negative for small values of z_0, no resonance of the magnetic dipole occurs. Although the plots of Fig. 5.2 only show the first solutions of the conditions (5.5) for $n = 1$, one has to keep in mind that these conditions are transcendental equations and have an infinity of solutions. However, in what follows, we will mainly be interested in the first resonance of each multipolar order for subwavelength-sized scatterers. That is why we will first restrict our study to the limit of small size parameters $z_0 \to 0$. In this limit, it is possible to simplify the resonance conditions by approximating the functions of z_0 by the first term of their power-series expansion : $j_n(z_0) \simeq \frac{z_0^n}{(2n+1)!!}$, $\varphi_n^{(1)}(z_0) \simeq n+1$, $y_n(z_0) \simeq -\frac{(2n-1)!!}{z_0^{n+1}}$ and $\varphi_n^{(2)}(z_0) \simeq -n$, where !! is defined in Appendix C. That leads to the following approximate expressions of the K-matrix coefficients:

$$K_n^{(e)} \simeq -\kappa_n \frac{(n+1)\varepsilon_s - \varphi_n^{(1)}(z_s)}{n\varepsilon_s + \varphi_n^{(1)}(z_s)}, \tag{5.7}$$

$$K_n^{(h)} \simeq -\kappa_n \frac{(n+1) - \varphi_n^{(1)}(z_s)}{n + \varphi_n^{(1)}(z_s)}, \tag{5.8}$$

with $\kappa_n = \frac{z_0^{2n+1}}{(2n-1)!!(2n+1)!!}$. The exact expression of $\varphi_n^{(1)}(z_s)$ is kept because the in-medium size parameter $z_s = \sqrt{\varepsilon_s} z_0$ is not necessarily small even if z_0 is small. In fact, one should keep in mind that morphological resonances, for small particles occur for large permittivity so that z_s may not be small [14, 37]. It is then straightforward from Eqs. (5.5) and (5.7) to determine an approximation of the resonance conditions (5.5):

$$a_n = 1 \Rightarrow \varphi_n^{(1)}(z_s) \simeq -n\varepsilon_s, \tag{5.9}$$

$$b_n = 1 \Rightarrow \varphi_n^{(1)}(z_s) \simeq -n. \tag{5.10}$$

5.2.2 Resonances of plasmonic scatterers:

Only the assumption $z_0 << 1$ has been made so far but no assumption was made about z_s. Eq. 5.9 is in fact valid for both metallic and dielectric small particles. Let us derive the Taylor expansion to the 6^{th} order of the $\varphi_n^{(1)}$ function [106]:

$$\varphi_n^{(T1)}(z) = n + 1 - \frac{z^2}{2n+3} - \frac{z^4}{(2n+5)(2n+3)^2} + O(z^6). \tag{5.11}$$

In the limit ($z_s \to 0$), it is sufficient to consider the first term of this expansion (n+1) and it can easily be shown that Eq. (5.9) tends towards the well-known quasi-static resonance conditions for very small plasmonic particles for electric multipoles [93]:

$$\varepsilon \simeq -\frac{n+1}{n} \tag{5.12}$$

In this same limit Eq. (5.10) has no solution, confirming that sub-wavelength plasmonic particles do not support magnetic resonances.

5.2.3 Morphological Resonances of Mie scatterers:

Electric and magnetic morphological resonances in small dielectric particles can only occur when $z_s > 1$ requiring the permittivity to be sufficiently large [14]. Thus, approximations made with the assumption $z_s << 1$ will fail to predict the morphological resonances. That is why approximations of the Mie coefficients based on Taylor series expansion do not predict morphological resonances unless a lot of terms are taken into account. This result can be observed in Figs. 5.1 and 5.2 and

it will be further illustrated in section 5.5.
In fact, the electric morphological resonances can be better understood by studying the limit $|\varepsilon_s| \to \infty$. One can easily deduce from Eq. (5.9) that multipolar electric resonances occur at the poles of the $\varphi_n^{(1)}$ functions in this limit (see in particular [100] pp. 61-65). These poles correspond to the zeros of the Bessel functions [138, 139] and in what follows, the first zero of the n-th order Bessel functions will be noted r_n. For high index dielectric scatterers for which $|\varepsilon_s|$ is large but not infinite, it can then be safely inferred that the first resonance of the n-th order electric multipole occurs close to the position:

$$z_s \simeq r_n \tag{5.13}$$

This result can be observed in Fig. 5.2 where the electric resonance condition is seen to be close to the pole of $\varphi_1^{(1)}$ in the case of $n = 1$. The exact values of r_0, r_1 and r_n are provided in table 1 but it may be recalled that a good approximation of the l-th zero of the n-th order Bessel function can be provided by $r_{n,l} \simeq l\pi + \frac{n\pi}{2}$ [138, 139]. At this point, one should emphasize that the condition $z_s = r_n$ actually corresponds to the first TE modes of the n-th multipole of a spherical hollow resonator (a spherical cavity with perfectly conducting walls) [140–142]. This provides some insights on the origin of morphological resonances as will be further discussed in section 5.5.
A prediction of the magnetic resonance condition can then be easily deduced from Eq. (5.10) by noticing that $\varphi_n(r_{n-1}) = -n$ (see Appendix C)[100]. If $|\varepsilon_s|$ is large, it can then be assumed that the first resonance of the n-th magnetic multipole occurs close to the position:

$$z_s \simeq r_{n-1} \tag{5.14}$$

This is confirmed in Fig. 5.2 in the case of $n = 1$ where one clearly sees that the magnetic resonance is close to this condition. This resonance condition differs from the first TM mode of a spherical hollow resonator occurring for $z_s = r_n^{'}$, $r_n^{'}$ being the first zero of the derivative of the n-th order Bessel functions [140, 142]. This will be further discussed in section 5.5.
In order to get a good approximation of b_n at the vicinity of the magnetic resonance, one could then choose to approximate $\varphi_n^{(1)}(z_s)$ by its power series expansion around $z_s = r_{n-1}$ (calculations are made in Appendix D):

$$\begin{aligned}\varphi_n^{(T2)}(z) \simeq & -n - r_{n-1}\,(z - r_{n-1}) \\ & -(n+1)\,(z - r_{n-1})^2 \\ & -\frac{1}{3}\left(\frac{n(2n+1)}{r_{n-1}}\right)(z - r_{n-1})^3\end{aligned} \tag{5.15}$$

Fig. 5.3 shows that Eq. (5.15) provides a very good approximation of $\varphi_n^{(1)}(z_s)$, but only on a small interval of size parameters close to the resonance.
It can then be concluded from this study that the slow convergence of the Taylor series expansions does not allow accurate and compact approximated expressions of

the $\varphi_n^{(1)}$ functions. It will be confirmed by the results obtained on section 5.4.

5.3 Weierstrass approximations of $\varphi_n^{(1)}$

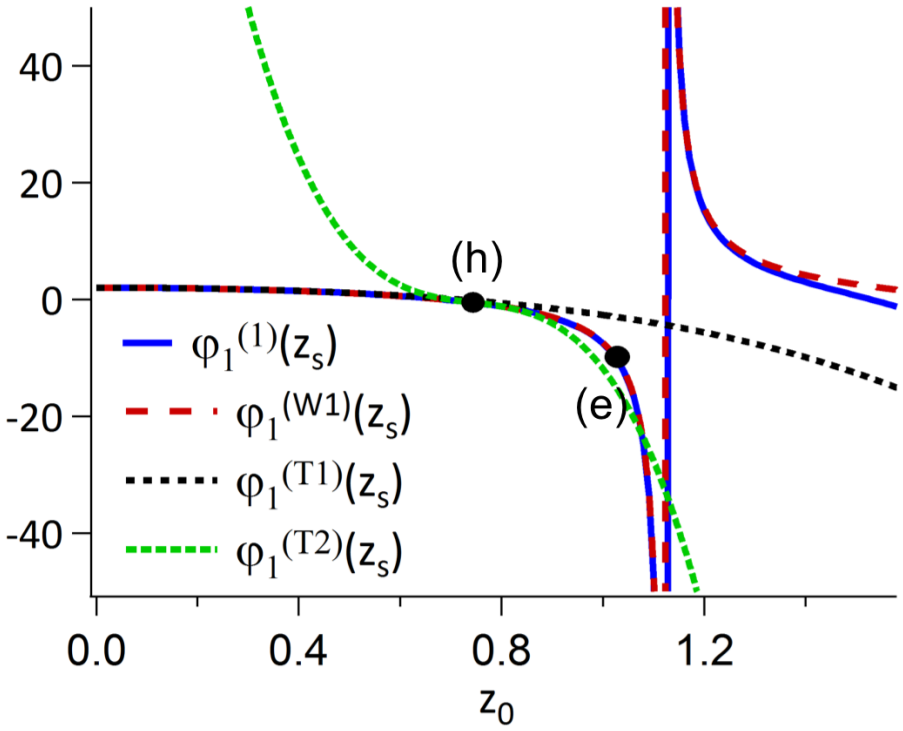

Figure 5.3: Comparison of the approximations of the $\varphi_1^{(1)}(z_s)$ function. Exact calculation (full blue line). $\varphi_1^{(T1)}(z_s)$: Taylor expansions around $z_s = 0$ (dashed black line), $\varphi_1^{(W1)}(z_s)$: approximation derived in Eq. 5.18 (dashed red line), $\varphi_1^{(T2)}(z_s)$: Taylor expansion around $z_s = r_{n-1}$ derived in Eq. 5.15 (dotted green line).

We propose to address this issue of the slow convergence of the Taylor descriptions in the proximity of the poles of $\varphi_n^{(1)}(z_s)$ by using the Weierstrass expansion of the Bessel function [138, 139]:

$$j_n(z) = \frac{z^n}{(2n+1)!!} \prod_{l=1}^{\infty} \left(1 - \left(\frac{z}{r_{n,l}}\right)^2\right), \tag{5.16}$$

where $r_{n,l}$ is the l-th zero of the n-th order Bessel function. The expression of the $\varphi_n^{(1)}$ function can then be deduced from Eqs. (A.12) and (5.16)[114, 143]:

$$\varphi_n^{(1)}(z) = n + 1 + \sum_{l=1}^{\infty} \frac{2z^2}{z^2 - (r_{n,l})^2}. \tag{5.17}$$

Expression (5.17) is an exact expansion of $\varphi_n^{(1)}$ which takes into account the existence of an infinite number of poles located on the real axis, as observed in Fig.5.2,

Table 5.1: Numerical values of the constants employed for the first multipole orders.

x	r_n	$\rho_n^{(e)}$	$\rho_n^{(h)}$
$n=0$	π	-0.065	x
$n=1$	4.49	-0.05	-0.055
$n=2$	5.76	-0.041	-0.047

and corresponding to the zeros of j_n. In the previous section, it was shown that those poles are of great importance in the emergence of the electric morphological resonances and that is why it is necessary to find approximations of $\varphi_n^{(1)}$ featuring the same poles. In our study, we are seeking for approximations capable to predict the first morphological resonance. Approximations of $\varphi_n^{(1)}$ can be obtained by truncating the infinite sum in Eq. (5.17) and by conserving only its first term. But, rather than completely neglecting the influence of higher order poles, one can also approximate their contributions. As shown in Appendix C.3, if we consider that $z_s << r_{n,2}$, we obtain the following approximation:

$$\varphi_n^{(W1)}(z_0) = n + 1 + \frac{2z_n^2}{z_n^2 - 1} + 2\rho_n^{(e)} z_0^2, \tag{5.18}$$

where we set for compact notations that $z_n \equiv z_0/r_{n,1} \equiv z_0/r_n$ and $\rho_n^{(e)} \equiv \frac{1}{r_n^2} - \frac{1}{2(2n+3)}$, with r_n being the first zero of j_n. Regarding the approximation of the magnetic coefficients, we have seen in section 5.2 that their first resonance occurs near the condition $z_s = r_{n-1}$. In order to have a good prediction of the magnetic resonances, an accurate approximation of $\varphi_n^{(1)}(z_s)$ near $z_s = r_{n-1}$ must be found. As seen in the previous section and in Fig. 5.3, a simple power series expansion of $\varphi_n^{(1)}(z_s)$ does not provide satisfying results. A better approximation has been found under the following form:

$$\varphi_n^{(W2)}(z_0) = n + 1 + \frac{2z_n^2}{z_n^2 - 1} + 2\rho_n^{(h)} z_0^2, \tag{5.19}$$

where $\rho_n^{(h)}$ has been derived to impose $\varphi_n^{(W2)}(r_{n-1}) = -n$. It can then be easily shown that $\rho_n^{(h)} \equiv \frac{1}{r_n^2 - r_{n-1}^2} - \frac{2n+1}{2r_{n-1}^2}$.

Approximations of the Bessel functions can also be derived by following a similar approach leading to the subsequent expression (see Appendix C.3):

$$j_n^{(W1)}(z_0) = \frac{z_0^n}{(2n+1)!!}\left(1 - z_n^2\right) e^{\rho_n z_0^2}. \tag{5.20}$$

The approximations obtained for the special functions appearing in the Mie theory can now be used to find approximations of the Mie coefficients.

5.4 Approximations of a_n and b_n

In order to find an accurate approximation of the a_n and b_n coefficients, in particular at the vicinity of their resonances [144–146], we start from the exact expression (A.22) defined in appendix (A) and make use of the approximations (5.18) and (5.20) derived with the sole assumption $z_s << r_{n,2}$. If the exact expressions of $h_n^{(+)}$ and $\varphi_n^{(+)}$ are kept, it can be shown, provided several steps of calculations, that the Mie coefficients can be cast (see Appendix C):

$$\begin{aligned} a_n^{(A1)} &= \frac{(n+1)z^{2n+1}}{(2n+1)!!}\frac{e^{-iz+\rho_n^{(e)}z^2}}{Q_n(z)}\times \\ &\quad \frac{(\varepsilon-1)\left(f_n(\varepsilon,z)-z_n^2\right)}{\varepsilon g_n(z) f_n(\varepsilon,z)-(n+1)} \\ b_n^{(A1)} &= \frac{z^{2n+1}}{(2n+1)!!}\frac{e^{-iz+\rho_n^{(h)}z^2}}{Q_n(z)}\times \\ &\quad \frac{(\varepsilon-1)L_n(\varepsilon,z)}{\varepsilon L_n(\varepsilon,z)-(n+1)+\varphi_n^{(+)}(z)} \end{aligned} \tag{5.21}$$

with $g_n(z) = \varphi_n^{(+)}(z) - 2\rho_n z^2$ and $Q_n(z)$ is a polynomial function detailed in Appendix C and $\varphi_n^{(+)}(z)$ being simply calculated thanks to equations (A.12) and (C.31). In the electric coefficient expression, $f_n(\varepsilon,z) = \frac{1-\varepsilon z_n^2}{1-\frac{n+3}{n+1}\varepsilon z_n^2}$ while in the magnetic coefficient expression $L_n(\varepsilon,z) = -\frac{2z_n^2}{\varepsilon z_n^2-1} - 2\rho_n^{(h)}z^2$.

Comparisons between these approximations and exact calculations are shown in the following figures. We also make comparisons with approximations based on power series expansions of the K_n coefficients in Eqs. 5.1 and 5.2 and that were already provided in chapter 3:

$$\begin{aligned} \left(a_1^{(T1)}\right)^{-1} &= -i\left(-\frac{3(\varepsilon+2)}{2z^3(\varepsilon-1)}+\frac{9(\varepsilon-2)}{10z(\varepsilon-1)}\right)+1 \\ \left(b_1^{(T1)}\right)^{-1} &= i\frac{45}{z^5(\varepsilon-1)}-\frac{15i(2\varepsilon-5)}{7z^3(\varepsilon-1)} \\ &\quad -\frac{i(\varepsilon^2+100\varepsilon-125)}{49z(\varepsilon-1)}+ \\ \left(a_1^{(T2)}\right)^{-1} &= i\frac{3(\varepsilon+2)}{2z^3(\varepsilon-1)}-\frac{9i(\varepsilon-2)}{10z(\varepsilon-1)} \\ &\quad -\frac{9iz(\varepsilon^2-24\varepsilon+16)}{700(\varepsilon-1)}+1 \end{aligned} \tag{5.22}$$

It is clearly observed in Fig. 5.4 that our approximations achieve to reproduce the resonances predicted by exact calculations in a more accurate way than state-

of-the-art approximations, even quite lengthy high-order Taylor expansions.

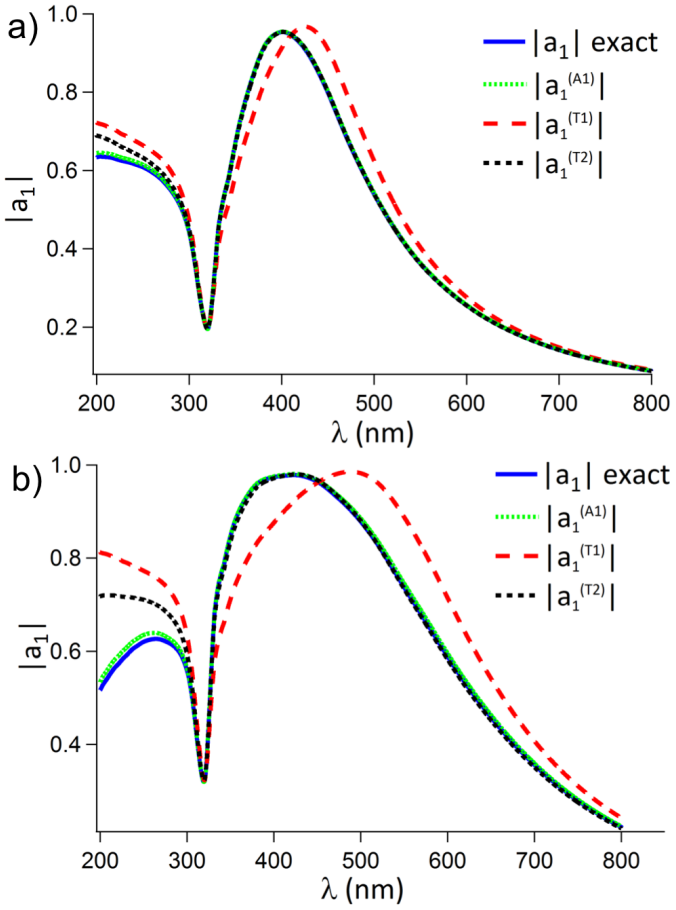

Figure 5.4: Comparison between exact (full blue line) and approximations (5.21) (dotted green line) and (5.22) (dashed red and black lines) of a_1 for a sphere of silver [136] 60 nm (a) and 80 nm (b) in radius.

Although we did not explicitly derive these approximations for describing plasmonic scatterers, these new approximations are more accurate than the approximations (5.22) as can be seen in Fig.5.4. However, the main interest of these new approximations is that they are highly accurate for high-index dielectric scatterers as shown in Fig. 5.5 for a silicon scatterer.

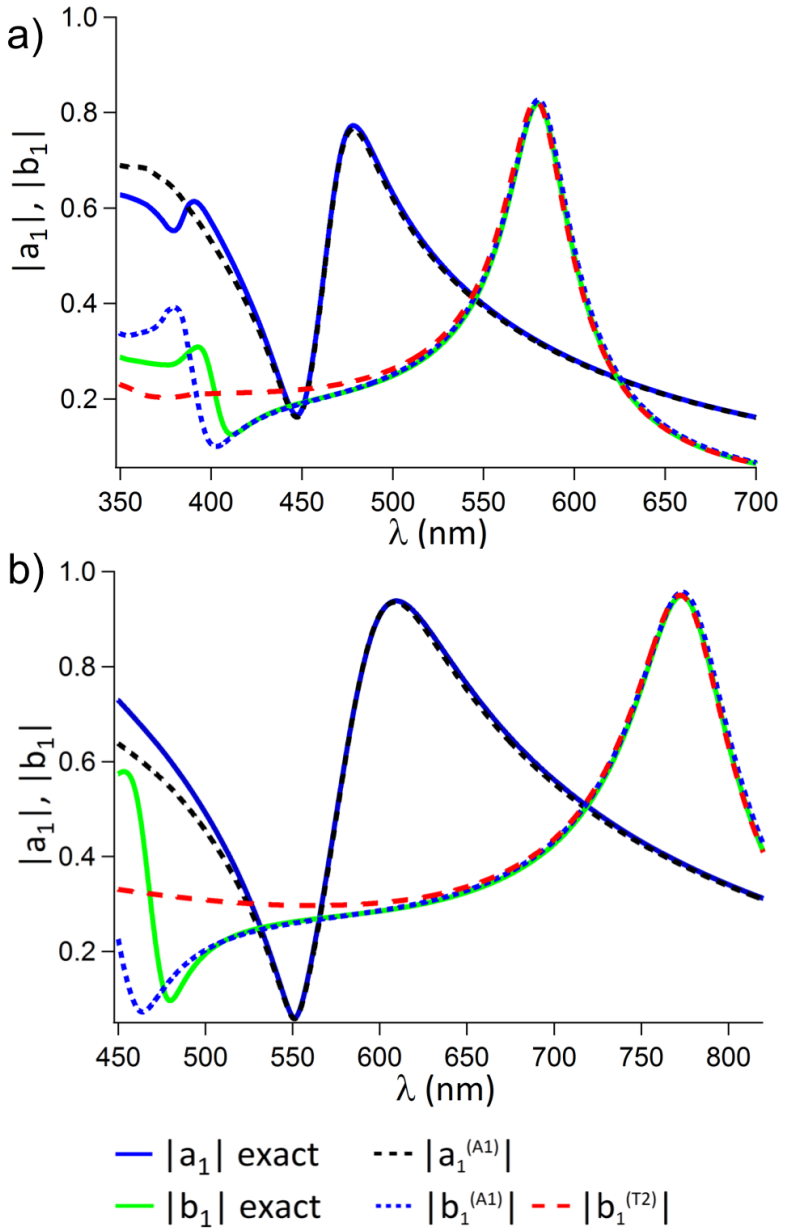

Figure 5.5: Comparison between exact calculations of a_1 (full blue line) and b_1 (full green line) with approximations (5.21) of a_1 (dashed black line) and b_1 (dotted blue line) and power-series approximations of b_1 (5.22) (dashed red line), for a sphere of silicon [135] of radius 70 nm (a) and 100 nm (b).

In fact, it was already shown in Fig. 5.1 that no approximation based on Taylor series expansions achieves to predict the resonance of a_1 but the approximation derived in this study (5.21) does predict these resonances accurately. Regarding the magnetic resonances, even though the approximation $b_1^{(T1)}$ in Eq. (5.22) which is a high-order power-series expansion of b_1 shows the dipolar magnetic resonance [106], our approximation stays more accurate for a larger range of sizes and wavelengths. We now aim at studying the validity of these expressions in the case of larger particles

made of lower refractive index. This will allow us to test the accuracy of higher orders expressions, in particular quadrupolar orders. For that purpose, we consider a sphere made of TiO_2, 140 nm in radius. We compare the calculations of the dipolar and quadrupolar electric and magnetic Mie coefficients obtained by exact calculations (Eq. 5.1) with the expressions (5.21). The plot in Fig. 5.6 shows the very good accuracy of these expressions for dipolar and quadrupolar orders, even when considering larger particles made of lower refractive indices.

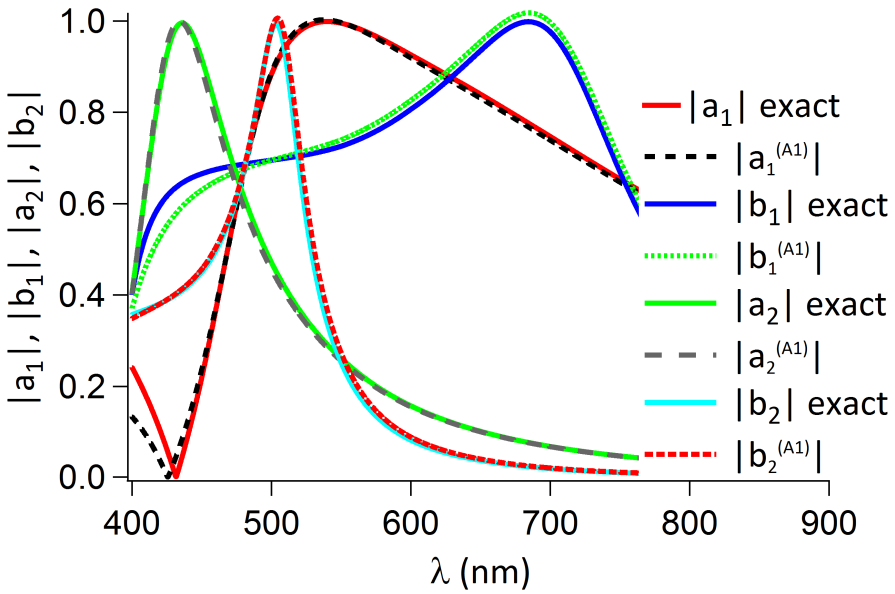

Figure 5.6: Comparison between exact calculations and approximations 5.21 for: a_1 (full red line and dashed black line), b_1 (full blue line and dotted green line), a_2 (full green line and dashed gray line) and b_2 (full cyan line and dotted red line) for a TiO_2 [147] 140 nm in radius.

5.5 Discussion

Conditions of resonance derived in section 5.2.3 have been very useful to derive accurate approximations of the Mie coefficients in the previous section. Here, we will show that they can also provide more insight on the origin of morphological resonances. Since condition (5.13) is close to the TE mode of a hollow resonator, one can infer that morphological resonances occur due to the ability of high index dielectric scatterers to play the role of a cavity. Since high index dielectric scatterers are not perfect cavities, the trapped electromagnetic field leaks in the surrounding medium driving to resonances of the scattered field. When $|\varepsilon_s| \to \infty$, the scatterer becomes a very good cavity for the electromagnetic field which can be trapped inside the resonator for a long time. It is not surprising then to find the same resonance condition as the one of a hollow resonator in this case.
Nonetheless, the resonance condition (5.14) for magnetic multipoles is different from

the TM modes of a hollow resonator. These TM modes normally occurs at $z_s \simeq r_n^{'}$, $r_n^{'}$ being the first zero of the derivative of the n-th order Bessel functions [140] and not $z_s \simeq r_{n-1}$. For $n = 1$, $r_1^{'}$ and $r_{n-1} = r_0$ take the following value $r_1^{'} = 2.744$ and $r_0 = \pi$. However, one can infer that magnetic morphological resonances also occur due to the ability of high index dielectric scatterers to confine light.
In section 5.2.3, these resonance conditions were derived in the limit $|\varepsilon_s| \to \infty$. One could then question the validity of such conditions of resonance for large but not infinite values of $|\varepsilon_s|$. A comparison between the exact values of $|\varepsilon_s|$ required to reach the resonance, also called unitary limit [106], and the predictions provided in section 5.2.3 needs then to be carried out. The exact values of the permittivity needed to reach the resonance for a given $z_0 = kR$ can be derived by numerically solving the equation $a_1 = 1$ for the electric dipole resonance and $b_1 = 1$ for the magnetic dipole resonance. In Fig. 5.7, the exact value of the unitary limit permittivity for the electric dipole $\varepsilon_{UL}^{(e)}$ in Fig. 5.7 is compared to the prediction provided by Eq. (5.13) in section 5.2.3: $z_s = r_1$ or equivalently: $\varepsilon_s^{(e1)} = \left(\frac{r_1}{z}\right)^2$. One can clearly see that this expression predicts accurately the asymptotic behavior of the exact $\varepsilon_{UL}^{(e)}$ for very small z_0 but is not very accurate for larger z_0. In Fig. 5.7, the same comparison is also carried out beween the exact unitary limit permittivity for the magnetic dipole $\varepsilon_{UL}^{(h)}$ and the prediction given by Eq. (5.14), $\varepsilon_s^{(h1)} = \left(\frac{r_0}{z}\right)^2$. A very good agreement is observed between the exact value and the prediction.
A more accurate prediction of $\varepsilon_{UL}^{(e)}$ can also be derived. To do so, one could solve Eq. (5.9) for $n = 1$: $\varphi_1^{(1)}(z_s) = -\varepsilon_s$. However, this equation can only be solved numerically. On the other hand, if the approximation $\varphi_1^{(W1)}(z_s)$ given by Eq. (5.18) is used, the previous equation reduces to a second order equation in ε and can be analytically solved leading to the prediction $\varepsilon_{UL}^{(e2)}$ (the exact expression of $\varepsilon_{UL}^{(e2)}$ is provided in appendix 3). This prediction proves to be quite accurate for a large range of z_0 as can be seen in Fig. 5.7.

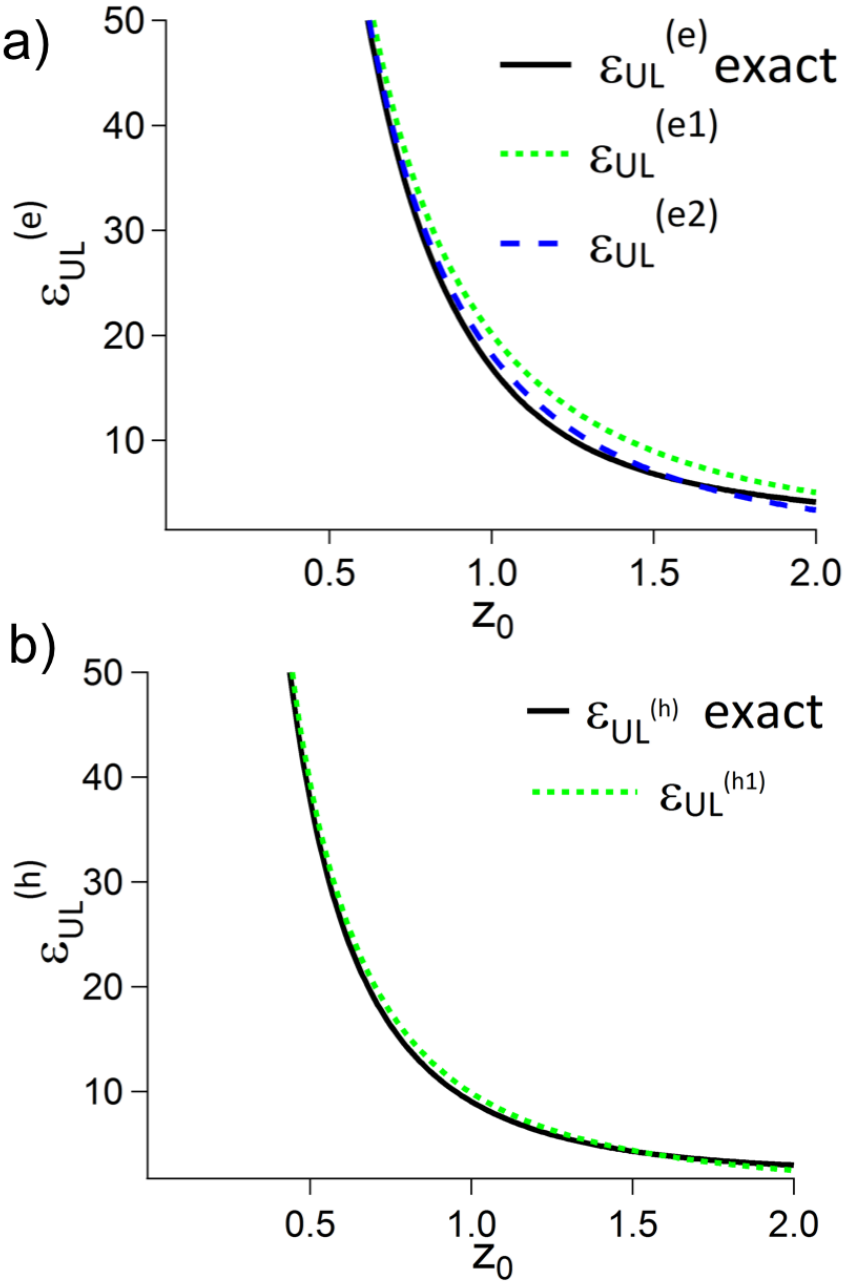

Figure 5.7: Comparison between the exact ε_{UL} (black full line) required to reach the resonance and the prediction provided by Eqs. (5.13) and (5.14) respectively labelled $\varepsilon_{UL}^{(e1)}$ and $\varepsilon_{UL}^{(h1)}$ (dotted green line). A better approximation of $\varepsilon_{UL}^{(e)}$ is obtained by solving $\varphi_n^{(W1)}(z_s) = -n\varepsilon_s$, labelled $\varepsilon_{UL}^{(e2)}$ (dashed blue line)

Finally it is also interesting to notice that the approximation (5.21) also predicts a zero of the Mie coefficients different from the trivial condition $(\varepsilon - 1)$. These zeros actually correspond to the anapoles in [148]. They are in fact reached when $f_n(\varepsilon, z) - z_n^2 = 0$ or equivalently $\frac{1}{z_n^2} f_n(\varepsilon, z) = 1$. This latter condition can be found while searching for solutions to $\varepsilon_{eq} = 1$, the definition of $\varepsilon_{eq}(z) = \left(\frac{r_1}{z}\right)^2 \frac{1-\varepsilon(z/r_1)^2}{1-2\varepsilon(z/r_1)^2}$

being provided in [143]. Expression (5.21) also provides a condition for which b_n is null corresponding to $L_n(\varepsilon, z) = 0$ that is different from the trivial solution $\varepsilon = 1$.

5.6 Conclusion

To conclude, the use of the K-matrix has allowed us to derive resonance conditions for both plasmonic and high-index dielectric resonant particles. We have thus been able to show that under the condition $|\varepsilon_s| >> 1$, the electric resonance is close to $z_s \simeq r_n$ and the magnetic resonance is close to $z_s \simeq r_{n-1}$. The proximity of the electric resonance to the pole of the $\varphi_n(z_s)$ function at $z_s = r_n$ explains the weak convergence of the Taylor series expansion for approximating Mie coefficients especially near the electric resonances. We proposed to solve this problem by using a Weierstrass expansion of the Bessel functions. This method allows us to derive for any multipolar order highly accurate electric and magnetic polarizability expressions. We evidenced the high accuracy of these expressions by calculating the dipolar and quadrupolar polarizability expressions of spherical particles made of silver, silicon and titania. These expressions bring analytical tools to explain the resonant light interaction with metallic or dielectric particles. They also permitted us to bring more physical insight on the origin of morphological resonances. In particular, these formulations allowed us to calculate a very accurate prediction of the dielectric permittivity required to reach the resonance, also called unitary limit.

Chapter 6

Quasi-normal mode analysis of high refractive-index scatterers:

Summary: The aim of this Chapter is to derive resonant state expansions of the S matrix coefficients and then apply them to the analysis of the optical response of high-refractive index scatterers in terms of their quasi-normal modes. In particular, the non-lorentzian shape of the scattered field resonances will be found to be due to the interference between resonant and non-resonant contributions. Finally, we should show how such resonant expansions allow for a study of the time-dependent scattering problem.

6.1 Introduction:

So far, we have been using the Lorenz-Mie theory and our study of light-scattering has been consequently limited to spherically-symmetric scatterers. With the progress in nano-fabrication techniques allowing to structure matter at the nanoscale comes the need for developing methods permitting the study of the electromagnetic response of more complex structures. As already pointed out in Chapter 3, the use of numerical methods such as FEM or FDTD permits to predict the electromagnetic response of arbitrary-shaped scatterers although it is often at the price of a lack of understanding of their physical behavior. Consequently when trying to design a photonic structure with a desired optical response, one would have to use extensive parametric studies. One way of overcoming this difficulty may be found in the use of optimization algorithms [85, 149].
On the other hand, the quasi-normal modes (QNM), otherwise called resonant states or leaky modes, have been attracting attention over the past few years and are seen as promising tools for studying the resonant interaction of light with complex nanostructures while keeping some physical insight. A review has in particular recently been written on this subject [4]. These quasi-normal modes are the solutions of the source-free Maxwell equations satisfying outgoing boundary conditions. Since these

structures suffer from radiative losses, their modes only have a finite lifetime. Consequently, the eigen-frequencies associated with these modes are complex numbers with a negative imaginary part: $\omega_n = \omega_{n,r} + i\omega_{n,i}$ with $\omega_{n,i} < 0$ (reminder: a $e^{-i\omega t}$ time dependence is assumed). As these modes also satisfy outgoing boundary conditions, their radial dependence asymptotically tends towards $\frac{e^{i\frac{\omega_n}{c}r}}{r}$. Consequently, these modes are exponentially diverging in the far field.
QNM expansions have however been shown to succesfully predict the Purcell factor of plasmonic [5, 150] and Mie resonators [151]. In all these studies, the apparent problem of the QNM divergence was addressed by using different schemes to normalize the QNM field [5, 152–154]. Nonetheless, some conceptual problems are yet to be addressed before applying QNM expansions to study the scattering properties of optical resonators. In particular, two main problems still remain:
(i) A first fundamental problem can be expressed as follows: how is it possible to expand the scattered field on the basis of asymptotically exponentially diverging fields?
(ii) A clear answer has not been found for another fundamental question relative the QNM: is the basis of QNM complete for expanding the scattered field? In other words, are there only resonant contributions to the scattered field or are there also additional non-resonant contributions? The completeness of the QNM basis has been demonstrated for the internal field by the calculation of the Green function pole expansion but attempts to generalize this result to the scattered field outside the scatterer have failed.

Despite these two fundamental problems, some studies have proven to successfully describe the optical response of plasmonic [33] and Mie resonators [34, 35] by means of QNM expansions. These studies relied on expansions of the internal field induced inside the resonator (or equivalent surface currents in [34, 35]). In [33], it was shown that quantities quantifying the far-field reponse of the resonators could then be computed by only knowing the internal field. On the other hand, in [34, 35] the scattered field was computed by means of the Green function.

In this Chapter, our approach will be based on the S-matrix, already presented in Chapter 3. Even though we will adopt a slightly different approach, we should point out the interesting work of Alpeggiani et al. [155] where a quasi-normal mode expansion of the S-matrix coefficients was obtained by starting from temporal coupled mode theory models [156, 157]. On the other hand, we will be starting from causality and energy conservation considerations in order to derive the pole expansion of the S-matrix coefficients for dispersionless media. We will then use this pole expansion to study the interaction of light with high refractive index scatterers. In particular, we should discuss the completeness of the QNM basis by comparing the shape between the resonances of the scattered field that have a Fano's type asymmetric shape and the resonances of the internal field that have a Lorentzian

shape. We will then conclude that the QNM basis cannot be complete for the scattered field and consequently an additional non-resonant contribution has to be taken into account. Finally, we will be considering the scattering problem in the time domain and we will show that the issue of divergence can be avoided by taking causality into account.

6.2 Resonant state expansions of the S and Ξ coefficients

6.2.1 Causality and analytical properties of the S-matrix coefficients

The analytical properties of the S-matrix coefficients are constrained by causality and energy conservation. It is in particular possible to determine the analytic continuation in the complex plane of the S-matrix coefficients by using causality and energy conservation arguments. To do so, we will follow the method employed in ([101], pp. 70-72) and study the scattering problem in the time domain. Causality is much easier to study in the far field area since, in this case, both incoming and outgoing fields are spherical waves propagating inward and outward respectively. As was shown in Chapter 3 in the harmonic domain, the total field tends towards:

$$\begin{aligned}
\lim_{r\to\infty} \mathbf{E}_{tot}(\mathbf{r},\omega) &= E_0 \sum_{n=1}^{\infty}\sum_{m=-n}^{n} i^{n+1} c_{n,m}^{(h)}(\omega)\mathbf{X}_{n,m}(\theta,\phi) + i^n c_{n,m}^{(e)}(\omega)\mathbf{Z}_{n,m}(\theta,\phi) \\
c_{n,m}^{(h)}(\omega) &= \frac{s_{n,m}^{(h,-)}(\omega)}{kr}\left(e^{-ikr} - (-1)^n S_n^{(h)} e^{ikr}\right) \\
c_{n,m}^{(e)}(\omega) &= \frac{s_{n,m}^{(e,-)}(\omega)}{kr}\left(e^{-ikr} - (-1)^{n-1} S_n^{(e)} e^{ikr}\right)
\end{aligned} \tag{6.1}$$

In the time domain, we will be considering an incoming field $\mathbf{E}_{\text{in}}(\mathbf{r},t)$ impinging on a spherical scatterer of radius R thus giving rise to an outgoing field $\mathbf{E}_{\text{out}}(\mathbf{r},t)$. In the far field area, the expression for the incoming electric fields can be shown to be:

$$\begin{aligned}
\lim_{r\to\infty} \mathbf{E}_{\text{in}}(\mathbf{r},t) &= E_0 \sum_{n=1}^{\infty}\sum_{m=-n}^{n} i^{n+1} c_{n,m}^{(h,-)}(t)\mathbf{X}_{n,m}(\theta,\phi) + i^n c_{n,m}^{(e,-)}(t)\mathbf{Z}_{n,m}(\theta,\phi) \\
c_{n,m}^{(h,-)}(t) &= \frac{1}{2\pi}\int_{-\infty}^{\infty} \frac{s_{n,m}^{(h,-)}(\omega)}{kr} e^{-ikr} e^{-i\omega t} d\omega \\
c_{n,m}^{(e,-)}(t) &= \frac{1}{2\pi}\int_{-\infty}^{\infty} \frac{s_{n,m}^{(e,-)}(\omega)}{kr} e^{-ikr} e^{-i\omega t} d\omega
\end{aligned} \tag{6.2}$$

Similarly, the time-dependent outgoing field expression can be shown to be:

$$\begin{aligned}\lim_{r\to\infty}\mathbf{E}_{\text{out}}(\mathbf{r},t) &= E_0\sum_{n=1}^{\infty}\sum_{m=-n}^{n}(-i)^{n+1}c_{n,m}^{(h,+)}(t)\mathbf{X}_{n,m}(\theta,\phi)+(-i)^n c_{n,m}^{(e,+)}(t)\mathbf{Z}_{n,m}(\theta,\phi)\\ c_{n,m}^{(h,+)}(t) &= \frac{1}{2\pi}\int_{-\infty}^{\infty}S_n^{(h)}(\omega)\frac{s_{n,m}^{(h,-)}(\omega)}{kr}e^{ikr}e^{-i\omega t}d\omega\\ c_{n,m}^{(e,+)}(t) &= \frac{1}{2\pi}\int_{-\infty}^{\infty}S_n^{(e)}(\omega)\frac{s_{n,m}^{(e,-)}(\omega)}{kr}e^{ikr}e^{-i\omega t}d\omega\end{aligned} \tag{6.3}$$

For a given point $\mathbf{r}$ located in the far field area, it is possible to define a time t_0 such that the incoming field in $\mathbf{r}$ vanishes for $t<t_0$. An outgoing field can only appear when the incoming field reaches the surface of the scatterer. Consequently, the outgoing field at $\mathbf{r}$ should vanish for $t<t_0+2\frac{r-R}{c}$ leaving enough time for the incoming field to reach the surface of the scatterer and to give rise to an outgoing field that will propagate back to the point $\mathbf{r}$ at the speed c. After some algebraic manipulations to introduce t_0, $c_{n,m}^{(i,-)}(\mathbf{r},t)$ and $c_{n,m}^{(i,+)}(\mathbf{r},t)$, where $i=e$ or h, can be rewritten in the following manner:

$$\begin{aligned}c_{n,m}^{(i,-)}(\mathbf{r},t) &= \frac{1}{2\pi}\int_{-\infty}^{\infty}\frac{s_{n,m}^{(i,-)}(\omega)}{kr}e^{-i\omega\left(t_0+\frac{r}{c}\right)}e^{-i\omega(t-t_0)}d\omega\\ c_{n,m}^{(i,+)}(\mathbf{r},t) &= \frac{1}{2\pi}\int_{-\infty}^{\infty}e^{i2\omega\frac{R}{c}}S_n^{(i)}(\omega)\frac{s_{n,m}^{(i,-)}(\omega)}{kr}e^{-i\omega\left(t_0+\frac{r}{c}\right)}e^{-i\omega\left(t-t_0-2\frac{r-R}{c}\right)}d\omega\end{aligned} \tag{6.4}$$

As $c_{n,m}^{(i,-)}(\mathbf{r},t)$ is null for $t<t_0$, $\frac{s_{n,m}^{(i,-)}(\omega)}{kr}e^{-i\omega\left(t_0+\frac{r}{c}\right)}$ should be holomorphic, i.e. should not possess poles, in the upper half of the complex plane [101]. The explanation for this property is readily found by use of the theorem of residues: while calculating the Fourier transform of $\frac{s_{n,m}^{(i,-)}}{kr}e^{-i\omega\left(t_0+\frac{r}{c}\right)}$ in Eq. (6.4) by means of the theorem of residues and for $t<t_0$, one has to close the contour in the upper half of the complex plane. In fact, in this case $t-t_0<0$ hence for complex $\omega=\omega_r+i\omega_i$ $e^{-i\omega(t-t_0)}$ would diverge when $\omega_i<0$ and $|\omega|\to\infty$ but it would converge when $\omega_i>0$. That is the reason why the contour should be closed in the upper half of the complex plane. Since, according to causality this integral should be null, $\frac{s_{n,m}^{(i,-)}}{kr}e^{-i\omega\left(t_0+\frac{r}{c}\right)}$ cannot admit any poles in the upper half of the complex plane.
Equivalently, one can show that as $c_{n,m}^{(i,+)}(\mathbf{r},t)$ vanishes for $t<t_0+2\frac{r-R}{c}$, $e^{i2\omega\frac{R}{c}}S_n^{(e)}(\omega)\frac{s_{n,m}^{(i,-)}(\omega)}{kr}e^{-i\omega\left(t_0+\frac{r}{c}\right)}$ is also an holomorphic function in the upper half of the complex plane. As a consequence, one finds that $e^{i2\omega\frac{R}{c}}S_n^{(e)}(\omega)$, as it is the quotient of the two previous functions that are regular in the upper half plane, should also be a holomorphic function in the upper half of the complex plane but can admit zeros there.
On the other hand, the presence of poles of S in the lower half of the complex is not prohibited by causality. These poles are related to the resonant states of the

scatterer and in the case of spherical scatterers they should occur when $D_n^{(e,h)}(z) = 0$. $D_n^{(e,h)}(z)$ being the denominator functions associated with the S-matrix coefficients introduced in Chapter 3. To conclude, it has been shown by using causality principle that the S-matrix coefficients can be cast:

$$S(\omega) = e^{-2i\frac{\omega}{c}R} f(\omega) \tag{6.5}$$

where $f(\omega)$ is a holomorphic function but can admit zeros in the upper complex plane and it is analytic in the lower complex plane except for poles.

In addition, there are some properties of symmetry between poles and zeros of the S-matrix coefficients:
First, since the fields are real, the following relation holds for real ω:

$$S(-\omega) = S^*(\omega) \tag{6.6}$$

This relation can be extended to complex values of ω [101] leading to:

$$S(-\omega^*) = S^*(\omega) \tag{6.7}$$

Consequently, if $\omega_\mathrm{p} = \omega_\mathrm{pr} - i\omega_\mathrm{pi}$ is a pole of S located in the lower half of the complex plane (ω_pr and ω_pi are then real and positive), according to (6.7), $-\omega_\mathrm{p}^* = -\omega_\mathrm{pr} - i\omega_\mathrm{pi}$ is also a pole of S. The relation (6.7) thus imposes that the poles of S are symmetric with respect to the imaginary axis.
Furthermore, as was shown in Chapter 3, energy conservation imposes that for a lossless scatterer:

$$S(\omega)S^*(\omega) = 1 \tag{6.8}$$

We can then combine relations (6.7), (6.6) and (6.8) leading to $S(\omega)S^*(\omega^*) = 1$ or:

$$S(\omega) = \frac{1}{S^*(\omega^*)} \tag{6.9}$$

Consequently, if $\omega_\mathrm{p} = \omega_\mathrm{pr} - i\omega_\mathrm{pi}$ is a pole of S, relation (6.9) imposes that for lossless scatterers $\omega_\mathrm{p}^* = \omega_\mathrm{pr} + i\omega_\mathrm{pi}$ is a zero of S. It then follows that there are zeros of the S-matrix that are symmetric of the poles of the S matrix with regards to the real axis. All these symmetry relations of zeros and poles of the S matrix are summarized in Fig. (6.1) with respect to $z = \frac{\omega}{c}R$.

The presence of the $e^{-2i\frac{\omega}{c}R}$ factor is deeply related to causality because it means that an outgoing field cannot be created until the incoming field reaches the surface of the scatterer.

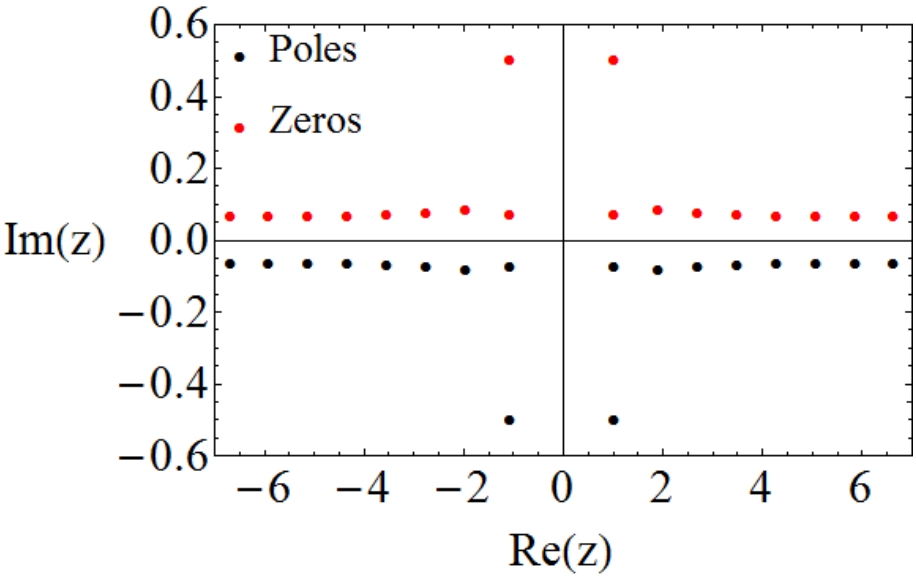

Figure 6.1: Poles and zeros of the S matrix in the z complex plane

6.2.2 Pole expansion of S-matrix coefficients:

Causality considerations have allowed us to show that the S-matrix coefficients could be expressed under the form given in Eq. (6.5). However, an exact expression of the S-matrix coefficients is yet to be determined. Such an expression can be found in the seminal work of Van Kampen [158] and in some textbooks (see in particular [101] pp. 59-72 and [100] Chapter 12). This expression was also re-demonstrated more recently and applied to the particular case of optical nanoresonators [159] leading to the following general expression which is also called Weierstrass factorization of the S-matrix coefficients:

$$\begin{aligned} S_n^{(e)}(\omega) &= A_n^{(e)} e^{-iB_n^{(e)}\omega} \prod_{\alpha=-\infty}^{\infty} \frac{\omega - z_{n,\alpha}^{(e)}}{\omega - p_{n,\alpha}^{(e)}} \\ S_n^{(h)}(\omega) &= A_n^{(h)} e^{-iB_n^{(h)}\omega} \prod_{\alpha=-\infty}^{\infty} \frac{\omega - z_{n,\alpha}^{(h)}}{\omega - p_{n,\alpha}^{(h)}} \end{aligned} \tag{6.10}$$

where $A_n^{e,h} = S_n^{e,h}(0) \prod_{\alpha=-\infty}^{\infty} \frac{z_{n,\alpha}^{(e,h)}}{p_{n,\alpha}^{(e,h)}}$ and $-iB_n^{(e,h)} = \frac{S^{(e,h)\prime}(0)}{S^{(e,h)}(0)} + \sum_{\alpha=-\infty}^{\infty} \frac{1}{z_{n,\alpha}^{(e,h)}} - \frac{1}{p_{n,\alpha}^{(e,h)}}$. $z_{n,\alpha}^{(e,h)}$ and $p_{n,\alpha}^{(e,h)}$ are respectively the zeros and the poles of $S_n^{(e,h)}$. For a spherical scatterer, the zeros should verify the relation $N_{S,n}^{(e,h)}\left(z_{n,\alpha}^{(e,h)}\right) = 0$, $N_{S,n}^{(e,h)}$ being the numerator functions introduced in Chapter 3 while the poles are solutions of $D_n^{(e,h)}\left(p_{n,\alpha}^{(e,h)}\right) = 0$, $D_n^{(e,h)}\left(p_{n,\alpha}^{(e,h)}\right)$ being the denominator functions. In the case of a

lossless scatterer, the $A_n^{(e,h)}$ factors can be shown to be equal to [160]

$$\begin{aligned} A_n^{(e)} &= (-1)^{n+1} \\ A_n^{(h)} &= (-1)^n \end{aligned} \tag{6.11}$$

Regarding the factor $B_n^{(e,h)}$, one can show that $\frac{S^{(e,h)'}(0)}{S^{(e,h)}(0)} = 0$ [160]. The discussion of the previous section helps us show that:

$$\sum_{\alpha=-\infty}^{\infty} \frac{1}{z_{n,\alpha}^{(e,h)}} - \frac{1}{p_{n,\alpha}^{(e,h)}} = 2\frac{R}{c} \tag{6.12}$$

It then follows that the S-matrix coefficients can be cast:

$$\begin{aligned} S_n^{(e)}(\omega) &= (-1)^{n+1} e^{-2i\frac{\omega}{c}R} \prod_{\alpha=-\infty}^{\infty} \frac{\omega - z_{n,\alpha}^{(e)}}{\omega - p_{n,\alpha}^{(e)}} \\ S_n^{(h)}(\omega) &= (-1)^{n} e^{-2i\frac{\omega}{c}R} \prod_{\alpha=-\infty}^{\infty} \frac{\omega - z_{n,\alpha}^{(h)}}{\omega - p_{n,\alpha}^{(h)}} \end{aligned} \tag{6.13}$$

According to the results presented in the previous Section, for lossless scatterers, the zeros $z_{n,\alpha}^{(e)}$ should be equal to the transpose of the poles $z_{n,\alpha}^{(e)} = \left(p_{n,\alpha}^{(e)}\right)^*$. The previous expressions can consequently be rewritten in the following way:

$$\begin{aligned} S_n^{(e)}(\omega) &= (-1)^{n+1} e^{-2i\frac{\omega}{c}R} \prod_{\alpha=-\infty}^{\infty} \frac{\omega - \left(p_{n,\alpha}^{(e)}\right)^*}{\omega - p_{n,\alpha}^{(e)}} \\ S_n^{(h)}(\omega) &= (-1)^{n} e^{-2i\frac{\omega}{c}R} \prod_{\alpha=-\infty}^{\infty} \frac{\omega - \left(p_{n,\alpha}^{(h)}\right)^*}{\omega - p_{n,\alpha}^{(h)}} \end{aligned} \tag{6.14}$$

The previous infinite product form can be converted into an infinite sum form [159]:

$$\begin{aligned} S_n^{(e)}(\omega) &= (-1)^{n+1} e^{-2i\frac{\omega}{c}R} \left(1 + \sum_{\alpha=-\infty}^{\infty} \frac{r_{n,\alpha}^{(e)}}{\omega - p_{n,\alpha}^{(e)}}\right) \\ S_n^{(h)}(\omega) &= (-1)^{n} e^{-2i\frac{\omega}{c}R} \left(1 + \sum_{\alpha=-\infty}^{\infty} \frac{r_{n,\alpha}^{(h)}}{\omega - p_{n,\alpha}^{(h)}}\right) \end{aligned} \tag{6.15}$$

where $r_{n,\alpha}^{(e,h)}$ are the residues associated with the poles $p_{n,\alpha}^{(e,h)}$. This pole expansion is close to the quasi-nomal mode expansion of the S-matrix coefficient derived in [155]. Here, however we also predict the presence of a factor $e^{-2i\frac{\omega}{c}R}$ that was shown to be deeply related to causality. Furthermore, by means of Eq. (6.14), one can

show that:

$$r_{n,\alpha}^{(e,h)} = \left(p_{n,\alpha}^{(e,h)} - z_{n,\alpha}^{(e,h)}\right) \prod_{\beta \neq \alpha} \frac{p_{n,\alpha}^{(e,h)} - z_{n,\beta}^{(e)}}{p_{n,\alpha}^{(e,h)} - p_{n,\beta}^{(e)}} \tag{6.16}$$

As a consequence of the symmetry relations (6.7), $r_{n,-\alpha}^{(e,h)} = -\left(r_{n,\alpha}^{(e,h)}\right)^*$ where $r_{n,-\alpha}^{(e,h)}$ is the residue associated with $p_{n,-\alpha}^{(e,h)} = -\left(p_{n,\alpha}^{(e,h)}\right)^*$. In what follows, an expression of the S-matrix coefficients in terms of the size parameter $z = kR = \frac{\omega}{c}R$ rather than the frequency ω will be preferred:

$$\begin{aligned}
S_n^{(e)}(z) &= (-1)^{n+1} e^{-2iz} \left(1 + \sum_{\alpha=-\infty}^{\infty} \frac{r_{z,n,\alpha}^{(e)}}{z - p_{z,n,\alpha}^{(e)}}\right) \\
S_n^{(e)}(z) &= (-1)^{n+1} e^{-2iz} \prod_{\alpha=-\infty}^{\infty} \frac{z - \left(p_{z,n,\alpha}^{(e)}\right)^*}{z - p_{z,n,\alpha}^{(e)}} \\
S_n^{(h)}(z) &= (-1)^{n} e^{-2iz} \left(1 + \sum_{\alpha=-\infty}^{\infty} \frac{r_{z,n,\alpha}^{(h)}}{z - p_{z,n,\alpha}^{(h)}}\right) \\
S_n^{(h)}(z) &= (-1)^{n} e^{-2iz} \prod_{\alpha=-\infty}^{\infty} \frac{z - \left(p_{z,n,\alpha}^{(h)}\right)^*}{z - p_{z,n,\alpha}^{(h)}}
\end{aligned} \tag{6.17}$$

By using the symmetry relation (6.7), the previous expansions can be re-expressed in the following way:

$$\begin{aligned}
S_n^{(e)}(z) &= (-1)^{n+1} e^{-2iz} \left(1 + 2\sum_{\alpha=1}^{\infty} \frac{zi\mathrm{Im}\left(r_{z,n,\alpha}^{(e)}\right) + \mathrm{Re}\left(r_{z,n,\alpha}^{(e)}.\, {p_{z,n,\alpha}^{(e)}}^*\right)}{z^2 - \left|p_{z,n,\alpha}^{(e)}\right|^2 - 2iz\mathrm{Im}\left(p_{z,n,\alpha}^{(e)}\right)}\right) \\
S_n^{(e)}(z) &= (-1)^{n+1} e^{-2iz} \prod_{\alpha=1}^{\infty} \frac{z^2 - \left|p_{z,n,\alpha}^{(e)}\right|^2 + 2iz\mathrm{Im}\left(p_{z,n,\alpha}^{(e)}\right)}{z^2 - \left|p_{z,n,\alpha}^{(e)}\right|^2 - 2iz\mathrm{Im}\left(p_{z,n,\alpha}^{(e)}\right)} \\
S_n^{(h)}(z) &= (-1)^{n} e^{-2iz} \left(1 + 2\sum_{\alpha=1}^{\infty} \frac{zi\mathrm{Im}\left(r_{z,n,\alpha}^{(h)}\right) + \mathrm{Re}\left(r_{z,n,\alpha}^{(h)}.\, {p_{z,n,\alpha}^{(h)}}^*\right)}{z^2 - \left|p_{z,n,\alpha}^{(h)}\right|^2 - 2iz\mathrm{Im}\left(p_{z,n,\alpha}^{(h)}\right)}\right) \\
S_n^{(h)}(z) &= (-1)^{n} e^{-2iz} \prod_{\alpha=1}^{\infty} \frac{z^2 - \left|p_{z,n,\alpha}^{(h)}\right|^2 + 2iz\mathrm{Im}\left(p_{z,n,\alpha}^{(h)}\right)}{z^2 - \left|p_{z,n,\alpha}^{(h)}\right|^2 - 2iz\mathrm{Im}\left(p_{z,n,\alpha}^{(h)}\right)}
\end{aligned} \tag{6.18}$$

These expansions will be applied in Section 6.3 to the study of resonant scattering by high refractive dielectric particles. However, in order to have a complete understanding of the interaction of light with these scatterers, one should also determine the internal field inside the scatterer. For this purpose, in the next Section,

we should be concerned with the derivation of a pole expansion of the Ξ-matrix coefficients defined in Chapter 3.

6.2.3 Lorentzian expansion of Ξ-matrix coefficients:

Only few results can be found in the literature regarding the pole expansion of the Ξ-matrix coefficients. Therefore, we will then try to use the results of the previous sections to derive such an expansion for the Ξ matrix as well.

The first noticeable difference of the Ξ matrix coefficients in comparison to the S-matrix coefficients is that the former are not bound by unitarity (6.8). In fact, $|\Xi_n^{(e,h)}|$ can be arbitrarily large as it is the case for example for very high-refractive index particles [127]. The possibility for $\Xi_n^{(e,h)}$ to have an arbitrarily large modulus is not in contradiction with energy conservation. In fact it arises from the fact that when there is a large contrast of permittivity between the scatterer and the background medium, the field can remain trapped for a long time inside scatterers. A large field enhancement can thus build up inside this scatterer. It follows that, unlike for $S_n^{(e,h)}$, the relation (6.9) does not hold for $\Xi_n^{(e,h)}$. Consequently, these coefficients do not have zeros on the upper half of the complex plane.
For spherical scatterers, this property could also have been directly seen by a comparison of the analytical expressions of $S_n^{(e,h)}$ and $\Xi_n^{(e,h)}$ for spherical scatterers introduced in Chapter 3:

$$S_n^{(e,h)} = -\frac{N_{S,n}^{(e,h)}(kR)}{D_n^{(e,h)}(kR)}, \; \Xi_n^{(e,h)} = \frac{1}{D_n^{(e,h)}(kR)} \tag{6.19}$$

From these expressions, it is obvious that the zeros $S_n^{(e,h)}$ are the roots of the numerator function $N_{S,n}^{(e,h)}$ while the numerator of $\Xi_n^{(e,h)}$ does not admit roots.
On the other hand, $\Xi_n^{(e,h)}$ and $S_n^{(e,h)}$ poles appear to be identical and are the roots of the denominator functions $D_n^{(e,h)}$. One can consequently infer that $\Xi_n^{(e,h)}$ coefficients admit the following pole expansion:

$$\begin{aligned} \Xi_n^{(e)}(z) &= A_{\Xi,n}^{(e)} e^{-iB_{\Xi,z}z} \sum_{\alpha=-\infty}^{\infty} \frac{r_{\Xi,z,n,\alpha}^{(e)}}{z - p_{z,n,\alpha}^{(e)}} \\ \Xi_n^{(h)}(z) &= A_{\Xi,n}^{(h)} e^{-iB_{\Xi,z}z} \sum_{\alpha=-\infty}^{\infty} \frac{r_{\Xi,z,n,\alpha}^{(h)}}{z - p_{z,n,\alpha}^{(h)}} \end{aligned} \tag{6.20}$$

$A_{\Xi,n}^{(e,h)}$ are found to be identical to $A_n^{(e,h)}$ given in Eq. (6.11). Regarding $B_{\Xi,z}$ we found that $B_{\Xi,z} = 0$. Using the symmetry relation (6.7), the expressions of $\Xi_n^{(e,h)}(z)$

can be shown to be:

$$\begin{aligned}\Xi_n^{(e)}(z) &= 2.(-1)^{n+1}\sum_{\alpha=1}^{\infty}\frac{iz\mathrm{Im}\left(r_{\Xi,z,n,\alpha}^{(e)}\right)+\mathrm{Re}\left(r_{\Xi,z,n,\alpha}^{(e)}.\,{p_{z,n,\alpha}^{(e)}}^{*}\right)}{z^2-\left|p_{z,n,\alpha}^{(e)}\right|^2-2iz\mathrm{Im}\left(p_{z,n,\alpha}^{(e)}\right)}\\ \Xi_n^{(h)}(z) &= 2.(-1)^{n}\sum_{\alpha=1}^{\infty}\frac{iz\mathrm{Im}\left(r_{\Xi,z,n,\alpha}^{(h)}\right)+\mathrm{Re}\left(r_{\Xi,z,n,\alpha}^{(h)}.\,{p_{z,n,\alpha}^{(h)}}^{*}\right)}{z^2-\left|p_{z,n,\alpha}^{(h)}\right|^2-2iz\mathrm{Im}\left(p_{z,n,\alpha}^{(h)}\right)}\end{aligned} \tag{6.21}$$

Comparing the expansions (6.18) and (6.21), one notices the presence of the additional 1 in (6.18). This is related to the existence of zeros of the S-matrix coefficients and will be further discussed in section 6.3. It will be in particular shown to be one of the origins a non-resonant contribution to the scattering field.

6.2.4 Residues of $S_n^{(e,h)}$ and $\Xi_n^{(e,h)}$:

In principle, the residues $r_{z,n,\alpha}^{(e,h)}$ can be determined directly from Eq. (6.16). However, in practice a large number of quasi-normal modes would have to be derived to converge towards an accurate value of $r_{z,n,\alpha}^{(e,h)}$ with expression (6.16). That is why, here we propose to take advantage of the analytical expressions of $S_n^{(e,h)}$ and $\Xi_n^{(e,h)}$ for determining $r_{z,n,\alpha}^{(e,h)}$ and $r_{\Xi,z,n,\alpha}^{(e,h)}$. The residues associated with the poles of $\Xi_n^{(e,h)}$ can be directly computed in the following way [160]:

$$r_{\Xi,z,n,\alpha}^{(e)}=\frac{(-1)^{n+1}}{\frac{\partial D_n^{(e)}}{\partial z}(z)\Big|_{p_{z,n,\alpha}^{(e)}}},\ r_{\Xi,z,n,\alpha}^{(h)}=\frac{(-1)^{n}}{\frac{\partial D_n^{(h)}}{\partial z}(z)\Big|_{p_{z,n,\alpha}^{(h)}}} \tag{6.22}$$

Exact calculations lead to the following analytical expressions for the residues:

$$\begin{aligned}r_{\Xi,z,n,\alpha}^{(e)} &= \frac{(-1)^{n+1}2in_s}{(\varepsilon_s-1)\left(\xi_n^{(+)'}\left(p_{z,n,\alpha}^{(e)}\right)\psi_n'\left(n_s p_{z,n,\alpha}^{(e)}\right)+n(n+1)j_n\left(n_s p_{z,n,\alpha}^{(e)}\right)h_n^{(+)}\left(p_{z,n,\alpha}^{(e)}\right)\right)}\\ r_{\Xi,z,n,\alpha}^{(h)} &= \frac{(-1)^{n}2i}{(\varepsilon_s-1)\left(p_{z,n,\alpha}^{(h)}\right)^2 h_n^{(+)}\left(p_{z,n,\alpha}^{(h)}\right)j_n\left(n_s p_{z,n,\alpha}^{(h)}\right)}\end{aligned} \tag{6.23}$$

An analytical expression of the residues of the S matrix can also be computed directly from (6.23) along with the continuity condition. Let us start by recalling the conditions of continuity of the field:

$$\begin{aligned}h_n^{(-)}(kR)+S_n^{(h)}h_n^{(+)}(kR) &= \Xi_n^{(h)}.j_n(k_sR)\\ \xi_n^{(-)'}(kR)+S_n^{(e)}\xi_n^{(+)'}(kR) &= \Xi_n^{(e)}\frac{\psi_n'(k_sR)}{n_s}\end{aligned} \tag{6.24}$$

If the infinite sum forms of $S_n^{(e,h)}$ and $\Xi_n^{(h)}$ are used:

$$\begin{aligned}
&h_n^{(-)}(z)+(-1)^{n+1}e^{-2iz}\left(1+\sum_{\alpha=-\infty}^{\infty}\frac{r_{z,n,\alpha}^{(h)}}{z-p_{z,n,\alpha}^{(h)}}\right)h_n^{(+)}(z)=(-1)^{n+1}\sum_{\alpha=-\infty}^{\infty}\frac{r_{\Xi,z,n,\alpha}^{(h)}}{z-p_{z,n,\alpha}^{(h)}}.j_n(n_sz)\\
&\xi_n^{(-)'}(z)+(-1)^{n}e^{-2iz}\left(1+\sum_{\alpha=-\infty}^{\infty}\frac{r_{z,n,\alpha}^{(e)}}{z-p_{z,n,\alpha}^{(e)}}\right)\xi_n^{(+)'}(z)=(-1)^{n}\sum_{\alpha=-\infty}^{\infty}\frac{r_{\Xi,z,n,\alpha}^{(e)}}{z-p_{z,n,\alpha}^{(e)}}\frac{\psi_n'(n_sz)}{n_s}
\end{aligned} \tag{6.25}$$

Multiplying both sides of the previous equations by $z-p_{z,n,\alpha}^{(h)}$ or $z-p_{z,n,\alpha}^{(e)}$ and choosing $z=p_{z,n,\alpha}^{(h)}$ or $z=p_{z,n,\alpha}^{(e)}$, yields the following relations:

$$\begin{aligned}
e^{-2ip_{z,n,\alpha}^{(h)}}r_{z,n,\alpha}^{(h)}h_n^{(+)}(p_{z,n,\alpha}^{(h)})&=r_{\Xi,z,n,\alpha}^{(h)}.j_n(n_sp_{z,n,\alpha}^{(h)})\\
e^{-2ip_{z,n,\alpha}^{(e)}}r_{z,n,\alpha}^{(e)}\xi_n^{(+)'}(p_{z,n,\alpha}^{(e)})&=r_{\Xi,z,n,\alpha}^{(e)}\frac{\psi_n'(n_sp_{z,n,\alpha}^{(e)})}{n_s}
\end{aligned} \tag{6.26}$$

As a consequence, the expression of the residues of the S matrix in terms of those of the Ξ matrix are:

$$\begin{aligned}
r_{z,n,\alpha}^{(h)}&=e^{2ip_{z,n,\alpha}^{(h)}}\frac{j_n(n_sp_{z,n,\alpha}^{(h)})}{h_n^{(+)}(p_{z,n,\alpha}^{(h)})}r_{\Xi,z,n,\alpha}^{(h)}\\
r_{z,n,\alpha}^{(e)}&=e^{2ip_{z,n,\alpha}^{(e)}}\frac{\psi_n'(n_sp_{z,n,\alpha}^{(e)})}{n_s\xi_n^{(+)'}(p_{z,n,\alpha}^{(e)})}r_{\Xi,z,n,\alpha}^{(e)}
\end{aligned} \tag{6.27}$$

It is also possible to rewrite $r_{x,n,\alpha}^{(e)}$ in terms of Bessel and Hankel functions. As, by definition,

$$\begin{aligned}
&D_n^{(e)}(p_{z,n,\alpha}^{(e)})=0\\
\implies\ &n_s\frac{j_n(n_sp_{z,n,\alpha}^{(e)})}{h_n^{(+)}(p_{z,n,\alpha}^{(e)})}=\frac{\psi_n^{'}(n_sp_{z,n,\alpha}^{(e)})}{n_s\xi_n^{(+)'}(p_{z,n,\alpha}^{(e)})},
\end{aligned} \tag{6.28}$$

It follows that:

$$\begin{aligned}
r_{z,n,\alpha}^{(h)}&=e^{2ip_{z,n,\alpha}^{(h)}}\frac{j_n(n_sp_{z,n,\alpha}^{(h)})}{h_n^{(+)}(p_{z,n,\alpha}^{(h)})}r_{\Xi,z,n,\alpha}^{(h)}\\
r_{z,n,\alpha}^{(e)}&=e^{2ip_{z,n,\alpha}^{(e)}}n_s\frac{j_n(n_sp_{z,n,\alpha}^{(e)})}{h_n^{(+)}(p_{z,n,\alpha}^{(e)})}r_{\Xi,z,n,\alpha}^{(e)}
\end{aligned} \tag{6.29}$$

6.3 Resonant scattering by a High Refractive Index scatterer:

In this section, we will try to show how the analytical expressions derived in the preceding section can be used to get a better understanding of the resonant behavior

of high refractive index scatterers. This will also allow us to gain a better physical understanding of the terms of these expansions. This study will in turn help us understand the physical meaning of the expansions derived in the previous section.

6.3.1 Resonances of the scattered field and internal field:

In fig. 6.3, the evolution of the scattering efficiency Q_{scat} and the average of the squared modulus of the internal field $\langle|\mathbf{E}_{int}|^2\rangle$ of a $\varepsilon_s = 16$ with the size parameter $z = kR$ have been plotted. It appears that the shape of their resonances is slightly different.

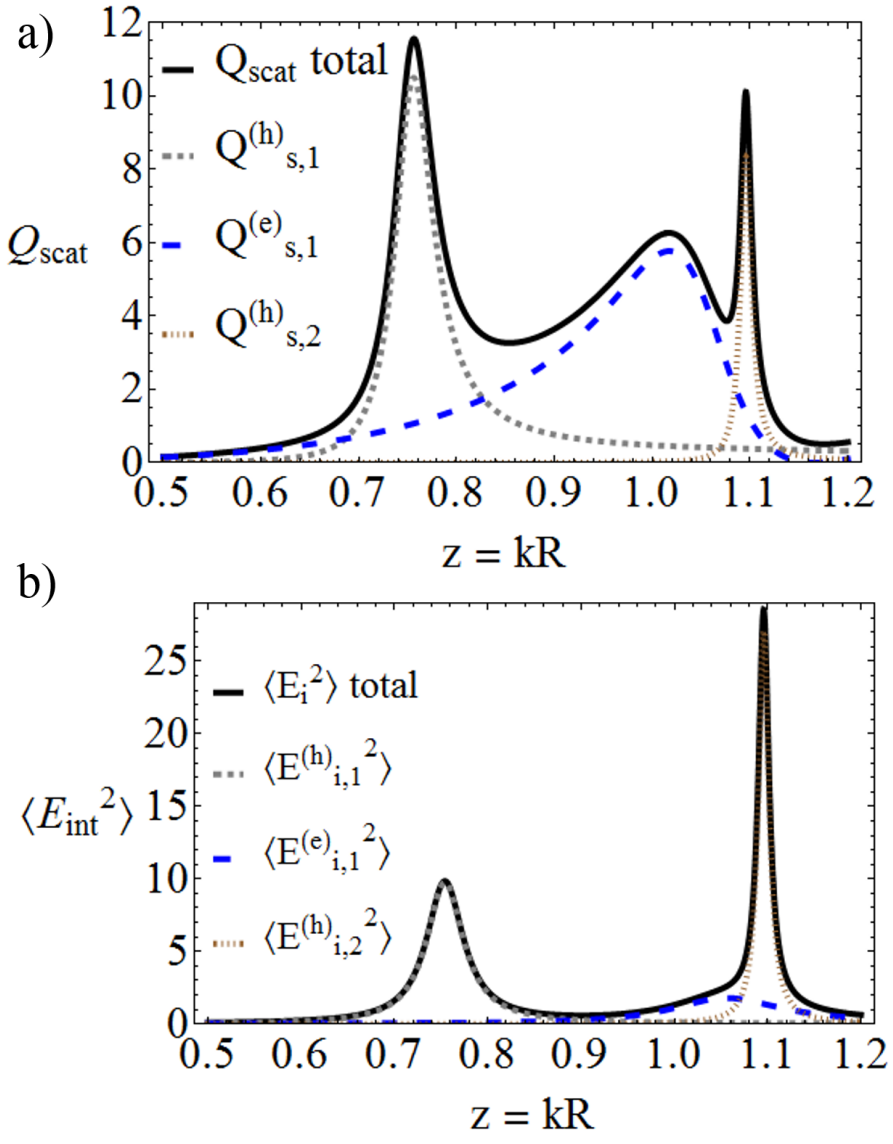

Figure 6.2: Plot of the scattering efficiency Q_{scat} and the average of the squared modulus of the internal field versus the size parameter $z = kR$ of a $\varepsilon = 16$ sphere

As was shown in Chapter 4, the total scattering efficiency can be obtained by summing up the contributions of each multipole that are related to the squared modulus of the Mie coefficients $|a_n|^2$ or $|b_n|^2$. On the other hand, the contribution of each multipole to $\langle|\mathbf{E}_{int}|^2\rangle$ can be shown to be related to $|\Omega_n^{(e,h)}|^2$ (see appendix D). This difference in the shape of resonances of the scattered field compared to those of the internal becomes even more obvious if one plots directly the evolution of $|a_n|^2$ or $|b_n|^2$ and $|\Omega_n^{(e,h)}|^2$ with regards to the size parameter z as was done in Fig. 6.3.

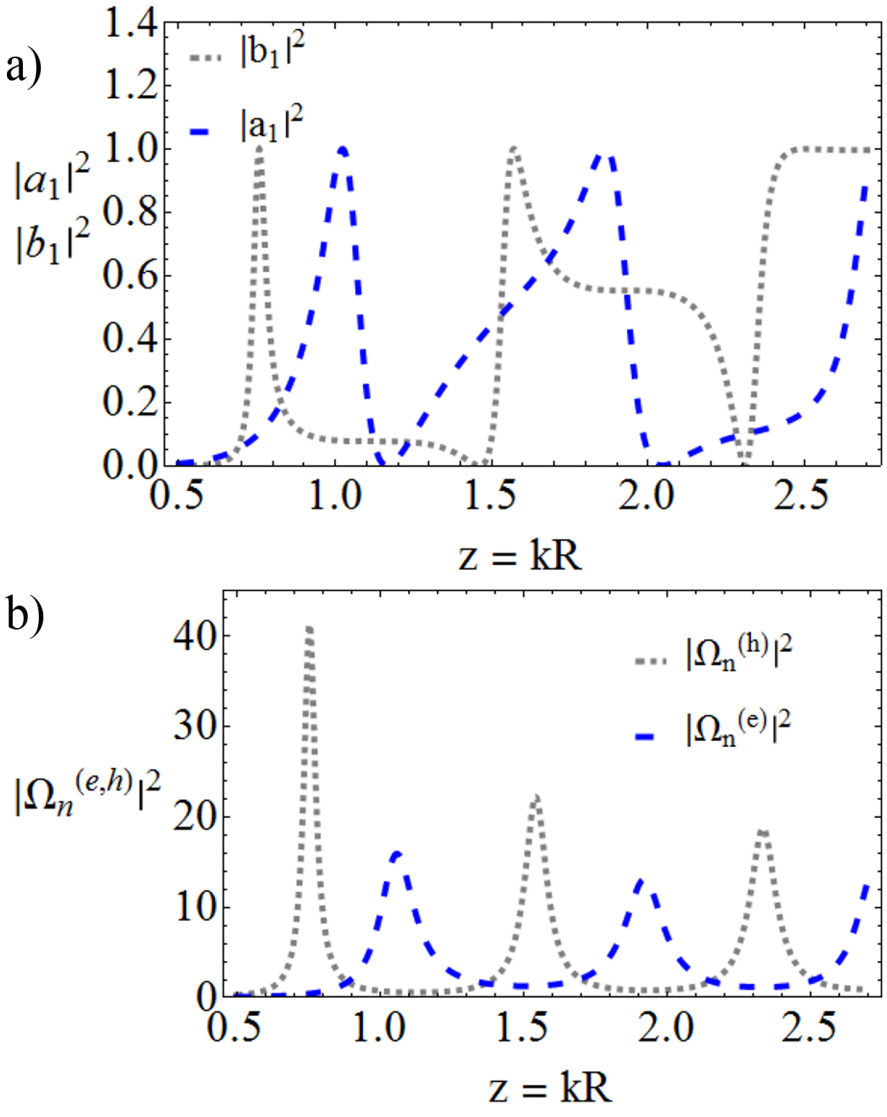

Figure 6.3: Plot of $|a_n|^2$ or $|b_n|^2$ and $|\Omega_n^{(e,h)}|^2$ versus the size parameter $z = kR$ of a $\varepsilon = 16$ sphere

More precisely, the resonances of the internal field are seen to have lorentzian shapes while the shape of the resonances of the scattered field are found to be asymmetric with zeros and peaks located close one to another. This asymmetric

shape of the resonances of high refractive index scatterers has already been observed for 2D scattering by high-refractive index cylinders [161, 162] as well as 3D scattering by Mie resonators [127]. They are usually explained to be Fano-type resonances, as they can be fitted by the Fano formula [163]. Fano found that this asymmetric shape originated from the interference of a sharp resonance with a continuum. It is always admitted that this explanation also holds for optical resonators. One can also point out that one of the consequences of this difference of shape between the internal and the scattered field resonances is that, for some carefully designed and lossless scatterers, the scattered field can vanish at frequencies where the internal field is not necessarily null. This phenomenon has recently attracted a lot of attention [148, 160, 164, 165] and is usually referred as anapole condition.

In the following section, we will use the pole expansions previously derived to explain the origin of this difference of shape between the resonances of the internal field compared to those of the scattered field.

6.3.2 Resonant and non-resonant contributions to the scattered field:

In this section, we shall apply the resonant-state expansions derived in Section 6.2 to understand the origin the apparent difference of the resonance shapes observed in the previous section. In this case, the T-matrix formalism may prove more appropriate. Pole expansions of the T and Ω matrix coefficients can easily be derived from those of the S and Ξ matrix coefficients by a simple use of the following relations:

$$\begin{aligned} T &= \frac{S-1}{2} \\ \Omega &= \frac{\Xi}{2} \end{aligned} \tag{6.30}$$

Consequently, the coefficients of the T and Ξ matrices admit the following expansions:

$$\begin{aligned} T_n^{(e)}(z) &= \frac{(-1)^{n+1}e^{-2iz}-1}{2} + (-1)^{n+1}e^{-2iz}\sum_{\alpha=1}^{\infty}\frac{iz\mathrm{Im}\left(r_{z,n,\alpha}^{(e)}\right)+\mathrm{Re}\left(r_{z,n,\alpha}^{(e)}.\,{p_{z,n,\alpha}^{(e)}}^{*}\right)}{z^2-\left|p_{z,n,\alpha}^{(e)}\right|^2-2iz\mathrm{Im}\left(p_{z,n,\alpha}^{(e)}\right)} \\ T_n^{(e)}(z) &= -\frac{1}{2}\left(1-(-1)^{n+1}e^{-2iz}\prod_{\alpha=1}^{\infty}\frac{z^2-\left|p_{z,n,\alpha}^{(e)}\right|^2+2iz\mathrm{Im}\left(p_{z,n,\alpha}^{(e)}\right)}{z^2-\left|p_{z,n,\alpha}^{(e)}\right|^2-2iz\mathrm{Im}\left(p_{z,n,\alpha}^{(e)}\right)}\right) \\ \Omega_n^{(e)}(z) &= (-1)^{n+1}\sum_{\alpha=1}^{\infty}\frac{iz\mathrm{Im}\left(r_{\Xi,z,n,\alpha}^{(e)}\right)+\mathrm{Re}\left(r_{\Xi,z,n,\alpha}^{(e)}.\,{p_{z,n,\alpha}^{(e)}}^{*}\right)}{z^2-\left|p_{z,n,\alpha}^{(e)}\right|^2-2iz\mathrm{Im}\left(p_{z,n,\alpha}^{(e)}\right)} \end{aligned} \tag{6.31}$$

And similar expansions can be derived for $T_n^{(h)}$ and $\Omega_n^{(h)}$ by replacing $(-1)^{n+1}$ by $(-1)^n$. Obviously, the frequencies of the modes need first to be determined. We will only present the calculations for the electric dipolar coefficients but the following derivations could easily be generalized to higher multipolar orders. For spherical scatterers, the poles of $T_1^{(e,h)}$, also the poles $\Omega_n^{(e,h)}$, can be determined by solving $D_1^{(e,h)} = 0$ as can be seen in (6.19). Since we only consider non-dispersive media here, the permittivity will be assumed constant over the complex frequency plane. However for dispersive media, it would have been necessary to define a function representing the analytic continuation of the permittivity in the complex plane. In a first approximation, Drude models or even Lorentz-Drude models can be used as an analytic continuation of the permittivity. More accurate models could even be employed but they should not violate the causality principle [166]. Assuming a constant permittivity $\varepsilon_s = 16$, we derived the roots of $D_1^{(e)} = 0$ that are represented in Fig. 6.4.

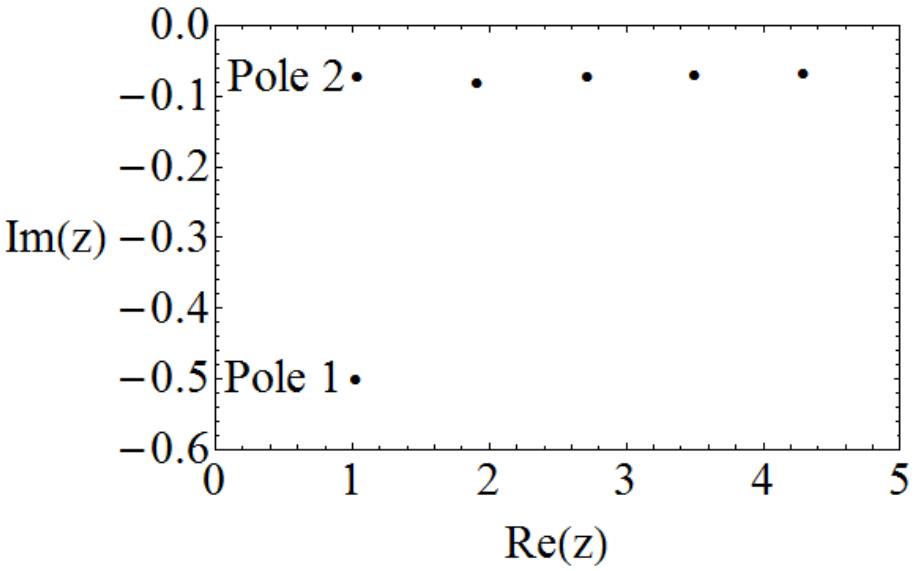

Figure 6.4: Position of the poles of $S_1^{(e)}$ of a $\varepsilon_s = 16$ sphere with regards to the $z = \frac{\omega}{c}R$

Using the multipolar expansion of the internal field, one can show that the average of the square of the electric field inside the scatterer has the following expression:

$$\frac{\langle |\mathbf{E}_{int}|^2 \rangle}{|\mathbf{E}_0|^2} = \sum_{n=1}^{\infty} \frac{\langle \left| E_{i,n}^{(e)} \right|^2 \rangle}{|\mathbf{E}_0|^2} + \frac{\langle \left| E_{i,n}^{(h)} \right|^2 \rangle}{|\mathbf{E}_0|^2} \tag{6.32}$$

where

$$\begin{aligned}\frac{\left\langle\left|E_{i,n}^{(e)}\right|^2\right\rangle}{|\mathbf{E}_0|^2} &= \frac{3(2n+1)}{2z^2} I_n \left|\Omega_n^{(e)}\right|^2 \\ \frac{\left\langle\left|E_{i,n}^{(h)}\right|^2\right\rangle}{|\mathbf{E}_0|^2} &= \frac{3(2n+1)}{2z^2} J_n \left|\Omega_n^{(h)}\right|^2\end{aligned} \tag{6.33}$$

The expressions of $I_n(\varepsilon_s, z)$ and $J_n(\varepsilon_s, z)$ are provided in Appendix D. We begin by comparing the exact calculation of $\left\langle\left|E_{i,n}^{(e)}\right|^2\right\rangle$ to its truncated pole expansion:

$$\frac{\left\langle\left|E_{i,n}^{(e)}\right|^2\right\rangle}{|\mathbf{E}_0|^2} = \frac{3(2n+1)}{2z^2} I_n \left| (-1)^{n+1} \sum_{\alpha=1}^{\alpha_{max}} \frac{iz\mathrm{Im}\left(r_{\Xi,z,n,\alpha}^{(e)}\right) + \mathrm{Re}\left(r_{\Xi,z,n,\alpha}^{(e)} \cdot p_{z,n,\alpha}^{(e)\,*}\right)}{z^2 - \left|p_{z,n,\alpha}^{(e)}\right|^2 - 2iz\mathrm{Im}\left(p_{z,n,\alpha}^{(e)}\right)} \right|^2 \tag{6.34}$$

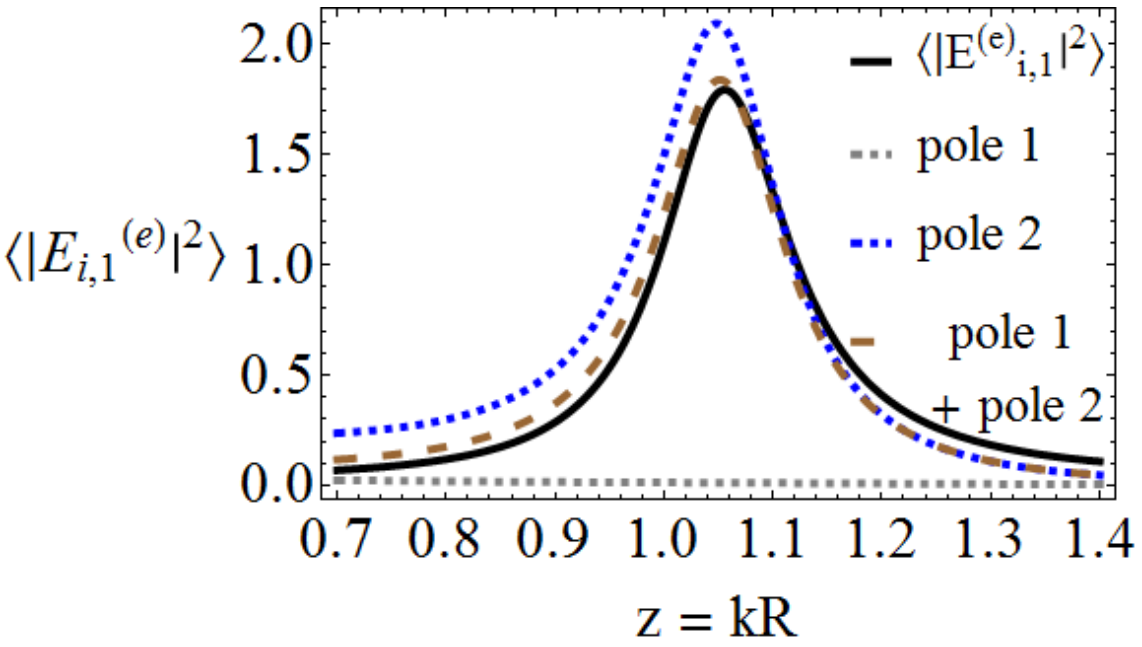

Figure 6.5: Comparison between exact calculations and pole expansions of $\left\langle\left|E_{i,n}^{(e)}\right|^2\right\rangle$

In Fig. 6.5, a comparison between the values of $\left\langle\left|E_{i,n}^{(e)}\right|^2\right\rangle$ predicted by exact calculations and using expression (6.34) is shown for a spherical scatterer with a relative permittivity $\varepsilon_s = 16$. We do not specify the radius R since we consider the size parameter $z = \frac{\omega}{c}R$ instead. It can be clearly observed that a good prediction of the first resonance of $\left\langle\left|E_{i,n}^{(e)}\right|^2\right\rangle$ is obtained when the first two terms in the pole expansion (6.34), corresponding to the poles 1 ($z_{1,1}^{(e)} = 1.0395 - i0.501$) and 2 ($z_{1,2}^{(e)} = 1.05274 - i0.07236$) in Fig. 6.4, are taken into account. The residues asso-

ciated with these poles are $r^{(e)}_{\Xi,z,1,1} = 0.323 - i0.0168$ and $r^{(e)}_{\Xi,z,1,2} = -0.597 - i0.218$. The internal field is consequently well described by a sum of resonant terms. This result can be seen as a consequence of the completeness of the Quasi-normal mode basis inside a scatterer that has already been demonstrated in [167].

We shall now repeat the study for the scattered field. Let us recall that the scattering efficiency, which corresponds to the scattering cross section normalized by the geometrical cross section of the scatterer, can be expressed in terms of the T-matrix coefficients:

$$Q_{scat} = \sum_{n=1}^{\infty} Q^{(e)}_{s,n} + Q^{(h)}_{s,n} \tag{6.35}$$

where

$$\begin{aligned} Q^{(e)}_{s,n} &= 2\frac{2n+1}{z^2}\left|T^{(e)}_n\right|^2 \\ Q^{(h)}_{s,n} &= 2\frac{2n+1}{z^2}\left|T^{(h)}_n\right|^2 \end{aligned} \tag{6.36}$$

Here again, we will focus on the electric dipolar term but a generalization to higher order multipoles is straightforward. The results provided by the two types of pole expansions of $T^{(e,h)}_n$ in Eqs (6.31) will be compared and in particular we will see what happens when the infinite product or infinite sum are truncated:

$$\begin{aligned} T^{(e)}_n(z) &= \frac{(-1)^{n+1}e^{-2iz}-1}{2} + (-1)^{n+1}e^{-2iz}\sum_{\alpha=1}^{\alpha_{\max}} \frac{iz\mathrm{Im}\left(r^{(e)}_{z,n,\alpha}\right) + \mathrm{Re}\left(r^{(e)}_{z,n,\alpha}.\ {p^{(e)}_{z,n,\alpha}}^*\right)}{z^2 - \left|p^{(e)}_{z,n,\alpha}\right|^2 - 2iz\mathrm{Im}\left(p^{(e)}_{z,n,\alpha}\right)} \\ T^{(e)}_n(z) &= -\frac{1}{2}\left(1 - (-1)^{n+1}e^{-2iz}\prod_{\alpha=1}^{\alpha_{\max}} \frac{z^2 - \left|p^{(e)}_{z,n,\alpha}\right|^2 + 2iz\mathrm{Im}\left(p^{(e)}_{z,n,\alpha}\right)}{z^2 - \left|p^{(e)}_{z,n,\alpha}\right|^2 - 2iz\mathrm{Im}\left(p^{(e)}_{z,n,\alpha}\right)}\right) \end{aligned} \tag{6.37}$$

In Fig. 6.6, such a comparison is again performed for the same $\varepsilon = 16$ spherical scatterer.

For the first resonance of $Q^{(e)}_{s,1}$, while the contributions from the first two poles (and from the corresponding zeros for the product form) are taken into account, we can clearly see that the two forms of pole expansions do not provide the same result. In fact, the infinite sum and product expansions of $T^{(e)}_n$ are mathematically equivalent as shown in section 6.2.2 and in [159]. However as soon as they are truncated the equivalence is lost and the product form seems to provide a better result while being truncated. Even though the sum form is not as accurate as the product form, it still predicts quite correctly the general trend of this first resonance. It can be assumed that it will be even more accurate when a larger number of poles is taken into account. It is furthermore much more convenient to use this sum form to provide an interpretation of this asymmetric shape of the resonances of $Q^{(e)}_{s,1}$.

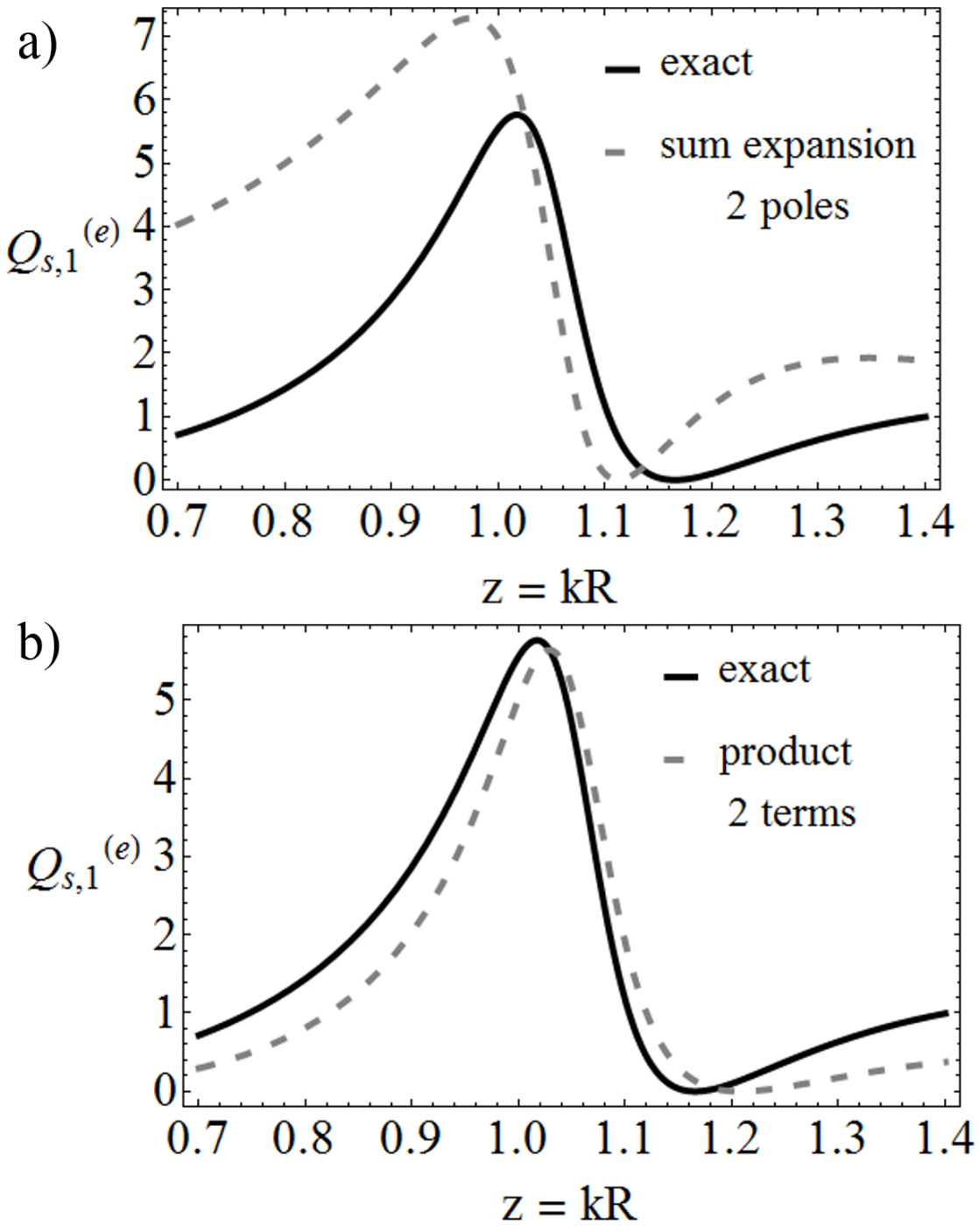

Figure 6.6: Comparison between exact calculations and a) the sum pole expansions of $Q_{s,1}^{(e)}$ b) the product pole expansion of $Q_{s,1}^{(e)}$ for a $\varepsilon = 16$ sphere

In fact, two types of contributions can be distinguished in expression (6.37). On the one hand, there is a non-resonant term : $\frac{(-1)^{n+1}e^{-2iz}-1}{2}$ that was not present for the internal field. In the Fano resonance picture, this term plays the role of the continuum. The origin of this term should be further investigated in the next section.

On the other hand, the resonant terms have of the form: $\frac{iz\mathrm{Im}\left(r^{(e)}_{z,n,\alpha}\right)+\mathrm{Re}\left(r^{(e)}_{z,n,\alpha}.{p^{(e)}_{z,n,\alpha}}^{*}\right)}{z^2-\left|p^{(e)}_{z,n,\alpha}\right|^2-2iz\mathrm{Im}\left(p^{(e)}_{z,n,\alpha}\right)}$ that also corresponds to the resonances of the internal field.

It clearly appears here that it is the superposition of these two types of responses that causes the asymmetric shape of the scattered field resonances. At the vicinity of a resonance of the internal field, there are conditions where the resonant and the non-resonant contributions to the scattered field are constructively interfering yielding a peak in the scattering cross section. On the other hand, there are also conditions where those contributions destructively interfere creating a dip in the cross-section spectrum.

As a consequence of this result, it now becomes clear that while the quasi-normal mode basis is complete when one tries to expand the internal field (as was already demonstrated in [167]), it is necessary to include an additional non-resonant contribution when considering the scattered field. So far, we have based our discussion on resonant expansion of the S and T matrices. In the following section, we will be discussing the possibility of using the field associated with the QNM as a basis.

6.4 QNM field and time-dependent scattering:

In their seminal paper [5], Sauvan et al. achieved to predict the Purcell Factor for a dipole located in the vicinity of a plasmonic resonator by using the fields associated with the QNM as a basis for the field radiated by the dipole:

$$\mathbf{E}\left(\mathbf{r},\omega\right)\approx\sum_{m=1}^{M}\alpha_m(\omega)\mathbf{E}_m(\mathbf{r}) \tag{6.38}$$

where $\mathbf{E}_m(\mathbf{r})$ are the fields associated with the QNM and M is the number of QNM necessary to accurately reproduce exact calculations. Even though it was clearly explained in this article that the validity of such an expansion had yet to be demonstrated, such an expansion clearly appeared to provide very accurate results. In short, in this section we will study the validity of such an expansion for the scattered field. As this expansion will be based on the S-matrix coefficient expansions derived in section 6.2.2, it will strictly be valid only for lossless scatterers.

6.4.1 Time-dependent scattering problem:

Leaving aside the "completeness" problem that was partially treated in the preceding section and may be further discussed in what follows, there is another striking problem appearing while considering expansion (6.38). As was already pointed out in the introduction, the fact that the QNM fields $\mathbf{E}_m(\mathbf{r})$ are exponentially diverging in the far-field region should proscribe such an expansion of the scattered field.

Fortunately, this issue has been known for a long time as it is well explained in [101, 168]. In the late nineteenth century, J.J. Thomson working on the interaction of an electromagnetic field with a perfectly conducting sphere found that it could be well described by introducing outgoing modes, that we would call now quasi-normal modes, associated with complex frequencies $\omega_n = \omega_{r,n} - i\omega_{i,n}$, $\omega_{i,n}$ being positive and representing the damping constant of these modes [169]. However, Lamb later noticed that since Thomson's modes were satisfying outgoing boundary conditions they should asymptotically behave like $\frac{1}{r}e^{-i\omega_n\left(t-\frac{r}{c}\right)}$[170]. Their complex frequency should then give rise to an exponential divergence, or as he put it an "exponential catastrophe". However, he also pointed out that the origin of this exponential divergence could be found in the wrong and hidden assumption that the modes had been existing since $t = -\infty$. In fact, if the mode is excited at a time t_0, causality imposes that after a time interval Δt it can only propagate over a distance $\Delta r = c\Delta t$. In other words, causality imposes that r and t are related one to another. That is why while considering the scattering problem in the time domain and clearly defining the initial condition of the problem, i.e. the time when the excitation field reaches the scatterer, one can avoid the "exponential catastrophe" and derive an expansion of the scattered field in terms of the QNM field. In the next section, we should present our derivations of an expansion of scattered field in terms of the fields associated with the QNM in the time domain. It is worth pointing out that QNM expansions were recently applied to describe the temporal dynamic of plasmonic resonators [171]. The study carried out in this article was however focused on the temporal response in the near field region of the optical resonators. Here, on the contrary, we will restrict our study to the far-field region in order to make calculations more tractable.

6.4.1.1 S-matrix description of the time-dependent scattering problem:

In the S-matrix picture of the scattering problem, causality is readily expressed as was seen in Section 6.2.1. That is why we will start by considering the time-dependent scattering problem by using the S-matrix formalism.

In the time domain, the incoming field is derived by a simple inverse Fourier transform of the incoming field in the harmonic domain:

$$\mathbf{E}_{\text{in}}(\mathbf{r},t) = \frac{1}{2\pi}\int_{-\infty}^{+\infty}\mathbf{E}_{\text{in}}(\mathbf{r},\omega)e^{-i\omega t}d\omega \tag{6.39}$$

Using the multipolar expansion of the incoming field, $\mathbf{E}_{\text{in}}(\mathbf{r},t)$ can be shown to be

equal to:

$$\mathbf{E}_{\text{in}}(\mathbf{r},t) = \frac{E_0}{2\pi}\int_{-\infty}^{+\infty}\left(\sum_{n=1}^{\infty}\sum_{m=-n}^{n} s_{n,m}^{(h,-)}(\omega)\mathbf{M}_{n,m}^{(-)}(k\mathbf{r}) + s_{n,m}^{(e,-)}(\omega)\mathbf{N}_{n,m}^{(-)}(k\mathbf{r})\right)e^{-i\omega t}d\omega \tag{6.40}$$

where $k = \frac{\omega}{c}$. Let us consider only one term in the previous sum:

$$\mathbf{E}_{\text{in},n,m}^{(e)}(\mathbf{r},t) = \frac{E_0}{2\pi}\int_{-\infty}^{+\infty} s_{n,m}^{(e,-)}(\omega)\mathbf{N}_{n,m}^{(-)}(k\mathbf{r})e^{-i\omega t}d\omega. \tag{6.41}$$

The derivation of this integral is not trivial in the general case. However, in the far-field region this expression simplifies as already pointed out in section 6.2:

$$\lim_{r\to\infty}\mathbf{E}_{\text{in},n,m}^{(e)}(\mathbf{r},t) = i^n\frac{E_0}{2\pi r}\mathbf{Z}_{n,m}(\theta,\phi)\int_{-\infty}^{+\infty} A_{n,m}^{(e,-)}(\omega)e^{-i\omega\left(t+\frac{r}{c}\right)}d\omega \tag{6.42}$$

where we have introduced $A_{n,m}^{(e,-)}(\omega) = \frac{s_{n,m}^{(e,-)}(\omega)}{k}$. By use of the convolution theorem, one could even show that $\lim_{r\to\infty}\mathbf{E}_{\text{in},n,m}^{(e)}(\mathbf{r},t) \propto A_{n,m}^{(e,-)}(t) * \delta\left(t+\frac{r}{c}\right)\mathbf{Z}_{n,m}(\theta,\phi)$ where $A_{n,m}^{(e,-)}(t)$ is the inverse Fourier transform of $A_{n,m}^{(e,-)}(\omega)$. This just means that $\mathbf{E}_{\text{in},n,m}^{(e)}(\mathbf{r},t)$ is an incoming wave with a temporal envelope $A_{n,m}^{(e,-)}(t)$. Repeating what was already done in section 6.2, for a point $\mathbf{r}_0$ a time t_0 can be defined such that the incoming field vanishes at $\mathbf{r}_0$ for $t < t_0$. Eq. (6.42) can consequently be rewritten in the following way:

$$\mathbf{E}_{\text{in},n,m}^{(e)}(\mathbf{r}_0,t) \approx H(t-t_0)i^n\frac{E_0}{2\pi r_0}\mathbf{Z}_{n,m}(\theta,\phi)\int_{-\infty}^{\infty} A_{n,m}^{(e,-)}(\omega)e^{-i\omega\left(t_0+\frac{r_0}{c}\right)}e^{-i\omega(t-t_0)}d\omega \tag{6.43}$$

Given this definition of the incoming field, we will try to determine the outgoing field at the point $\mathbf{r}$ also located in the far-field area. It can be determined by this inverse Fourier transform:

$$\begin{aligned}\mathbf{E}_{\text{out},n,m}^{(e)}(\mathbf{r},t) \approx (-i)^n\frac{E_0}{2\pi r}\mathbf{Z}_{n,m}(\theta,\phi)\times \\ \int_{-\infty}^{\infty} e^{i2\omega\frac{R}{c}}S_n^{(e)}(\omega)A_{n,m}^{(e,-)}(\omega)e^{-i\omega\left(t_0+\frac{r_0}{c}\right)}e^{-i\omega\left(t-t_0-\frac{r_0}{c}-\frac{r}{c}+2\frac{R}{c}\right)}d\omega\end{aligned} \tag{6.44}$$

where we have used the initial conditions on the incoming field. We can now intro-

duce the pole expansion of $S_n^{(e)}$ provided in Eq. (6.15):

$$\begin{aligned}&\mathbf{E}^{(e)}_{\text{out},n,m}(\mathbf{r},t) \approx (-1)^{n+1}(-i)^n \frac{E_0}{2\pi r}\mathbf{Z}_{n,m}(\theta,\phi)\times \\ &\left(\int_{-\infty}^{\infty} A^{(e,-)}_{n,m}(\omega) e^{-i\omega\left(t_0+\frac{r_0}{c}\right)} e^{-i\omega\left(t-t_0-\frac{r_0}{c}-\frac{r}{c}+2\frac{R}{c}\right)} d\omega + \right. \\ &\left. \int_{-\infty}^{\infty} \sum_{\alpha=-\infty}^{\infty} \frac{r^{(e)}_{n,\alpha}}{\omega - p^{(e)}_{n,\alpha}} A^{(e,-)}_{n,m}(\omega) e^{-i\omega\left(t_0+\frac{r_0}{c}\right)} e^{-i\omega\left(t-t_0-\frac{r_0}{c}-\frac{r}{c}+2\frac{R}{c}\right)} d\omega \right)\end{aligned} \tag{6.45}$$

The first integral corresponds to the non-resonant response. By applying again the convolution theorem, it can be shown to be proportional to $A^{(e,-)}_{n,m}(t) * \delta\left(t - \frac{r}{c} + \frac{2R}{c}\right)$ which is obviously an outgoing wave with a time advance of $\frac{2R}{c}$ and with the same temporal envelope $A^{(e,-)}_{n,m}(t)$ as the incoming wave. This non resonant response can consequently be seen as a "reflection" of the incoming wave by the surface of the scatterer.

On the other hand, in Eq. (6.45), there is also a resonant part of the response which is associated with each resonant term of the S-matrix. Again this resonant part of the scattered field can be assumed to be a convolution between the temporal envelope of the incoming field $A^{(e,-)}_{n,m}(t)$ and a function describing the temporal response associated with the resonance $p^{(e)}_{n,\alpha}$ that is given by:

$$\frac{1}{2\pi}\int_{-\infty}^{\infty} \frac{r^{(e)}_{n,\alpha}}{\omega - p^{(e)}_{n,\alpha}} e^{-i\omega\left(t_0+\frac{r_0}{c}\right)} e^{-i\omega\left(t-t_0-\frac{r_0}{c}-\frac{r}{c}+2\frac{R}{c}\right)} d\omega \tag{6.46}$$

Detailed calculations for the derivation of this integral are provided in appendix D. In summary, this integral can be calculated by means of the residues theorem. When $t - t_0 - \frac{r_0}{c} - \frac{r}{c} + 2\frac{R}{c} \geq 0$, it can be derived by closing the contour of integration in the lower half of the complex plane as shown in Fig. 6.7 leading to:

$$\begin{aligned}&\int_{-\infty}^{\infty} \frac{r^{(e)}_{n,\alpha}}{\omega - p^{(e)}_{n,\alpha}} e^{-i\omega\left(t_0+\frac{r_0}{c}\right)} e^{-i\omega\left(t-t_0-2\frac{r_0-R}{c}\right)} d\omega = \\ &-2\pi.i.r^{(e)}_{n,\alpha} e^{-ip^{(e)}_{n,\alpha}\left(t_0+\frac{r_0}{c}\right)} e^{-ip^{(e)}_{n,\alpha}\left(t-t_0-\frac{r_0}{c}-\frac{r}{c}+2\frac{R}{c}\right)} \\ &-\lim_{R_C\to\infty}\int_0^{-\pi} \frac{r^{(e)}_{n,\alpha}}{R_C e^{i\theta_C} - p^{(e)}_{n,\alpha}} e^{-iR_C e^{i\theta_C}\left(t_0+\frac{r_0}{c}\right)} e^{-iR_C e^{i\theta_C}\left(t-t_0-\frac{r_0}{c}-\frac{r}{c}+2\frac{R}{c}\right)} R_C e^{i\theta_C} d\theta_C\end{aligned} \tag{6.47}$$

The second term which is an integral over the semi-circle in the lower part of the complex plane can be shown to vanish for $t - t_0 - \frac{r_0}{c} - \frac{r}{c} + 2\frac{R}{c} \geq 0$ (see detailed calculations in appendix D). Consequently only the first term remains. This term is in fact proportional to the field created by the Quasi-Normal Mode associated with the frequency $p^{(e)}_{n,\alpha}$

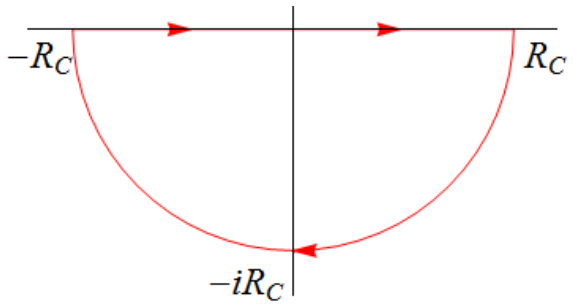

Figure 6.7: Contour used to derive integral 6.46

On the other hand when $t - t_0 - \frac{r_0}{c} - \frac{r}{c} + 2\frac{R}{c} < 0$, the integral in (6.46) can be derived by closing the contour in the upper half of the complex plane. There is no pole in the upper half of the complex plane, consequently this integral is null (see appendix D). In summary, this integral has been shown to be equal to:

$$\begin{aligned}
&\text{For } t \geq t_0 + \frac{r_0}{c} + \frac{r}{c} - 2\frac{R}{c} \\
&\int_{-\infty}^{\infty} \frac{r_{n,\alpha}^{(e)}}{\omega - p_{n,\alpha}^{(e)}} e^{-i\omega\left(t_0 + \frac{r_0}{c}\right)} e^{-i\omega\left(t - t_0 - \frac{r_0}{c} - \frac{r}{c} + 2\frac{R}{c}\right)} d\omega = -2\pi.i.r_{n,\alpha}^{(e)} e^{-ip_{n,\alpha}^{(e)}\left(t - \frac{r}{c} + 2\frac{R}{c}\right)} \\
&\text{For } t < t_0 + \frac{r_0}{c} + \frac{r}{c} - 2\frac{R}{c} \\
&\int_{-\infty}^{\infty} \frac{r_{n,\alpha}^{(e)}}{\omega - p_{n,\alpha}^{(e)}} e^{-i\omega\left(t_0 + \frac{r_0}{c}\right)} e^{-i\omega\left(t - t_0 - \frac{r_0}{c} - \frac{r}{c} + 2\frac{R}{c}\right)} d\omega = 0
\end{aligned} \tag{6.48}$$

The result obtained by rigorously deriving the integral in Eq. (6.47) also appears to be in perfect agreement with causality discussions of section 6.2. We should emphasize that $t \geq t_0 + \frac{r_0}{c} + \frac{r}{c} - 2\frac{R}{c}$ implies that $t - \frac{r}{c} + 2\frac{R}{c} \geq t_0 + \frac{r_0}{c} \geq 0$. It then follows that $|e^{-ip_{n,\alpha}^{(e)}\left(t - \frac{r}{c} + 2\frac{R}{c}\right)}| \leq 1$. That is why there is not any divergence of the field associated with the QNM when causality is taken into account. We can also point out that $t \geq t_0 + \frac{r_0}{c} + \frac{r}{c} - 2\frac{R}{c}$ is equivalent to $r \leq c\,(t - t_0) - r_0 + 2R$, meaning that at a given time t, the outgoing field has only been able to reach at best the position $r = c\,(t - t_0) - r_0 + 2R$. The requirement that $-(p_{n,\alpha}^{(e)})^*$ should also be a pole of the S-matrix implies that the actual field corresponds to the real part of the preceding equation.

To sum up, we have shown that Eq. (6.45), which represents the outgoing field produced by the interaction of the scatterer with the incoming field of Eq. (6.43),

was equal to:

$$\begin{aligned}\mathbf{E}^{(e)}_{\text{out},n,m}(\mathbf{r},t) \approx H\left(t-t_0-\frac{r_0}{c}-\frac{r}{c}+2\frac{R}{c}\right)(-1)^{n+1}(-i)^n\frac{E_0}{r}\mathbf{Z}_{n,m}(\theta,\phi)\\ A^{(e,-)}_{n,m}(t) * \left(\delta\left(t-\frac{r}{c}+\frac{2R}{c}\right)-i\sum_{\alpha=-\infty}^{\infty} r^{(e)}_{n,\alpha}e^{-ip^{(e)}_{n,\alpha}\left(t-\frac{r}{c}+2\frac{R}{c}\right)}\right)\end{aligned} \tag{6.49}$$

The Heaviside function has been introduced to show that this expression is only valid when $t-t_0-\frac{r_0}{c}-\frac{r}{c}+2\frac{R}{c}\geq 0$ and null for $t-t_0-\frac{r_0}{c}-\frac{r}{c}+2\frac{R}{c}<0$ as was shown in Eq. (6.48). It can then be concluded that the outgoing field associated with each multipole $\mathbf{E}^{(e)}_{\text{out},n,m}(\mathbf{r},t)$ is the convolution of the temporal envelope of the incoming field with two types of responses. The first type of response is the non-resonant response that can be seen as a reflection by the surface of the scatterer and the second one is the resonant contributions associated with eigen-frequencies $p^{(e)}_{n,\alpha}$ that are exponentially decreasing. Finally, the total outgoing field can be obtained by summing the contributions of all multipoles.

6.4.1.2 Scattered field expansion:

Now that the outgoing field expansion has been derived, it is relatively easy to derive the scattered field expansion. In fact, the excitation field being regular it is a superposition of incoming and outgoing waves as was pointed out in Chapter 3. Consequently, in order to derive the scattered field, one only needs to subtract the outgoing part of the excitation field to the outgoing field given in Eq. (6.49). The scattered field associated with each multipole $\mathbf{E}^{(e)}_{\text{scat},n,m}(\mathbf{r},t)$ can be expressed in the following way:

$$\begin{aligned}\mathbf{E}^{(e)}_{\text{scat},n,m}(\mathbf{r},t) \approx & H\left(t-t_0-\frac{r_0}{c}-\frac{r}{c}+2\frac{R}{c}\right)A^{(e,-)}_{n,m}(t)*\\ & \left(\mathbf{E}^{(e,\text{nr})}_{\text{scat},n,m}(\mathbf{r},t)+\sum_{\alpha=-\infty}^{\infty}(-i)r^{(e)}_{n,\alpha}\mathbf{E}^{(e,\text{res})}_{\text{scat},n,m,\alpha}(\mathbf{r},t)\right)\end{aligned} \tag{6.50}$$

where we have introduced $\mathbf{E}^{(e,\text{nr})}_{\text{scat},n,m}(\mathbf{r},t)$ and $\mathbf{E}^{(e,\text{res})}_{\text{scat},n,m,\alpha}(\mathbf{r},t)$ that are respectively the non-resonant and the resonant parts of the scattered field and can be expressed as follows:

$$\begin{aligned}\mathbf{E}^{(e,\text{nr})}_{\text{scat},n,m}(\mathbf{r},t) &= (-i)^n\frac{E_0}{r}\left((-1)^{n+1}\delta\left(t-\frac{r}{c}+\frac{2R}{c}\right)-\delta\left(t-\frac{r}{c}\right)\right)\mathbf{Z}_{n,m}(\theta,\phi)\\ \mathbf{E}^{(e,\text{res})}_{\text{scat},n,m,\alpha}(\mathbf{r},t) &= (-1)^{n+1}(-i)^n\frac{E_0}{r}e^{-ip^{(e)}_{n,\alpha}\left(t-\frac{r}{c}+2\frac{R}{c}\right)}\mathbf{Z}_{n,m}(\theta,\phi)\end{aligned} \tag{6.51}$$

Similar calculations would allow us to show that:

$$\begin{aligned}\mathbf{E}^{(h,\mathrm{nr})}_{\mathrm{scat},n,m}(\mathbf{r},t) &= (-i)^{n+1}\frac{E_0}{r}\left((-1)^n\delta\left(t-\frac{r}{c}+\frac{2R}{c}\right)-\delta\left(t-\frac{r}{c}\right)\right)\mathbf{X}_{n,m}(\theta,\phi)\\ \mathbf{E}^{(h,\mathrm{res})}_{\mathrm{scat},n,m,\alpha}(\mathbf{r},t) &= (-1)^n(-i)^{n+1}\frac{E_0}{r}e^{-ip^{(h)}_{n,\alpha}\left(t-\frac{r}{c}+2\frac{R}{c}\right)}\mathbf{X}_{n,m}(\theta,\phi)\end{aligned} \tag{6.52}$$

To conclude this section, we have shown that in the far-field region the expansion of the scattered field in terms of the quasi normal mode of the scatterer should take the following form:

$$\begin{aligned}\mathbf{E}_{\mathrm{scat}}(\mathbf{r},t) =& H\left(t-t_0-\frac{r_0}{c}-\frac{r}{c}+2\frac{R}{c}\right)\\ &\left(\mathbf{E}_{\mathrm{scat,nr}}(\mathbf{r},t)+\sum_{u=1}^{\infty}(-i)r_u\mathbf{E}_{\mathrm{scat,res},u}(\mathbf{r},t)\right)\end{aligned} \tag{6.53}$$

where

$$\mathbf{E}_{\mathrm{scat,nr}}(\mathbf{r},t)=\sum_{n=1}^{\infty}\sum_{m=-n}^{n}A^{(e,-)}_{n,m}(t)*\mathbf{E}^{(e,\mathrm{nr})}_{\mathrm{scat},n,m}(\mathbf{r},t)+A^{(h,-)}_{n,m}(t)*\mathbf{E}^{(h,\mathrm{nr})}_{\mathrm{scat},n,m}(\mathbf{r},t) \tag{6.54}$$

and we have introduced the sum over u to avoid writing the following triple summation

$$\begin{aligned}\sum_{u=1}^{\infty}(-i)r_u\mathbf{E}_{\mathrm{scat,res},u}(\mathbf{r},t) = \sum_{n=1}^{\infty}\sum_{m=-n}^{n}\sum_{\alpha=-\infty}^{\infty}&(-i)r^{(e)}_{n,\alpha}A^{(e,-)}_{n,m}(t)*\mathbf{E}^{(e,\mathrm{res})}_{\mathrm{scat},n,m,\alpha}(\mathbf{r},t)\\ &+(-i)r^{(h)}_{n,\alpha}A^{(h,-)}_{n,m}(t)*\mathbf{E}^{(h,\mathrm{res})}_{\mathrm{scat},n,m,\alpha}(\mathbf{r},t)\end{aligned} \tag{6.55}$$

6.4.2 Outlooks:

First, the pole expansions of the S matrix presented here were only restricted to dispersionless media. A generalization to dispersive media would nonetheless be possible. In this case, a function representing an analytic continuation of the permittivity in the complex plane would have to be employed. Moreover, the unitary condition of the S-matrix (6.8) would not be valid anymore. The pole expansion of the S-matrix would also be modified in order to account for dispersion 6.15.
Regarding the scattering problem in the time domain, we have had to restrict our study to the far-field region in order to make more tractable the derivations of the expansions of the scattered field in terms of quasi-normal mode. The next step would be to prove that these expansions are valid everywhere, even in the near-field region. It will also be interesting to derive the expansion of the internal field [167]. It should also be pointed out that the results obtained for spherical scatterers could certainly be generalized to arbitrary-shaped scatterers. In fact, the S-matrix of non spherical scatterers can also be computed by coupling numerical methods with

multipolar expansions. Since the pole expansion of the S-matrix coefficients were derived by using causality and energy conservation considerations, they should stay valid for nonspherical scatterers.
More generally, we believe that the theory of the quasi-normal modes could certainly be clarified by studying more thoroughly the pole expansions of the S-matrix coefficients.
Finally, this theory could also provide a theoretical ground to the phenolomenogical models of the temporal coupled mode theory.

6.5 Conclusion:

In summary, the first part of this chapter was devoted to the derivation of pole expansions of the S and Ξ matrix coefficients. These pole expansions are only valid for dispersionless media but could be generalized to dispersive media. While the Ξ matrix coefficients could be cast as a sum of lorentzian terms, in the case of the S matrix coefficients, the introduction of an additional non-resonant term was necessary.
This difference was then demonstrated to be the origin of the different shapes between the internal and scattered field resonances. In particular, it was shown that the asymmetric or Fano-type shape of the resonances of the scattered field could be explained by an interference of the non-resonant and the resonant responses of the scatterer.
Finally, the QNM fields were introduced and were shown to be an appropriate basis for the scattered field only in the time domain. In particular, we could establish that the divergence of the QNM fields could be avoided by taking causality into account.

Chapter 7

Four-wave mixing in Mie resonators:

Summary: In the previous chapters, the resonant interaction of light with subwavelength silicon spheres was studied. In particular, it was shown that the excitation of this resonant response came with an enhancement of the field inside these resonators. A similar resonant behavior can be observed in the optical response of subwavelength silicon nanodisks. This field enhancement can in turn be used to enhance nonlinear effects. Here, we will experimentally study the possibility of taking advantage of the field enhancement associated with two resonances to enhance degenerate four-wave mixing.

7.1 Introduction:

Due to their ability to confine and control light at the nanoscale, nanoresonators have long been considered as promising structures to enhance intensity-dependent effects. Nonlinear optical phenomena could in particular greatly benefit from the light concentration created by resonant nanostructures. Plasmonic nanoparticles were first considered to enhance nonlinear effects [7, 172]. In particular, second harmonic generation has been observed from gold nanoparticles whereas second-order nonlinear effects are usually inhibited from bulk gold as it is a centrosymmetric material. Second-harmonic generation is actually allowed in gold nanoparticles since the inversion symmetry is broken at their surface or by the excitation of higher order responses than simple dipole electric resonances [60, 173–175]. The third-harmonic generation [176, 177] and four-wave mixing [178] from single plasmonic nanoparticles as well as ensembles of nanoparticles have also been investigated.
Following the pionneering work [56] where third-harmonic generation by silicon nanodisks was studied, high-refractive index resonators are now being considered as a promising alternative to plasmonic nanoresonators for enhancing non-linear effects. Several reasons have motivated the study of the nonlinear response of Mie

resonators.
First, high-refractive index materials usually suffer from less losses than plasmonic materials in the visible and near infrared regions. Secondly, the excitation of Mie resonances in high-refractive index scatterers, especially magnetic-type Mie resonances as can be seen from Fig. 6.3 in Chapter 6, can lead to reasonably large electric field enhancements inside these resonators. Unlike plasmonic resonators for which field enhancements are usually restricted to the surface of the scatterers, field enhancements in Mie resonators are usually sustained over larger effective mode volumes and are mostly occurring inside the resonators. As, on top of that, materials used to fabricate Mie resonators such as silicon and germanium usually have quite large third-order optical susceptibilities [179–181], a large nonlinear response can be expected at the vicinity of their resonances. This was confirmed by the measurement of large third harmonic generation inside single silicon nanodisks [56, 182] as well as germanium single resonators [181, 183]. Oligomers, i.e. ensemble of coupled resonators, have been considered to further enhance nonlinearities [57, 58]. The third harmonic generation of metasurfaces and arrays of closely spaced resonators proved to be largely enhanced too [56, 59].

In addition, it is worth pointing out that an enhancement of the second harmonic generation at the magnetic resonance of AlGaAs nanodisks and GaAs nanopillars has been predicted and observed [62, 63, 184–186].

Finally, in addition to allow for an enhancement of nonlinear effects by creating resonant field enhancements, high refractive index scatterers offer the unique possibility of shaping the radiation pattern of the nonlinear field. For linear light-scattering, the interference between electric and magnetic type responses of Mie scatterers already proved to allow for the control of the scattered field radiation pattern. In particular, the interference between the field radiated by electric and magnetic dipoles [37, 38] has been shown to result in directive scattering either in the backward or in the forward direction. This phenomenon is usually called the Kerker effect [36]. This effect has also been generalized to higher order mulitpoles [42, 43]. This property of linear scattering can actually be used in nonlinear scattering. It was in particular demonstrated that the radiation pattern of the third harmonic generation could also be tailored [60, 61] for a dimer of silicon nanodisks. In addition, it has been shown that it was theoretically possible to control the shape of second harmonic generation from an AlGaAs dielectric nanoantenna [64].

Four-wave mixing was recently studied in germanium nanodisks [187] but in this chapter we shall be concerned with the experimental study of degenerate four-wave mixing inside silicon nanodisks that was. For that purpose, the nanodisk will be illuminated by laser radiations at two different wavelengths λ_1 and λ_2. In particular, we will study the four-wave mixing signal obtained when the two pump wavelengths λ_1 and λ_2 are close to two resonances of a silicon nanodisk. But let us start by

introducing the theoretical framework of non-linear optics.

7.2 Non-linear optics:

In all the previous chapters, only linear light-scattering by high-refractive index nanospheres was considered. The interaction between light and matter was consequently assumed to be fully described by introducing an induced polarization $P(t)$ with a linear relationship with the electric field. For homogeneous, isotropic, local, dispersionless media, this linear relationship reads as follows:

$$P(t) = \epsilon_0 \chi^{(1)} E(t) \tag{7.1}$$

$\chi^{(1)}$ being the linear susceptibility of the medium. This assumption is completely valid when the amplitude of the applied field $E(t)$ is reasonably low. However, as soon as the amplitude increases, it becomes necessary to take into account the non-linear response of the medium. In this case, the polarization (7.1) can be generalized by expressing $P(t)$ as a power series expansion in terms of the electric field amplitude [188]:

$$P(t) = \epsilon_0 \left(\chi^{(1)} E(t) + \chi^{(2)} E(t)^2 + \chi^{(3)} E(t)^3 + ... \right) \tag{7.2}$$

where $\chi^{(2)}$ and $\chi^{(3)}$ are the second order and third order susceptibilities. For simplifying the notations, P(t) and E(t) were taken to be scalar quantities. However, in practice these quantities are vectors and the nonlinear susceptibilities are consequently tensors, $\chi^{(2)}$ being a third-rank tensor and $\chi^{(3)}$ being a fourth-rank tensor. The symmetry constraints on the elements of these tensors shall be discussed in the next section.
As the amplitude of the field increases, a second-order nonlinear response from the material is consequently expected to appear. However, second-order nonlinear effects are inhibited in centrosymmetric media [188]. As a consequence, no second-order nonlinear response can be observed from either amorphous or crystalline silicon that both verify inversion symmetry. That is why we will only be considering the third-order nonlinear responses that do not suffer from the same symmetry restrictions as second order processes. The nonlinear polarization will consequently read as follows:

$$P_{\mathrm{NL}}(t) = \chi^{(3)} E(t)^3 \tag{7.3}$$

In the most general case of an applied field with three different frequency components:

$$E(t) = E_1 e^{-i\omega_1 t} + E_2 e^{-i\omega_2 t} + E_3 e^{-i\omega_3 t} + c.c. \tag{7.4}$$

the non-linear polarization would contain 44 different frequency components [188]:

$$P_{\mathrm{NL}}(t) = \sum_n P(\omega_n) e^{-i\omega_n t} \tag{7.5}$$

In our particular experiment however, we will be considering an applied field with only two frequency components ω_1 and ω_2. The principal frequency components of the non-linear polarization will consequently be:

$$\begin{aligned}
P(3\omega_1) &= \epsilon_0 \chi^{(3)} \left(E_1^3 e^{-i3\omega_1 t} + c.c. \right) \\
P(3\omega_2) &= \epsilon_0 \chi^{(3)} \left(E_2^3 e^{-i3\omega_2 t} + c.c. \right) \\
P(\omega_1) &= \epsilon_0 \chi^{(3)} \left(\left(6E_2^* E_2 E_1 + 3E_1^2 E_1^* \right) e^{-i\omega_1 t} + c.c. \right) \\
P(\omega_2) &= \epsilon_0 \chi^{(3)} \left(6E_1^* E_1 E_2 + 3E_2^2 E_2^* e^{-i\omega_2 t} + c.c. \right) \\
P(2\omega_1 + \omega_2) &= \epsilon_0 \chi^{(3)} \left(3E_1^2 E_2 e^{-i(2\omega_1 + \omega_2)t} + c.c. \right) \\
P(2\omega_2 + \omega_1) &= \epsilon_0 \chi^{(3)} \left(3E_2^2 E_1 e^{-i(2\omega_2 + \omega_1)t} + c.c. \right) \\
P(2\omega_1 - \omega_2) &= \epsilon_0 \chi^{(3)} \left(3E_1^2 E_2^* e^{-i(2\omega_1 - \omega_2)t} + c.c. \right) \\
P(2\omega_2 - \omega_1) &= \epsilon_0 \chi^{(3)} \left(3E_2^2 E_1^* e^{-i(2\omega_2 - \omega_1)t} + c.c. \right)
\end{aligned} \tag{7.6}$$

Here, we should mainly be interested in the processes of four-wave mixing, that correspond to the four last terms in (7.6).

7.2.1 Symmetries and tensor components of the third order susceptibility:

Even though, for the sake of simplicity, we have been considering $P(t)$ and $E(t)$ as scalar quantities so far, these quantities are actually vectors. The third-order susceptibility is consequently a fourth-rank tensor. That means in practice that it should normally be described by 81 separate elements $\chi^{(3)}_{ijkl}$, i j k and l being the indices associated with each component [188]. However, the number of independent elements can be drastically reduced when the symmetries of the system are considered. As will be discussed in the experimental section, the silicon nanodisks will be fabricated from a thin film of amorphous silicon. We will consequently determine here the form of the third-order susceptibility tensor of amorphous silicon.

One can start by making use of the spatial symmetry of the medium to establish the relationship between the different elements of the tensor. Amorphous silicon being an isotropic medium, all the coordinate axes should be equivalent. As a consequence, the tensor elements should remain unchanged by a change of coordinate axis. That leads to the following symmetry properties [188]:

$$\chi^{(3)}_{1111} = \chi^{(3)}_{2222} = \chi^{(3)}_{3333} \tag{7.7}$$
$$\chi^{(3)}_{1122} = \chi^{(3)}_{1133} = \chi^{(3)}_{2211} = \chi^{(3)}_{2233} = \chi^{(3)}_{3311} = \chi^{(3)}_{3322} \tag{7.8}$$
$$\chi^{(3)}_{1212} = \chi^{(3)}_{1313} = \chi^{(3)}_{2323} = \chi^{(3)}_{2121} = \chi^{(3)}_{3131} = \chi^{(3)}_{3232} \tag{7.9}$$
$$\chi^{(3)}_{1221} = \chi^{(3)}_{1331} = \chi^{(3)}_{2112} = \chi^{(3)}_{2332} = \chi^{(3)}_{3113} = \chi^{(3)}_{3223} \tag{7.10}$$

All the other tensor-elements, different from those listed above, should vanish [188]. Finally, one can also show that the following relation holds between the 4 types of tensor elements listed above:

$$\chi^{(3)}_{1111} = \chi^{(3)}_{1122} + \chi^{(3)}_{1212} + \chi^{(3)}_{1221} \tag{7.11}$$

The problem of determining a fourth-rank tensor comprising 81 different elements has then been reduced by means of symmetry considerations to the determination of the 3 linearly independent tensor components out of the tensor components in Eq. 7.10. Here, we consider the process of degenerate four-wave mixing. In what follows, we will measure the signal at the frequency $\omega_s = 2\omega_I - \omega_{II}$ obtained when illuminating the nanodisk with two pumps at the wavelengths ω_I and ω_{II}. In this case, ω_I appears twice in the arguments of the susceptibility $\chi_{ijkl}(\omega_s = 2\omega_I - \omega_{II}, \omega_I, \omega_I, \omega_{II})$. χ_{ijkl} should consequently remain unchanged by permutation of its second and third arguments. As a consequence, $\chi_{ijkl}(\omega_s = 2\omega_I - \omega_{II}, \omega_I, \omega_I, \omega_{II})$ can be cast [188]:

$$\begin{aligned}
&\chi_{ijkl}(\omega_s = 2\omega_I - \omega_{II}, \omega_I, \omega_I, \omega_{II}) = \\
&\chi_{1122}(\omega_s = 2\omega_I - \omega_{II}, \omega_I, \omega_I, \omega_{II})\,(\delta_{ij}\delta_{kl} + \delta_{ik}\delta_{jl}) \\
&+ \chi_{1221}(\omega_s = 2\omega_I - \omega_{II}, \omega_I, \omega_I, \omega_{II})\delta_{il}\delta_{jk}
\end{aligned} \tag{7.12}$$

where δ_{ij} is the Kronecker delta equal to 1 if $i = j$ and null if $i \neq j$. That finally leads to the following expression for the non-linear polarization for a signal at the frequency $\omega_s = 2\omega_I - \omega_{II}$:

$$\mathbf{P}_{NL}(\omega_s) = 6\epsilon_0\chi^{(3)}_{1122}\left(\mathbf{E}(\omega_I)\cdot\mathbf{E}^*(\omega_{II})\right)\mathbf{E}(\omega_I) + 3\epsilon_0\chi^{(3)}_{1221}\left(\mathbf{E}(\omega_I)\cdot\mathbf{E}(\omega_I)\right)\mathbf{E}^*(\omega_{II}) \tag{7.13}$$

Consequently, it is still necessary to know the tensor components $\chi^{(3)}_{1122}$ and $\chi^{(3)}_{1221}$ to compute the non-linear polarization $\mathbf{P}_{NL}$. The numerical values of these components are however not easily found in the literature. While the dispersion of the $\chi^{(3)}$ of crystalline silicon may be found in several papers [179, 189], we only found one measurement performed at 1550 nm for the $\chi^{(3)}$ of amorphous silicon [180]. In what follows, in order to overcome this difficulty and get an estimate of the non-linear polarization we may calculate the overlap integral of the field at the wavelengths ω_I and ω_{II}.

7.3 Four-wave mixing in Mie resonators:

7.3.1 Introduction:

Since we are concerned with the process of degenerate four-wave mixing, the applied field illuminating the sample has two different frequency components ω_I and ω_{II}. As was explained before, nonlinear effects can only be observed with strong enough applied field amplitudes. Such amplitudes can only be provided by powerful laser sources. The laser source we are using consists of a titanium sapphire laser pumping an optical parametric oscillator (O.P.O). The titanium sapphire laser module is a Coherent Chameleon Ultra capable of delivering femtosecond pulses centered around a wavelength that can be tuned between roughly 680 and 950 nm. The temporal width of the pulses is roughly equal to 140 fs. When the wavelength of the Ti:sapphire laser is kept between 780 and 880 nm, it can be used to pump the O.P.O. module (Coherent Chameleon) that also delivers femtosecond pulses with a center wavelength ranging from 1050 nm to 1500 nm. In our experiment, one frequency component of the applied field will be provided by the Ti:sapphire laser module while the other will come from the O.P.O. module.
On the other hand, the nonlinear signal will be collected and analyzed by means of the spectrometer IsoPlane SCT 320 of Princeton Instruments along with the camera PIXIS 1024 of Princeton Instruments. This camera permits to detect a signal with a wavelength ranging from roughly 350 nm to 1000 nm. All the constraints on both the pump frequencies ω_I and ω_{II} and the signal frequencies ω_s are summarized in Fig. 7.1.

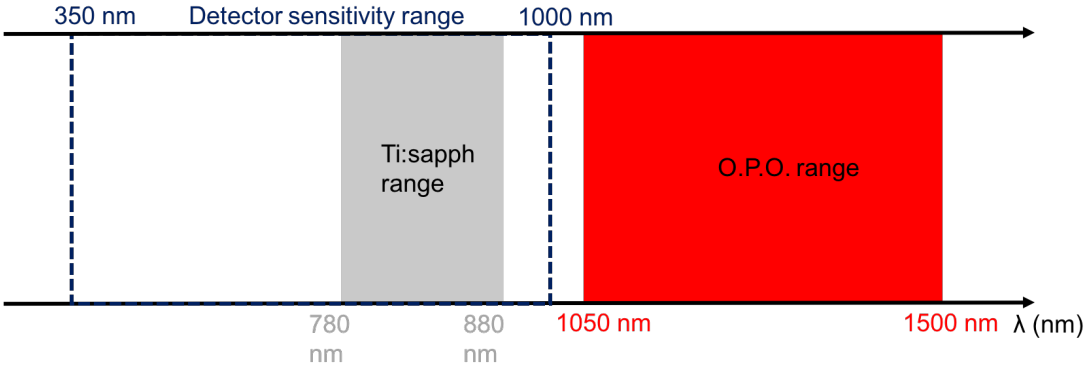

Figure 7.1: Summary of the ranges allowed for the 2 pumps and the range of sensitivity of the camera.

7.3.2 Design and fabrication

7.3.2.1 Design

We want to design a nanostructure which exhibits two resonances in the range of the 2 available pumps. Because of the constraints listed in the previous section, one of the pumps should be in the range 800 and 880 nm while the other one should be located between 1100 nm and 1500 nm. Even though in the previous chapters,

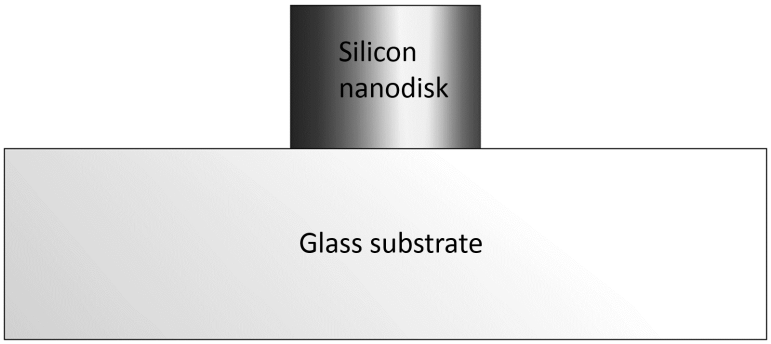

Figure 7.2: Silicon nanodisk on top of a glass substrate: the optical response of the silicon nanodisk can be controlled by changing the radius or the height of the nanodisk

we have only been considering spherical Mie resonators, the same kind of resonant behavior can be obtained using resonators with different geometries [11]. Nanodisks or nanocylinders appear in particular to be a very good geometry: a control of the wavelength of both electric and magnetic type resonances of silicon has been demonstrated by varying either the height or the diameter of these resonators [19]. These nanodisks can moreover be fabricated by patterning a silicon film by electron beam lithography with a fairly good control over both their height and diameter [20]. Detailed information regarding the techniques employed for fabricating these nanodisks will be provided in the next section. However, here we will start by defining the design of the nanodisks.
To do so, we will first determine the linear scattering properties of nanodisks by use of the commercial software COMSOL based on Finite Element Method. The COMSOL model consists of an amorphous silicon nanodisk (refractive index taken from [190]) located on top of a glass substrate (refractive index is taken to be constant and equal to 1.5). The incident field is a plane wave coming from the substrate. To characterize the scattering properties of the disks, the scattering cross sections can then be computed. The evolution of the average field inside the resonator $\langle|\mathbf{E}_{\text{int}}|\rangle$ can also be computed, where:

$$\langle|\mathbf{E}_{\text{int}}|\rangle = \frac{\int_{V_D} |\mathbf{E}_{\text{int}}| d\mathbf{r}}{\int_{V_D} |\mathbf{E}_0| d\mathbf{r}} \tag{7.14}$$

V_D being the volume of the scatterer while $\mathbf{E}_0$ is the amplitude of the excitation field. We computed the scattering properties for a wide range of sizes of silicon nanodisks with various heights and diameters. We found that a silicon nanodisk with a 240 nm height and a 340 nm diameter had resonances in the desired ranges. In Fig. 7.3, the evolution of the scattering cross section for a nanodisk with a 240 nm height and a 340 nm diameter is plotted.

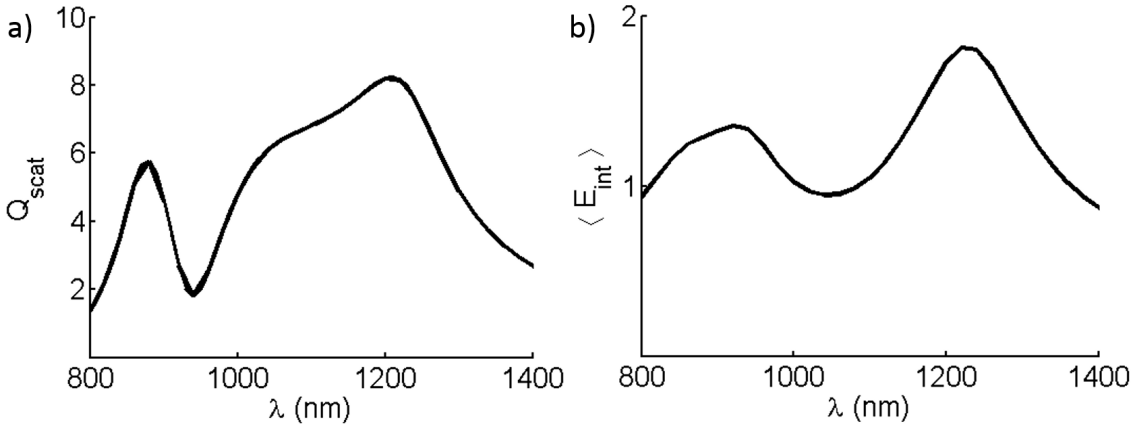

Figure 7.3: Calculated scattering efficiency and average internal field $\langle|\mathbf{E}_{\text{int}}|\rangle$ for a nanodisk 240 nm in height and 340 nm in diameter.

For this geometry, an enhancement of the average internal field is clearly observed near 1200 nm, which is inside the range of the O.P.O., and another resonance between 800 and 900 nm which is inside the range that can be reached with the Ti:sapphire. That is why nanodisks with a 240 nm height will be fabricated. The diameter of the fabricated nanodiks will vary between 250 nm to 360 nm.

7.3.2.2 Overlap integrals:

Even though we could not calculate the exact value of the nonlinear polarization because we did not know the exact values of the susceptibility tensors. We calculated the overlap integrals between the fields at the frequencies ω_I and ω_{II} to have at least an estimate of the evolution of the degenerate four-wave mixing signal. The overlap integrals are defined as follows:

$$I_{NL1} = \left| \iiint_{V_D} \left(\mathbf{E}(\omega_I) \cdot \mathbf{E}^*(\omega_{II})\right) \mathbf{E}(\omega_I) d\mathbf{r} \right| \tag{7.15}$$

$$I_{NL2} = \left| \iiint_{V_D} \left(\mathbf{E}(\omega_I) \cdot \mathbf{E}(\omega_I)\right) \mathbf{E}^*(\omega_{II}) d\mathbf{r} \right| \tag{7.16}$$

where V_D is the volume of the nanodisk. The first integral I_{NL1} is associated with the first term in the nonlinear polarization (7.13) whereas the second integral is associated with the second term. We calculate these integrals for a nanodisk h =

240 nm in height and D = 320 nm in diameter slightly smaller than the one in the previous section. The scattering efficiency and field enhancement associated with this nanodisk geometry are plotted in Fig. 7.4.

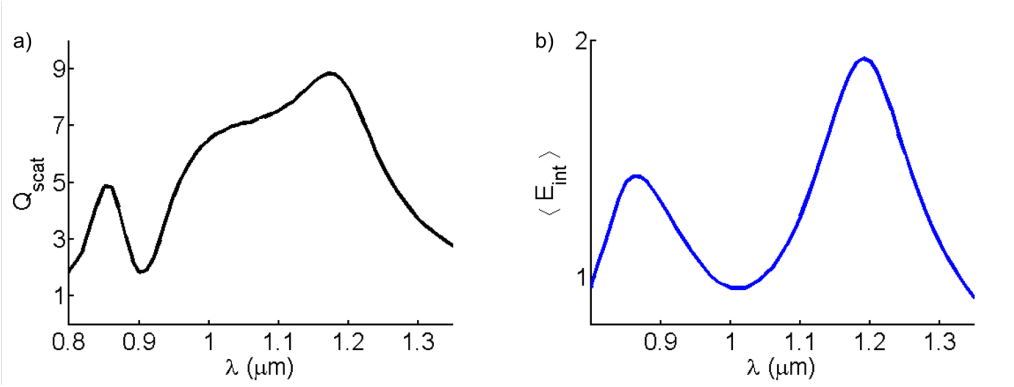

Figure 7.4: Scattering efficiency Q_{scat} and average internal field enhancement of a D = 320 nm and h = 240 nm amorphous silicon nanodisk

In Fig. 7.4, resonances and enhancements of the internal field are clearly observed at the two wavelengths 1200 nm and at roughly 860 nm. In Fig. 7.5, we show the overlap integrals for the same geometry

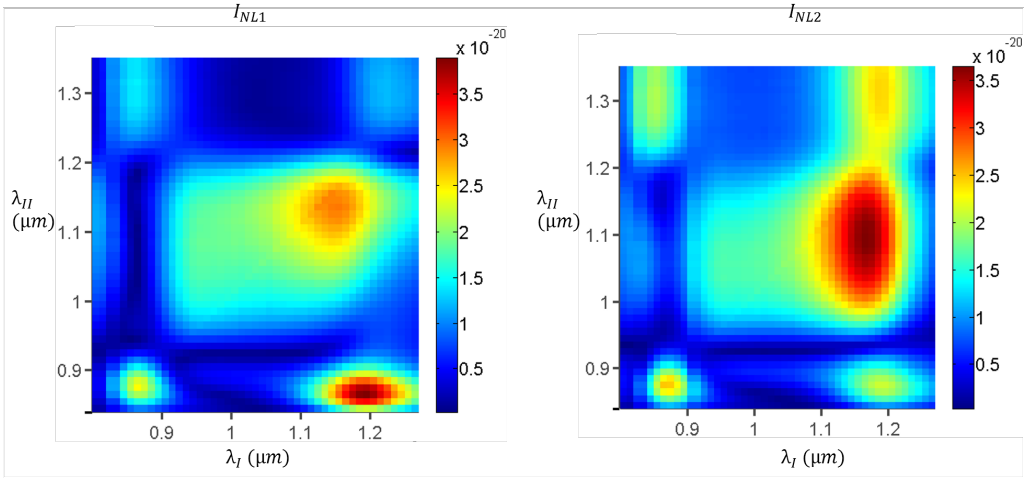

Figure 7.5: Overlap integrals of the field at the frequencies ω_I and ω_{II} of a D = 320 nm and h = 240 nm amorphous silicon nanodisk

We can observe an enhancement of the overlap integrals when λ_I is roughly equal to 860 nm and λ_{II} is between 1250 nm and 1300 nm which is slightly shifted with respect to the resonance of the internal field occuring at 1200 nm. The four-wave mixing process at those wavelengths would give rise to a signal at the wavelength:

$$\lambda_s = \frac{\lambda_I \lambda_{II}}{2\lambda_{II} - \lambda_I} \simeq 660 \text{ nm} \tag{7.17}$$

The signal at this wavelength would be detectable by our camera. The calculation of these overlap integrals were meant to provide a qualitative prediction of the evolution of the four-wave mixing signal. We will see in the following that our experimental results do not fully agree with these predictions.

7.3.2.3 Fabrication of the nanodisks:

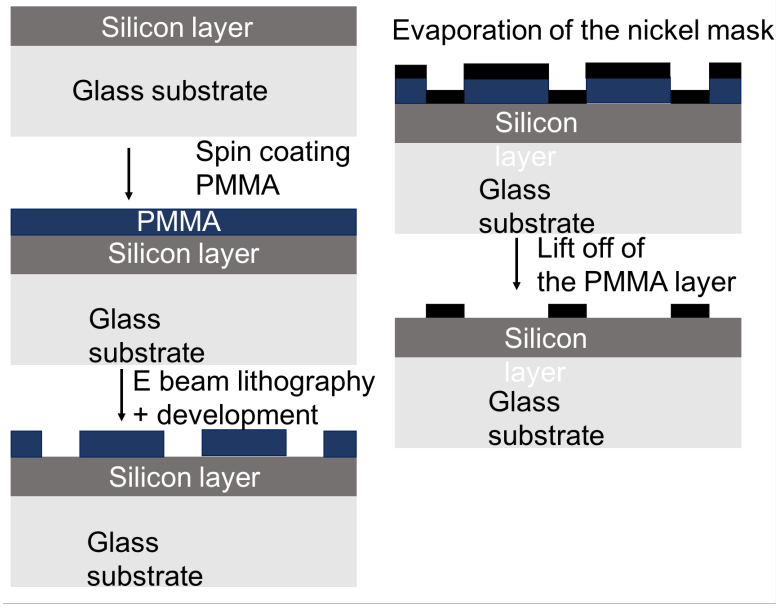

Figure 7.6: First steps of the fabrication: a PMMA layer is spin-coated on the silicon film. After the electron beam lithography and development steps, the PMMA layer is removed from the areas exposed during the electron beam lithography stage. A 16 nm thick nickel layer that will be a mask during the reactive-ion etching is evaporated onto the sample. The lift-off step is performed to remove the remaining PMMA resist on the sample. At the end of this step, the nickel mask only protects the zones that had been exposed during the EBL step.

The nanodisks have been fabricated by structuring an amorphous silicon thin film by electron-beam lithography (performed at the Planete CT PACA cleanroom facility). A 240 nm thick amorphous silicon layer is deposited on top of a 150 μm thick glass cover slip by plasma assisted reactive magnetron (performed at the photonic space, Institut Fresnel)(see supplementary material of [191]).
As illustrated in Fig. 7.6, a 60 nm thick PMMA (Poly(methyl methacrylate)) layer, which is an electron beam positive resist, is spin-coated on top of the silicon layer. An additional conduction layer can be deposited on top of the PMMA layer by spin coating in order to improve the resolution of the Electron Beam Lithography (EBL). The EBL is then performed in an EBL tool (Pioneer, Raith). Only the areas that will not be etched, i.e. the nanodisks, are exposed by the electron beam. Several arrays of isolated disks with different diameters ranging from 250 nm to 360 nm are

patterned. All these arrays have a 10 μm pitch in order to make sure that there is no coupling effect between the resonators. After washing away the conducting layer with deionized water, the sample is developed in a commercial solution (see supplementary material of [191]). During the development stage, the PMMA is removed from the zones that have been exposed to the electron beam during the process of electron beam lithography. A 16 nm thick nickel layer, that will be a mask during the reactive ion etching step, is subsequently evaporated onto the sample (Auto 306, Edwards). A lift-off is then performed in an ultrasonic cleaning bath of ethyl lactate. During this lift-off step, the remaining PMMA and the nickel layer on top of it are removed. Consequently, after this stage only the zones that had been exposed to the electron beam are still protected by the nickel mask as can be seen in Fig. 7.6.

The zones of the silicon layer no more protected by the nickel mask are then

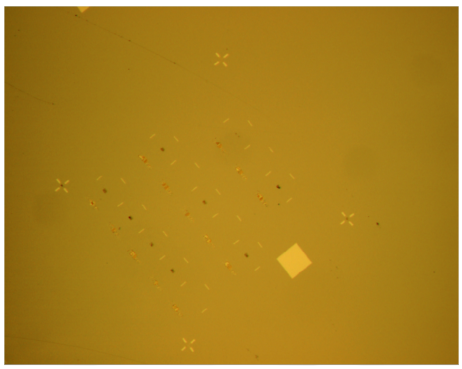

Figure 7.7: Optical microscope image of the nickel mask through a ten times magnifying objective. The bright square in the image is a 100 microns per 100 microns square.

etched by Reactive-Ion Etching in a RIE tool (MG-200, Plassys) by a gas mixture containing SF_6, O_2 and CHF_3 alternating with a pure O_2 plasma . Finally, the remaining nickel mask is chemically removed in the acid solution of HCl and $FeCl_3$ as shown in Fig. 7.8.

7.3.3 Linear characterization:

A linear characterization of the isolated silicon nanodisks has then to be performed to verify that the measured extinction of these isolated silicon nanodisks are comparable with those predicted by Comsol simulations. For that purpose, a confocal microscope is used. A schematic representation of the setup is shown in Fig. 7.9. The sample is illumimated by a collimated white light source that has just been slightly focused in order to obtain an intense enough and homogeneous illumination on the sample. This setup allows for a collection of the light only from the zone of the sample corresponding to the image of the spatial filter put in the focal plane of the second lens.

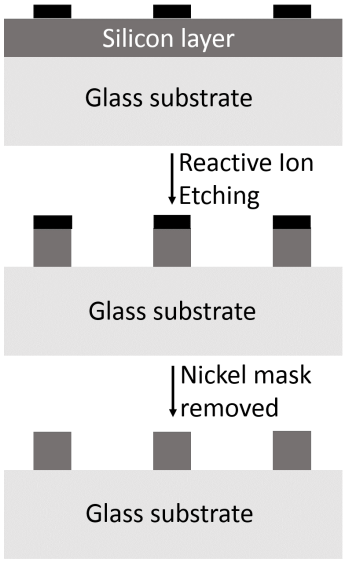

Figure 7.8: Last two steps of the nanofabrication process: during the Reactive Ion Etching step, the silicon that is not protected by the nickel mask is removed. In the last step, the remaining nickel mask is removed.

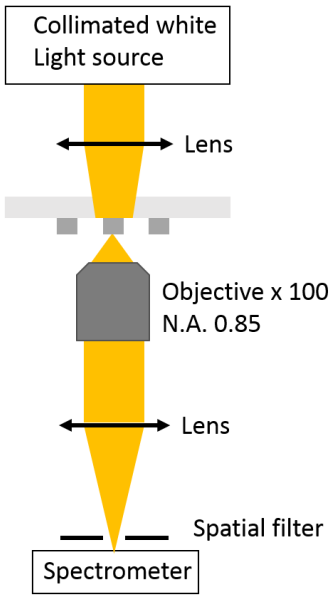

Figure 7.9: Schematic representation of the confocal microscope

The extinction measurement are performed by taking a measurement of the light transmitted by the substrate I_s, another measurement of the light transmitted by an isolated disk I_d and finally one measurement of the noise I_n. The extinction is then obtained by computing:

$$Ext = -\frac{I_d - I_s}{I_s - I_n} \tag{7.18}$$

In Fig. 7.10, a comparison between the measured extinction for a nanodisk 340 nm in diameter (measured diameter 335 nm) and 240 nm in height and the simulated extinction efficiency is carried out. The camera used for the measurements in the near-infrared region is a Princeton Instruments NIRvana 640 while for visible measurements, the Princeton Instruments camera PIXIS 1024 is used.

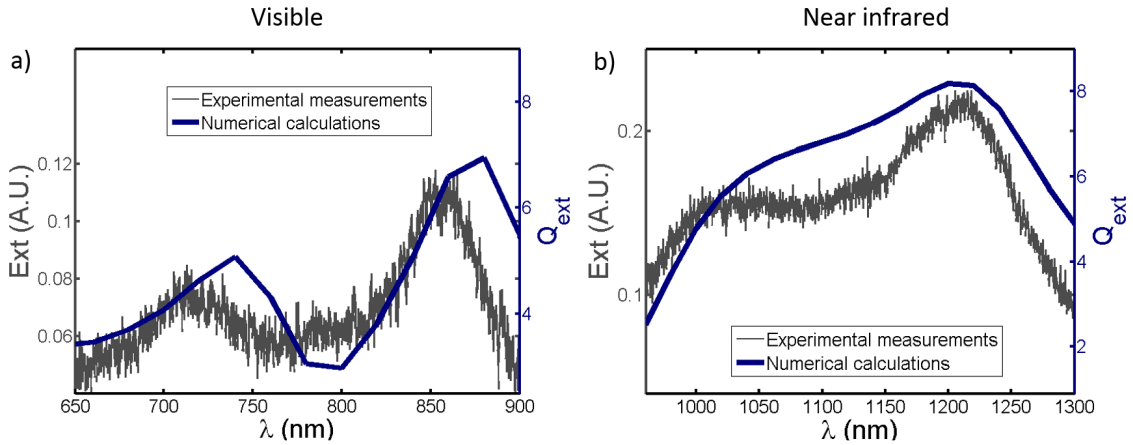

Figure 7.10: Comparison between experimental measurments of the extinction of a silicon nanodisk with a $h = 240$ nm height and a $D = 340$ nm diameter and calculated extinction cross sections.

In Fig. 7.10, a general qualitative agreement between the measurements of the extinction and the extinction efficiency computed with COMSOL is observed. It might have been worth using a less rough wavelength step for comsol simulations. Since these simulations have been carried out while using textbook values for amorphous silicon [190], it further confirms that it is safe to assume that the silicon of the sample is indeed amorphous. In particular, the presence of the two desired resonances at wavelengths around 1210 nm and 850 nm is confirmed. From these extinction measurements and the simulations previously done, we can expect a field enhancement inside the silicon nanodisks at around 1210 nm and 850 nm. In the next section, we will be making degenerate four wave-mixing measurements and we will in particular study how the four-wave mixing signal varies when pump wavelengths are swept around these two resonance wavelengths.

7.4 Four-wave mixing experimental results:

7.4.1 Experimental setup:

The four-wave mixing measurements are performed with the experimental setup represented in Fig. 7.11. The pump at the wavelength λ_1 (between 800 nm and 880 nm) is provided by the Ti:sapphire laser. The other pump at the wavelength λ_2 (between 1050 nm and 1500 nm) is provided by the O.P.O. module. The paths of

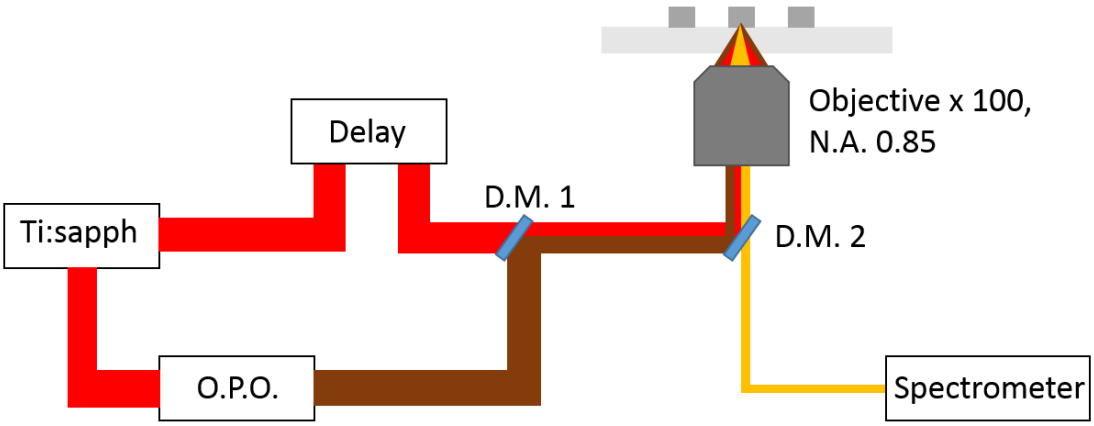

Figure 7.11: Experimental setup for four-wave mixing measurements. D.M. 1 is a short pass dichroic mirror with a cut-off wavelength of 1000 nm (Thorlabs, DMSP1000R). D.M. 2 is a short-pass dichroic mirror with a cut-off wavelength of 805 nm (Thor Labs, DMSP805R).

both pumps are then merged by inserting a short pass dichroic mirror with a cut-off wavelength of 1000 nm (Thor labs, DMSP1000R). They are then reflected towards the objective by another dichroic mirror with a cut-off wavelength of 805 nm (Thor Labs, DMSP805R). They are focused on the sample with a 100 times magnifying objective with a 0.85 numerical aperture (Olympus LCPLN100XIR). This objective is specifically designed for working with wavelengths between 700 and 1300 nm where it best transmits light and where it has also been corrected for chromatic aberrations. For the four-wave mixing process to occur, the two pumps focal spots have to spatially overlap. Therefore, we checked that both pumps were focused on the same focal plane. This was expected since both pumps belong to the working range of the objective, where it is chromatically corrected. A good spatial overlap can then be obtained by independently tuning the position in the focal plane of the focal spot of each pump. This can be done by independently tuning the orientations of mirrors located in the Ti:sapphire beam path and in the O.P.O. beam paths. However, the spatial overlap is not sufficient to obtain a four-wave mixing signal. In fact, since the two pumps are provided by pulsed sources, the pulses from both pumps also have to temporally overlap when they reach the sample for the four-wave mixing process to occur. In other words, pulses from both pumps should arrive on the sample at the same time. That is why a delay line has been introduced in the Ti:sapphire beam path. It allows for a compensation of the path difference between the Ti:sapphire and the O.P.O. beam and it thus permits to reach a good temporal overlap of the two pulsed pumps. This is illustrated in Fig. 7.12.

In order to maximize the temporal overlap, we search the position of the delay line that permits to maximize the four-wave mixing signal. Once both temporal and spatial overlaps are reached, the four-wave mixing process can occur. For our experiments, the four-wave mixing signal will typically be in the range 580 nm to 650

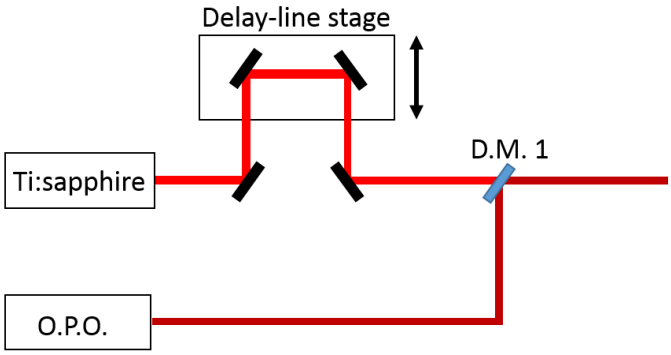

Figure 7.12: The temporal overlap of the two pulsed pumps can be reached by tuning the delay line postion.

nm. It is important to note that the signal is collected in the reflection configuration and not in transmission as shown in Fig 7.11. The signal is consequently collected with the same objective as the one used to focus the two pumps on the sample. The signal wavelength does not belong to the working range of the objective. However, we have however checked that in practice the focal plane height difference at the signal wavelength was within the Rayleigh range. Once the signal is collected by the objective, it is then analyzed by the spectrometer (Princeton Instruments, Isoplane 320) along with a visible camera (Princeton Instruments, Pixis 1024).

7.4.2 Crystallization of the amorphous silicon:

As was explained in section 7.3.2.3, the nanodisks are fabricated by structuring an amorphous silicon film. The fact that silicon is amorphous rather than crystalline was further confirmed by comparing the experimentally measured extinction with simulations obtained using the refractive index of amorphous silicon. However, after our first attempts for measuring a four-wave mixing signal, a blue-shift of the resonances of the extinction spectrum of the silicon nanodisks was observed. The shift observed after illumination by both pumps with an intensity at each pump of roughly 0.2 MW/cm^2 is illustrated in Fig. 7.13.

In [17], such a blue-shift was also obtained for the resonances appearing in the scattering spectrum of spherical amorphous silicon after irradiation by a femtosecond laser. They explained that this blue-shift was due to the crystallization of the amorphous silicon. This was clearly supported by transmission electron microscopy images showing the crystalline structure of the silicon [17]. The amorphous to crystalline phase transition of the silicon induced by femtosecond laser illumiation had already been studied in thin films [192–194]. For that reason, we assume that the blue shift we observed is due to the crystallization or at least the partial crystallization of the amorphous silicon in the silicon nanodisks.
We however wanted to make sure that no further blue-shift of the resonances occurred when the silicon nanodisks were illuminated several times. For that purpose,

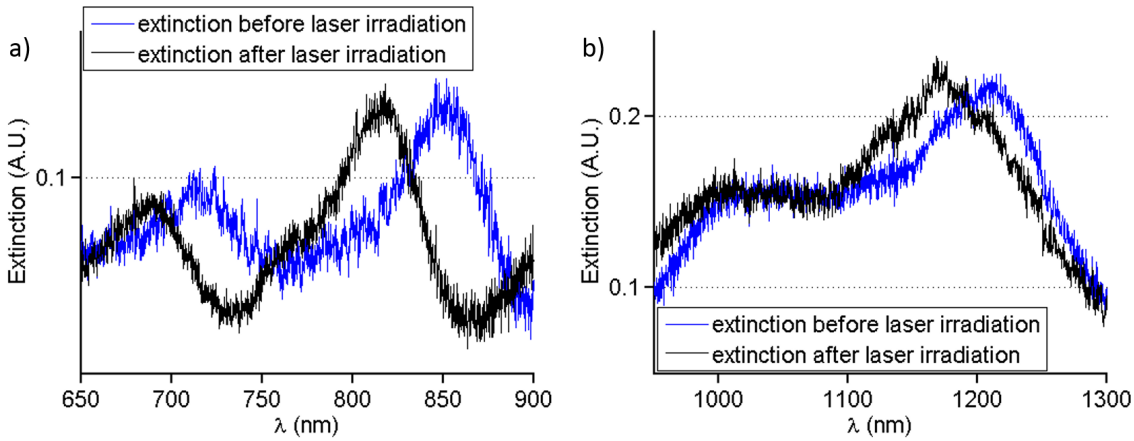

Figure 7.13: Blue shift of the resonances of the silicon nanodisks after illumination by a laser pulses of a femto-second lasers

we illuminated the same nanodisk several times with the same intensity as before for the two pumps to confirm that the resonances do not shift any further. This is indeed confirmed in Fig. 7.14 where no further shift occurs for the resonances in the visible range.

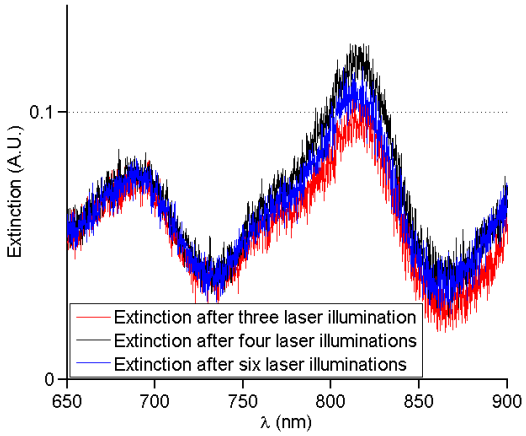

Figure 7.14: Resonances position after several illuminations by the laser

We can consequently proceed to four-wave mixing measurements. In the next section, we will then present the results for the measurements of degenerate four-wave mixing with the pump set around the shifted resonance wavelengths obtained after crystallization.

7.4.3 Four-wave mixing measurements:

In this section, the degenerate four-wave mixing by the silicon nanodisks will be studied when the pump wavelengths are close to the resonance wavelengths of the nanodisks. In Fig. 7.15 we plot again the extinction spectrum after crystallization

of the nanodisk we are considering. The wavelength of the nanodisks resonance in

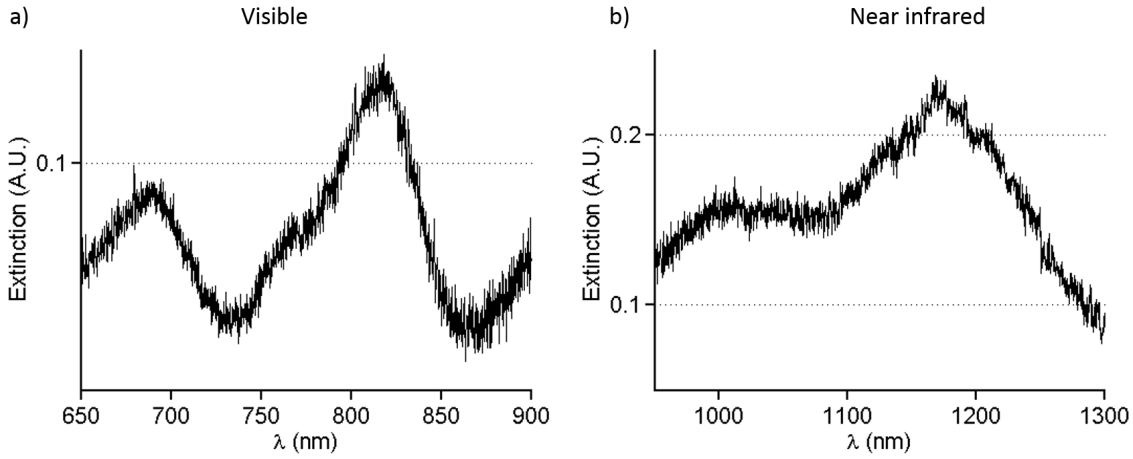

Figure 7.15: Resonances after laser-induced crystallization of the silicon nanodisks

the near infrared appears to be around 1180 nm while the resonance in the visible is around 810 nm. For that reason, we will fix the wavelength of the first pump to be $\lambda_1 = 810$ nm while the second pump wavelength will be swept between 1100 and 1350 nm. We will then compare these measurements to the degenerate four-wave mixing signal from the non patterned silicon film of the same height as the disk as a reference. It is of crucial importance to know the power delivered on the sample, because the measurements at different wavelengths need to be done at a constant intensity in order to be comparable. For that reason, we have calibrated the setup to control the power delivered on the sample by the two pumps. Even though we can keep the power of the second pump constant when varying its wavelength thanks to our calibration, the size of the focal spot is also wavelength dependent and as a consequence the intensity will vary. We will assume that the diffraction limit $d(\lambda) = \frac{\lambda}{2NA}$, where NA is the numerical aperture of the objective, provides a good estimate of the evolution with the wavelength of the focal spot diameter. The four-wave mixing signal will consequently be normalized by

$$N_{norm} = \left(\frac{P\lambda_1}{\pi \left(\frac{d(\lambda_1)}{2} \right)^2} \right)^2 \cdot \frac{P_{\lambda_2}}{\pi \left(\frac{d(\lambda_2)}{2} \right)^2} \tag{7.19}$$

where P_{λ_1} and P_{λ_2} are the pump powers, as the four-wave mixing intensity depends on the squared intensity at λ_1 and the intensity at λ_2. The experimental results for both the nanodisk and the homogeneous film are plotted in Fig. 7.16.

First, it clearly appears in Fig. 7.16a that there is a peak for the four-wave mixing signal at around $\lambda_2 = 1200$ nm, close to the resonance wavelength observed in the extinction cross section (1180 nm). This result is not in complete agreement with the predictions from the calculation of the overlap integrals but these overlap integrals

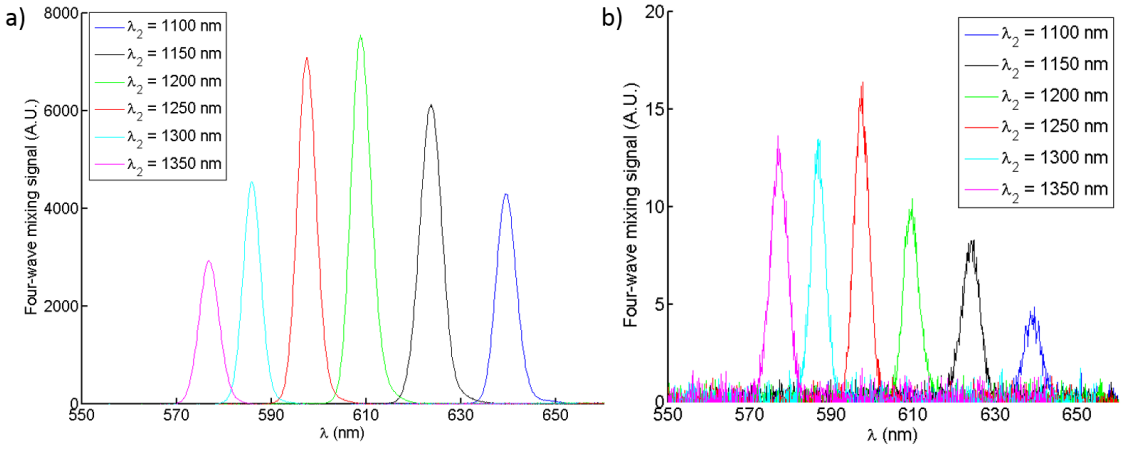

Figure 7.16: Four-wave mixing signal normalized by the factor N_{norm} at each wavelength for a) the silicon nanodisk with a diameter equal to 340 nm and height equal to 240 nm and b) for a silicon film of the same height.

can only provide a rough estimate of the evolution of the four-wave mixing signal. Moreover, the derivation of these overlap integrals were based on the expression of the non-linear polarization assuming our disk were made of amorphous silicon. However, the amorphous silicon were crystallized or at least partially crystallized during the measurements, it is consequently not strictly valid to compare these calculations to our measurements. We can thus assume that this peak is associated with the field enhancement occurring at resonance. Moreover, at a given wavelength, a comparison can be carried out between the four-wave mixing signal from the silicon nanodisk and the four-wave mixing signal from the silicon film that has not been patterned. The signal from the film also exhibits a large wavelength dependence. This could be explained by the presence of Fabry-Perot resonances for the silicon film. In fact, the four-wave mixing signal depends on the optical response and on the internal field inside the silicon thin film at the two pump wavelengths. It also depends on the optical response of the thin film at the signal wavelength. It is consequently not easy to interpret the dispersion of the signal from the thin film. The enhancement factor from the disk compared to the film of the signal clearly depends on the wavelength and it roughly varies between 200 and 1000. This large enhancement must have several contributing factors, the first of which being the enhancement of the four-wave mixing process due to the enhancement of the field inside the disk. The radiation pattern of the field can also be assumed to be different for the disk as compared to the film. In particular, more field can be assumed to be radiated in the backward direction for the silicon nanodisk. This could be confirmed by imaging the radiated signal in the back focal plane.

7.5 Conclusion:

In this chapter, we have experimentally studied the possibility of enhancing the four-wave mixing process inside a silicon nanodisk. By choosing the right nanodisk geometry, we have seen that we could obtain two resonances and consequently enhance the internal field in the wavelength ranges of the laser two pumps. We then wanted to see if these enhancements of the internal field could in turn lead to an enhancement of the four-wave mixing process in the silicon nanodisk. However, we noticed that the illumination of the amorphous silicon by the femtosecond laser pulses lead to a blue shit of the resonances of these disks. This blue shift was assumed to originate from the crystallization or at least the partial crystallization of the amorphous silicon. After crystallization of the silicon, four-wave mixing measurements from the nanodisks were performed in the reflection configuration. A clear resonant behavior was observed when the pump wavelength λ_2 was swept around the resonance of the nanodisk in the near-infrared region. Moreover, as a reference we also performed the same four-wave mixing measurements on a non patterned silicon film. The signal from the nanodisks was found to be larger by a factor varying between 2 and 3 orders of magnitude compared to the thin film. This large enhancement can certainly be explained by several factors. First, the four-wave mixing process is enhanced thanks to the enhancement of the internal field. Another factor that can explain this enhancement is the difference in the radiation pattern of the nanodisk compared to the film. This could be confirmed by a measurement of the radiation patterns in the Fourier plane of the objective. Finally it would also be worth sweeping the wavelength of the other pump λ_1 around the other resonance of the nanodisk to see if a resonant behavior can be also observed.

Chapter 8

Conclusion

Throughout this thesis, the interaction of light with high-refractive index scatterers was studied from both a theoretical and an experimental point of view. We were particularly interested in the resonant behavior such structures exhibit while interacting with light making them a good platform to control and enhance light-matter interactions. Theoretical studies were performed in the framework of the multipolar theory and were aiming at improving our understanding of Mie resonances. The main theoretical result presented in this thesis is certainly the modal analysis of high refractive index scatterers presented in Chapter 6. We finally experimentally studied degenerate four-wave mixing enhancement in a silicon nanodisk. Here we should provide a slightly more detailed summary of the work.

After presenting an overview of the latest advances of the field of Mie resonators in Chapter 2, an introduction of the multipolar theory, which was framework of the subsequent theoretical studies was provided in Chapter 3. Several formulation of the scattering problem were in particular introduced: the S, T and K matrix formulations.

In Chapter 4, the conditions of optimal interations between light and a scatterer were studied. The objective was in fact to determine the conditions that optimize the scattering or absorption of light by subwavelength sized scatterers. Since this study was performed in the framework of the multipolar basis, it consisted to determine the conditions that allowed to reach the upper bound of the partial scattering and absorption cross sections for one given multipolar order.

The objective of the work presented in Chapter 5 was twofold. First, we aimed to present the asymptotic resonance conditions for high-refractive index sub-wavelength resonators. We subsequently used these resoance conditions in order to derive approximate models capable of predicting the behavior of both plasmonic and Mie resonators.

In Chapter 6, we performed a modal analysis of Mie resonators. This analysis was based on pole expansions of the S matrix coefficients. Using considerations based on energy conservation and causality, the S-matrix coefficients pole expansions were first derived. The presence of an additional non-resonant term in these pole expansions was in particular evidenced.
These pole expansions were subsequently used to study the resonant behavior of high refractive index scatterers. We showed in particular that the asymmetric shape of the resonances observed in the scattering cross-sections spectra could be explained by the interference between resonant and non-resonant terms. On the other hand, resonances of the internal field were shown to have a lorentzian shape as there are only resonant contributions to the internal field. It has already been shown in the literature that these modal expansions could be beneficial to study the coupling of a quantum emitter to optical resonators [5, 45]. Here we showed that the quasi-normal mode expansions could be used to study the scattering problem in the time domain. They are consequently a very powerful tool since they would enable analytical predictions of the temporal dynamic of photonic resonators [171]. This analysis was however only restricted to lossless scatterers. It would consequently be interesting to generalize this study to lossy materials. In this case, the pole expansion derived for the S-matrix coefficients would have to be modified to take temporal dispersion into account.
The use of quasi-normal modes analysis would certainly prove to be useful in the more general context of the study of open systems described by a non-hermitian Hamiltonian [195]. A number of interesting phenomena occur in such kind of systems. For instance, the appearance of bound states in the continuum has lately been evidenced in open photonic cavities [196, 197] and were shown to be a good platform to implement nanolasers [198].

Chapter 7 was finally devoted to the experimental study of non-linear effects in silicon sub-wavelength resonators. The enhancement of the internal field associated with the excitation of Mie resonances in silicon resonators can be very beneficial when considering non-linear effects. Here, we wanted to study degenerate four-wave mixing. We consequently designed and fabricated silicon nanodisks possessing two resonances showing field enhancements in the near-infrared region. The degenerate four-wave mixing signal from the nanodisks was measured when two laser pumps at wavelengths close to the resonance wavelengths were shown on the nanodisks. A clear enhancement of the four-wave mixing signal was measured as compared to the signal measured from an unpatterned silicon thin film. This study further confirms that silicon nanodisks and more generally high-index dielectric resonators are a good platform to enhance nonlinear effects.

Appendix A

Appendix A

A.1 Mie theory: S, T and K matrices of spherically-symmetric scatterers:

Here, we will derive the analytical expressions of the S, T and K-matrix coefficients for spherical scatterers. For that purpose, we will be using the continuity conditions of the electromagnetic field at an interface:

$$\begin{aligned} \mathbf{n}_{12} \times (\mathbf{E}_2 - \mathbf{E}_1) &= \mathbf{0} \\ \mathbf{n}_{12} \times (\mathbf{H}_2 - \mathbf{H}_1) &= \mathbf{0} \end{aligned} \tag{A.1}$$

The subscripts 1 and 2 correspond respectively to the field inside and outside the scatterer of radius R and refractive index n_s. The vector $\mathbf{n}_{12}$ is the normal to the surface of the scatterer and thus for spherically-symmetric scatterers $\mathbf{n}_{12} = \mathbf{r}$. Eqs. (A.1) can be interpreted as the continuity of the tangential part of the electromagnetic field at the interface. From the discussion of chapter 1, we can show that both the total fields existing inside and outside the scatterer admit the following expansion on the Vector Spherical Harmonics (VSH) basis:

$$\begin{aligned} \mathbf{E}(k\mathbf{r}) &= \sum_{n=1}^{\infty} \sum_{m=-n}^{n} E_{n,m}^{(X)}(r)\mathbf{X}_{n,m}(\theta,\phi) + E_{n,m}^{(Y)}(r)\mathbf{Y}_{n,m}(\theta,\phi) + E_{n,m}^{(Z)}(r)\mathbf{Z}_{n,m}(\theta,\phi) \\ \mathbf{H}(k\mathbf{r}) &= \sum_{n=1}^{\infty} \sum_{m=-n}^{n} H_{n,m}^{(X)}(r)\mathbf{X}_{n,m}(\theta,\phi) + H_{n,m}^{(Y)}(r)\mathbf{Y}_{n,m}(\theta,\phi) + H_{n,m}^{(Z)}(r)\mathbf{Z}_{n,m}(\theta,\phi) \end{aligned} \tag{A.2}$$

At the interface, only the contributions from $\mathbf{X}_{n,m}(\theta,\phi)$ and $\mathbf{Z}_{n,m}(\theta,\phi)$ are actually tangential to the surface, on the other hand, the contribution from $\mathbf{Y}_{n,m}(\theta,\phi)$ is normal to the surface. By using the previous expansion (A.2) along with the orthogonality of the vector spherical harmonics, the continuity conditions (A.1) become:

$$\begin{aligned} E^{(X)}_{1,n,m}(R) &= E^{(X)}_{2,n,m}(R) \\ E^{(Z)}_{1,n,m}(R) &= E^{(Z)}_{2,n,m}(R) \\ H^{(X)}_{1,n,m}(R) &= H^{(X)}_{2,n,m}(R) \\ H^{(Z)}_{1,n,m}(R) &= H^{(Z)}_{2,n,m}(R) \end{aligned} \tag{A.3}$$

where again the subscripts 1 and 2 refer respectively to the internal and external fields. In what follows we will use the conditions (A.3) to derive the analytical expressions of the S, T and K-matrix coefficients for spherical scatterers.

A.2 S-matrix coefficients of a spherical scatterer:

Let us recall the expressions of the external and internal fields in the S-matrix formalism:

$$\begin{aligned} \mathbf{E}_{tot}(k\mathbf{r}) &= E_0 \sum_{n=1}^{\infty}\sum_{m=-n}^{n} s^{(h,-)}_{n,m}\left(\mathbf{M}^{(-)}_{n,m}(k\mathbf{r}) + S^{(h)}_n \mathbf{M}^{(+)}_{n,m}(k\mathbf{r})\right) \\ &\quad + s^{(e,-)}_{n,m}\left(\mathbf{N}^{(-)}_{n,m}(k\mathbf{r}) + S^{(e)}_n \mathbf{N}^{(+)}_{n,m}(k\mathbf{r})\right) \\ \mathbf{H}_{tot}(k\mathbf{r}) &= \frac{kE_0}{i\mu_0\omega} \sum_{n=1}^{\infty}\sum_{m=-n}^{n} s^{(e,-)}_{n,m}\left(\mathbf{M}^{(-)}_{n,m}(k\mathbf{r}) + S^{(e)}_n \mathbf{M}^{(+)}_{n,m}(k\mathbf{r})\right) \\ &\quad + s^{(h,-)}_{n,m}\left(\mathbf{N}^{(-)}_{n,m}(k\mathbf{r}) + S^{(h)}_n \mathbf{N}^{(+)}_{n,m}(k\mathbf{r})\right) \\ \mathbf{E}_{int}(k\mathbf{r}) &= E_0 \sum_{n=1}^{\infty}\sum_{m=-n}^{n} u^{(h)}_{n,m}\mathbf{M}^{(1)}_{n,m}(k_s\mathbf{r}) + u^{(e)}_{n,m}\mathbf{N}^{(1)}_{n,m}(k_s\mathbf{r}) \\ \mathbf{H}_{int}(k\mathbf{r}) &= \frac{k_s E_0}{i\mu_0\omega} \sum_{n=1}^{\infty}\sum_{m=-n}^{n} u^{(e)}_{n,m}\mathbf{M}^{(1)}_{n,m}(k_s\mathbf{r}) + u^{(h)}_{n,m}\mathbf{N}^{(1)}_{n,m}(k_s\mathbf{r}) \end{aligned} \tag{A.4}$$

It follows that in the S-matrix formalism, Eqs. (A.3) become:

$$\begin{aligned}
E_0.s_{n,m}^{(h,-)}\left(h_n^{(-)}(kR)+S_n^{(h)}h_n^{(+)}(kR)\right) &= E_0.u_{n,m}^{(h)}.j_n(k_sR)\\
E_0.s_{n,m}^{(e,-)}\left(\frac{\xi_n^{(-)'}(kR)}{kR}+S_n^{(e)}\frac{\xi_n^{(+)'}(kR)}{kR}\right) &= E_0.u_{n,m}^{(e)}\frac{\psi_n'(k_sR)}{k_sR}\\
\frac{kE_0}{i\mu_0\omega}s_{n,m}^{(e,-)}\left(h_n^{(-)}(kR)+S_n^{(e)}h_n^{(+)}(kR)\right) &= \frac{k_sE_0}{i\mu_0\omega}u_{n,m}^{(e)}.j_n(k_sR)\\
\frac{kE_0}{i\mu_0\omega}s_{n,m}^{(h,-)}\left(\frac{\xi_n^{(-)'}(kR)}{kR}+S_n^{(h)}\frac{\xi_n^{(+)'}(kR)}{kR}\right) &= \frac{k_sE_0}{i\mu_0\omega}u_{n,m}^{(h)}\frac{\psi_n'(k_sR)}{k_sR}
\end{aligned} \tag{A.5}$$

As $s_{n,m}^{(e,-)}$ and $s_{n,m}^{(h,-)}$ can be directly computed from the excitation field, we end up with 4 unknowns and 4 equations. The expressions of $S_n^{(e)}$ and $S_n^{(h)}$ are then found to be:

$$\begin{aligned}
S_n^{(e)} &= \frac{\varepsilon_s\xi_n^{(-)'}(kR)j_n(k_sR)-h_n^{(-)}(kR)\psi_n'(k_sR)}{h_n^{(+)}(kR)\psi_n'(k_sR)-\varepsilon_s j_n(k_sR)\xi_n^{(+)'}(kR)}\\
S_n^{(h)} &= \frac{h_n^{(-)}(kR)\psi_n'(k_sR)-\xi_n^{(-)'}(kR)j_n(k_sR)}{j_n(k_sR)\xi_n^{(+)'}(kR)-h_n^{(+)}(kR)\psi_n'(k_sR)}
\end{aligned} \tag{A.6}$$

Recalling that:

$$\Xi_n^{(e)}=\frac{u_{n,m}^{(e)}}{s_{n,m}^{(e,-)}},\ \Xi_n^{(h)}=\frac{u_{n,m}^{(h)}}{s_{n,m}^{(h,-)}} \tag{A.7}$$

The analytical expressions of $\Xi_n^{(e)}$ and $\Xi_n^{(h)}$ can also be found from Eq. (A.5):

$$\begin{aligned}
\Xi_n^{(e)} &= \frac{n_s\left(h_n^{(+)}(kR)\xi_n^{(-)'}(kR)-h_n^{(-)}(kR)\xi_n^{(+)'}(kR)\right)}{h_n^{(+)}(kR)\psi_n'(k_sR)-\varepsilon_s j_n(k_sR)\xi_n^{(+)'}(kR)}\\
\Xi_n^{(h)} &= \frac{h_n^{(-)}(kR)\xi_n^{(+)'}(kR)-\xi_n^{(-)'}(kR)h_n^{(+)}(kR)}{j_n(k_sR)\xi_n^{(+)'}(kR)-h_n^{(+)}(kR)\psi_n'(k_sR)}
\end{aligned} \tag{A.8}$$

the numerator of the $\Xi_n^{(e,h)}$ can be re-expressed by using the wronskian of Hankel functions: $W\left(h_n^{(+)}(z),h_n^{(-)}(z)\right)=-2iz^{-2}$

$$\begin{aligned}\Xi_n^{(e)} &= \frac{2in_s}{kR\left(\varepsilon_s j_n(k_sR)\xi_n^{(+)'}(kR) - h_n^{(+)}(kR)\psi_n'(k_sR)\right)}\\ \Xi_n^{(h)} &= \frac{2i}{kR\left(j_n(k_sR)\xi_n^{(+)'}(kR) - h_n^{(+)}(kR)\psi_n'(k_sR)\right)}\end{aligned} \tag{A.9}$$

In Chapter 3, we can then introduce numerator and denominator functions:

$$\begin{aligned}N_{S,n}^{(e)}(kR) &= kR\frac{\varepsilon_s\xi_n^{(-)'}(kR)j_n(k_sR) - \psi_n'(k_sR)h_n^{(-)}(kR)}{2in_s}\\ N_{S,n}^{(h)}(kR) &= kR\frac{\xi_n^{(-)'}(kR)j_n(k_sR) - \psi_n'(k_sR)h_n^{(-)}(kR)}{2i}\\ D_n^{(e)}(kR) &= kR\frac{\varepsilon_s\xi_n^{(+)'}(kR)j_n(k_sR) - \psi_n'(k_sR)h_n^{(+)}(kR)}{2in_s}\\ D_n^{(h)}(kR) &= kR\frac{\xi_n^{(+)'}(kR)j_n(k_sR) - \psi_n'(k_sR)h_n^{(+)}(kR)}{2i}\end{aligned} \tag{A.10}$$

and rewrite the $S_n^{(e,h)}$ and $\Xi_n^{(e)}$ coefficients:

$$S_n^{(e,h)} = -\frac{N_{S,n}^{(e,h)}(kR)}{D_n^{(e,h)}(kR)},\ \Xi_n^{(e,h)} = \frac{1}{D_n^{(e,h)}(kR)} \tag{A.11}$$

Finally, we can also introduce the partial logarithmic derivatives of the Bessel, Neumann and Hankel functions:

$$\varphi_n^{(1)}(z) = \frac{\psi_n'(z)}{j_n(z)},\ \varphi_n^{(2)}(z) = \frac{\chi_n'(z)}{y_n(z)},\ \varphi_n^{(\pm)}(z) = \frac{\xi_n^{(\pm)'}(z)}{h_n^{(\pm)}(z)} \tag{A.12}$$

and rewrite the S-matrix coefficients as:

$$\begin{aligned}S_n^{(e)} &= -\frac{h_n^{(-)}(kR)}{h_n^{(+)}(kR)}\frac{\varepsilon_s\varphi_n^{(-)}(kR) - \varphi_n^{(1)}(k_sR)}{\varepsilon_s\varphi_n^{(+)}(kR) - \varphi_n^{(1)}(k_sR)}\\ S_n^{(h)} &= -\frac{h_n^{(-)}(kR)}{h_n^{(+)}(kR)}\frac{\varphi_n^{(-)}(kR) - \varphi_n^{(1)}(k_sR)}{\varphi_n^{(+)}(kR) - \varphi_n^{(1)}(k_sR)}\end{aligned} \tag{A.13}$$

A.2.1 T-matrix coefficients of a spherical scatterer:

Calculations of the previous section can be repeated to evaluate the analytical expressions of the T and Ω matrix coefficients. In this case, the internal and external total field expansions are:

$$\begin{aligned}
\mathbf{E}_{tot}(k\mathbf{r}) &= E_0 \sum_{n=1}^{\infty} \sum_{m=-n}^{n} e_{n,m}^{(h)} \left(\mathbf{M}_{n,m}^{(1)}(k\mathbf{r}) + T_{n,m}^{(h)} \mathbf{M}_{n,m}^{(+)}(k\mathbf{r}) \right) \\
&\quad + e_{n,m}^{(e)} \left(\mathbf{N}_{n,m}^{(1)}(k\mathbf{r}) + T_{n,m}^{(e)} \mathbf{N}_{n,m}^{(+)}(k\mathbf{r}) \right) \\
\mathbf{H}_{tot}(k\mathbf{r}) &= \frac{kE_0}{i\mu_0\omega} \sum_{n=1}^{\infty} \sum_{m=-n}^{n} e_{n,m}^{(e)} \left(\mathbf{M}_{n,m}^{(1)}(k\mathbf{r}) + T_{n,m}^{(e)} \mathbf{M}_{n,m}^{(+)}(k\mathbf{r}) \right) \\
&\quad + e_{n,m}^{(h)} \left(\mathbf{N}_{n,m}^{(1)}(k\mathbf{r}) + T_{n,m}^{(h)} \mathbf{N}_{n,m}^{(+)}(k\mathbf{r}) \right) \\
\mathbf{E}_{int}(k\mathbf{r}) &= E_0 \sum_{n=1}^{\infty} \sum_{m=-n}^{n} u_{n,m}^{(h)} \mathbf{M}_{n,m}^{(1)}(k_s\mathbf{r}) + u_{n,m}^{(e)} \mathbf{N}_{n,m}^{(1)}(k_s\mathbf{r}) \\
\mathbf{H}_{int}(k\mathbf{r}) &= \frac{k_s E_0}{i\mu_0\omega} \sum_{n=1}^{\infty} \sum_{m=-n}^{n} u_{n,m}^{(e)} \mathbf{M}_{n,m}^{(1)}(k_s\mathbf{r}) + u_{n,m}^{(h)} \mathbf{N}_{n,m}^{(1)}(k_s\mathbf{r})
\end{aligned} \tag{A.14}$$

The continuity conditions (A.3) thus become:

$$\begin{aligned}
E_0 . e_{n,m}^{(h)} \left(j_n(kR) + T_n^{(h)} h_n^{(+)}(kR) \right) &= E_0 . u_{n,m}^{(h)} . j_n(k_s R) \\
E_0 . e_{n,m}^{(e)} \left(\frac{\psi_n'(kR)}{kR} + T_n^{(e)} \frac{\xi_n^{(+)'}(kR)}{kR} \right) &= E_0 . u_{n,m}^{(e)} \frac{\psi_n'(k_s R)}{k_s R} \\
\frac{kE_0}{i\mu_0\omega} e_{n,m}^{(e)} \left(j_n(kR) + T_n^{(e)} h_n^{(+)}(kR) \right) &= \frac{k_s E_0}{i\mu_0\omega} u_{n,m}^{(e)} . j_n(k_s R) \\
\frac{kE_0}{i\mu_0\omega} e_{n,m}^{(h)} \left(\frac{\psi_n'(kR)}{kR} + T_n^{(h)} \frac{\xi_n^{(+)'}(kR)}{kR} \right) &= \frac{k_s E_0}{i\mu_0\omega} u_{n,m}^{(h)} \frac{\psi_n'(k_s R)}{k_s R}
\end{aligned} \tag{A.15}$$

We obtain the following expression of the T-matrix coefficients:

$$\begin{aligned}
T_n^{(e)} &= \frac{\varepsilon_s \psi_n'(kR) j_n(k_s R) - j_n(kR) \psi_n'(k_s R)}{\psi_n'(k_s R) h_n^{(+)}(kR) - \varepsilon_s \xi_n^{(+)'}(kR) j_n(k_s R)} \\
T_n^{(h)} &= \frac{\psi_n'(k_s R) j_n(kR) - \psi_n'(kR) j_n(k_s R)}{j_n(k_s R) \xi_n^{(+)'}(kR) - h_n^{(+)}(kR) \psi_n'(k_s R)}
\end{aligned} \tag{A.16}$$

and recalling the Ω matrix coefficient definitions:

$$\Omega_n^{(e)} = \frac{u_{n,m}^{(e)}}{e_{n,m}^{(e)}}, \; \Omega_n^{(h)} = \frac{u_{n,m}^{(h)}}{e_{n,m}^{(h)}} \tag{A.17}$$

we can also derive the following analytical expression for $\Omega_n^{(e,h)}$:

$$\begin{aligned}\Omega_n^{(e)} &= \frac{n_s\left(\psi_n'(kR)h_n^{(+)}(kR) - \xi_n^{(+)'}(kR)j_n(kR)\right)}{\psi_n'(k_sR)h_n^{(+)}(kR) - \varepsilon_s\xi_n^{(+)'}(kR)j_n(k_sR)} \\ \Omega_n^{(h)} &= \frac{j_n(kR)\xi_n^{(+)'}(kR) - h_n^{(+)}(kR)\psi_n'(kR)}{j_n(k_sR)\xi_n^{(+)'}(kR) - h_n^{(+)}(kR)\psi_n'(k_sR)}\end{aligned} \tag{A.18}$$

Again, we can use the wronskian between Bessel and Hankel functions $W\left(j_n(z), h_n(z)\right) = iz^{-2}$ calculated from $W\left(j_n(z), y_n(z)\right) = z^{-2}$, the previous expressions become:

$$\begin{aligned}\Omega_n^{(e)} &= \frac{in_s}{kR\left(\varepsilon_s\xi_n^{(+)'}(kR)j_n(k_sR) - \psi_n'(k_sR)h_n^{(+)}(kR)\right)} \\ \Omega_n^{(h)} &= \frac{i}{kR\left(j_n(k_sR)\xi_n^{(+)'}(kR) - h_n^{(+)}(kR)\psi_n'(k_sR)\right)}\end{aligned} \tag{A.19}$$

Once again, we can use numerator and denominator functions to rewrite the T-matrix coefficients. The same denominator functions as for the S-matrix are used but different numerator functions have to be introduced:

$$\begin{aligned}N_{T,n}^{(e)}(kR) &= kR\frac{\varepsilon_s\psi_n'(kR)j_n(k_sR) - j_n(kR)\psi_n'(k_sR)}{2in_s} \\ N_{T,n}^{(h)}(kR) &= kR\frac{\psi_n'(kR)j_n(k_sR) - \psi_n'(k_sR)j_n(kR)}{2i} \\ D_n^{(e)}(kR) &= kR\frac{\varepsilon_s\xi_n^{(+)'}(kR)j_n(k_sR) - \psi_n'(k_sR)h_n^{(+)}(kR)}{2in_s} \\ D_n^{(h)}(kR) &= kR\frac{\xi_n^{(+)'}(kR)j_n(k_sR) - \psi_n'(k_sR)h_n^{(+)}(kR)}{2i}\end{aligned} \tag{A.20}$$

leading to the following expressions for the T matrix coefficients:

$$T_n^{(e,h)} = -\frac{N_{T,n}^{(e,h)}(kR)}{D_n^{(e,h)}(kR)},\ \Omega_n^{(e,h)} = \frac{1}{2D_n^{(e,h)}(kR)} \tag{A.21}$$

That also leads to the following expressions of the T-matrix coefficients in terms of the partial logarithmic derivative of the Bessel and Hankel functions:

$$
\begin{aligned}
T_n^{(e)} &= -\frac{j_n(kR)}{h_n^{(+)}(kR)} \frac{\varepsilon_s \varphi_n^{(1)}(kR) - \varphi_n^{(1)}(k_s R)}{\varepsilon_s \varphi_n^{(+)}(kR) - \varphi_n^{(1)}(k_s R)} \\
T_n^{(h)} &= -\frac{j_n(kR)}{h_n^{(+)}(kR)} \frac{\varphi_n^{(1)}(kR) - \varphi_n^{(1)}(k_s R)}{\varphi_n^{(+)}(kR) - \varphi_n^{(1)}(k_s R)}
\end{aligned}
\tag{A.22}
$$

A.2.2 K-matrix coefficients of a spherical scatterer:

Finally, the K-matrix ceofficients of spherically symmetric scatterers can also be obtained in similar way leading to:

$$
\begin{aligned}
K_n^{(e)} &= \frac{\varepsilon_s \psi_n'(kR) j_n(k_s R) - j_n(kR) \psi_n'(k_s R)}{y_n(kR) \psi_n'(k_s R) - \varepsilon_s \chi_n'(kR) j_n(k_s R)} \\
K_n^{(h)} &= \frac{\psi_n'(kR) j_n(k_s R) - j_n(kR) \psi_n'(k_s R)}{y_n(kR) \psi_n'(k_s R) - \chi_n'(kR) j_n(k_s R)}
\end{aligned}
\tag{A.23}
$$

Introducing new denominator functions:

$$
\begin{aligned}
N_{T,n}^{(e)}(kR) &= kR \frac{\varepsilon_s \psi_n'(kR) j_n(k_s R) - j_n(kR) \psi_n'(k_s R)}{2 i n_s} \\
N_{T,n}^{(h)}(kR) &= kR \frac{\psi_n'(kR) j_n(k_s R) - \psi_n'(k_s R) j_n(kR)}{2i} \\
D_{K,n}^{(e)}(kR) &= kR \frac{\varepsilon_s \chi_n^{(+)'}(kR) j_n(k_s R) - \psi_n^{'}(k_s R) y_n(kR)}{2 i n_s} \\
D_{K,n}^{(h)}(kR) &= kR \frac{\chi_n^{(+)'}(kR) j_n(k_s R) - \psi_n^{'}(k_s R) y_n(kR)}{2i}
\end{aligned}
\tag{A.24}
$$

Expressions (A.26) can be cast:

$$
K_n^{(e,h)} = -\frac{N_{T,n}^{(e,h)}(kR)}{D_{K,n}^{(e,h)}(kR)}
\tag{A.25}
$$

and they can also be reexpressed in terms of the partial logarithmic derivative of Bessel and Neumann functions:

$$
\begin{aligned}
K_n^{(e)} &= -\frac{j_n(kR)}{y_n(kR)} \frac{\varepsilon_s \varphi_n^{(1)}(kR) - \varphi_n^{(1)}(k_s R)}{\varepsilon_s \varphi_n^{(2)}(kR) - \varphi_n^{(1)}(k_s R)} \\
K_n^{(h)} &= -\frac{j_n(kR)}{y_n(kR)} \frac{\varphi_n^{(1)}(kR) - \varphi_n^{(1)}(k_s R)}{\varphi_n^{(2)}(kR) - \varphi_n^{(1)}(k_s R)}
\end{aligned}
\tag{A.26}
$$

A.3 Multipole expansion of the power:

We aim at deriving the flow of the Poynting vector over a spherical surface Ω:

$$\lim_{r\to\infty}\iint_{\Omega}\hat{\mathbf{r}}\cdot\langle\mathbf{S}\rangle_{\omega}r^2d\Omega=\lim_{r\to\infty}\frac{1}{2}\frac{kr^2}{\omega\mu_0}\iint_{\Omega}\mathbf{E}_{out}\cdot\mathbf{E}_{out}^{*}d\Omega-\lim_{r\to\infty}\frac{1}{2}\frac{kr^2}{\omega\mu_0}\iint_{\Omega}\mathbf{E}_{in}\cdot\mathbf{E}_{in}^{*}d\Omega \tag{A.27}$$

One can calculate independently the 2 terms on the right hand side of the previous equation by using the multipolar formulation of the incoming and outgoing fields:

$$\begin{aligned}\lim_{r\to\infty}\mathbf{E}_{in}(k\mathbf{r})&=\frac{E_0}{kr}e^{-ikr}\sum_{n=1}^{\infty}\sum_{m=-n}^{n}i^{n+1}s_{n,m}^{(e,-)}\mathbf{X}_{n,m}(\theta,\phi)+i^{n}s_{n,m}^{(h,-)}\mathbf{Z}_{n,m}(\theta,\phi)\\\lim_{r\to\infty}\mathbf{E}_{out}(k\mathbf{r})&=\frac{E_0}{kr}e^{ikr}\sum_{n=1}^{\infty}\sum_{m=-n}^{n}(-i)^{n+1}s_{n,m}^{(e,-)}S_n^{(e)}\mathbf{X}_{n,m}(\theta,\phi)+(-i)^{n}s_{n,m}^{(h,-)}S_n^{(h)}\mathbf{Z}_{n,m}(\theta,\phi)\end{aligned} \tag{A.28}$$

It follows that the contributions of the outgoing and incoming fields to the Poynting vector are:

$$\begin{aligned}\lim_{r\to\infty}\frac{1}{2}\frac{kr^2}{\omega\mu_0}\iint_{\Omega}\mathbf{E}_{out}\cdot\mathbf{E}_{out}^{*}d\Omega&=\lim_{r\to\infty}\frac{c|E_0|^2}{2\omega^2\mu_0}\sum_{n=1}^{\infty}\sum_{m=-n}^{n}|s_{n,m}^{(e,-)}|^2\left|S_n^{(e)}\right|^2+|s_{n,m}^{(h,-)}|^2\left|S_n^{(h)}\right|^2\\\lim_{r\to\infty}\frac{1}{2}\frac{kr^2}{\omega\mu_0}\iint_{\Omega}\mathbf{E}_{in}\cdot\mathbf{E}_{in}^{*}d\Omega&=\lim_{r\to\infty}\frac{c|E_0|^2}{2\omega^2\mu_0}\sum_{n=1}^{\infty}\sum_{m=-n}^{n}|s_{n,m}^{(e,-)}|^2+|s_{n,m}^{(h,-)}|^2\end{aligned} \tag{A.29}$$

where the orthogonality relation of the vector spherical harmonics has been used:

$$\langle\mathbf{W}_{n,m}^{(i)}|\mathbf{W}_{n,m}^{(j)}\rangle=\int_0^{4\pi}\mathbf{W}_{n,m}^{(i)*}.\mathbf{W}_{n,m}^{(j)}d\Omega=\delta_{ij}\delta_{n\nu}\delta_{m\mu} \tag{A.30}$$

A.3.1 Taylor series Expansions of K_n

We give below the development up to the 6th order in kR of the inverse reaction matrix. In most of the predictions and simulations of this work, a fourth order expansion in kR suffices, but the 6^{th} order sometimes proved useful to test convergence

or to achieve additional accuracy.

$$[K_n^{(e)}]^{-1} \simeq -\frac{(2n-1)!!(2n+1)!!}{(n+1)(\overline{\varepsilon}_s-1)x^{2n+1}}\left((n\overline{\varepsilon}_s+n+1)+\frac{(2n+1)((n-2)\overline{\varepsilon}_s+n+1)}{(2n-1)(2n+3)}x^2\right. \tag{A.31a}$$

$$\left.+x^4C_4^{(e)}+x^6C_6^{(e)}\right) \tag{A.31b}$$

$$[K_n^{(h)}]^{-1} \simeq -\frac{(2n+1)\,(2n+3)\,(2n-1)!!\,(2n+1)!!}{(\overline{\varepsilon}_s-1)\,x^{2n+3}}\left(1+\frac{(2n-2\overline{\varepsilon}_s+3)}{(2n+1)(2n+5)}x^2\right. \tag{A.31c}$$

$$\left.+x^4C_4^{(h)}+x^6C_6^{(h)}\right) \tag{A.31d}$$

where the fourth and sixth order coefficients, respectively C_4 and C_6, are given by:

$$C_4^{(e)} = (2n+1)\frac{(n+3)(n+1)^2+(n-4)(n+3)(n+1)\overline{\varepsilon}_s-(2n-3)\overline{\varepsilon}_s^2}{(n+1)(2n-3)(2n+3)^2(2n+5)} \tag{A.32a}$$

$$C_4^{(h)} = \frac{(n+4)(2n+3)^2-4(n+4)(2n+3)\overline{\varepsilon}_s-(2n-1)\overline{\varepsilon}_s^2}{(2n-1)(2n+3)(2n+5)^2(2n+7)} \tag{A.32b}$$

$$C_6^{(e)} = (2n+1)\frac{(n+1)\,(2n^2+15n+30)\,[(n+1)+(n-6)\overline{\varepsilon}_s]-3(2n-5)\overline{\varepsilon}_s^2\,[(2n+9)+2\overline{\varepsilon}_s]}{3(n+1)(2n-5)(2n+3)^3(2n+5)(2n+7)} \tag{A.32c}$$

$$C_6^{(h)} = \frac{(2n+3)\,(2n^2+19n+47)\,[(2n+3)-6\overline{\varepsilon}_s]-3(2n-3)\overline{\varepsilon}^2\,[(2n+11)+2\overline{\varepsilon}]}{3(2n-3)(2n+3)(2n+5)^3(2n+7)(2n+9)} \tag{A.32d}$$

which for the $n=1$ case are:

$$C_6^{(e)} = -\frac{188-470\varepsilon_s+99\varepsilon_s^2+18\varepsilon_s^3}{47250(\varepsilon_s+2)} \tag{A.33a}$$

$$C_6^{(h)} = -\frac{1700-2040\varepsilon_s+39\varepsilon_s^2+6\varepsilon_s^3}{509355} \tag{A.33b}$$

and the double factorial operator !! is defined such that:

$$n!! = \prod_{k=0}^{m}(n-2k) = n(n-2)(n-4)\ldots \tag{A.34}$$

where $m = \mathrm{Int}\,[(n+1)/2]-1$ with $0!!=1$; or in terms of ordinary factorials via the relations $(2n-1)!! = \frac{(2n)!}{2^n n!}$ and $(2n)!! = 2^n n!$ for $n=0,1,2,\ldots$

Appendix B

Appendix B

B.1 Exact formulas for near-field enhancements

Formally exact expressions for the field enhancement factors, Eq.(4.22) can be written:

$$\begin{aligned}\left\langle I_{\text{enh}}^{(e)}\right\rangle &= \sum_{n=1}^{\infty}\left\{\widetilde{g}_n^{(1,e)}(\eta)\left|T_n^{(h)}\right|^2 + \widetilde{g}_n^{(2,e)}(\eta)\left|T_n^{(e)}\right|^2\right\}\\ \left\langle I_{\text{enh}}^{(h)}\right\rangle &= \sum_{n=1}^{\infty}\left\{\widetilde{g}_n^{(1,h)}(kr)\left|T_n^{(e)}\right|^2 + \widetilde{g}_n^{(2,h)}(kr)\left|T_n^{(h)}\right|^2\right\}\end{aligned} \tag{B.1}$$

We remark that Eq.(B.1) is valid numerically only if the infinite multipole summation is cutoff to a value $n_{\max} > kr$ with r being the distance from the center of the particle. This differs from approximate formula of Eq.(4.22) where the multipole summation can be be stopped at the usual Mie cutoff condition of $n_{\max} > kR$.

The enhancement functions of Eq.(B.1) are written:

$$\begin{aligned}\widetilde{g}_n^{(1,e)}(\eta) &= \frac{2n+1}{2}\left|\frac{j_n(\eta)}{T_n^{(h)}} + h_n^{(+)}(\eta)\right|^2\\ \widetilde{g}_n^{(2,e)}(\eta) &= \frac{n+1}{2}\left|\frac{j_{n-1}(\eta)}{T_n^{(e)}} + h_{n-1}^{(+)}(\eta)\right|^2 + \frac{n}{2}\left|\frac{j_{n+1}(\eta)}{T_n^{(e)}} + h_{n+1}^{(+)}(\eta)\right|^2\\ \widetilde{g}_n^{(1,h)}(\eta) &= \frac{2n+1}{2}\left|\frac{j_n(\eta)}{T_n^{(e)}} + h_n^{(+)}(\eta)\right|^2\\ \widetilde{g}_n^{(2,h)}(\eta) &= \frac{n+1}{2}\left|\frac{j_{n-1}(\eta)}{T_n^{(h)}} + h_{n-1}^{(+)}(\eta)\right|^2 + \frac{n}{2}\left|\frac{j_{n+1}(\eta)}{T_n^{(h)}} + h_{n+1}^{(+)}(\eta)\right|^2\end{aligned} \tag{B.2}$$

Appendix C

Appendix C

C.1 Resonance and zero conditions of b_n

It has been shown in section 5.2 that a good prediction of the first resonance of b_n in the limit $z_0 << 1$ could be provided by the solution of the following equation:

$$\varphi_n^{(1)}(z) = -n \tag{C.1}$$

If we use the following recurrence relation for spherical Bessel functions (ref.[139],p.439):

$$\begin{aligned} j_n'(z) &= -\frac{n+1}{z} j_n(z) + j_{n-1}(z) \\ \Rightarrow [z j_n(z)]' &= -n j_n(z) + z j_{n-1}(z) \\ \Rightarrow \varphi_n^{(1)}(z) &= -n + z\frac{j_{n-1}(z)}{j_n(z)} \end{aligned} \tag{C.2}$$

It then follows that Eq. C.1 is verified for the zeros of Bessel functions of order $n-1$: $z = r_{n-1,l}$.

C.2 Weierstrass factorization of Bessel functions

As demonstrated by Watson in [138] (p 497-498), it is possible to express cylindrical Bessel functions as an infinite product of factors involving their zeros:

$$J_\nu(z) = \frac{1}{\Gamma(\nu+1)}\left(\frac{z}{2}\right)^\nu \prod_{n=1}^{\infty}\left(1-\left(\frac{z}{z_{\nu,n}}\right)^2\right) \tag{C.3}$$

where $z_{\nu,n}$ is the n^{th} zero of the cylindrical Bessel functions of order ν. This expression can be generalized to the spherical Bessel functions j_n by means of the relation: $j_n(z) = \sqrt{\frac{\pi}{2z}}J_{n+1/2}(z)$. If we set $r_{n,j} \equiv z_{n+1/2,j}$ and if we notice that $\Gamma(n+1/2) = 2^{-n}\sqrt{\pi}(2n-1)!!$, we get the following expression (5.16):

$$j_n(z) = \frac{z^n}{(2n+1)!!}\prod_{l=1}^{\infty}\left(1-\left(\frac{z}{r_{n,l}}\right)^2\right) \tag{C.4}$$

The double factorial operator !! is defined such that:

$$n!! = \prod_{k=0}^{m}(n-2k) = n(n-2)(n-4)\ldots \tag{C.5}$$

where $m = \mathrm{Int}\left[(n+1)/2\right]-1$ with $0!! = 1$; or in terms of ordinary factorials *via* the relations $(2n-1)!! = \frac{(2n)!}{2^n n!}$ and $(2n)!! = 2^n n!$ for $n = 0, 1, 2, \ldots$.

These expressions are designated as Weierstrass factorizations throughout the article as it can also be obtained by using the Weierstrass factorization theorem. It can then be used to derive an expression of $\varphi_n^{(1)}$ functions also appearing in our formulation of the Mie coefficients. One should first notice that $\varphi_n^{(1)}$ as defined in (A.12) is equal to z times the logarithmic derivative of the Ricatti Bessel functions $zj_n(z)$. From (5.16), it is then straightforward to show that:

$$\begin{aligned}
&\varphi_n^{(1)}(z) = \\
&z\left((n+1)\frac{1}{z} + \sum_{l=1}^{\infty}\left(-\frac{2z}{(r_{n,l})^2}\right)\frac{1}{1-\left(\frac{z}{r_{n,l}}\right)^2}\right), \\
&\varphi_n^{(1)}(z) = n+1+\sum_{l=1}^{\infty}\frac{2z^2}{z^2-(r_{n,l})^2}.
\end{aligned} \tag{C.6}$$

C.3 Approximation of $\varphi_n^{(1)}$ for a_n

As suggested in [159] (see notably the supplementary material), the expressions derived in Appendix C.1 can be used to approximate functions j_n and $\varphi_n^{(1)}$ as an alternative to their Taylor series expansions. It was this method that was followed to derive the approximations (5.18), (5.19) and (5.20). Here, we provide a demonstration of these two expressions. $\varphi_n^{(1)}$ is equal to:

$$\begin{aligned}\varphi_n^{(1)}(z) &= n+1+\frac{2z^2}{z^2-r_n^2}+\sum_{l=2}^{\infty}\frac{2z^2}{z^2-(r_{n,l})^2} \\ &= n+1+\frac{2z^2}{z^2-r_n^2}-2z^2\sum_{l=2}^{\infty}\frac{1}{(r_{n,l})^2}\frac{1}{1-\frac{z^2}{(r_{n,l})^2}}\end{aligned} \tag{C.7}$$

As in our study $z << r_{n,2}$, for $l \geq 2$ $\frac{1}{1-\frac{z^2}{(r_{n,l})^2}} \simeq 1$ which leads to:

$$\varphi_1^{(1)}(z) \simeq 2+\frac{2z^2}{z^2-r_n^2}-2z^2\sum_{l=2}^{\infty}\frac{1}{(r_{1,l})^2}. \tag{C.8}$$

Finally, as $\sum_{l=1}^{\infty}\frac{1}{(r_{n,l})^2} = \frac{1}{2(2n+3)}$ (see [138], p 502), Eq. C.8 simplifies to:

$$\varphi_n(z) \approx n+1+\frac{2z^2}{z^2-(r_n)^2}+2\rho_n z^2, \tag{C.9}$$

where $\rho_n \equiv \frac{1}{r_n^2}-\frac{1}{2(2n+3)}$.

Moreover, we can apply the same idea to approximate the spherical bessel functions j_n:

$$j_n(z) = \frac{z^n}{(2n+1)!!}\left(1-\left(\frac{z}{r_{n,1}}\right)^2\right)\prod_{l=2}^{\infty}\left(1-\left(\frac{z}{r_{n,l}}\right)^2\right), \tag{C.10}$$

and $\prod_{l=2}^{\infty}\left(1-\left(\frac{z}{r_{n,l}}\right)^2\right)$ can be approximated:

$$\begin{aligned}\prod_{l=2}^{\infty}\left(1-\left(\frac{z}{r_{n,l}}\right)^2\right) &= exp(ln(\prod_{l=2}^{\infty}\left(1-\left(\frac{z}{r_{n,l}}\right)^2\right))) \\ &= exp(\sum_{l=2}^{\infty} ln\left(1-\left(\frac{z}{r_{n,l}}\right)^2\right)).\end{aligned} \tag{C.11}$$

If $z << r_{n,2}$, $\sum_{l=2}^{\infty} ln\left(1-\left(\frac{z}{r_{n,l}}\right)^2\right) \rightarrow -\sum_{l=2}^{\infty}\left(\frac{z}{r_{n,l}}\right)^2$, it then follows from the previous results that:

$$\prod_{l=2}^{\infty}\left(1-\left(\frac{z}{r_{n,l}}\right)^2\right) \simeq exp(\rho_n z^2), \tag{C.12}$$

which leads to the following approximation for j_n:

$$j_n(z) \simeq \frac{z^n}{(2n+1)!!}\left(1-\left(\frac{z}{r_{n,1}}\right)^2\right) exp(\rho_n z^2) \tag{C.13}$$

C.4 Approximation of $\varphi_n^{(1)}$ for b_n

In order to approximate the function $\varphi_n^{(1)}$ at the vicinity of the resonance condition of b_n, we can make the choice to take the power series expansion around $z_s = r_{n-1}$:

$$\varphi_n^{(1)}(z) \simeq \varphi_n^{(1)}(r_{n-1}) + (z-r_{n-1})\left.\frac{d\varphi_n^{(1)}}{dz}\right|_{r_{n-1}} + ... \tag{C.14}$$

$$\begin{aligned}\frac{d\varphi_n^{(1)}}{dz}(z) &= \frac{d}{dz}\left(z\frac{j_{n-1}(z)}{j_n(z)}\right)\\ &= \frac{j_{n-1}(z)}{j_n(z)} + zj_{n-1}(z)\frac{d}{dz}\left(\frac{1}{j_n(z)}\right)\\ &+ \frac{z}{j_n(z)}\frac{dj_{n-1}}{dz}(z)\end{aligned} \tag{C.15}$$

which leads to:

$$\left.\frac{d\varphi_n^{(1)}}{dz}\right|_{r_{n-1}} = \frac{r_{n-1}}{j_n(r_{n-1})}j'_{n-1}(r_{n-1}) \tag{C.16}$$

By using a recurrence relation for spherical Bessel functions (ref.[139],p.439):

$$-\frac{n}{z}j_n(z) + j'_n(z) = -j_{n+1}(z), \tag{C.17}$$

we can show that $j'_{n-1}(r_{n-1}) = -j_n(r_{n-1})$. This result leads to:

$$\left.\frac{d\varphi_n^{(1)}}{dz}\right|_{r_{n-1}} = -r_{n-1} \tag{C.18}$$

Similar calculations allow us to show that $\varphi_n^{(1)''}(r_{n-1}) = -2(n+1)$ and $\left.\frac{d^3\varphi_n^{(1)}}{dz^3}\right|_{r_{n-1}} = -2\frac{n(2n+1)}{r_{n-1}} - 2r_{n-1}$.

C.5 Approximation of a_n

$\varphi_n^{(A1)}$ may be re-expressed in the following way:

$$\varphi_n^{(A1)}(z_0) = n + 1 + \frac{2z_n^2}{z_n^2-1} + 2\rho_n.z_0^2 \tag{C.19}$$

$$= \frac{(n+3)z_n^2-(n+1)}{z_n^2-1} + 2\rho_n.z_0^2 \tag{C.20}$$

$$\varphi_n^{(A1)}(z_0) = (n+1)\frac{\frac{(n+3)}{(n+1)}z_n^2-1}{z_n^2-1} + 2\rho_n.z_0^2 \tag{C.21}$$

that leads to:

$$\begin{aligned}
&\varepsilon_s\varphi_n^{(A1)}(z_0) - \varphi_n^{(A1)}(z_s) = \\
&\varepsilon_s\left((n+1)\frac{\frac{(n+3)}{(n+1)}z_n^2-1}{z_n^2-1} + 2\rho_n.z_0^2\right) - \\
&\left((n+1)\frac{\frac{(n+3)}{(n+1)}\varepsilon_s z_n^2-1}{\varepsilon_s z_n^2-1} + 2\rho_n.\varepsilon_s.z_0^2\right) \\
&= \frac{(n+1)(\varepsilon_s-1)}{1-z_n^2}\left(1 - z_n^2\frac{\frac{(n+3)}{(n+1)}\varepsilon_s z_n^2-1}{\varepsilon_s z_n^2-1}\right) \\
&\varepsilon_s\varphi_n^{(A1)}(z_0) - \varphi_n^{(A1)}(z_s) = \\
&\frac{(n+1)(\varepsilon_s-1)\left(f_n(\varepsilon_s,z_0) - z_n^2\right)}{(1-z_n^2)f_n(\varepsilon_s,z_0)}
\end{aligned} \tag{C.22}$$

The numerator of a_n can then be re-expressed in the following way:

$$\begin{aligned}
&j_n^{(A1)}(z_0)\left(\varepsilon_s\varphi_n^{(A1)}(z_0) - \varphi_n^{(A1)}(z_s)\right) = \\
&\frac{(n+1)z_0^n}{(2n+1)!!}\frac{e^{\rho_n z_0^2}}{f_n(\varepsilon_s,z_0)}(\varepsilon_s-1)\left(f_n(\varepsilon_s,z_0) - z_n^2\right)
\end{aligned} \tag{C.23}$$

where the function f_n has been defined in the article. The denominator can be also

simplified:

$$\begin{aligned}
&h_n^{(+)}(z_0)\left(\varepsilon_s\varphi_n^{(+)}(z_0)-\varphi_n^{(A1)}(z_s)\right)= \\
&\frac{e^{iz_0}}{z_0^{n+1}}Q_n(z_0)\times \\
&\left(\varepsilon_s\varphi_n^{(+)}(z_0)-(n+1)\frac{\frac{(n+3)}{(n+1)}\varepsilon_s.z_n^2-1}{\varepsilon_s.z_n^2-1}-2\rho_n.\varepsilon_s z_0^2\right) \\
&h_n^{(+)}(z_0)\left(\varepsilon_s\varphi_n^{(+)}(z_0)-\varphi_n^{(A1)}(z_s)\right)= \\
&\frac{e^{iz_0}}{z_0^{n+1}}\frac{Q_n(z_0)}{.f_n(\varepsilon_s,z_0)}\left(\varepsilon_s.f_n(\varepsilon_s,z_0)g_n(z_0)-(n+1)\right)
\end{aligned} \tag{C.24}$$

where g_n has been defined in the article. That finally leads to the following approximation of the electric Mie coefficients:

$$\begin{aligned}
a_n^{(A1)} &= \frac{(n+1)z_0^{2n+1}}{(2n+1)!!}\frac{e^{\rho_n z_0^2-iz_0}}{Q_n(z_0)}\times \\
&\frac{(\varepsilon_s-1)\left(f_n(\varepsilon_s,z_0)-z_n^2\right)}{\varepsilon_s.f_n(\varepsilon_s,z_0)g_n(z_0)-(n+1)}
\end{aligned} \tag{C.25}$$

C.6 Approximation of b_n

$$\begin{aligned}
&\varphi_n^{(A1)}(z_0)-\varphi_n^{(A1)}(z_s)= \\
&\frac{2z_n^2}{z_n^2-1}+2\rho_n.z_0^2-\frac{2\varepsilon_s z_n^2}{\varepsilon_s z_n^2-1}-2\rho_n.\varepsilon_s.z_0^2 \\
&=-2\rho_n.z_0^2(\varepsilon_s-1)+2z_n^2\left(\frac{\varepsilon_s-1}{(z_n^2-1)(\varepsilon_s z_n^2-1)}\right)
\end{aligned} \tag{C.26}$$

if we assume that $z_n^2 << 1$ it then leads to:

$$\varphi_n^{(A1)}(z_0)-\varphi_n^{(A1)}(z_s)\simeq(\varepsilon_s-1)\left(-\frac{2z_n^2}{\varepsilon_s z_n^2-1}-2\rho_n.z_0^2\right) \tag{C.27}$$

keeping the assumption $z_n^2 << 1$ in the approximation $j_n^{(A1)}$, it then follows that

$$\begin{aligned}
&j_n^{(A1)}(z_0)\left(\varepsilon_s\varphi_n^{(A1)}(z_0)-\varphi_n^{(A1)}(z_s)\right) \\
&\simeq\frac{z_0^{2n+1}}{(2n+1)!!}e^{\rho_n z_0^2}(\varepsilon_s-1)L_n(\varepsilon_s,z_0)
\end{aligned} \tag{C.28}$$

the denominator can be also approximated:

$$\begin{aligned}
&\varphi_n^{(+)}(z_0) - \varphi_n^{(A1)}(z_s) = \\
&\varphi_n^{(+)}(z_0) - (n+1) - \varepsilon_s \left(\frac{2z_n^2}{z_n^2 - 1} + 2\rho_n . z_0^2 \right) \\
&= \varepsilon_s L_n(\varepsilon_s, z_0) + \varphi_n^{(+)}(z_0) - (n+1)
\end{aligned} \tag{C.29}$$

that then leads to the following approximation for b_n :

$$\begin{aligned}
&b_n^{(A1)} = \frac{z_0^{2n+1}}{(2n+1)!!} \times \\
&\frac{e^{\rho_n z_0^2 - i z_0}}{Q_n(z_0)} \frac{(\varepsilon_s - 1) L_n(\varepsilon_s, z_0)}{\varepsilon_s L_n(\varepsilon_s, z_0) + \varphi_n^{(+)}(z_0) - (n+1)}
\end{aligned} \tag{C.30}$$

C.7

The outgoing spherical Hankel functions can be written in the following form:

$$\begin{aligned}
h_n^{(+)}(z) &= (-i)^{n+1} \frac{e^{iz}}{z} \sum_{s=0}^{n} \frac{i^s}{s!(2z)^s} \frac{(n+s)!}{(n-s)!} \\
&= \frac{e^{iz}}{z^{n+1}} \sum_{s=0}^{n} (-1)^{n+1} \frac{i^{n+s+1}}{s!(2)^s} \frac{(n+s)!}{(n-s)!} z^{n-s} \\
h_n^{(+)}(z) &= \frac{e^{iz}}{z^{n+1}} Q_n(z)
\end{aligned} \tag{C.31}$$

where the polynomial function $Q_n(z) = \sum_{s=0}^{n} (-1)^{n+1} \frac{i^{n+s+1}}{s!(2)^s} \frac{(n+s)!}{(n-s)!} z^{n-s}$

C.8

$$\varepsilon_{UL}^{(e2)} = \frac{-\left(\left(\frac{n+3}{r_n^2} - 2\rho_n^{(e)} \right) z_0^2 - n \right) + \sqrt{\left(\left(\frac{n+3}{r_n^2} - 2\rho_n^{(e)} \right) z_0^2 - n \right)^2 + 4(n+1) \left(n \left(\frac{z}{r_n} \right)^2 + 2\rho_n^{(e)} \frac{z^4}{r_n^2} \right)}}{\left(n \left(\frac{z}{r_n} \right)^2 + 2\rho_n^{(e)} \frac{z^4}{r_n^2} \right)} \tag{C.32}$$

Appendix D

Appendix D

D.0.1 Average of the squared modulus of the internal field:

If the internal field is expanded on the VPW basis, it can be shown that the average of the squared modulus of the internal field takes the following expression:

$$\frac{\langle |\mathbf{E}_{int}|^2 \rangle}{|\mathbf{E}_0|^2} = \sum_{n=1}^{\infty} \frac{\langle \left| E_{i,n}^{(e)} \right|^2 \rangle}{|\mathbf{E}_0|^2} + \frac{\langle \left| E_{i,n}^{(h)} \right|^2 \rangle}{|\mathbf{E}_0|^2} \tag{D.1}$$

where

$$\begin{aligned} \frac{\langle \left| E_{i,n}^{(e)} \right|^2 \rangle}{|\mathbf{E}_0|^2} &= \frac{3(2n+1)}{2z^2} I_n \left| \Omega_n^{(e)} \right|^2 \\ \frac{\langle \left| E_{i,n}^{(h)} \right|^2 \rangle}{|\mathbf{E}_0|^2} &= \frac{3(2n+1)}{2z^2} J_n \left| \Omega_n^{(h)} \right|^2 \end{aligned} \tag{D.2}$$

The functions $I_n(\varepsilon_s, z)$ and $J_n(\varepsilon_s, z)$ that have been used have the following expression:

$$\begin{aligned} I_n(\varepsilon_s, z) &= \frac{z}{2\varepsilon_s} \left(\psi_n'(n_s z) \left(\psi_n'(n_s z) + j_s(n_s z) \right) + (\varepsilon_s z^2 - n(n+1)) j_n^2(n_s z) \right) \\ J_n(\varepsilon_s, z) &= \frac{z}{2\varepsilon_s} \left(\psi_n'(n_s z) \left(\psi_n'(n_s z) - j_s(n_s z) \right) + (\varepsilon_s z^2 - n(n+1)) j_n^2(n_s z) \right) \end{aligned} \tag{D.3}$$

D.0.2 Calculation of the resonant part of the outgoing field:

In Chapter 6, the calculation of the resonant part of the outgoing field required the derivation of the following integral:

$$\int_{-\infty}^{\infty} \frac{r_{n,\alpha}^{(e)}}{\omega - p_{n,\alpha}^{(e)}} e^{-i\omega\left(t_0+\frac{r_0}{c}\right)} e^{-i\omega\left(t-t_0-\frac{r_0}{c}-\frac{r}{c}+2\frac{R}{c}\right)} d\omega \tag{D.4}$$

As was pointed out in Chapter 6, due to the presence of poles, this integral can be computed by using the theorem of residues. In particular, when $t-t_0-\frac{r_0}{c}-\frac{r}{c}+2\frac{R}{c} \leq 0$ one needs to close the contour of integration in the lower part of the complex plane as shown in Fig. D.1.

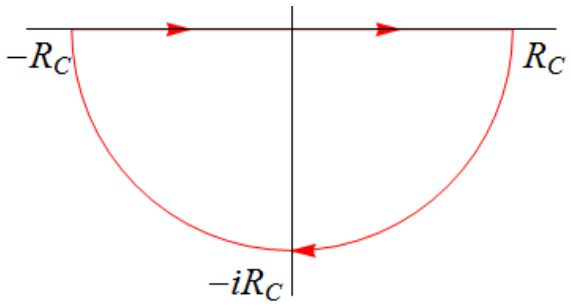

Figure D.1: Contour used to derive integral D.4

This integral thus becomes:

$$\begin{aligned}
&\int_{-\infty}^{\infty} \frac{r_{n,\alpha}^{(e)}}{\omega - p_{n,\alpha}^{(e)}} e^{-i\omega\left(t_0+\frac{r_0}{c}\right)} e^{-i\omega\left(t-t_0-\frac{r_0}{c}-\frac{r}{c}+2\frac{R}{c}\right)} d\omega = \\
&- 2\pi.i.r_{n,\alpha}^{(e)} e^{-ip_{n,\alpha}^{(e)}\left(t_0+\frac{r_0}{c}\right)} e^{-ip_{n,\alpha}^{(e)}\left(t-t_0-\frac{r_0}{c}-\frac{r}{c}+2\frac{R}{c}\right)} \\
&- \lim_{R_C\to\infty} \int_0^{-\pi} \frac{r_{n,\alpha}^{(e)}}{R_C e^{i\theta_C} - p_{n,\alpha}^{(e)}} e^{-iR_C e^{i\theta_C}\left(t_0+\frac{r_0}{c}\right)} e^{-iR_C e^{i\theta_C}\left(t-t_0-\frac{r_0}{c}-\frac{r}{c}+2\frac{R}{c}\right)} R_C e^{i\theta_C} d\theta_C
\end{aligned} \tag{D.5}$$

We will now try to demonstrate that the integration over the semi-circle in the lower part of the complex plane is null. Since $t - t_0 - \frac{r_0}{c} - \frac{r}{c} + 2\frac{R}{c} \geq 0$, $\left|e^{-i\omega\left(t-t_0-\frac{r_0}{c}-\frac{r}{c}+2\frac{R}{c}\right)}\right| \leq 1$ for all ω belonging to the lower part of the complex plane. Consequently,

$$\begin{aligned}
&\left| \frac{r_{n,\alpha}^{(e)}}{R_C e^{i\theta_C} - p_{n,\alpha}^{(e)}} e^{-iR_C e^{i\theta_C}\left(t_0+\frac{r_0}{c}\right)} e^{-iR_C e^{i\theta_C}\left(t-t_0-\frac{r_0}{c}-\frac{r}{c}+2\frac{R}{c}\right)} R_C e^{i\theta_C} d\theta_C \right| \leq \\
&\left| \frac{r_{n,\alpha}^{(e)}}{R_C e^{i\theta_C} - p_{n,\alpha}^{(e)}} e^{-iR_C e^{i\theta_C}\left(t_0+\frac{r_0}{c}\right)} \right|
\end{aligned} \tag{D.6}$$

$t_0 + \frac{r_0}{c}$ being positive, the previous expression tends towards zero faster than $\frac{1}{R_C^2}$ when $R_C \to \infty$. According to [199] (see in particular pp 422-424), the integral over the semi-circle in the lower half of the complex plane vanishes when $R_C \to \infty$. Equation (D.6) consequently becomes:

$$\int_{-\infty}^{\infty} \frac{r_{n,\alpha}^{(e)}}{\omega - p_{n,\alpha}^{(e)}} e^{-i\omega\left(t_0+\frac{r_0}{c}\right)} e^{-i\omega\left(t-t_0-\frac{r_0}{c}-\frac{r}{c}+2\frac{R}{c}\right)} d\omega = \\ -2\pi.i.r_{n,\alpha}^{(e)} e^{-ip_{n,\alpha}^{(e)}\left(t_0+\frac{r_0}{c}\right)} e^{-ip_{n,\alpha}^{(e)}\left(t-t_0-\frac{r_0}{c}-\frac{r}{c}+2\frac{R}{c}\right)} \tag{D.7}$$

On the other hand, when $t - t_0 - \frac{r_0}{c} - \frac{r}{c} + 2\frac{R}{c} > 0$, the contour of integration has to be closed in the upper part as shown in Fig. D.2. As the integrand in Eq.

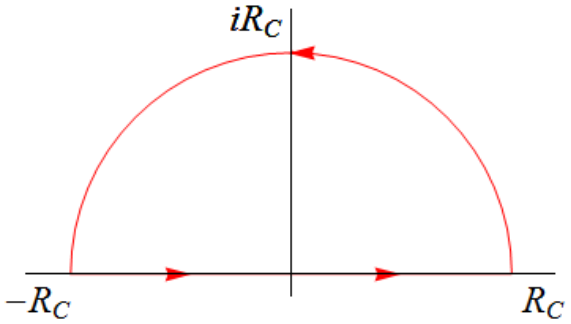

Figure D.2: contour of integration upper half complex plane

(D.4) does not admit any poles in the upper half of the complex plane and as the integration over the semi-circle in the upper half of the complex plane can be shown to vanish with similar calculations as those done previously, Eq. (D.4) turns out to be null for $t - t_0 - \frac{r_0}{c} - \frac{r}{c} + 2\frac{R}{c} > 0$. These results are in complete agreement with the causality principle.

References

[1] A. Krasnok, M. Caldarola, N. Bonod, and A. Alú. *Spectroscopy and Biosensing with Optically Resonant Dielectric Nanostructures*. arXiv preprint arXiv:1710.10233, 2017. 1

[2] M. L. Brongersma, Y. Cui, and S. Fan. *Light management for photovoltaics using high-index nanostructures*. Nature Materials, 13, 451–460, 2014. 1, 12

[3] L. R. Hirsch, R. J. Stafford, J. Bankson, S. R. Sershen, B. Rivera, R. Price, J. D. Hazle, N. J. Halas, and J. L. West. *Nanoshell-mediated near-infrared thermal therapy of tumors under magnetic resonance guidance*. Proceedings of the National Academy of Sciences, 100, 13549–13554, 2003. 1

[4] P. Lalanne, W. Yan, K. Vynck, C. Sauvan, and J.-P. Hugonin. *Light interaction with photonic and plasmonic resonances*. arXiv preprint arXiv:1705.02433, 2017. 1, 2, 10, 67

[5] C. Sauvan, J.-P. Hugonin, I. Maksymov, and P. Lalanne. *Theory of the spontaneous optical emission of nanosize photonic and plasmon resonators*. Physical Review Letters, 110, 237401, 2013. 1, 10, 11, 37, 68, 85, 114

[6] K. J. Vahala. *Optical microcavities*. Nature, 424, 839–846, 2003. 2

[7] J. A. Schuller, E. S. Barnard, W. Cai, Y. C. Jun, J. S. White, and M. L. Brongersma. *Plasmonics for extreme light concentration and manipulation*. Nature Materials, 9, 2010. 2, 93

[8] L. Lorenz. *Sur la lumière réfléchie et réfractée par une sphère transparente*. Oeuvres Scientifiques, pages 405–529, 1898. 5, 15

[9] G. Mie. *Beiträge zur Optik trüber Medien, speziell kolloidaler Metallösungen*. Annalen der Physik, 330, 377–445, 1908. 5

[10] A. I. Kuznetsov, A. E. Miroshnichenko, M. L. Brongersma, Y. S. Kivshar, and B. Luk'anchuk. *Optically resonant dielectric nanostructures*. Science, 354, aag2472, 2016. 5, 7, 14

[11] A. B. Evlyukhin, C. Reinhardt, and B. N. Chichkov. *Multipole light scattering by nonspherical nanoparticles in the discrete dipole approximation*. Physical Review B: Condensed Matter and Materials Physics, 84, 235429, 2011. 6, 7, 9, 99

[12] L. Cao, J. S. White, J.-S. Park, J. A. Schuller, B. M. Clemens, and M. L. Brongersma. *Engineering light absorption in semiconductor nanowire devices.* Nature Materials, 8, 643–647, 2009. 6, 12

[13] L. Cao, P. Fan, E. S. Barnard, A. M. Brown, and M. L. Brongersma. *Tuning the color of silicon nanostructures.* Nano Letters, 10, 2649–2654, 2010. 6, 13

[14] A. I. Kuznetsov, A. E. Miroshnichenko, Y. H. Fu, J. Zhang, and B. Luk'yanchuk. *Magnetic light.* Scientific Reports, 2, 2012. 6, 7, 56

[15] A. B. Evlyukhin, S. M. Novikov, U. Zywietz, R. L. Eriksen, C. Reinhardt, S. I. Bozhevolnyi, and B. N. Chichkov. *Demonstration of magnetic dipole resonances of dielectric nanospheres in the visible region.* Nano Letters, 12, 3749–3755, 2012. 7

[16] D. G. Baranov, D. A. Zuev, S. I. Lepeshov, O. V. Kotov, A. E. Krasnok, A. B. Evlyukhin, and B. N. Chichkov. *All-dielectric nanophotonics: the quest for better materials and fabrication techniques.* arXiv preprint arXiv:1702.00677, 2017. 7, 8, 14

[17] U. Zywietz, A. B. Evlyukhin, C. Reinhardt, and B. N. Chichkov. *Laser printing of silicon nanoparticles with resonant optical electric and magnetic responses.* Nature Communications, 5, 3402, 2014. 7, 8, 107

[18] U. Zywietz, M. K. Schmidt, A. B. Evlyukhin, C. Reinhardt, J. Aizpurua, and B. N. Chichkov. *Electromagnetic resonances of silicon nanoparticle dimers in the visible.* ACS Photonics, 2, 913–920, 2015. 7

[19] I. Staude, A. E. Miroshnichenko, M. Decker, N. T. Fofang, S. Liu, E. Gonzales, J. Dominguez, T. S. Luk, D. N. Neshev, I. Brener, et al. *Tailoring directional scattering through magnetic and electric resonances in subwavelength silicon nanodisks.* ACS Nano, 7, 7824–7832, 2013. 8, 9, 99

[20] J. Proust, F. Bedu, B. Gallas, I. Ozerov, and N. Bonod. *All-dielectric colored metasurfaces with silicon Mie resonators.* ACS Nano, 10, 7761–7767, 2016. 8, 13, 14, 99

[21] M. A. van de Haar, J. van de Groep, B. J. Brenny, and A. Polman. *Controlling magnetic and electric dipole modes in hollow silicon nanocylinders.* Optics Express, 24, 2047–2064, 2016. 8

[22] M. Abbarchi, M. Naffouti, B. Vial, A. Benkouider, L. Lermusiaux, L. Favre, A. Ronda, S. Bidault, I. Berbezier, and N. Bonod. *Wafer scale formation of monocrystalline silicon-based mie resonators via silicon-on-insulator dewetting.* ACS Nano, 8, 11181–11190, 2014. 8

[23] L. Shi, T. U. Tuzer, R. Fenollosa, and F. Meseguer. *A New Dielectric Metamaterial Building Block with a Strong Magnetic Response in the Sub-1.5-Micrometer Region: Silicon Colloid Nanocavities.* Advanced Materials, 24, 5934–5938, 2012. 8

[24] R. Fenollosa, F. Meseguer, and M. Tymczenko. *Silicon colloids: from microcavities to photonic sponges.* Advanced Materials, 20, 95–98, 2008. 8

[25] J. Proust, F. Bedu, S. Chenot, I. Soumahoro, I. Ozerov, B. Gallas, R. Abdeddaim, and N. Bonod. *Chemical alkaline etching of silicon mie particles.* Advanced Optical Materials, 3, 1280–1286, 2015. 8

[26] M. Naffouti, T. David, A. Benkouider, L. Favre, A. Ronda, I. Berbezier, S. Bidault, N. Bonod, and M. Abbarchi. *Fabrication of poly-crystalline Si-based Mie resonators via amorphous Si on SiO2 dewetting.* Nanoscale, 8, 2844–2849, 2016. 8

[27] I. Staude and J. Schilling. *Metamaterial-inspired silicon nanophotonics.* Nature Photonics, 11, 274–284, 2017. 8, 14

[28] J. Petschulat, J. Yang, C. Menzel, C. Rockstuhl, A. Chipouline, P. Lalanne, A. Tüennermann, F. Lederer, and T. Pertsch. *Understanding the electric and magnetic response of isolated metaatoms by means of a multipolar field decomposition.* Optics Express, 18, 14454–14466, 2010. 9

[29] P. Grahn, A. Shevchenko, and M. Kaivola. *Electromagnetic multipole theory for optical nanomaterials.* New Journal of Physics, 14, 093033, 2012. 9

[30] P. T. Kristensen and S. Hughes. *Modes and mode volumes of leaky optical cavities and plasmonic nanoresonators.* ACS Photonics, 1, 2–10, 2013. 10

[31] E. Muljarov, M. Doost, and W. Langbein. *Exact mode volume and Purcell factor of open optical systems.* arXiv preprint arXiv:1409.6877, 2014.

[32] B. Vial, F. Zolla, A. Nicolet, and M. Commandré. *Quasimodal expansion of electromagnetic fields in open two-dimensional structures.* Physical Review A, 89, 023829, 2014.

[33] Q. Bai, M. Perrin, C. Sauvan, J.-P. Hugonin, and P. Lalanne. *Efficient and intuitive method for the analysis of light scattering by a resonant nanostructure.* Opt. Express, 21, 27371–27382, 2013. 10, 68

[34] D. A. Powell. *Resonant dynamics of arbitrarily shaped meta-atoms.* Physical Review B, 90, 075108, 2014. 10, 68

[35] D. A. Powell. *Interference between the Modes of an All-Dielectric Meta-atom.* Physical Review Applied, 7, 034006, 2017. 10, 68

[36] M. Kerker, D.-S. Wang, and C. L. Giles. *Electromagnetic scattering by magnetic spheres.* Journal of the Optical Society of America, 73, 765–767, 1983. 10, 94

[37] A. García-Etxarri, R. Gómez-Medina, L. S. Froufe-Pérez, C. López, L. Chantada, F. Scheffold, J. Aizpurua, M. Nieto-Vesperinas, and J. J. Sáenz. *Strong magnetic response of submicron Silicon particles in the infrared.* Optics Express, 19, 4815–4826, 2011. 10, 56, 94

[38] J. Geffrin, B. García-Cámara, R. Gómez-Medina, P. Albella, L. Froufe-Pérez, C. Eyraud, A. Litman, R. Vaillon, F. González, M. Nieto-Vesperinas, et al. *Magnetic and electric coherence in forward-and back-scattered electromagnetic waves by a single dielectric subwavelength sphere.* Nature Communications, 3, 1171, 2012. 10, 94

[39] Y. H. Fu, A. I. Kuznetsov, A. E. Miroshnichenko, Y. F. Yu, and B. Luk'yanchuk. *Directional visible light scattering by silicon nanoparticles.* Nature Communications, 4, 1527, 2013. 10

[40] S. Person, M. Jain, Z. Lapin, J. J. Saenz, G. Wicks, and L. Novotny. *Demonstration of zero optical backscattering from single nanoparticles.* Nano Letters, 13, 1806–1809, 2013. 11

[41] A. E. Krasnok, C. R. Simovski, P. A. Belov, and Y. S. Kivshar. *Superdirective dielectric nanoantennas.* Nanoscale, 2014. 11

[42] R. Alaee, R. Filter, D. Lehr, F. Lederer, and C. Rockstuhl. *A generalized Kerker condition for highly directive nanoantennas.* Optics Letters, 40, 2645–2648, 2015. 94

[43] W. Liu, J. Zhang, B. Lei, H. Ma, W. Xie, and H. Hu. *Ultra-directional forward scattering by individual core-shell nanoparticles.* Optics Express, 22, 16178–16187, 2014. 11, 94

[44] L. Novotny and N. van Hulst. *Antennas for light.* Nature Photonics, 5, 83-90, 2011. 11

[45] X. Zambrana-Puyalto and N. Bonod. *Purcell factor of spherical Mie resonators.* Phys. Rev. B, 91, 195422, 2015. 11, 114

[46] B. Rolly, B. Stout, and N. Bonod. *Boosting the directivity of optical antennas with magnetic and electric dipolar resonant particles.* Optics Express, 20, 20376–20386, 2012. 11

[47] A. Devilez, B. Stout, and N. Bonod. *Compact Metallo-Dielectric Optical Antenna for Ultra Directional and Enhanced Radiative Emission.* ACS Nano, 4, 3390-3396, 2010. 11

[48] S. Karaveli and R. Zia. *Strong enhancement of magnetic dipole emission in a multilevel electronic system.* Optics Letters, 35, 3318–3320, 2010. 11

[49] S. Karaveli and R. Zia. *Spectral Tuning by Selective Enhancement of Electric and Magnetic Dipole Emission.* Physical Review Letters, 106, 193004, 2011. 11

[50] M. K. Schmidt, R. Esteban, J. J. Sáenz, I. Suárez-Lacalle, S. Mackowski, and J. Aizpurua. *Dielectric antennas - a suitable platform for controlling magnetic dipolar emission.* Optics Express, 20, 13636–13650, 2012. 11

[51] B. Rolly, B. Bebey, S. Bidault, B. Stout, and N. Bonod. *Promoting magnetic dipolar transition in trivalent lanthanide ions with lossless Mie resonances.* Physical Review B: Condensed Matter and Materials Physics, 85, 245432, 2012. 11

[52] G. Boudarham, R. Abdeddaim, and N. Bonod. *Enhancing the magnetic field intensity with a dielectric gap antenna.* Applied Physics Letters, 104, 021117, 2014. 11

[53] R. M. Bakker, D. Permyakov, Y. F. Yu, D. Markovich, R. Paniagua-Domínguez, L. Gonzaga, A. Samusev, Y. Kivshar, B. Lukyanchuk, and A. I. Kuznetsov. *Magnetic and electric hotspots with silicon nanodimers.* Nano Letters, 15, 2137–2142, 2015.

[54] A. E. Miroshnichenko and Y. S. Kivshar. *Fano resonances in all-dielectric oligomers.* Nano Letters, 12, 6459–6463, 2012.

[55] K. E. Chong, B. Hopkins, I. Staude, A. E. Miroshnichenko, J. Dominguez, M. Decker, D. N. Neshev, I. Brener, and Y. S. Kivshar. *Observation of Fano resonances in all-dielectric nanoparticle oligomers.* Small, 10, 1985–1990, 2014. 11

[56] M. R. Shcherbakov, D. N. Neshev, B. Hopkins, A. S. Shorokhov, I. Staude, E. V. Melik-Gaykazyan, M. Decker, A. A. Ezhov, A. E. Miroshnichenko, I. Brener, et al. *Enhanced Third-Harmonic Generation in Silicon Nanoparticles Driven by Magnetic Response.* Nano Letters, 14, 6488–6492, 2014. 12, 93, 94

[57] A. S. Shorokhov, E. V. Melik-Gaykazyan, D. A. Smirnova, B. Hopkins, K. E. Chong, D.-Y. Choi, M. R. Shcherbakov, A. E. Miroshnichenko, D. N. Neshev, A. A. Fedyanin, et al. *Multifold enhancement of third-harmonic generation in dielectric nanoparticles driven by magnetic Fano resonances.* Nano letters, 16, 4857–4861, 2016. 12, 94

[58] M. R. Shcherbakov, A. S. Shorokhov, D. N. Neshev, B. Hopkins, I. Staude, E. V. Melik-Gaykazyan, A. A. Ezhov, A. E. Miroshnichenko, I. Brener, A. A. Fedyanin, et al. *Nonlinear interference and tailorable third-harmonic generation from dielectric oligomers.* ACS Photonics, 2, 578–582, 2015. 94

[59] Y. Yang, W. Wang, A. Boulesbaa, I. I. Kravchenko, D. P. Briggs, A. Puretzky, D. Geohegan, and J. Valentine. *Nonlinear Fano-resonant dielectric metasurfaces.* Nano Letters, 15, 2015. 12, 94

[60] D. Smirnova and Y. S. Kivshar. *Multipolar nonlinear nanophotonics.* Optica, 3, 1241–1255, 2016. 12, 93, 94

[61] D. A. Smirnova, A. B. Khanikaev, L. A. Smirnov, and Y. S. Kivshar. *Multipolar third-harmonic generation driven by optically-induced magnetic resonances.* arXiv preprint arXiv:1601.04109, 2016. 12, 14, 94

[62] V. Gili, L. Carletti, A. Locatelli, D. Rocco, M. Finazzi, L. Ghirardini, I. Favero, C. Gomez, A. Lemaître, M. Celebrano, et al. *Monolithic AlGaAs second-harmonic nanoantennas*. Optics Express, 24, 15965–15971, 2016. 12, 94

[63] L. Carletti, A. Locatelli, O. Stepanenko, G. Leo, and C. De Angelis. *Enhanced second-harmonic generation from magnetic resonance in AlGaAs nanoantennas*. Optics Express, 23, 26544–26550, 2015. 94

[64] L. Carletti, A. Locatelli, D. Neshev, and C. De Angelis. *Shaping the radiation pattern of second-harmonic generation from AlGaAs dielectric nanoantennas*. ACS Photonics, 3, 1500–1507, 2016. 12, 94

[65] P. A. Dmitriev, D. G. Baranov, V. A. Milichko, S. V. Makarov, I. S. Mukhin, A. K. Samusev, A. E. Krasnok, P. A. Belov, and Y. S. Kivshar. *Resonant Raman scattering from silicon nanoparticles enhanced by magnetic response*. Nanoscale, 8, 9721–9726, 2016. 12

[66] G. P. Zograf, M. I. Petrov, D. A. Zuev, P. A. Dmitriev, V. A. Milichko, S. V. Makarov, and P. A. Belov. *Resonant Nonplasmonic Nanoparticles for Efficient Temperature-Feedback Optical Heating*. Nano Letters, 17, 2945–2952, 2017. 12

[67] M. Garín, R. Fenollosa, R. Alcubilla, L. Shi, L. Marsal, and F. Meseguer. *All-silicon spherical-Mie-resonator photodiode with spectral response in the infrared region*. Nature Communications, 5, ncomms4440, 2014. 12

[68] S. J. Kim, I. Thomann, J. Park, J. Kang, A. Vasudev, and M. L. Brongersma. *Light Trapping for Solar Fuel Generation with Mie Resonances*. Nano Letters, 2014. 12

[69] G. Grzela, R. Paniagua-Domínguez, T. Barten, Y. Fontana, J. A. Sánchez-Gil, and J. Gómez Rivas. *Nanowire antenna emission*. Nano letters, 12, 5481–5486, 2012. 12

[70] Y. Yang, W. Wang, A. Boulesbaa, I. I. Kravchenko, D. P. Briggs, A. Puretzky, D. Geohegan, and J. Valentine. *Nonlinear Fano-resonant dielectric metasurfaces*. Nano letters, 15, 2015. 12

[71] O. Yavas, M. Svedendahl, P. Dobosz, V. Sanz, and R. Quidant. *On-a-chip biosensing based on all-dielectric nanoresonators*. Nano Letters, 2017. 12

[72] B. García-Cámara, R. Gómez-Medina, J. J. Sáenz, and B. Sepúlveda. *Sensing with magnetic dipolar resonances in semiconductor nanospheres*. Optics Express, 21, 23007–23020, 2013. 12

[73] N. Bontempi, K. E. Chong, H. W. Orton, I. Staude, D.-Y. Choi, I. Alessandri, Y. S. Kivshar, and D. N. Neshev. *Highly sensitive biosensors based on all-dielectric nanoresonators*. Nanoscale, 9, 4972–4980, 2017. 12

[74] Y. Yang, I. I. Kravchenko, D. Briggs, and J. Valentine. *Dielectric metasurface analogue of electromagnetically induced transparency.* In *CLEO: QELS_Fundamental Science*, pages FW4C–7. Optical Society of America, 2015. 12

[75] A. Arbabi, Y. Horie, M. Bagheri, and A. Faraon. *Dielectric metasurfaces for complete control of phase and polarization with subwavelength spatial resolution and high transmission.* Nature Nanotechnology, 10, 937–943, 2015. 13

[76] S. Kruk, B. Hopkins, I. I. Kravchenko, A. Miroshnichenko, D. N. Neshev, and Y. S. Kivshar. *Invited Article: Broadband highly efficient dielectric metadevices for polarization control.* APL Photonics, 1, 030801, 2016.

[77] P. Lalanne, S. Astilean, P. Chavel, E. Cambril, and H. Launois. *Design and fabrication of blazed binary diffractive elements with sampling periods smaller than the structural cutoff.* JOSA A, 16, 1143–1156, 1999. 13

[78] D. Lin, P. Fan, E. Hasman, and M. L. Brongersma. *Dielectric gradient metasurface optical elements.* Science, 345, 298–302, 2014. 13

[79] M. Decker, I. Staude, M. Falkner, J. Dominguez, D. N. Neshev, I. Brener, T. Pertsch, and Y. S. Kivshar. *High-efficiency dielectric Huygens surfaces.* Advanced Optical Materials, 3, 813–820, 2015. 13

[80] K. E. Chong, I. Staude, A. James, J. Dominguez, S. Liu, S. Campione, G. S. Subramania, T. S. Luk, M. Decker, D. N. Neshev, et al. *Polarization-independent silicon metadevices for efficient optical wavefront control.* Nano Letters, 15, 5369–5374, 2015. 13

[81] P. Lalanne and P. Chavel. *Metalenses at visible wavelengths: past, present, perspectives.* Laser & Photonics Reviews, 11, 2017. 13, 14

[82] E. Arbabi, A. Arbabi, S. M. Kamali, Y. Horie, and A. Faraon. *Multi-wavelength polarization-insensitive lenses based on dielectric metasurfaces with meta-molecules.* Optica, 3, 628–633, 2016. 13

[83] K. Seo, M. Wober, P. Steinvurzel, E. Schonbrun, Y. Dan, T. Ellenbogen, and K. B. Crozier. *Multicolored vertical silicon nanowires.* Nano Letters, 11, 1851–1856, 2011. 13

[84] V. Flauraud, M. Reyes, R. Paniagua-Domínguez, A. I. Kuznetsov, and J. Brugger. *Silicon nanostructures for bright field full color prints.* ACS Photonics, 4, 1913–1919, 2017. 13, 14

[85] P. R. Wiecha, A. Arbouet, C. Girard, A. Lecestre, G. Larrieu, and V. Paillard. *Evolutionary multi-objective optimisation of colour pixels based on dielectric nano-antennas.* arXiv preprint arXiv:1609.06709, 2016. 13, 67

[86] J. Sautter, I. Staude, M. Decker, E. Rusak, D. N. Neshev, I. Brener, and Y. S. Kivshar. *Active tuning of all-dielectric metasurfaces.* ACS Nano, 9, 4308–4315, 2015. 13

[87] T. Lewi, H. A. Evans, N. A. Butakov, and J. A. Schuller. *Ultrawide Thermo-Optic Tuning of PbTe Meta-atoms*. Nano Letters, 2017. 13

[88] P. P. Iyer, M. Pendharkar, and J. A. Schuller. *Electrically reconfigurable metasurfaces using heterojunction resonators*. Advanced Optical Materials, 4, 1582–1588, 2016. 13

[89] M. Decker and I. Staude. *Resonant dielectric nanostructures: a low-loss platform for functional nanophotonics*. Journal of Optics, 18, 103001, 2016. 14

[90] K. Yee. *Numerical solution of initial boundary value problems involving Maxwell's equations in isotropic media*. IEEE Transactions on antennas and propagation, 14, 302–307, 1966. 15

[91] A. Taflove and S. C. Hagness. *Computational electrodynamics: the finite-difference time-domain method*. Artech house, 2005. 15

[92] G. Mie. *Beiträge zur Optik trüber Medien, speziell kolloidaler Metallösungen*. Annalen der physik, 330, 377–445, 1908. 15

[93] C. F. Bohren and D. R. Huffman. *Absorption and scattering of light by small particles*. Wiley science paperback series. Wiley, 1983. 16, 18, 19, 28, 40, 51, 56

[94] M. I. Mishchenko, L. D. Travis, and A. A. Lacis. *Scattering, absorption, and emission of light by small particles*. Cambridge university press, 2002.

[95] M. I. Mishchenko, N. T. Zakharova, N. G. Khlebtsov, G. Videen, and T. Wriedt. *Comprehensive thematic T-matrix reference database: A 2015–2017 update*. Journal of Quantitative Spectroscopy and Radiative Transfer, 2017. 28

[96] P. C. Waterman. *Symmetry, unitarity, and geometry in electromagnetic scattering*. Physical Review D: Particles and Fields, 3, 825, 1971. 16

[97] J. D. Jackson. *Classical Electrodynamics : Third Edition*. John Wiley & Sons, New York, 1999. 16, 51

[98] J. A. Stratton. *Electromagnetic theory*. John Wiley & Sons, 2007. 16, 31

[99] W. Chew. *Waves and fields in inhomogeneous media*. Van Nostrand Reinhold, 1990. 18, 19

[100] R. G. Newton. *Scattering theory of waves and particles*. International series in pure and applied physics. McGraw-Hill (New York), 1966. 19, 20, 27, 28, 31, 57, 72

[101] H. M. Nussenzveig. *Causality and dispersion relations*. 1972. 23, 27, 69, 70, 71, 72, 86

[102] I. Fernandez-Corbaton and C. Rockstuhl. *Unified theory to describe and engineer conservation laws in light-matter interactions*. Physical Review A, 95, 053829, 2017. 23

[103] H. Hulst. *Light scattering by small particles*. Structure of matter series. Wiley, 1957. 27, 28, 40, 51

[104] M. I. Mishchenko, L. D. Travis, and A. A. Lacis. *Multiple scattering of light by particles: radiative transfer and coherent backscattering*. Cambridge University Press, 2006. 28

[105] E. C. Le Ru, W. R. Somerville, and B. Auguié. *Radiative correction in approximate treatments of electromagnetic scattering by point and body scatterers*. Physical Review A, 87, 012504, 2013. 31, 33, 35, 52, 53

[106] R. Colom, A. Devilez, N. Bonod, and B. Stout. *Optimal interactions of light with magnetic and electric resonant particles*. Physical Review B, 93, 045427, 2016. 31, 41, 52, 53, 54, 56, 62, 64

[107] S. Albaladejo, R. Gómez-Medina, L. Froufe-Pérez, H. Marinchio, R. Carminati, J. Torrado, G. Armelles, A. García-Martín, and J. J. Saénz. *Radiative corrections to the polarizability tensor of an electrically small anisotropic dielectric particle*. Optics Express, 18, 3556–3567, 2010. 33, 52

[108] G. C. des Francs, A. Bouhelier, E. Finot, J. C. Weeber, A. Dereux, C. Girard, and E. Dujardin. *Fluorescence relaxation in the near–field of a mesoscopic metallic particle: distance dependence and role of plasmon modes*. Optics Express, 16, 17654–17666, 2008. 33

[109] F. Monticone and A. Alu. *Embedded photonic eigenvalues in 3D nanostructures*. Physical Review Letters, 112, 213903, 2014. 34

[110] É. Castanié, R. Vincent, R. Pierrat, and R. Carminati. *Absorption by an optical dipole antenna in a structured environment*. International Journal of Optics, 2012, 2012. 34

[111] M. P. Busson, B. Rolly, B. Stout, N. Bonod, and S. Bidault. *Accelerated single photon emission from dye molecule-driven nanoantennas assembled on DNA*. Nature Communications, 3, 962–, 2012. 34

[112] D. Schebarchov, B. Auguié, and E. C. Le Ru. *Simple accurate approximations for the optical properties of metallic nanospheres and nanoshells*. Physical Chemistry Chemical Physics, 15, 4233–4242, 2013. 35

[113] P. B. Johnson and R.-W. Christy. *Optical constants of the noble metals*. Physical review B, 6, 4370, 1972. 35

[114] V. Grigoriev, N. Bonod, J. Wenger, and B. Stout. *Optimizing nanoparticle designs for ideal absorption of light*. ACS Photonics, 2, 263–270, 2015. 40, 42, 58

[115] R. Fleury, J. Soric, and A. Alù. *Physical bounds on absorption and scattering for cloaked sensors.* Physical Review B, 89, 045122, 2014. 41

[116] S. Tretyakov. *Maximizing absorption and scattering by dipole particles.* Plasmonics, 9, 935–944, 2014. 42

[117] F. Moreno, P. Albella, and M. Nieto-Vesperinas. *Analysis of the spectral behavior of localized plasmon resonances in the near-and far-field regimes.* Langmuir, 29, 6715–6721, 2013. 44, 45

[118] C. Menzel, E. Hebestreit, S. Mühlig, C. Rockstuhl, S. Burger, F. Lederer, and T. Pertsch. *The spectral shift between near-and far-field resonances of optical nano-antennas.* Optics Express, 22, 9971–9982, 2014.

[119] A. J. Yuffa, Y. Gutierrez, J. M. Sanz, R. A. de la Osa, J. M. Saiz, F. González, F. Moreno, and G. Videen. *Frequency shift between near-and far-field scattering resonances in dielectric particles.* JOSA A, 32, 1638–1642, 2015. 44

[120] E. Wolf and M. Nieto-Vesperinas. *Analyticity of the angular spectrum amplitude of scattered fields and some of its consequences.* JOSA A, 2, 886–890, 1985. 45

[121] R. Colom, A. Devilez, S. Enoch, B. Stout, and N. Bonod. *Polarizability expressions for predicting resonances in plasmonic and Mie scatterers.* Phys. Rev. A, 95, 063833, 2017. 51

[122] M. Mishchenko, L. Travis, and A. Lacis. *Scattering, Absorption, and Emission of Light by Small Particles.* Cambridge University Press, 2002. 51

[123] L. Novotny and B. Hecht. *Principles of Nano-Optics.* Cambridge University Press, 2006. 52

[124] M. I. Tribelsky and B. S. Luk'yanchuk. *Anomalous light scattering by small particles.* Phys. Rev. Lett., 97, 263902, 2006. 51

[125] S. Enoch and N. Bonod. *Plasmonics: From Basics to Advanced Topics.* Springer, Berlin, 2012. 51

[126] J. A. Schuller, R. Zia, T. Taubner, and M. L. Brongersma. *Dielectric Metamaterials Based on Electric and Magnetic Resonances of Silicon Carbide Particles.* Physical Review Letters, 99, 107401, 2007. 51, 54

[127] M. I. Tribelsky and A. E. Miroshnichenko. *Giant in-particle field concentration and Fano resonances at light scattering by high-refractive-index particles.* Physical Review A, 93, 053837, 2016. 52, 75, 80

[128] K. L. Kelly, E. Coronado, L. L. Zhao, and G. C. Schatz. *The optical properties of metal nanoparticles: the influence of size, shape, and dielectric environment.* J. Phys. Chem. B, 107, 668–677, 2003. 52

[129] B. Stout, A. Devilez, B. Rolly, and N. Bonod. *Multipole methods for nanoantennas design: applications to Yagi-Uda configurations.* Journal of the Optical Society of America B: Optical Physics, 28, 1213–1223, 2011. 52

[130] A. Wokaun, J. Gordon, and P. Liao. *Radiation damping in surface-enhanced Raman scattering.* Phys. Rev. Lett., 48, 957, 1982. 52

[131] M. Meier and A. Wokaun. *Enhanced fields on large metal particles: dynamic depolarization.* Opt. Lett., 8, 581–583, 1983.

[132] H. Kuwata, H. Tamaru, K. Esumi, and K. Miyano. *Resonant light scattering from metal nanoparticles: Practical analysis beyond Rayleigh approximation.* Appl. Phys. Lett., 83, 4625–4627, 2003.

[133] A. Moroz. *Depolarization field of spheroidal particles.* J. Opt. Soc. Am. B, 26, 517–527, 2009. 53

[134] G. C. des Francs. *Molecule non-radiative coupling to a metallic nanosphere: an optical theorem treatment.* Int. J. Mol. Sci., 10, 3931–3936, 2009. 52

[135] D. Aspnes and A. Studna. *Dielectric functions and optical parameters of si, ge, gap, gaas, gasb, inp, inas, and insb from 1.5 to 6.0 ev.* Phys. Rev. B, 27, 985, 1983. 52, 62

[136] P. B. Johnson and R. W. Christy. *Optical Constants of the Noble Metals.* Phys. Rev. B, 6, 4370–4379, 1972. 52, 61

[137] G. Videen, J. Li, and P. Chỳlek. *Resonances and poles of weakly absorbing spheres.* J. Opt. Soc. Am. A, 12, 916–921, 1995. 54

[138] G. Watson. *A Treatise on the Theory of Bessel Functions.* Cambridge mathematical library. Cambridge University Press, 1944. 57, 58, 128, 129

[139] M. Abramowitz and I. A. Stegun. *Handbook of mathematical functions: with formulas, graphs, and mathematical tables.* Applied mathematics series. Dover Publications, New York, ninth dover printing edition, 1964. 57, 58, 127, 130

[140] C. A. Balanis. *Advanced engineering electromagnetics.* John Wiley & Sons, 2012. 57, 64

[141] R.-L. Chern and X.-X. Liu. *Effective parameters and quasi-static resonances for periodic arrays of dielectric spheres.* J. Opt. Soc. Am. B, 27, 488–497, 2010.

[142] L. Landau, E. Lifshits, and L. Pitaevskiĭ. *Electrodynamics of continuous media, 2nd edition*, volume 8 of *Course of theoretical physics.* Butterworth-Heinemann, 1995. 57

[143] A. Devilez, X. Zambrana-Puyalto, B. Stout, and N. Bonod. *Mimicking localized surface plasmons with dielectric particles.* Phys. Rev. B, 92, 241412, 2015. 58, 66

[144] B. García-Cámara, F. Moreno, F. González, J. Saiz, and G. Videen. *Light scattering resonances in small particles with electric and magnetic properties.* JOSA A, 25, 327–334, 2008. 60

[145] G. Videen and W. S. Bickel. *Light-scattering resonances in small spheres.* Physical Review A, 45, 6008, 1992.

[146] A. E. Miroshnichenko. *Non-Rayleigh limit of the Lorenz-Mie solution and suppression of scattering by spheres of negative refractive index.* Physical Review A, 80, 013808, 2009. 60

[147] Y. Yamada, H. Uyama, S. Watanabe, and H. Nozoye. *Deposition at low substrate temperatures of high-quality TiO 2 films by radical beam–assisted evaporation.* Applied Optics, 38, 6638–6641, 1999. 63

[148] A. E. Miroshnichenko, A. B. Evlyukhin, Y. F. Yu, R. M. Bakker, A. Chipouline, A. I. Kuznetsov, B. Luk'yanchuk, B. N. Chichkov, and Y. S. Kivshar. *Nonradiating anapole modes in dielectric nanoparticles.* Nature Communications, 6, 2015. 65, 80

[149] A. Mirzaei, A. E. Miroshnichenko, I. V. Shadrivov, and Y. S. Kivshar. *Superscattering of light optimized by a genetic algorithm.* Applied Physics Letters, 105, 011109, 2014. 67

[150] R.-C. Ge, P. T. Kristensen, J. F. Young, and S. Hughes. *Quasinormal mode approach to modelling light-emission and propagation in nanoplasmonics.* New Journal of Physics, 16, 113048, 2014. 68

[151] X. Zambrana-Puyalto and N. Bonod. *Purcell factor of spherical Mie resonators.* Physical Review B, 91, 195422, 2015. 68

[152] E. Muljarov and W. Langbein. *Exact mode volume and Purcell factor of open optical systems.* Physical Review B, 94, 235438, 2016. 68

[153] M. B. Doost, W. Langbein, and E. A. Muljarov. *Resonant-state expansion applied to three-dimensional open optical systems.* Phys. Rev. A, 90, 013834, 2014.

[154] P. T. Kristensen, R.-C. Ge, and S. Hughes. *Normalization of quasinormal modes in leaky optical cavities and plasmonic resonators.* Physical Review A, 92, 053810, 2015. 68

[155] F. Alpeggiani, N. Parappurath, E. Verhagen, and L. Kuipers. *Quasinormal-mode expansion of the scattering matrix.* Physical Review X, 7, 021035, 2017. 68, 73

[156] S. Fan, W. Suh, and J. Joannopoulos. *Temporal coupled-mode theory for the Fano resonance in optical resonators.* JOSA A, 20, 569–572, 2003. 68

[157] W. Suh, Z. Wang, and S. Fan. *Temporal coupled-mode theory and the presence of non-orthogonal modes in lossless multimode cavities.* IEEE Journal of Quantum Electronics, 40, 1511–1518, 2004. 68

[158] N. Van Kampen. *S-Matrix and causality condition. I. Maxwell field.* Physical Review, 89, 1072, 1953. 72

[159] V. Grigoriev, A. Tahri, S. Varault, B. Rolly, B. Stout, J. Wenger, and N. Bonod. *Optimization of resonant effects in nanostructures via Weierstrass factorization.* Physical Review A, 88, 011803, 2013. 72, 73, 83, 129

[160] B. Stout and R. McPhedran. *Egocentric physics: just about Mie.* arXiv preprint arXiv:1707.06811, 2017. 73, 76, 80

[161] M. V. Rybin, K. B. Samusev, I. S. Sinev, G. Semouchkin, E. Semouchkina, Y. S. Kivshar, and M. F. Limonov. *Mie scattering as a cascade of Fano resonances.* Optics Express, 21, 30107–30113, 2013. 80

[162] M. V. Rybin, D. S. Filonov, P. A. Belov, Y. S. Kivshar, and M. F. Limonov. *Switching from visibility to invisibility via Fano resonances: theory and experiment.* Scientific Reports, 5, 2015. 80

[163] U. Fano. *Effects of configuration interaction on intensities and phase shifts.* Physical Review, 124, 1866, 1961. 80

[164] B. Luk'yanchuk, R. Paniagua-Domínguez, A. I. Kuznetsov, A. E. Miroshnichenko, and Y. S. Kivshar. *Hybrid anapole modes of high-index dielectric nanoparticles.* Physical Review A, 95, 063820, 2017. 80

[165] B. Luk'yanchuk, R. Paniagua-Domínguez, A. I. Kuznetsov, A. E. Miroshnichenko, and Y. S. Kivshar. *Suppression of scattering for small dielectric particles: anapole mode and invisibility.* Phil. Trans. R. Soc. A, 375, 20160069, 2017. 80

[166] M. Garcia-Vergara, G. Demésy, and F. Zolla. *Extracting an accurate model for permittivity from experimental data: hunting complex poles from the real line.* Optics Letters, 42, 1145–1148, 2017. 81

[167] P. Leung and K. Pang. *Completeness and time-independent perturbation of morphology-dependent resonances in dielectric spheres.* JOSA B, 13, 805–817, 1996. 83, 85, 91

[168] G. Beck and H. M. Nussenzveig. *On the physical interpretation of complex poles of theS-matrix-I.* Il Nuovo Cimento (1955-1965), 16, 416–449, 1960. 86

[169] J. J. Thomson. *On Electrical Oscillations and the effects produced by the motion of an Electrified Sphere.* Proceedings of the London Mathematical Society, 1, 197–219, 1883. 86

[170] H. Lamb. *On a peculiarity of the wave-system due to the free vibrations of a nucleus in an extended medium.* Proceedings of the London Mathematical Society, 1, 208–213, 1900. 86

[171] R. Faggiani, A. Losquin, J. Yang, E. Mrsell, A. Mikkelsen, and P. Lalanne. *Modal Analysis of the Ultrafast Dynamics of Optical Nanoresonators.* ACS Photonics, 4, 897–904, 2017. 86, 114

[172] M. Kauranen and A. V. Zayats. *Nonlinear plasmonics.* Nature Photonics, 6, 737–748, 2012. 93

[173] G. Bachelier, J. Butet, I. Russier-Antoine, C. Jonin, E. Benichou, and P.-F. Brevet. *Origin of optical second-harmonic generation in spherical gold nanoparticles: Local surface and nonlocal bulk contributions.* Physical Review B, 82, 235403, 2010. 93

[174] J. Butet, P.-F. Brevet, and O. J. Martin. *Optical second harmonic generation in plasmonic nanostructures: From fundamental principles to advanced applications.* ACS nano, 9, 10545–10562, 2015.

[175] S. Palomba, M. Danckwerts, and L. Novotny. *Nonlinear plasmonics with gold nanoparticle antennas.* Journal of Optics A: Pure and Applied Optics, 11, 114030, 2009. 93

[176] M. Lippitz, M. A. van Dijk, and M. Orrit. *Third-harmonic generation from single gold nanoparticles.* Nano letters, 5, 799–802, 2005. 93

[177] M. Hentschel, T. Utikal, H. Giessen, and M. Lippitz. *Quantitative modeling of the third harmonic emission spectrum of plasmonic nanoantennas.* Nano Letters, 12, 3778–3782, 2012. 93

[178] Y. Zhang, F. Wen, Y.-R. Zhen, P. Nordlander, and N. J. Halas. *Coherent Fano resonances in a plasmonic nanocluster enhance optical four-wave mixing.* Proceedings of the National Academy of Sciences, 110, 9215–9219, 2013. 93

[179] Q. Lin, J. Zhang, G. Piredda, R. W. Boyd, P. M. Fauchet, and G. P. Agrawal. *Dispersion of silicon nonlinearities in the near infrared region.* Applied Physics Letters, 91, 021111, 2007. 94, 97

[180] K. Ikeda, Y. Shen, and Y. Fainman. *Enhanced optical nonlinearity in amorphous silicon and its application to waveguide devices.* Optics Express, 15, 17761–17771, 2007. 97

[181] G. Grinblat, Y. Li, M. P. Nielsen, R. F. Oulton, and S. A. Maier. *Enhanced third harmonic generation in single germanium nanodisks excited at the anapole mode.* Nano Letters, 16, 4635–4640, 2016. 94

[182] E. V. Melik-Gaykazyan, M. R. Shcherbakov, A. S. Shorokhov, I. Staude, I. Brener, D. N. Neshev, Y. S. Kivshar, and A. A. Fedyanin. *Third-harmonic generation from Mie-type resonances of isolated all-dielectric nanoparticles.* Phil. Trans. R. Soc. A, 375, 20160281, 2017. 94

[183] G. Grinblat, Y. Li, M. P. Nielsen, R. F. Oulton, and S. A. Maier. *Efficient Third Harmonic Generation and Nonlinear Subwavelength Imaging at a Higher-Order Anapole Mode in a Single Germanium Nanodisk.* ACS Nano, 11, 953–960, 2016. 94

[184] L. Ghirardini, L. Carletti, V. Gili, G. Pellegrini, L. Duò, M. Finazzi, D. Rocco, A. Locatelli, C. De Angelis, I. Favero, et al. *Polarization properties of second-harmonic generation in AlGaAs optical nanoantennas.* Optics Letters, 42, 559–562, 2017. 94

[185] L. Carletti, D. Rocco, A. Locatelli, C. De Angelis, V. Gili, M. Ravaro, I. Favero, G. Leo, M. Finazzi, L. Ghirardini, et al. *Controlling second-harmonic generation at the nanoscale with monolithic AlGaAs-on-AlOx antennas.* Nanotechnology, 28, 114005, 2017.

[186] S. Liu, M. B. Sinclair, S. Saravi, G. A. Keeler, Y. Yang, J. Reno, G. M. Peake, F. Setzpfandt, I. Staude, T. Pertsch, et al. *Resonantly enhanced second-harmonic generation using III–V semiconductor all-dielectric metasurfaces.* Nano letters, 16, 5426–5432, 2016. 94

[187] G. Grinblat, Y. Li, M. P. Nielsen, R. F. Oulton, and S. A. Maier. *Degenerate Four-Wave Mixing in a Multiresonant Germanium Nanodisk.* ACS Photonics, 4, 2144–2149, 2017. 94

[188] R. W. Boyd. *Nonlinear optics.* Academic press, 2003. 95, 96, 97

[189] A. D. Bristow, N. Rotenberg, and H. M. Van Driel. *Two-photon absorption and Kerr coefficients of silicon for 850–2200 nm.* Applied Physics Letters, 90, 191104, 2007. 97

[190] D. Pierce and W. E. Spicer. *Electronic structure of amorphous Si from photoemission and optical studies.* Physical Review B, 5, 3017, 1972. 99, 105

[191] R. Regmi, J. Berthelot, P. M. Winkler, M. Mivelle, J. Proust, F. Bedu, I. Ozerov, T. Begou, J. Lumeau, H. Rigneault, et al. *All-dielectric silicon nanogap antennas to enhance the fluorescence of single molecules.* Nano Letters, 16, 5143–5151, 2016. 102, 103

[192] S. Sundaram and E. Mazur. *Inducing and probing non-thermal transitions in semiconductors using femtosecond laser pulses.* Nature Materials, 1, 217, 2002. 107

[193] T. Y. Choi, D. J. Hwang, and C. P. Grigoropoulos. *Ultrafast laser-induced crystallization of amorphous silicon films.* Optical Engineering, 42, 3383–3388, 2003.

[194] J.-M. Shieh, Z.-H. Chen, B.-T. Dai, Y.-C. Wang, A. Zaitsev, and C.-L. Pan. *Near-infrared femtosecond laser-induced crystallization of amorphous silicon.* Applied Physics Letters, 85, 1232–1234, 2004. 107

[195] I. Rotter. *A non-Hermitian Hamilton operator and the physics of open quantum systems.* Journal of Physics A: Mathematical and Theoretical, 42, 153001, 2009. 114

[196] C. W. Hsu, B. Zhen, A. D. Stone, J. D. Joannopoulos, and M. Soljačić. *Bound states in the continuum.* Nature Reviews Materials, 1, 16048, 2016. 114

[197] M. V. Rybin, K. L. Koshelev, Z. F. Sadrieva, K. B. Samusev, A. A. Bogdanov, M. F. Limonov, and Y. S. Kivshar. *High-Q supercavity modes in subwavelength dielectric resonators.* arXiv preprint arXiv:1706.02099, 2017. 114

[198] A. Kodigala, T. Lepetit, Q. Gu, B. Bahari, Y. Fainman, and B. Kanté. *Lasing action from photonic bound states in continuum.* Nature, 541, 196–199, 2017. 114

[199] G. B. Arfken and H. J. Weber. *Mathematical methods for physicists*, 1999. 137